WESTERN SYDNEY
UNIVERSITY

A Radio Continuum Study of Planetary Nebulae and Extended Emissions in the Magellanic Clouds

Howard Leverenz

A thesis submitted for the degree of
Doctor of Philosophy
at
Western Sydney University

August 2018

Supervisors:
M. D. Filipović
N. F. H. Tothill
E. J. Crawford

Dedication

I would like to dedicate this thesis to my wife, Everdeen Tree, who has stood beside me over these years far beyond any reasonable expectations. Thank you, I love you.

Acknowledgements

First of all, I would like to express my sincere thanks to my supervisor, Miroslav Filipović, who believed in me and who has guided and supported me over the long course of this study.

I would like to express my thanks to my supervisors, Nick Tothill and Evan Crawford, for their guidance, reviews of this thesis, and comments which resulted in many improvements. I also appreciate the knowledge and expertise provided by I. S. Bojičić, J. D. Collier, K. Grieve, D. Drašković, W. A. Reid, B. Vukotić, and D. Urošević during this study.

This thesis is built upon the work of so many organizations. I used the Australia Telescope Compact Array (ATCA) and the Parkes radio telescope which are part of the Australia Telescope National Facility which is funded by the Australian Government for operation as a national facility managed by the Commonwealth Scientific and Industrial Research Organization of Australia (CSIRO). These data were made available by CSIRO through the Australia Telescope Online Archive (ATOA).[1] CSIRO also made possible critical software used for the analysis of this data: MIRIAD (Sault et al., 1995) and KARMA (Gooch, 1996).

This research has made use of the SIMBAD database and ALADIN, operated by CDS, Strasbourg, France (Wenger et al., 2000). Also used was the NASA/IPAC Extragalactic Database which is operated by the Jet Propulsion Laboratory, California Institute of Technology, under contract with the National Aeronautics and Space Administration. Data were also used from the Magellanic Cloud Emission Line Survey (MCELS) which is funded through the support of the Dean B. McLaughlin Fund at the University of Michigan and through NSF grant 9540747.

Additional software tools used were SCILAB (Scilab, 2013), MATLAB (Matlab, 2010), DS9 (Joye et al., 2003), FTOOLS (Blackburn, 1995)[2], and the PYTHON programming language.

[1] http://atoa.atnf.csiro.au/.
[2] http://heasarc.gsfc.nasa.gov/ftools/

The work presented in this thesis is, to the best of my knowledge and belief, original except as acknowledged in the text.

I hereby declare that I have not submitted this material, either in full or in part, for a degree at this or any other institution.

.....

Howard Leverenz August 27, 2018

Contents

List of Tables

List of Figures

Abstract

This thesis examines emissions from the interstellar medium (ISM) of the Small Magellanic Cloud (SMC) and reports the detection of planetary nebulae in the radio continuum (RC) from both Magellanic Clouds (MCs). New RC measurements of the planetary nebulae are used to calibrate a statistical distance scale based on the surface brightness–diameter relation (Σ–D) (defined as $\Sigma = A \times D^{-\beta}$).

The correlation between far-infrared (FIR) and RC emissions from the ISM of the SMC was investigated over scales from 3 kpc to 0.01 kpc. Good far-infrared/radio continuum (FIR/RC) correlation down to ∼15 pc was seen. The reciprocal slope of the FIR/RC emission correlation, RC/FIR, in the SMC was shown to be greatest in the most active star–forming regions with a power law slope of ∼1.14 indicating that the RC emission increases faster than the FIR emission. The slope of the other regions and the entire SMC are much flatter and in the range of 0.63–0.85. The slopes tend to follow the thermal fractions of the regions with a range of 0.5–0.95. It was found that the thermal fraction of the RC emission alone can provide the expected FIR/RC correlation. This result was consistent with a common source for ultraviolet (UV) photons which heat dust and which ionise H I to produce thermal electrons leading to free-free (FF) radiation. The UV photons, which ionise the ISM and heat the dust, come from hot young stars, the largest of which will eventually become supernovae. Non-thermal emission, in the form of synchrotron radio emission, is from ultra-relativistic electrons accelerated by supernovae. These ultra-relativistic electrons interact with the galactic magnetic field and the acceleration produces the synchrotron radiation observed. The SMC results with minimal non-thermal contributions may not provide support for coupling between the local gas density and the magnetic field intensity.

Planetary nebulae detected in the RC are frequently referred to by the shorthand "radio planetary nebulae". A search for radio planetary nebulae in the SMC resulted in ten new RC detections reported here from the 105 catalogued planetary nebula positions in the SMC (SMP S6, LIN 41, LIN 142, SMP S13, SMP S14, SMP S16, J 18, SMP S18, SMP S19, and SMP S22). Six SMC radio planetary nebulae previously detected (LIN 45, SMP S11, SMP S17,

LIN 321, LIN 339, and SMP S24) were re-observed. These sixteen radio detections represent ∼15% of the total catalogued planetary nebula population in the SMC. Six of these objects, however, were shown to have characteristics that suggest they are likely planetary nebula mimics (LIN 41, LIN 45, SMP S11, LIN 142, LIN 321, and LIN 339).

The SMC radio planetary nebula population was also used in a (Σ–D) relation study. The results of this study were consistent with previous SMC and Large Magellanic Cloud (LMC) planetary nebula measurements of the (Σ-D) relation.

This study contributed twenty-one new radio detections of planetary nebulae to the total of thirty-one radio planetary nebulae that have been detected in the LMC. The search for these radio planetary nebulae in the LMC began with the exploration of all 629 validated planetary nebula positions. All presently available data from the ATOA at 3, 6, 13, and 20 cm were examined at these positions. The newly detected planetary nebulae were: SMP L13, SMP L15, SMP L21, SMP L23, SMP L29, SMP L37, SMP L38, SMP L45, SMP L50, SMP L52, SMP L53, SMP L58, SMP L63, SMP L66, SMP L73, SMP L75, SMP L76, SMP L78, RP 659, SMP L85, and SMP L92. Seven previously detected radio planetary nebulae (Filipović et al., 2009) were also detected: SMP L47, SMP L48, SMP L62, SMP L74, SMP L83, SMP L84, and SMP L89.

An additional three planetary nebulae from the study by Filipović et al. (2009): SMP L25, SMP L33, and SMP L39 were not detected in this study but were included in the complete catalogue compilation of radio planetary nebulae presented here. One of the previous detections from that study, SMP L8, had been reclassified as a planetary nebula mimic, a compact H II region.

With the available planetary nebula 6 cm surface brightness measurements and the corresponding planetary nebula diameter data, a bootstrap resampled sample was constructed from twenty-eight LMC radio planetary nebulae and nine SMC radio planetary nebulae which revealed that Magellanic Cloud (MC) planetary nebulae were not likely to follow linear evolutionary paths. The best fitting parameters from this resampled sample were comparable to previous results from the MCs and the Galactic planetary nebulae. A value of $\beta = 2.9 \pm 0.4$ was obtained for MC planetary nebulae compared to $\beta = 3.1 \pm 0.4$ for the Galaxy. The MC planetary nebula resampled sample was used to calibrate a planetary nebula (Σ–D) statistical distance model which resulted in a predicted statistical distance error of 17%.

Since a value of $\beta = 2.9 \pm 0.4$ was found for the MC sample which is just below the minimum predicted theoretical value of $\beta = 3$, sensitivity selection effects were examined. To estimate the significance of the sensitivity selection effects, a Monte Carlo bootstrap resampled sample was created which included various sensitivity bias parameters. The best fitting parameters from the bias effects on the bootstrap resampled sample created in this way indicated that selection

effects were significant for β values larger than $\beta \sim 2.6$. The selection effect was shown to produce a measured value of $\beta = 2.9$ when the unbiased sample had a value of $\beta \sim 3.4$.

A continuous probability density function (PDF) was also constructed using a Monte Carlo bootstrap resampled sample with more advanced techniques. This approach resulted in an enhanced accuracy for the statistical distance calculation with a distance error of 16%. This error was comparable to a study by Frew et al. (2016b) which used the ($S_{H\alpha}$ -r) relation and reported a distance measurement error of 18% with a calibration sample of 1100 planetary nebulae.

List of Abbreviations

AAO	Anglo-Australian Observatory
AGB	asymptotic giant branch
ATCA	Australia Telescope Compact Array
ATOA	Australia Telescope Online Archive
CABB	Compact Array Broadband Backend
C/O	carbon/oxygen
FF	free-free
FIR	far-infrared
FIR/RC	far-infrared/radio continuum
FWHM	full width half max
HST	Hubble Space Telescope
IR	infrared
IRAS	Infrared Astronomical Satellite
ISM	interstellar medium
LMC	Large Magellanic Cloud
MASH	Macquarie/AAO/Strasbourg Hα Planetary Nebula Catalogue
MC	Magellanic Cloud
MCELS	Magellanic Cloud Emission Line Survey
MCs	Magellanic Clouds
MIR	mid-infrared

NIR	near-infrared
OLS	ordinary least squares fitting
PAH	polycyclic aromatic hydrocarbon
PDF	probability density function
PDFs	probability density functions
PNLF	planetary nebula luminosity function
RC	radio continuum
RMS	root mean square
SED	spectral energy distribution
SMC	Small Magellanic Cloud
UV	ultraviolet
VISTA	Visual and Infrared Survey Telescope for Astronomy
VMC	VISTA survey of the Magellanic Clouds
WLS	weighted least squares fitting

Publications

The research in this thesis has been presented in the following refereed journal articles which were published during my candidature:

1. Leverenz, H. and Filipović, M. D. (2013). An analysis of the FIR/RADIO continuum correlation in the small Magellanic cloud. *Astrophysics and Space Science*, 343(1):301–317

   Citations: 3

2. Leverenz, H., Filipović, M. D., Bojičić, I. S., Crawford, E. J., Collier, J. D., Grieve, K., Drašković, D., and Reid, W. A. (2016). Radio planetary nebulae in the Small Magellanic Cloud. *Astrophysics and Space Science*, 361(3):108

   Citations: 2

3. Leverenz, H., Filipovic, M. D., Vukotić, B., Urošević, D., and Grieve, K. (2017). Radio Planetary Nebulae in the Large Magellanic Cloud. *Monthly Notices of the Royal Astronomical Society*, 1811:1794–1811

Chapter 1

Goals of this Research

1.1 Primary Goal of this Research

In a galaxy, such as the Milky Way Galaxy, almost 5% of its mass consists of stars, approximately 0.5% make up the ISM, and the remainder is composed of dark matter (Lequeux, 2005). The ISM, however, can be considered the most important component of galaxies because it is the material from which stars form (Draine, 2011). The ISM consists of gas and dust and is the baryonic mass that is not in stars. The idea that the balance between the ISM and stars define galaxies as we see them was expressed by Herbig (1977). He suggested that, if the balance were even slightly different, the change in galactic character would make galaxies virtually unrecognizable.

The physics of the ISM controls galaxy formation and evolution: the formation of stars and the growth of the dust grains which provide the building blocks of planets. In spite of its fundamental importance, much of the physics of the ISM is not well understood (Klessen and Glover, 2016). Observations have shown that the ISM is very turbulent. It has a complex structure on all spatial resolutions measured and it consists of different chemical phases which evolve in time (Klessen, 2011). It appears to be a complex network of feedback loops with components linked in ways that can be influenced very significantly by galaxy-galaxy interactions. Understanding the relation between large and small scale dynamics is crucial to understanding the initial mass function and the statistics of stellar formation (Klessen and Glover, 2016).

The primary goal of this thesis is to investigate the ISM of the SMC in infrared (IR), RC, radio, optical, and mm bands. Images in the following electromagnetic bands were acquired from published sources or developed using primary data from the ATCA and the Parkes radio telescope:

1. IR: 60 μm, 100 μm from the Infrared Astronomical Satellite (IRAS)

2. IR: 70 μm, 160 μm from the Spitzer Satellite

3. RC: 3 cm, 6 cm, 13 cm, 21 cm from the ATCA and Parkes telescopes

4. Radio: H I emission at 21.1 cm from the ATCA and Parkes telescopes

5. Optical: Hα emission at 656.28 nm from the NFCCD/CTIO[1]

6. mm: CO emission at 2.6 mm from the NANTEN 4 m telescope

These images were employed to investigate the FIR/RC ratio and to compare the SMC derived ratio to the consensus value. They were also used to correlate different electromagnetic bands by applying wavelet analysis to reveal underlying structure in the spatial frequencies present in those images. Since we are unable to observe our own Galaxy from a distant vantage point, the SMC could be a proxy for the Galaxy to expose some of these features.

1.2 Secondary Goals of this Research

In order to understand the population and distribution of stars in galaxies, it is crucial to understand the creation process. The material for this process consists primarily of H I and H_2 in the form of the cold neutral medium. The cold neutral medium also contains dust and other fusion products contributed by a large population of low- to medium-mass stars that evolve into planetary nebulae.

Applying the initial mass function from (Salpeter, 1955, *The Luminosity Function and Stellar Evolution*), $\sim 95\%$ of stars formed with a mass greater than $1\,M_\odot$ have a mass between 1 and $10\,M_\odot$. This is the mass range from which stars eventually evolve off the main sequence into asymptotic giant branch (AGB) stars, to proto-planetary nebulae, then planetary nebulae, and finally white dwarf stars. The mass of white dwarf stars is on the order of $0.5\,M_\odot$. Fontaine et al. (2001) suggested that the mass returned to the ISM is $\sim 10 - 90\%$ of the initial mass of $\sim 1 - 10\,M_\odot$ main sequence stars.

This evolution into white dwarf stars of the numerous stars in this mass range is a major source of "recycled" matter. This "recycled" matter consists of hydrogen, helium, and metals.[2] The metals are produced through various fusion reactions which also release a significant amount of energy during the lifetime of the star before it enters its final phases.

Stars with a mass over $\sim 10\,M_\odot$ typically end their lives in a supernova. This very violent life-ending event occurs after a lifetime inversely proportional to the initial stellar mass cubed, $t \sim M_*^{-3}$. Supernovae inject large amounts of kinetic energy into the ISM, on the order of 10^{44} J

[1] Newtonian Focus CCD Imager/Cerro Tololo Inter-American Observatory

[2] In an astronomical context, any atom with an atomic number > 2 is referred to as a metal.

(Prialnik, 2010). This energy may produce the turbulence in the ISM leading to a cold neutral medium hierarchy of clumps which collapse into stellar systems (Klessen, 2011). Supernovae also contribute higher atomic number atoms, above Fe, which provide additional diversity to the mass of the cold neutral medium.

In the Galaxy only one new supernova is expected to emerge every 20 to 50 yr (Adams et al., 2013). On the other hand, in the Galaxy, there are ~ 3500 known planetary nebulae (Parker et al., 2016) with an estimate of 24000 ± 4000 planetary nebulae with radii $r < 1.5\,\mathrm{pc}$ (Frew, 2008). Assuming the planetary nebula phase lasts 10000 yr on average, this suggests that there are ~ 20 planetary nebulae formed each year in the Galaxy.

Most supernovae develop in the Galactic disk making them almost impossible to detect at optical wavelengths due to dust obscuration. It may be possible, though, to detect them with neutrino detectors or gravitational wave detectors (Powell et al., 2016). For planetary nebulae in the Galactic disk, the RC offers a promise of detection. RC detection of all Galactic planetary nebulae, including those otherwise hidden by gas and dust, would inform studies of the Galactic ISM by providing more accurate statistics on locations and planetary nebula formation. The well established distances to the MCs provide a basis for reliable measurements of MC planetary nebula parameters for this research. For Galactic research, however, there would still remain the problem of unambiguously identifying planetary nebulae without optical wavelengths being available for robust verification.

A secondary goal of this thesis is to use the RC bands to detect as many radio planetary nebulae in the MCs as possible within the limits of the current radio telescope technology and available RC data. These detections can contribute to understanding the ISM of the MCs and also provide measurements for a radio (Σ–D) relation study.

An additional secondary goal is to investigate the (Σ–D) relation for planetary nebulae as the basis of statistical distance measurements. A reliable distance measurement is crucial to understanding planetary nebulae (Ciardullo et al., 1999). A statistical distance measurement calculation was developed by Shklovskii (1960) who examined RC emission from Galactic supernovae and proposed that the (Σ–D) relation of Type II supernovae could be employed to determine distances to those supernovae. This idea was later applied to planetary nebulae by Amnuel et al. (1984).

The MCs offer an advantage and a disadvantage over Galactic studies when applying Amnuel's approach. First, the distances to planetary nebulae in the MCs are known to $\sim 10\%$ while the distances to Galactic planetary nebulae frequently have had large fractional errors. Even for nearby objects in the Galaxy, distance variations for different methods frequently exceed a factor of two (Hajian, 2006). On the other hand, MC RC emission flux densities are at

the limits of the current instrumentation sensitivity and only the brightest planetary nebulae are detectable in the RC. A proper sample for use with the planetary nebula (Σ–D) calculation must be based on high– and low–surface brightness planetary nebula measurements. The sensitivity issues with the available measurements require a new statistical approach to devise the distance scale based on RC measurements. The procedure in this thesis used (Σ–D) measurements with bootstrap resampled samples to simulate the full range of surface brightness values. This enabled the creation of optimal probability density functions (PDFs) for statistical distance calibration of (Σ–D) distance measurements.

Chapter 2

Introduction

2.1 Far-Infrared and Radio Continuum Emissions

This discussion of RC emissions from galaxies closely follows the development of this topic in Condon (1992). Figure 2.1 displays a representative galactic emission spectrum from the starburst galaxy M82. The figure shows the spectral energy distribution (SED) as a function of frequency which includes synchrotron and FF emissions as well as FIR radiation. This figure can be compared to the MC SEDs shown in Figures 2.6 and 2.9. The overall structure is very similar in the three examples of galactic SEDs from these three very different galaxies.

Electromagnetic energy emissions from normal galaxies are primarily from the ISM in the frequency range of 30 MHz to 3 THz (10 m $\leq \lambda \leq$ 0.1 mm). This, however, accounts for only 0.0001% of a galaxy's overall luminosity.[1] The SED of the electromagnetic emission, Figure 2.1, is primarily from three sources: thermal FF emissions, FIR emissions from heated dust, and non-thermal synchrotron emissions (e.g., Klein et al., 1988).

Thermal FF emissions are the result of interactions between electrons and ions in an ionised gas. Specifically, they are bremsstrahlung radiation created by the interaction of thermal electrons with ions. H II regions are one environment where emission from this mechanism originates. In most normal galaxies, thermal emissions are expected to comprise only 10% of the integrated output with emissions significantly less than synchrotron radiation below $\sim$ 10 GHz. FF emissions tend to dominate from 10 GHz up to the point where the FIR emission dominates, above $\sim$ 100 GHz.

FIR radiation is from dust heated mainly by UV radiation from young high mass stars ($M \geq 5_{\odot}$) and is thus a good measure of the bolometric luminosity produced by those stars (Condon, 1992). This mechanism dominates above $\sim$ 100 GHz.

[1] Also known as bolometric luminosity, which is defined as the total electromagnetic energy emitted per unit time.

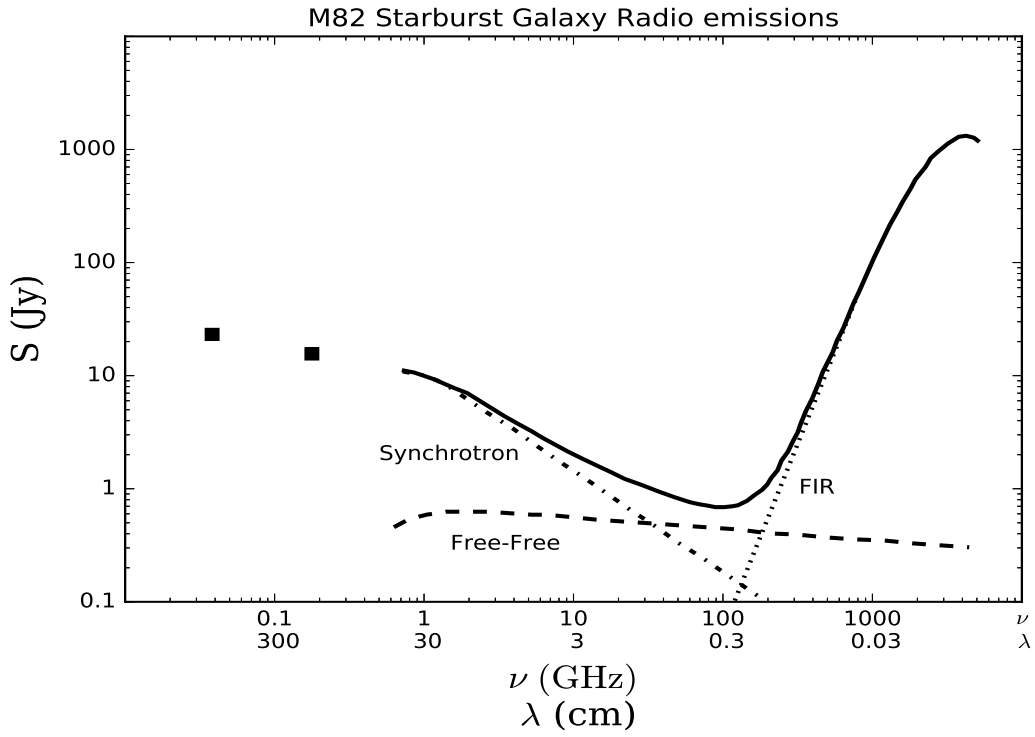

Figure 2.1: FIR and Radio Spectrum of Galaxy Messier 82. This figure after Condon (1992) is an example of a starburst galaxy and shows the sum of the FIR and RC SED of M82. It shows both thermal and non-thermal radio emissions as well as the FIR emissions from dust. It also shows the decomposition into its components: synchrotron (dash-dot), FF (dash), and FIR (dots).

Synchrotron radiation is produced by ultra-relativistic non-thermal electrons. These electrons are produced in supernovae and are responsible for the radio frequency emissions observed. These ultra-relativistic electrons from old supernovae ($> 10^5$ yr old) diffuse through the galaxy and radiate at radio frequencies due to their interaction with the galaxy's magnetic field. This is usually the dominant radio emission mechanism at lower frequencies with emissions primarily below ~ 100 GHz.

There are also emission lines in the radio spectrum which can be used as tracers for the constituents of the ISM. The H I 21 cm line at 1.4 GHz is an important probe of the most common element in the ISM, enabling both density and temperature to be determined (e.g., Burke and Graham-Smith, 2002). H_2 lacks emissions in the radio spectrum but its strong correlation with CO emission has been extensively studied in objects from the local group (Leroy et al., 2011, and references therein). The 1.3 mm and the 2.6 mm lines from the CO molecule are important tracers of the cold neutral medium in luminous galaxies because of its correlation with H_2 neutral gas. The rotational energy levels of CO molecules are populated by collisions which create the 1.3 mm and the 2.6 mm lines. This requires a high collision frequency and hence a particle density of at least $100\,\mathrm{cm}^{-3}$ (Verter, 1987; Young and Scoville, 1991).

In the ISM, over one hundred molecular species have been discovered. Most of these are detected in the radio part of the spectrum (Burke and Graham-Smith, 2002); but they are mainly found in small dense clumps and so are not useful to trace the galactic ISM as a whole.

2.1.1 Free-Free Emissions

Thermal FF emissions arise from the interaction of electrons and ions in an ionised gas, such as H II, which is created by the photoionisation of neutral hydrogen, H I, by UV photons from nearby young high mass stars. Since this is the result of the ionisation of H I, the number density of electron and protons are approximately equal, maintaining electrical neutrality. These emissions are a good measure of the total number of young massive stars in a galaxy. FF absorption is the process whereby photons lose energy to electrons in H II regions. The basic equation for the FF absorption coefficient is (Condon, 1992)

$$\left(\frac{\kappa_\nu}{\mathrm{pc}^{-1}}\right) \sim 3.3 \cdot 10^{-7} \cdot \left(\frac{n_e}{\mathrm{cm}^{-3}}\right)^2 \cdot \left(\frac{T_e}{10^4\,\mathrm{K}}\right)^{-1.35} \cdot \left(\frac{\nu}{\mathrm{GHz}}\right)^{-2.1}. \tag{2.1}$$

This equation relates the electron density, n_e; the electron temperature, T_e; and the radio frequency, ν; to the absorption coefficient, κ_ν. The opacity is defined by the integral of the absorption coefficient along the path length as

$$\tau_\nu = \int \kappa_\nu dl. \tag{2.2}$$

The emission coefficient in the radio regime, using Kirchhoff's law, can be written as

$$\varepsilon_\nu \left(T_e\right) = B_\nu \left(T_e\right) \kappa_\nu, \tag{2.3}$$

which uses the Rayleigh-Jeans approximation, B_ν, of the blackbody emission law,

$$B_\nu \left(T_e\right) = 2kT_e \frac{\nu^2}{c^2}. \tag{2.4}$$

The typical temperature of this hot hydrogen plasma is $\sim 10^6\,\mathrm{K}$. To use the Rayleigh-Jeans approximation, the emitted photon must not carry away a significant portion of the electron's energy; basically, $h\nu \ll kT_e$ needs to be satisfied. For typical RC emission frequencies of $\sim$ 1 GHz , $h\nu \sim 10^{-25}$ J. For a typical T_e of $10^6\,\mathrm{K}$, $k\,T_e \sim 10^{-19}$ J. Thus, the Rayleigh-Jeans approximation is appropriate.

The optical depth can also be defined in terms of the emission measure (Wilson et al., 2009) and the FF emission Gaunt factor, gff, (see eq. 2.26). The emission measure is defined as

$$EM = \int_0^s N_e^2 ds, \tag{2.5}$$

which is a measure of the number of electrons along the path of interest in the plasma. This can be useful for calculating the optical depth,

$$\tau_\nu \sim T_e^{-3/2} \nu^{-2} EM\, gff. \tag{2.6}$$

The compelling reason that RC frequencies are useful is that the extinction from dust is typically minimal. The efficiency of scattering, described by Mie theory (e.g., Whittet, 2002), is $Q_{sca} \sim \left(\frac{a}{\lambda}\right)^4$, where a is the dust particle radius and λ is the wavelength of the radio energy. For 1 μm grains and 1 GHz radio emission, the scattering efficiency is $\sim 10^{-22}$.

Substituting the expression for the Rayleigh-Jeans blackbody emission, Equation 2.4, and the expression for absorption, Equation 2.1, into Equation 2.3, shows that the opacity varies in frequency as $\nu^{-0.1}$. This means that, at some sufficiently high frequency, $\tau \ll 1$, and the observed thermal luminosity, L_T, will be proportional to the production rate of Lyman continuum photons, N_{UV}. This can be estimated from

$$\left(\frac{N_{UV}}{\mathrm{s}^{-1}}\right) \geq 6.3 \cdot 10^{52} \left(\frac{T_e}{10^4\,\mathrm{K}}\right)^{-0.45} \left(\frac{\nu}{\mathrm{GHz}}\right)^{0.1} \left(\frac{L_T}{10^{20}\,\mathrm{W}\cdot\mathrm{Hz}^{-1}}\right). \tag{2.7}$$

The value of T_e was measured for 169 H II regions in our Galaxy (Downes et al., 1980). From those values, the average value is calculated as $T_e = 7224 \pm 2064\,\mathrm{K}$. These H II regions are thought to be representative of H II regions in most normal galaxies. An analysis by Kennicutt and Pogge (1990) has shown that radio observations are usually the best way of detecting luminous H II regions or starburst regions which may contain high extinction due to dust.

The spectrum of FF emissions is fairly flat: $\alpha \sim 0.1$ (using $S \sim \nu^{-\alpha}$). Synchrotron emission has a spectral index of $\alpha \sim 0.8$. Because of this difference it should be possible to distinguish between the thermal FF emission and the non-thermal synchrotron emission. In many galaxies, however, the flux density has been too small to be accurately measured above $\nu \sim 10\,\mathrm{GHz}$. It is possible to remove the non-thermal contribution to the integrated flux densities by measuring low frequencies where there is little thermal contribution and then extrapolating to higher frequencies. This has been done to correct for the non-thermal contribution to measurements made at 10.7 GHz (Klein and Emerson, 1981). This procedure enables the smaller thermal flux density to be extracted from the total flux density to determine that the SMC emits primarily by way of FF radiation with negligible synchrotron emission. These measurements, as well as those of Gioia et al. (1982) who measured fifty-six spiral galaxies, produced a spectral index of $\alpha \sim 0.74$. This value suggests that the upper limit on S_T/S, the ratio of the thermal emission flux to the total flux, is $\frac{S_T}{S} \leq 0.4$ at 10.7 GHz.

This approach of extracting the thermal emission from the spectrum is not without problems. If the synchrotron emission is actually non-linear, then large errors can occur. Data from M82 were extrapolated to 32 GHz by Klein et al. (1988). They assumed a straight line non-thermal spectrum and predicted a value of $N_{UV} \sim 2 \cdot 10^{53}\,\mathrm{s}^{-1}$. Another analysis, by Carlstrom and Kronberg (1991), used essentially the same data but assumed that the non-thermal spectrum became steeper at higher frequencies. This analysis predicted a value of $N_{UV} \sim 9 \cdot 10^{53}\,\mathrm{s}^{-1}$, which is almost a factor of five higher.

Kennicutt (1983) demonstrated that $\frac{S}{F(H\alpha)}$ can provide an independent constraint on the thermal fraction of normal galaxies. Furthermore, even though $S_{1.4\,\mathrm{GHz}}$ is mostly non-thermal radiation, the observed average $\left\langle \frac{S_T}{S} \right\rangle \sim 0.1$ at $\nu = 1.4\,\mathrm{GHz}$ is accurate to within a factor of two. Discrete FIR sources in the IRAS data were not found to coincide with supernovae remnants but rather with luminous H II regions (Haslam and Osborne, 1987). Additionally, the FIR/RC correlation can be used in normal galaxies to estimate $\left\langle \frac{S_T}{S} \right\rangle$ (Condon and Yin, 1990). At high frequencies where the FF opacity is small, the following approximation, with $\alpha \sim 0.8$, provides an estimate of the global thermal fraction of the total flux density measured (Condon and Yin, 1990)

$$\frac{S}{S_T} \approx 1 + 10 \left(\frac{\nu}{\mathrm{GHz}}\right)^{0.1-\alpha}. \tag{2.8}$$

The radio brightness-temperature spectrum of a galaxy that has thermal and non-thermal radio sources co-located can be approximated (Condon, 1992) as

$$T_b \approx T_e \left[1 - e^{-\tau}\right] \left[1 + 10 \left(\frac{\nu}{\mathrm{GHz}}\right)^{0.1-\alpha}\right]. \tag{2.9}$$

In this expression, τ is the average FF optical depth from the observer and α is the non-thermal spectral index. Typically, $T_e \sim 10^4\,\mathrm{K}$ and $\alpha \sim 0.8$.

Figure 2.2 shows a family of integrated RC spectral curves of normal galaxies with a thermal to non-thermal ratio of 0.1. The spectra are characterized by different critical frequencies, ν_1. The critical frequencies are the frequencies at which the emission transitions from optically–thick frequencies to optically–thin frequencies, where $\tau = 1$. The dotted lines are the constant brightness temperature curves, T_b, showing that the thermal brightness will not exceed $10^5\,\mathrm{K}$ above 1 GHz.

The observed brightness spectrum for our Galaxy lies just above the $\nu_2 = 0.003$ GHz curve. This is shown on the curve in Figure 2.3 (Cane, 1979) with units of brightness added to the right side of the figure in mJy arcsec^{-2} to allow direct comparison with Figure 2.2.

A survey of 280 spiral galaxies was made by Hummel (1981) and a value for the median face-on disk surface brightness from measurements made at 1.4 GHz was found to be $\langle T_b \rangle = 0.75 \pm 0.25\,\mathrm{K}$. This placed the brightness spectra of most normal galaxies, as seen in Figure 2.2, between the lower spectral lines of ν_1=0.003 to 0.01 GHz.

2.1.2 Synchrotron Emissions

Galactic synchrotron radio emissions arise from ultra-relativistic electrons with energies of $E \gg m_e\,c^2$. This radiation dominates the emission spectrum for $\nu \leq 30\,\mathrm{GHz}$ in most normal galaxies (Condon, 1992). This property is useful because quantities such as particle lifetimes and energy densities in other normal galaxies can be directly compared to measurements made in our Galaxy. In normal galaxies it is also reasonable to expect that field and particle energy densities are approximately equal.

This equipartition paradigm has recently been challenged by Urošević et al. (2018). In this paper, 3D hydrodynamic supercomputer simulations were reported which suggested that this energy equipartition could not be sustained in supernova remnants. They recommended that the term "constant partition" be used to more accurately describe the cosmic ray energy density and magnetic field energy density partitioning in a supernova remnant.

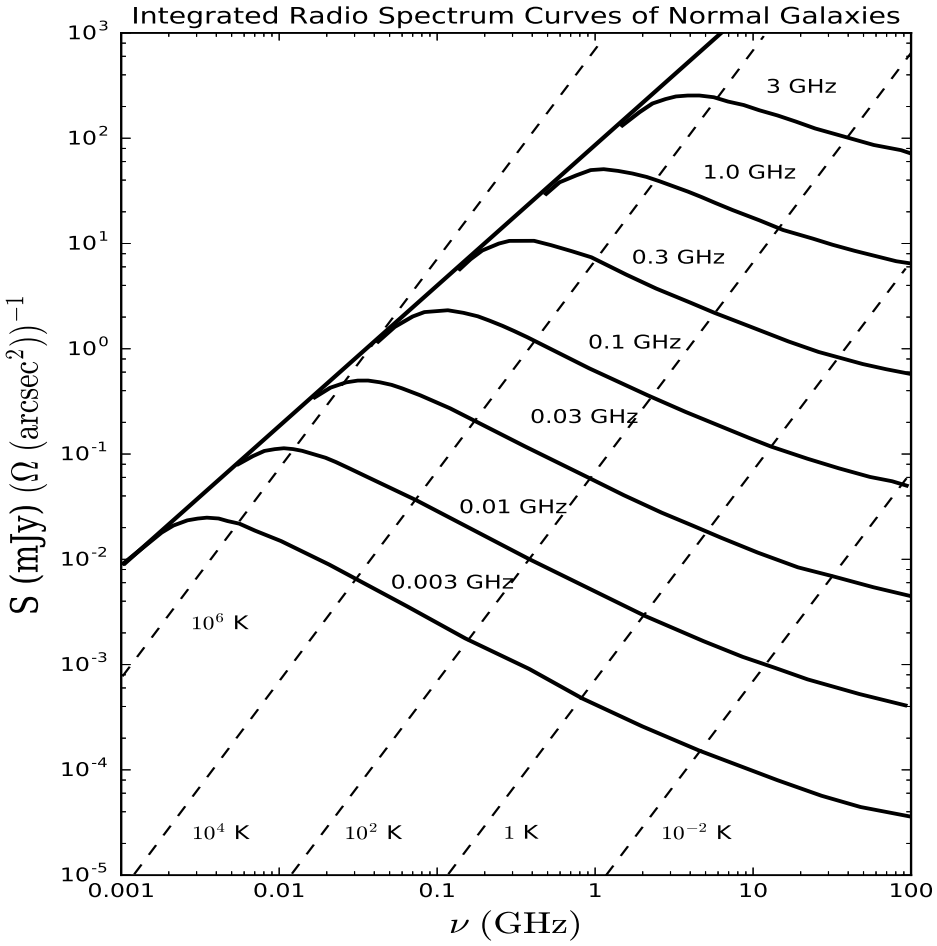

Figure 2.2: Integrated Radio Spectrum Curves and Brightness Spectra of Normal Galaxies. The galaxies represented here are assumed to have a thermal to non-thermal ratio of 0.1. From bottom to top, the successive solid line curves are labeled with the critical frequency ν_1 ($\tau = 1$). The dotted lines correspond to constant brightness temperature, T_b. This figure is after Condon (1992).

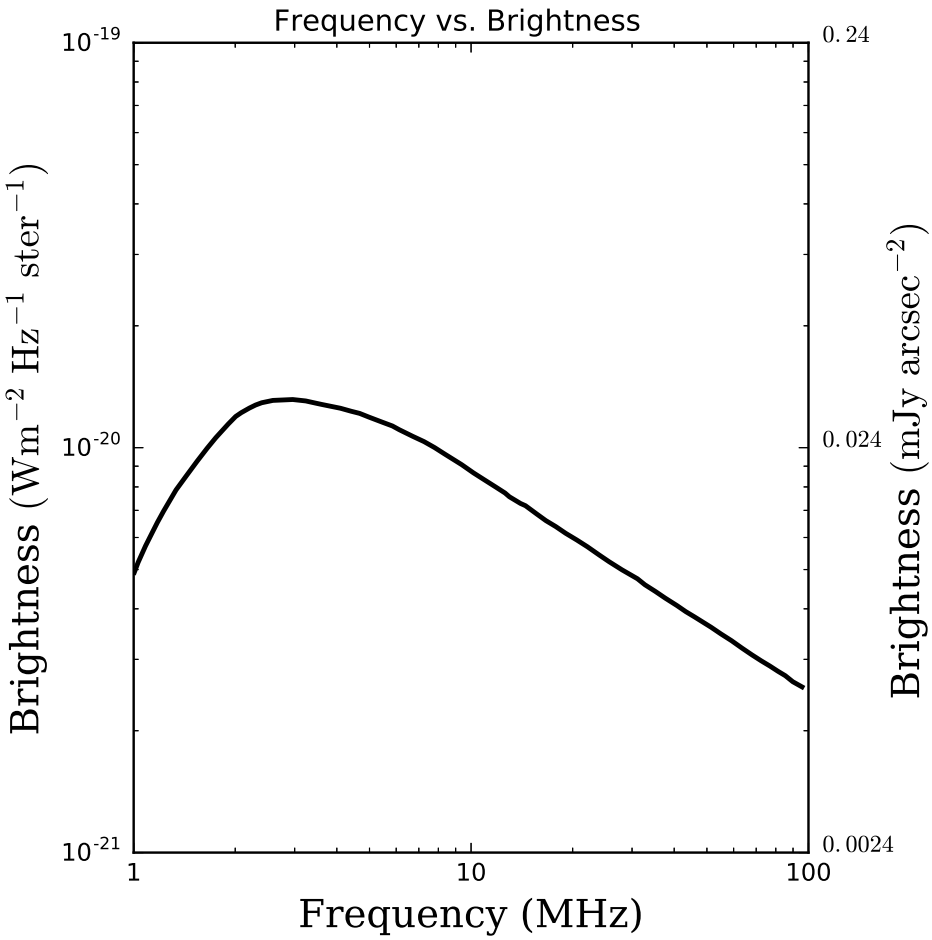

Figure 2.3: The Galaxy's RC Spectrum. After Cane (1979).

The primary frequency, also called the critical frequency, ν_c, emitted by synchrotron radio emissions is

$$\left(\frac{\nu_c}{\mathrm{GHz}}\right) \sim 0.016 \left(\frac{B \cdot \sin\theta}{\mu\mathrm{G}}\right) \left(\frac{E}{\mathrm{GeV}}\right)^2. \tag{2.10}$$

In this equation, E is the electron energy and θ is the pitch angle that the electron's velocity vector makes with the magnetic field B (Condon, 1992). In the Galaxy near us, the isotropic velocity distribution of electrons has a value of about $\langle \sin^2\theta \rangle = 2/3$. Assuming this value is about the same as in other normal galaxies suggests an electron lifetime of

$$\left(\frac{\tau_s}{\mathrm{yr}}\right) \sim 1.06 \cdot 10^9 \left(\frac{B \sin\theta}{\mu\mathrm{G}}\right)^{-3/2} \left(\frac{\nu_c}{\mathrm{GHz}}\right)^{-1/2}. \tag{2.11}$$

This is about 10^8 yr with $\nu_c = 1.5$ GHz and B = 5 μG.[2]

The electron energy loss mechanism due to inverse Compton scattering is very similar to that of synchrotron energy losses (Longair, 1992). Whereas synchrotron losses are due to acceleration from the local magnetic field density, inverse Compton scattering is due to acceleration from the local radiation field density. The synchrotron losses, however, can be considered due to electric fields from $\vec{v} \times \vec{B}$. This makes the equation for synchrotron losses identical to the equation for inverse Compton scattering except that synchrotron losses are proportional to the local magnetic energy density and inverse Compton scattering is proportional to the local radiation field density. The equations for the losses differ only in the source of the interacting energy density.

The ratio of the energy loss rate for inverse Compton scattering and synchrotron radiation is the ratio of the radiation energy density to the magnetic field energy density (Longair, 1992). This can be expressed as

$$\frac{\left(\frac{dE}{dt}\right)_{IC}}{\left(\frac{dE}{dt}\right)_{synch}} = \frac{U_{rad}}{U_{mag}}. \tag{2.12}$$

In our Galaxy, $B = 3 \times 10^{-10}$ T and $U_{rad} = 6 \times 10^5\,\mathrm{eV\,m^{-3}}$ for the optical photon field. The ratio predicted for these values is approximately three. The cosmic microwave background energy density is $U_{cmb} = 2.65 \times 10^5\,\mathrm{eV\,m^{-3}}$ which provides a limit to the ratio. This shows that the inverse Compton scattering loss compared to synchrotron radiation loss from high energy electrons can be defined by the ratio of the radiation to magnetic field energy density. With the total photon energy density taken to be the cosmic microwave background plus the stellar photon energy, if the cosmic background radiation changes, as in high redshift galaxies,

[2]The SMC has a comparable magnetic field strength of 5-10 μG (Ye and Turtle, 1991). But Sreekumar and Fichtel (1991) concluded that the cosmic ray energy density level was three to five times too low to be in equilibrium with the cosmic ray sources so this lifetime calculation might not be applicable to the SMC.

different loss characteristics can be predicted, see Murphy (2009), Schleicher and Beck (2013) and the discussion on page 21 following.

Consider a population of relativistic electrons which can be described by their number density, $N(E)dE$, with energies between E and $E+dE$. If the population has a number density of $N(E) = N_0 E^{-\gamma}$ with an isotropic velocity distribution, then their synchrotron emission coefficient is

$$\varepsilon \propto N_0 \left(B \sin\vartheta\right)^{(\gamma+1)/2} \upsilon^{(1-\gamma)/2}. \tag{2.13}$$

In this equation, ϑ is the angle between the magnetic field and the line of sight (Condon, 1992). Since the beamwidth of the synchrotron radiation is $\Delta\theta \sim m_e c^2/E \ll 1$ radian around the electron velocity vector, an observer sees synchrotron radiation only from electrons whose velocity vectors are virtually inline with the observer so that $\vartheta \sim \theta$. This means that a galaxy that has a significant z-component of magnetic field (perpendicular to the disk) will have most of its synchrotron radiation seen parallel to the disk or edge-on. The spectral index for the emission coefficient from a normal galaxy is $\alpha = (\gamma - 1)/2$ and at GHz frequencies $\alpha \sim 0.8$, suggesting that $\gamma \sim 2.6$.

Given a relativistic electron production rate of $q(E)$ and an electron energy loss rate dependent only on energy, $\varphi(E)$, then the equilibrium distribution of relativistic electrons is

$$N(E) = \varphi^{-1} \int q(E) dE. \tag{2.14}$$

Note that $\varphi(E)$ can be written as $\varphi(E) = -\zeta - \eta E - \xi E^2$. The terms are ζ for the ionisation losses, η for the relativistic bremsstrahlung and adiabatic losses, and ξ for the synchrotron and inverse Compton losses. For $q(E) \propto E^{-\gamma_0}$, the equilibrium distribution of the relativistic electron density is (Condon, 1992)

$$N\left(E\right) \propto E^{-\gamma_0} \left(\zeta E^{-1} + \eta + \xi E\right)^{-1}. \tag{2.15}$$

The break frequency, ν_b, is defined as the critical frequency (Equation 2.10) for electron energy $E = \eta/\xi$, since at energies above this value the combined synchrotron plus inverse Compton losses exceed the relativistic bremsstrahlung plus adiabatic losses of the relativistic electrons. Ionisation in normal galaxies can usually be neglected. This yields the non-thermal spectrum (Condon, 1992)

$$S_N \propto \frac{\nu^{-\alpha_0}}{1 + (\nu/\nu_b)^{\Delta\alpha}}, \tag{2.16}$$

where $\alpha_0 \equiv (\gamma_0 - 1)/2$ and $\Delta\alpha = 1/2$ is defined as the asymptotic change in the spectral index. Since ν_b is the break frequency where the spectral index changes from $\alpha = \alpha_0$ to $\alpha = \alpha_0 + \Delta\alpha$, it is much sought after. But, as Equation 2.16 shows, because the slope is actually changing very gradually, it is very difficult to determine accurately.

2.1.3 The Far-Infrared / Radio Continuum Ratio in Galaxies

One of the most puzzling and robust relationships in extragalactic astronomy is the virtually ubiquitous correlation between FIR and RC measurements of star-forming galaxies. All of the models examined here offer variations on the same basic picture. What the models attempt to do is to provide details for the process that result in the observed FIR/RC ratio. In general, the O and B stars directly heat the dust with UV radiation. The dust then emits IR radiation at wavelengths depending on their equilibrium temperature. Thermal electrons from UV ionisation are also the source of thermal RC emission (FF emission). The part of the model dealing with the thermal RC emission is pretty straightforward. The portion of the model dealing with supernovae and the overall RC emission is much less so.

In general, the model must account for the delay of 10^6 or 10^7 years before the star becomes a supernova at which time cosmic ray production commences as the mechanical energy from the explosion, $\sim 10^{44}$ J (Prialnik, 2010), propagates through the ISM as a shock wave. The shock wave accelerates electrons to highly relativistic energies. The interactions of the electrons with magnetic fields and the ISM produce non-thermal synchrotron emissions and emissions in the form of thermal FF radiation. As the supernova remnant expands from the relatively dense environment around the exploding supernova into the low density ISM, synchrotron radiation is the primary energy loss mechanism since the galactic magnetic fields typically fill most of a galaxy's volume. Non-thermal synchrotron radiation emission can continue for thousands of years as the shock front traverses the galaxy. The accepted primary source of supernova remnant radio emission, synchrotron radiation, was first proposed by Alfvén and Herlofson (1950). The turbulence caused by the supernovae may also amplify the effect of the ambient galactic magnetic field.

Thermal electrons are responsible for the thermal FF emissions. The models of FIR/RC emissions are generally crafted to produce a ratio of ten to one for non-thermal to thermal emissions (non-thermal synchrotron to thermal FF emissions). This is the predominant behavior seen in normal star-forming galaxies. This accounts for the lack of focus on the thermal FF emission in most models. However, small galaxies like the SMC, can have the preponderance of their radio continuum emission as thermal FF radiation. An overview of the primary processes that appear to control the FIR/RC correlation is shown in Figure 2.4.

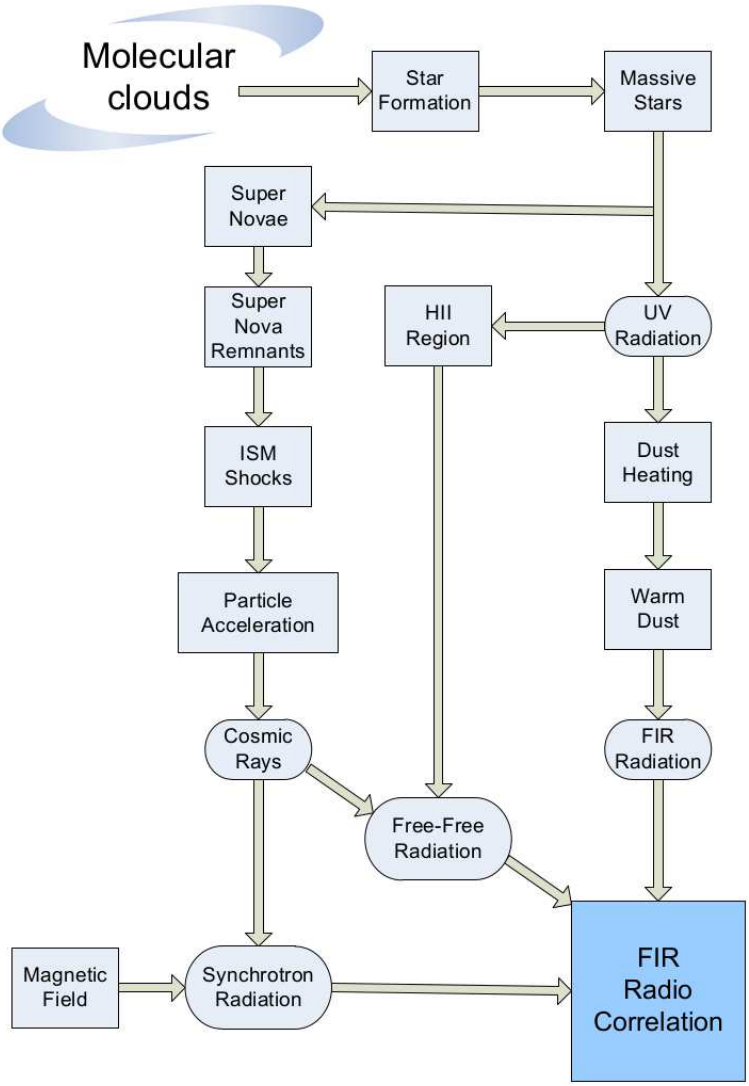

Figure 2.4: FIR/RC Correlation General Picture.

Yun et al. (2001) used the IR database created from the IRAS satellite (Neugebauer et al., 1984) to address the validity of using the RC from galaxies as a star formation tracer. The goal was to analyze RC and FIR emission from star-forming galaxies with the largest possible IR selected sample. The IR catalogue used was the 1.2 Jy IRAS Redshift Survey catalogue (Strauss et al., 1990, 1992). RC data came from the NRAO[3] VLA[4] Sky Survey (NVSS) (Condon et al., 1998). RC sources at 1.4 GHz were matched with FIR emission sources with positions separated by $< 30''$. The result was a catalogue of 1809 galaxies containing names, radial velocities, optical magnitudes, 1.4 GHz and 60 μm luninosities, and FIR/RC flux ratios.

This data set from Yun et al. (2001) yielded a best fitting linear equation in log space

$$\log\left(L_{1.4\,\mathrm{GHz}}\right) = (0.99 \pm 0.01) \times \log\left(\frac{L_{60\,\mu\mathrm{m}}}{\mathrm{L}_{\odot}}\right) + (12.07 \pm 0.08)\,, \tag{2.17}$$

which showed a very small scatter from the best fitting line. The value of q, expressed as the FIR/RC ratio, was determined with the following equation for FIR flux,

$$\left(\frac{F_{FIR}}{\mathrm{W\,m^{-2}}}\right) = 1.26 \cdot 10^{-14} \left(\frac{2.58 S_{60\,\mu m} + S_{100\,\mu m}}{\mathrm{Jy}}\right), \tag{2.18}$$

and

$$q = \log\left(\frac{F_{FIR}}{3.75 \cdot 10^{12} \mathrm{W\,m^{-2}}}\right) - \log\left(\frac{S_{RC}}{\mathrm{W\,m^{-2}Hz^{-1}}}\right)\ . \tag{2.19}$$

The overall value of q found was 2.34 ± 0.01.

Theories to explain this measurement began with the first paper to reveal the FIR/RC correlation (van der Kruit, 1971). His paper addressed emission from the cores of twenty-two galaxies, eight Seyfert galaxies, and ten normal spiral galaxies. He used 1.4 GHz RC measurements and 10 μm infrared measurements. When the two log luminosities were plotted against each other, the result was an apparent correlation that included all of the galaxies. He suggested that the correlation was due to the small size and co-location of the emission sources which he took to be the galactic nucleus.

Harwit and Pacini (1975) provided a connection between IR and RC emissions by suggesting that the galactic centres were the main emitters of IR and FF radiation along with the non-thermal RC radiation, synchrotron emission. They posited that galactic centres were the regions of star formation activity and that supernovae from massive stars were the sources of the energy that powered both the IR and the synchrotron RC emission. They viewed this process as a stage in the evolution of Seyfert galaxies.

[3]The National Radio Astronomy Observatory (NRAO) is a facility of the National Science Foundation operated under cooperative agreement by Associated Universities, Inc.

[4]Very Large Array operated by the NRAO.

A more comprehensive theory was offered by Voelk (1989) for the FIR/RC correlation of spiral galaxies which he referred to as a calorimeter theory. In this theory, he considered the entire galaxy as a single entity and made the following assumptions: The population of ionising photons and ultra-relativistic electrons is determined by the rate at which supernovae occur. The radiation field, mostly UV photons, is entirely absorbed by the dust in the ISM and this heated dust is the source of the IR emission. The ultra-relativistic cosmic ray electrons produced in the supernovae do not escape the galaxy but discharge all of their energy in synchrotron radiation due to the magnetic energy density in the galaxy.

A problem with this theory is the fate of the cosmic ray electrons. It appears to be inevitable that some to most of the cosmic ray electrons will leak out of a small galaxy with a substantial part of their energy. The "Leaky Bucket" theory offered by Helou and Bicay (1993) also addressed the FIR/RC correlation for spiral galaxies but posited a different fate for the ionising photons and relativistic electrons. In this theory, the source of energy is also the supernova rate. The supernova rate produces both UV photons and cosmic ray electrons in proportion to each other. But most UV photons escape the galaxy without heating the ISM dust and most cosmic ray electrons escape without losing much energy in RC emissions. Their approach created a phenomenological model based on the ratio $Q = \frac{IR}{RC}$ where IR is the luminosity in the range of $40 - 100\,\mu m$ and RC is the RC luminosity in the range of $\sim 2\,\mathrm{cm}$ to $\sim 20\,\mathrm{cm}$. Q was described as decreasing radially from the nucleus of a spiral galaxy to its outer edges. An important requirement for this theory was that the gas density and the magnetic field density must be well coupled on scales from 10–100 pc. This theory was applied to several spiral galaxies and appeared consistent with measurements. However, they reported that the LMC did not exhibit a radial gradient for Q. They suggested that the LMC was irregular; therefore, this model may not be applicable. No modeling attempt was reported for the SMC.

A non-calorimeter theory for spiral galaxies was published by Niklas and Beck (1997) which complemented the theory from Voelk (1989) by extending it to include thin-disk galaxies. Their analysis was predicated on the observation that the FIR/RC correlation is one of the tightest known in astrophysics which means that the underlying physics must be valid under strongly varying conditions without invoking other parameters to make the theory fit. They did this by considering the average volume density of the (almost) neutral gas as the most important quantity. They used the FF RC emissivity to indicate the star formation rate from which they obtained a "Schmidt law" -like equation (Schmidt, 1959)[5] to relate magnetic field energy density to gas density and star formation rate. They pointed out that deviations from the constant FIR/RC correlation could be due to external influences such as disruptions from an

[5]Which in its original form, $\Sigma_{SFR} \sim \Sigma_{gas}^{n}$, stated that the star formation surface density rate was proportional to the gas surface density to a power, ~ 2.

interacting galaxy. Or, it could possibly be due to variations in the radio emission process that were dependent on a central nucleus as in Seyfert galaxies. Other disruptions could come from variations in the star formation rate on the order of $\sim 10^8$ yr time scales.

The FIR/RC emission correlation from the spiral galaxy M31 was modeled by Hoernes et al. (1998) in a theory which decomposed the RC and the FIR each into two parts. The RC was decomposed into FF and synchrotron emissions and the FIR was decomposed into warm dust (27 K) and cool dust (19 K) emissions. Two correlations were studied: the FF with warm dust and the synchrotron emissions with cool dust. The FF correlation with warm dust was expected from the common source of energy which was primarily the UV radiation from massive stars. The correlation of synchrotron emission with cool dust arose from a very different mechanism. The physics behind the correlation of synchrotron emission with cool dust required that supernova cosmic ray electrons and cool dust be correlated. How this could be accomplished was not clear since cool dust heating was dominated by the interstellar radiation field, defined as blue light. This meant that two different stellar populations were needed to provide the energy for these emission mechanisms since the synchrotron radiation was not seen to correlate with the interstellar radiation field, but it did correlate with the cool dust emissions. The results from this paper showed that for UV optically-thin galaxies, like M31, coupling between gas mixed with dust and the magnetic field was responsible for the synchrotron emission correlation with the cool dust emission. This was apparently due to the local scale heights of the synchrotron disk and the dust disk being proportional to each other. In M31, with the synchrotron emission providing $\sim 80\%$ of the total radio emission, this mechanism was clearly dominant.

In the paper by Thompson et al. (2006) the FIR/RC ratio was addressed in both normal star-forming galaxies and in starburst galaxies. They examined gas surface density data over a range of four orders of magnitude in normal spirals and luminous starburst galaxies. Normal star-forming spiral galaxies were shown to have the expected magnetic energy density, from $B \sim B_{min}$, approximately equal to the cosmic ray electron energy density plus the turbulent pressure. Starburst galaxies, however, were measured to have very high gas surface densities. The analysis largely targeted meeting the observed FIR/RC ratio requirements. They suggested that, depending on the star formation rate, $B \sim B_{min}$ could describe a normal star-forming galaxy where the cosmic ray electrons must radiate virtually all of their energy as synchrotron radiation as stated in the calorimeter theory of Voelk (1989). For starburst galaxies, though, it appeared that $B \gg B_{min}$ must be the case to match the calorimeter theory with additional cooling from FF radiation. Generally, their analysis supported the Voelk (1989) calorimeter theory for FIR/RC correlation for normal spiral galaxies and starburst galaxies. Several predictions were offered to verify this analysis for starburst galaxies:

1. The RC SED should be flatter below $\sim$ 1 GHz than above.

2. There should be an appreciable γ-ray flux from starburst galaxies attributable to π^0 production.

3. Magnetic field strength should be found to have $B > B_{min}$.

4. If $B \gg B_{min}$, then inverse Compton emissions are not expected to contribute to X-ray emission.

The state and evolution of the ISM in a star-forming galaxy is primarily dependent on galaxy-galaxy interactions. The influx of gas and dust with the accompanying turbulence causes a great deal of new star formation. Another prominent process comes from feedback as the most massive stars produce strong stellar winds at the end point of their lives before they become supernovae. Then the explosive shocks from the supernova explosions cause turbulence which injects a tremendous amount of mass and energy into the ambient ISM (Wilcots, 2008). The massive stars that become supernovae have two important attributes: they are very hot and they live only some millions of years before becoming supernovae.

The ISM properties of twenty-nine galaxies were published by Murphy et al. (2008) in an examination of the physics and morphology of disk galaxies using Spitzer FIR and Westerbork Synthesis Radio Telescope RC images. In eighteen of the galaxies examined, 1 kpc resolution was achieved at 70 μm and at 22 cm. The wavelet analysis *à trous* algorithm (Biajaoui et al., 1989; Stark et al., 1998; van den Berg, 2004) was applied to decompose the 70 μm images into two components: the disk and the star-forming structures.

The ISM is frequently studied with the two-phase model from McKee (1995). In this model, atomic, ionised, and molecular components covering a large range of energetic states and densities were combined into two gaseous thermal phases. Murphy et al. (2008) noted that there was a third phase, which was frequently overlooked, the relativistic, or non-thermal, phase which consisted of cosmic rays and magnetic fields.

This third phase is dynamically important and contributes to regulating star formation and galactic evolution. Magnetic fields resist the collapse of interstellar matter into the galaxy's gravitational potential and help confine cosmic rays to galactic disks, providing a hydrostatic balance and possibly dictating the structure of spiral arms. If there is excessively large pressure from cosmic rays, Parker instability can occur which can breach the magnetic fields in the disk and allow for uncontrolled losses of cosmic ray electrons and other material from the galaxy's ISM (Murphy et al., 2008).

The mean free path of UV photons that cause heating of dust in the ISM is $\sim$100 pc. This is much shorter than the diffusion length expected of cosmic ray electrons. This leads to

the suggestion that the RC map of a galaxy should look like a smoothed representation of its infrared map (Bicay and Helou, 1990).

These ideas all apply to starburst galaxies or normal spiral galaxies, but not to dim irregular galaxies. Thermal emission was considered a contaminant by Murphy et al. (2008) for this two component analysis and steps were taken to remove that contribution in order to study the FIR/RC.

Murphy (2009) predicted observational changes due to large redshifts, including FIR/RC correlation. His paper primarily addressed starburst galaxies and ordinary spiral galaxies, which were modeled to have synchrotron emission as the main source of RC energy. In order to maintain the FIR/RC correlation at an approximately constant value,

$$\frac{U_B}{U_{CR} + U_{CMB}} \geq 1, \tag{2.20}$$

where U_B is the magnetic field energy density, U_{CR} is the cosmic ray radiation density, and U_{CMB} is the cosmic microwave background radiation density. The cosmic microwave background radiation density increases as a function of redshift,

$$U_{CMB} \propto (1+z)^4. \tag{2.21}$$

At $z = 0$, $U_{CMB} \sim 4.2 \times 10^{-13}\,\mathrm{erg\,cm^{-3}}$ and the radiation field in the Galaxy is $U_{MW} \sim 10^{-12}\,\mathrm{erg\,cm^{-3}}$. Thus inverse Compton losses in the Galaxy are negligible but at high redshifts like $z = 3$, U_B would need to be $\sim 50\,\mu$G in order to maintain the FIR/RC ratio. But since there is no basis to suggest that at higher redshifts the magnetic field strengths are higher than at low redshifts (in fact the opposite has been suggested by Beck et al. (1996)), the emission from galaxies at high redshifts would approach the thermal emission limit. In the galaxies considered by Murphy (2009), this was only $\sim 10\%$ of the expected emission so that the FIR/RC ratio would be expected to increase. The nominal FIR/RC ratio of 2.64 dex was calculated to approach an asymptote of ~ 3.6 dex as z increases to $z = 4$ for a magnetic field of $B = 10\,\mu$G. At higher values of B, the asymptotic value for FIR/RC was approached at increased redshift values.

Murphy (2009) also reported results for sub-millimeter galaxies which had FIR/RC ratios near the canonical value up to $z \sim 1$. At high redshifts, however, the FIR/RC ratios were *lower* than the canonical value. Synchrotron radiation would also be completely suppressed due to inverse Compton scattering from the cosmic microwave background. FF emission would be detectable particularly ≥ 10 GHz and could provide a probe for determining the high–z star formation history of galaxies.

Dumas et al. (2011) looked at the FIR/RC correlation in M51 at resolutions from 0.2 kpc to 30 kpc. They were able to show that the correlation was not uniform across the disk and that it displayed local extremes dependent on galactic structures. They suggested that changes in the FIR/RC correlation reflected variation in the ISM. Possible causes for the variations were discussed. These included changes in the opacity of the dust and changes in the relation between the gas density and magnetic field strength as well as the possibility of a synchrotron emission decrease due to cooling of the cosmic ray electrons.

A new analysis approach was proposed by Schleicher and Beck (2013). In this paper they formulated a model employing magnetic field amplification due to turbulence to maintain the canonical FIR/RC ratio at high redshifts. This magnetic field turbulence was caused by supernovae. They predicted that the redshift at which the FIR/RC ratio would break was essentially when inverse Compton losses began to dominate. They noted that frequencies of 1 to 10 GHz would be the best to explore this relationship since thermal emission could dominate at the lower frequencies.

The parameters which define the magnetic fields of galaxies were recently studied by Chyzy et al. (2017). They used Principal Component Analysis (PCA; Jolliffe, 2002) on a selection of fifty-five galaxies and found that the formation of the magnetic fields for dwarf and Magellanic-type galaxies was not significantly different from the formation of magnetic fields for massive spiral and starburst galaxies. The magnetic field intensity was mainly correlated to local star formation activity which invoked small-scale dynamo mechanisms.

It is not clear that any of these models yet account for the full range of galaxies which exhibit the canonical value of the FIR/RC ratio. It may be the case that different theories for various galactic types need to be developed.

2.2 The Magellanic Clouds

The MCs were known to the ancient peoples in the southern hemisphere but there is no evidence that they were known to northern hemisphere residents until the thirteenth century (e.g., (von Humboldt, 1866, p286); Shapley (1957, 1961); Hodge (1999)). The MCs were named after Magellan posthumously by Antonio Pigafetta who was on the circumnavigation trip during which Magellan died. Bringing the MCs to the attention of Europe is attributed to Anghiera (von Humboldt, 1866) eight years before the end of Magellan's circumnavigation. Anghiera actually compared his observation of the LMC to the appearance of the Galaxy. The first recorded observations of the MCs are likely those of the Arab astronomer Abdurrahman Sofi (von Humboldt, 1866).

Serious studies of southern hemisphere nebulae began in earnest in the 19^{th} century. A catalogue was published by James Dunlop (Dunlop, 1828) which listed stars and nebulae and included drawings of the SMC and LMC. About this time, Herschel set up his 20 foot telescope near Capetown, South Africa, and started his "General Catalogue" (Herschel, 1864) which became part of the "New General Catalogue" (Dreyer, 1888).

Herschel described and related his feeling that the MCs were remarkable objects with no other part of the sky having so many stars and nebulae with such a density. At the Cincinnati Observatory in Ohio, USA, the director, Cleveland Abbe, came to some far-reaching conclusions (Abbe, 1867) after studying the tables in Herschel's new "General Catalogue of Nebulae and Clusters of Stars" just published (Herschel, 1864). Abbe observed that:

1. The clusters are members of the *Via Lactea* (Milky Way) and are nearer to us than the average of its faint stars.

2. The nebulae [galaxies] resolved and unresolved lie in general outside of the *Via Lactea*, which is therefore essentially stellar.

3. The visible universe is composed of systems, of which the *Via Lactea*, the two *nubeculae* (MCs), and the nebulae, are the members. They are internally composed of stars (either simple, multiple, or in clusters) and of gaseous bodies of both regular and irregular outlines.

The rise of astronomical photography provided the technological advancement which changed astronomy from a predominantly descriptive science to a quantitative science. Photography was used for the first time in an astronomical setting to measure positions of astronomical objects, specifically the MCs by Gould (1889).

It took more than fifty years for the astronomy establishment to come to the conclusions that Abbe (1867) reported. There was little mention of the Herschel star clusters during the first half of the 20^{th} century. Some very important fundamental astronomy, however, was being done, primarily by Wilhelmina Fleming, Henrietta S. Leavitt, and Annie J. Cannon at Harvard (Shapley, 1957).

Progress in understanding the MCs accelerated in the middle of the 20^{th} century. Gascoigne and Kron (1953) used photoelectric photometry to examine Cepheid period-luminosity relations in the MCs. Distances to the MCs were measured by Thackeray and Wesselink (1953) using RR Lyrae variables which gave an independent measurement from those based on the Cepheids. Kerr et al. (1954) used radio astronomy in which the 21cm H I line was used to observe the MCs and the bridge between them.

Arp (1958) determined colour-magnitude diagrams for clusters and field stars in the SMC. This provided stellar evolutionary models and the capability of making age determinations. Feast et al. (1960) surveyed the brightest stars in the MCs generating the first extragalactic Hertzsprung-Russell diagram. Westerlund (1961) examined young stars in OB associations, discovering a relationship between these young objects and both neutral and ionised elements of the ISM in the MCs.

In the next decade, Payne-Gaposchkin (1971) produced a huge study of the Cepheids in the MCs, inventing light curve analysis and discovering the spatial distributions of the Cepheids as a function of age. The Magellanic Stream was discovered by Mathewson et al. (1974). Sanduleak et al. (1978) published the first comprehensive MC planetary nebula catalogue with 122 LMC planetary nebulae and 28 SMC planetary nebulae, establishing the "SMP" catalogue designation.

Klein et al. (1983, 1984) reported that, in a small sample of irregular nearby galaxies, the RC spectra of "MC - type" galaxies and dwarf irregular galaxies were found to be significantly flatter than normal spiral galaxies. This suggested that the "MC - type" galaxies lacked a synchrotron disk of RC emission as compared to normal spiral galaxies. This further suggested that there was a much larger proportion of thermal FF emissions compared to the non - thermal radiation from cosmic ray electrons which were able to quickly escape the "MC - type" galaxies due to their small magnetic field.

Jacoby (1989) and Ciardullo et al. (1989) using [O III] λ5007 applied the planetary nebula luminosity function (PNLF) as a method for extragalactic distance determination with the results comparing favorably to distances using the Cepheid distance scale. The PNLF technique was also applied by Jacoby et al. (1990) to the MCs with good results.

Martin et al. (1989) examined the structure of the SMC using H I 21 cm data, accurate visual spectroscopic radial velocities of 307 young stars, and very high spectral resolution measurements of the ISM absorption lines in 35 H II regions. This paper suggested that the H I in the main body of the SMC (the "bar") is composed of four parts in terms of radial velocities described as follows:

1. Component VL: very low velocity, primarily in the southwest of the SMC with a galactic standard of rest radial velocity of $RV_{GSR} = -40$ to $-50\,\mathrm{km\,s^{-1}}$.

2. Component L: low velocity, the major component which sits in front of most of the southern half of the SMC with $RV_{GSR} \sim -28\,\mathrm{km\,s^{-1}}$.

3. Component H: high velocity, the most important component seen everywhere *except* the southwest with $RV_{GSR} \sim 9\,\mathrm{km\,s^{-1}}$.

4. Component VH: very high velocity, a weaker component observed in the northeast of the SMC with $RV_{GSR} \sim 30\,\mathrm{km\,s^{-1}}$, probably connected to the H component.

They also reported that most young stars and H II regions are associated with one of the four H I components defined above. In the two regions where the stars are part of a single kinematic group, the velocity dispersion was found to be $< 5\,\mathrm{km\,s^{-1}}$. This value appears to be common for regions with star formation. The complex of H I gas motion described as component H is located behind the component L complex.

In addition, Martin et al. (1989) discussed previous results (Mathewson et al., 1986) which provided a case for a total depth for the SMC of 20 to 40 kpc. A newer result from Welch et al. (1987) suggested that the depth was actually on the order of 4 kpc. This was proposed as a more likely value for the depth of the SMC, disputing the assertion by Mathewson et al. (1986) that "[the SMC] is in the process of irreversible disintegration". Martin et al. (1989) also suggested that the younger stars in the SMC were found within a depth of 10 kpc. They acknowledged, however, that other papers were in disagreement.

Sreekumar and Fichtel (1991) studied the cosmic ray electrons in the SMC to attempt to understand whether the SMC is in dynamic quasi-stable equilibrium between several different aspects. These included the confining magnetic field, the expansive pressure of the hot cosmic-ray gas, the gravitational attraction of the matter present, and the kinetic motion of the interstellar gas. Considering synchrotron radiation, the cosmic ray electron density was found to be ~ 5 times lower in the SMC than in the Galaxy. This supported the observation by Klein et al. (1983, 1984) who reported a flatter spectrum than would be expected if synchrotron radiation were present to any great extent and suggested that the SMC is extremely leaky when it comes to keeping cosmic ray electrons contained. In contrast, Sreekumar and Fichtel (1991) reported that the LMC did not exhibit this leaky behavior.

At the end of the 20^{th} century, several review papers were published. Among them were the proceedings of "New Views of the Magellanic Clouds, IAU Symposium, No.190" in which Hodge (1999) discussed the history of MC science. This symposium focused on the following questions: What are the distances to the LMC and the SMC? What is the distribution of dark matter, gas, and stars in the MCs? What is the history of their evolution: where and how did they form? How did they arrive at their current positions? Highlighted results were those pertaining to new H I observations, many of which were from the ATCA.

Dickey et al. (1999) presented results of H I observations that showed that the cool atomic phase of neutral hydrogen is much less abundant in the MCs than in the Galaxy. The suggestion was made that much of this cool gas would have been transformed into molecular clouds in an environment which had a higher dust density, closer to that of the Galaxy. The cool cloud

temperatures were 30 to 40 K compared to the Galaxy temperatures of 60 to 75 K. The LMC was described as having a well-defined rotation curve whereas the motion in the SMC was apparently chaotic. Further results were published in Dickey et al. (2000) in which the cool phase gas was described as very scarce with an abundance of less that 15% of the total H I. The lack of diffuse, atomic clouds which could develop into cold clouds of molecular gas and dust, implied that the process of star formation was reduced in the SMC.

Oey et al. (1999) described intricate patterns of superbubbles in the MCs. Many of these bubble structures have no clear association with a central cluster or supernova remnant. They suggested that the origin of these superbubbles was clearly a target for new observations.

Li and Draine (2002) presented an analysis of the IR emission from interstellar dust in the SMC. The model incorporated polycyclic aromatic hydrocarbon (PAH) emission, allowing different mixtures of metalicities and dust with the PAH content. The low metalicity of the SMC compared to the Galaxy makes the SMC an appropriate prototype of the early high-redshift galaxies before their chemical enrichment through star formation and the resulting ISM dispersal of processed gas.

The dispersal of gas and dust can be partially attributed to AGB stars which were reviewed by Iben (1999) who highlighted advances in the understanding of these stars. The circumstellar mass from the AGB star around the planetary nebula precursor is important since it is this recycled mass which populates the ISM. A planetary nebula illuminates this gas for a short period of time after the AGB phase is ended. The observed line emission originates only from the gas that is recombining with electrons meaning that high density regions would not be detected. Only the edges of the high density regions can be ionised and provide this emission.

Kwok (2005) also suggested that the chemical abundances seen in planetary nebulae are produced by the history of the planetary nebula from its initial ISM composition to the ejection of its gaseous envelope. The original AGB star, with its nucleosynthesis products, preceded the brief planetary nebula stage of its life and provided the gas and dust for the planetary nebula. It was also suggested that the organic content of meteorites found here on the earth was from planetary nebula ejecta.

Meixner et al. (2006) examined the results of the SAGE program which was a five hundred hour Spitzer MIPS[6] and IRAC[7] image survey over a field of $7^\circ \times 7^\circ$ on the LMC. In this survey, 3.94×10^6 point sources were found in the $3.6\,\mu$m band. The longer MIPS wavelengths of 24, 70, and $160\,\mu$m along with the IRAC $8\,\mu$m were used to measure the dust emission in all three phases of the ISM gas. A classification system was employed to identify three groups of stars: stars without dust, dusty evolved stars, and young stellar objects.

[6] Multiband Imaging Photometer for Spitzer.
[7] Infrared Array Camera.

The classification system used a colour-colour diagram consisting of $[3.6\,\mu\text{m}] - [8.0\,\mu\text{m}]$ versus $[8.0\,\mu\text{m}] - [24\,\mu\text{m}]$ plots.

Hughes et al. (2006) published a paper on the FIR/RC correlation in the LMC. They investigated correlations at scale factors of 1.5 kpc to 0.05 kpc between 20 cm RC radiation, 60 μm FIR radiation, H I, and CO. Sixteen regions, each 1.35° by 1.35°, were established to cover the entire LMC. Strong correlation was shown for 20 cm with 60 μm over the entire LMC with a correlation coefficient of 0.86. The thermal fraction of the RC emission for the entire LMC was found to be 0.45 and the various regions were found to be from 0.0 to 0.9 compared with the normal spiral galaxy value of 0.1. Wavelet cross correlations were also shown over the full range of scale factors. Conclusions suggested that local FIR/RC ratios are dominated by high brightness thermal emission with a background of diffuse non-thermal emission.

Scowen et al. (2010) published a white paper for the Astro2010 Decadal Survey on the MCs in which they proposed a set of measurements on the MCs to aid in understanding other nearby galaxies. The suggestions focused primarily on studying massive stars and were designed to help answer a series of questions: How does the diffuse warm ISM affect the relationship between the formation, evolution, and destruction of massive stars? How does this affect the evolution of the stellar population in such regions? What is the difference between normal disk star–forming regions and starburst regions in galaxies? How can the star formation rate explosively increase to produce thousands of stars at essentially the same time? How to describe the velocity and density of stellar winds from massive stars? How does the assembly and evolution of the cold neutral medium occur? What are the global processes that dictate the developments?

Gordon et al. (2011) described the creation of a SMC resource as part of the Spitzer legacy program. The program's goals were to study the type and amount of dust present in the ISM of the SMC, the sources of dust from evolved stars, and the consumption of the dust in star formation. Gordon also reported on a SAGE Spitzer survey of the SMC with the same goals using techniques from Meixner et al. (2006) for the LMC.

Boyer et al. (2011) examined the red giant branch stars, AGB stars, and the ISM of the SMC and made a detailed comparison of the differences between the SMC and LMC in terms of those observations. They examined the entire extent of the SMC (bar, wing, and tail) from mid-infrared (MIR) to FIR with high resolution and sensitivity. This provided a way to study the SMC population of cool evolved stars at frequencies where the emission of circumstellar dust is prominent.

Cioni et al. (2011) outlined a new program which focuses on the MCs that would use the Visual and Infrared Survey Telescope for Astronomy (VISTA) telescope (Emerson and Sutherland, 2010) in the VISTA survey of the Magellanic Clouds (VMC). The purpose of this survey was

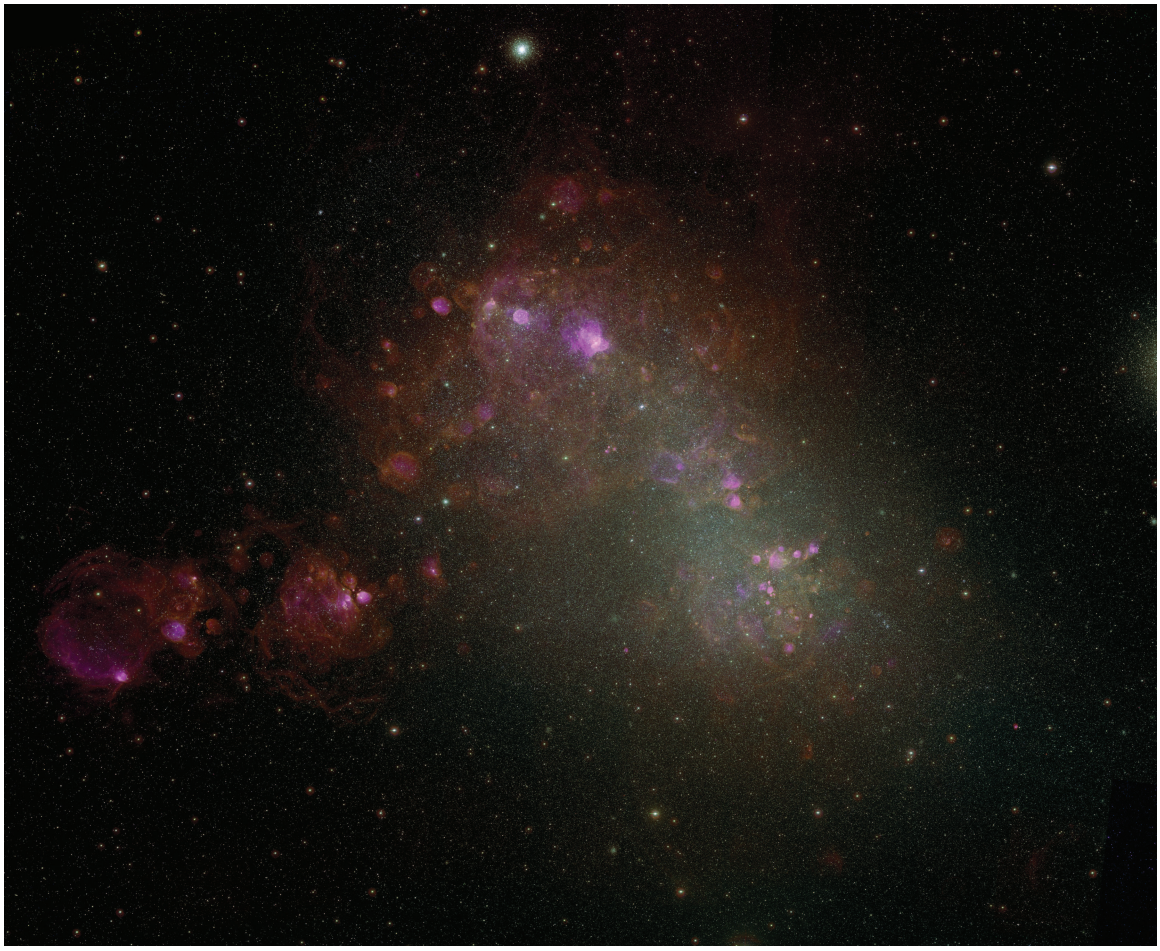

Figure 2.5: The Small Magellanic Cloud in Hα Light. North is up, east is to the left. The Bar is the major structure which extends from the lower right, southwest, to the upper left, northeast. The Wing is the structure which extends to the lower left, southeast, from the Bar. From MCELS (Smith et al., 2000).

to provide a uniform and homogeneous examination of the entire Magellanic system in the near-infrared (NIR) with specifications that included the following: an aperture of 4 m; a field of view of 1.65 deg^2; filters with central wavelengths of 1.02, 1.25, and 2.15 μm (YJK$_S$ System); filter widths of 0.1, 0.18, and 0.30 μm; and pixel size of 0.339 $''$. By 2017, more than twenty-four papers had been published on the MC system using the VMC data.

The MCs are small galaxies, relatively close, 50 - 60 kpc with well known distances and they have little extinction from the Galaxy. This makes them an ideal resource for research concerning the ISM and planetary nebulae.

2.2.1 The Small Magellanic Cloud

The SMC (Figure 2.5) can be described as a gas-rich late-type dwarf galaxy (Bolatto et al., 2006) and is classified as SB(s)m pec in the NASA/IPAC Extragalactic Database.[8] It is classified

[8] https://ned.ipac.caltech.edu/.

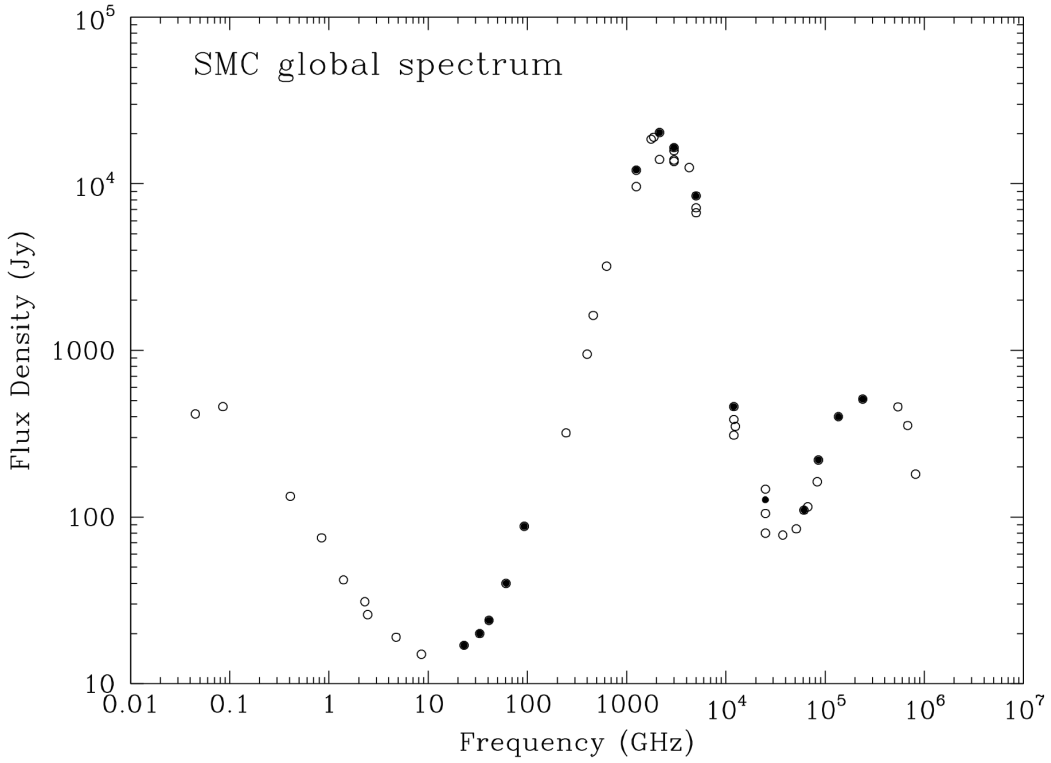

Figure 2.6: Small Magellanic Cloud Spectral Energy Distribution. From Israel et al. (2010).

as an irregular galaxy of type Ir IV-V in the David Dunlap Observatory system (Van den Bergh, 2000). It is a member of the local group and may be a satellite galaxy of the Galaxy (Westerlund, 1997).

The SED of the SMC is shown in Figure 2.6. It is interesting to compare its general shape to the SED for the starburst galaxy M82 in Figure 2.7. The position of the minimum is close to 10 GHz in the SMC while it is close to 100 GHz in M82. This suggests that there is a pronounced excess in FIR emission in the SMC compared to M82. Israel et al. (2010) suggested that the excess is much more extreme in the SMC than in the LMC and that the general character of the SED is consistent with low metallicity, particularly in the SMC.

The SMC is centred at 60.6 ± 3.8 kpc (Hilditch et al., 2005) from the Galaxy. The depth was examined as part of the structure of the SMC in Mathewson et al. (1986). The SMC was seen to be very complex and to have two different populations in velocity-space considering the H I distribution, each with a distinct stellar and nebular population. This study found that the Cepheids spanned a distance range of ~ 43 to 75 kpc with a concentration at 59 kpc. Examining the line of sight distribution of Cepheids with periods > 10 days split the sample into components with centres 12 kpc apart, each with a depth of ~ 6 kpc. The conclusion was that most of the young stars lie within a depth of 6 to 10 kpc. Subramanian and Subramaniam

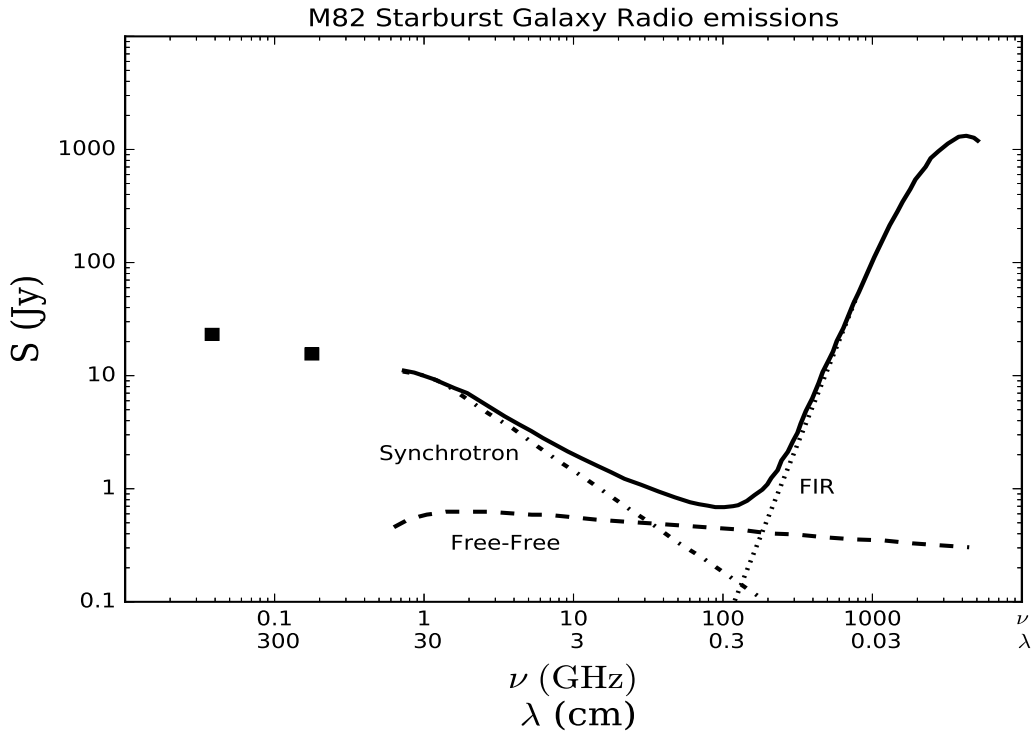

Figure 2.7: FIR and Radio Spectrum of Galaxy Messier 82. This figure after Condon (1992) is an example of a starburst galaxy and shows the sum of the FIR and RC SED of M82. It shows both thermal and non-thermal radio emissions as well as the FIR emissions from dust. It also shows the decomposition into its components: synchrotron (dash-dot), FF (dash), and FIR (dots).

(2009) using data from the OGLE II survey[9] (Udalski et al., 1998) determined a SMC depth of 4.9 ± 1.23 kpc in the bar and 4.23 ± 1.48 kpc at the optical centre of the SMC.

The line of sight to the SMC has an extinction of only $A_V \sim 0.2$ magnitudes and a reddening of $E(B-V) \sim 0.04$ (Bolatto et al., 2006; Schlegel et al., 1998). It appears to have been tidally disrupted by a recent close encounter with the LMC (Murai and Fujimoto, 1980). There is no trace of any spiral structure in the SMC (Sandage and Tammann, 1981) but both a "bar-like" structure and a "wing" have been reported (Westerlund, 1997). The bar structure is probably the body of the SMC and contains most of its gas and star formation activity. The wing feature continues into the bridge which is an H I region extending from the SMC to the LMC (Bolatto et al., 2006). In fact, the SMC is more complex than the LMC: various population centroids vary by 14 arcmin in right ascension and by a full degree of declination. The SMC has very faint absolute luminosity and surface brightness.

The SMC has the lowest metallicity of any gas–rich galaxy in close proximity (Bolatto et al., 2006). This makes it one of the best galaxies to study as a proxy for very high redshift galaxies. Measurements suggest that the dust grains are mostly silicates rather than carbonaceous grains which distinguishes the SMC ISM from that of the Galaxy (Weingartner and Draine, 2001).

The stars resolved in the SMC are blue and red supergiants with $M_B = -7^m$. These Population I stars are accompanied by a resolved disk of Population II stars with $M_V = -3^m$. The SMC is thus older than the resolved Population I stars suggest. Schwering and Israel (1993) identified 249 infrared sources in the SMC. The morphology of the Population II stars has been measured and appears to suggest a spheroidal distribution without the prominent irregular features seen in the distribution of younger stars (Bolatto et al., 2006; Cioni et al., 2000; Maragoudaki et al., 2001; Zaritsky et al., 2000). Measurements of 21 cm radiation suggests that the ISM of the SMC may be rotating (Filipovic et al., 1996).

Perhaps the best current star surveys of the SMC are from the VMC survey (Rubele et al., 2015). The compilations used colour-magnitude diagram reconstruction methods to provide star formation rates, age-metallicity relations, distance, and mean reddening. The results included the creation of high resolution population maps that vividly reveal young star–forming regions as having a feathery appearance unlike the very smooth appearance of older regions not engaged in new star formation. This survey found that the SMC wing was formed less than 0.2 Gyr ago with the star formation in the bar only ~ 0.2 Myr old. Periods of enhanced star formation were detected at 1.5 and 5 Gyr. The star formation rate was determined to be moderate at even earlier ages.

[9] Optical Gravitational Lensing Experiment.

2.2.2 The Large Magellanic Cloud

The LMC, see Figure 2.8, is classified by the NASA/IPAC Extragalactic Database as a barred spiral galaxy of the SB(s)m in the local group. It is classified as a Ir III-IV galaxy in the David Dunlap Observatory system (Van den Bergh, 2000). Its distance from the Galaxy is 49.97 ± 1.3 kpc as measured by Pietrzyński et al. (2013) using long-period, late-type eclipsing systems composed of cool giant stars. Reid and Parker (2006a,b, 2008) found that the planetary nebulae were located in a warped disk and that the innermost 2.6° possessed solid body rotation. The LMC rotation was characterized by van der Marel and Kallivayalil (2014) using three–dimensional velocity measurements. They measured 6790 stars using the Hubble Space Telescope (HST) and fitted the data to a model of circular rotation in a flat disk. They found that the dynamical centre of the stellar motion coincided with the H I dynamical centre. The depth was measured by Subramanian and Subramaniam (2009) using data from the OGLE II survey (Udalski et al., 2000) to have an average of 4.0 ± 1.4 kpc.

The SED of the LMC is shown in Figure 2.9. It is interesting to compare its general shape to the SED for the starburst galaxy M82 in Figure 2.7 and the SMC in Figure 2.6. The position of the minimum is close to 40 GHz in the LMC while it is close to 100 GHz in M82. This suggests that there is an excess in FIR emission in the LMC compared to M82, but not as severe as in the SMC which has a minimum at 10 GHz. Israel et al. (2010) suggested that the LMC exhibits the same general character of the SED which is consistent with low metallicity, but not as severely as in the SMC.[10]

2.3 Planetary Nebulae

Planetary nebulae are some of the most visually striking objects in the universe. Figure 2.10 is a small sample of possibly hundreds of unique morphologies seen from the vantage point of the Earth. They consist of a central star with a mass of $\sim 0.5\,M_\odot$ and ionised gas and dust that have been expelled from the planetary nebula precursor: a medium mass star ($\sim$1–10 $M_\odot$). The remaining central star, which will be transformed into a white dwarf, is the stellar remnant core of the original star consisting almost entirely of carbon and oxygen. The central star is the source of the intense UV radiation which ionises the gas ejected as a stellar wind from previous evolutionary stages. Planetary nebulae exist only a brief time, approximately thirty- to fifty-thousand years, before they dissipate into the ISM leaving behind a white dwarf star. Planetary nebulae are useful tools in the study of the dynamics of mass loss near the end of the life of low to moderate mass stars.

[10] The metallicity for [Fe/H] for the SMC, LMC, and the Galaxy was measured by Luck et al. (1998): 1) SMC: [–0.65, –0.79] average –0.65. 2) LMC: [–0.55, –0.19] average –0.19. 3) Galaxy [0.17, –0.24] average –0.03.

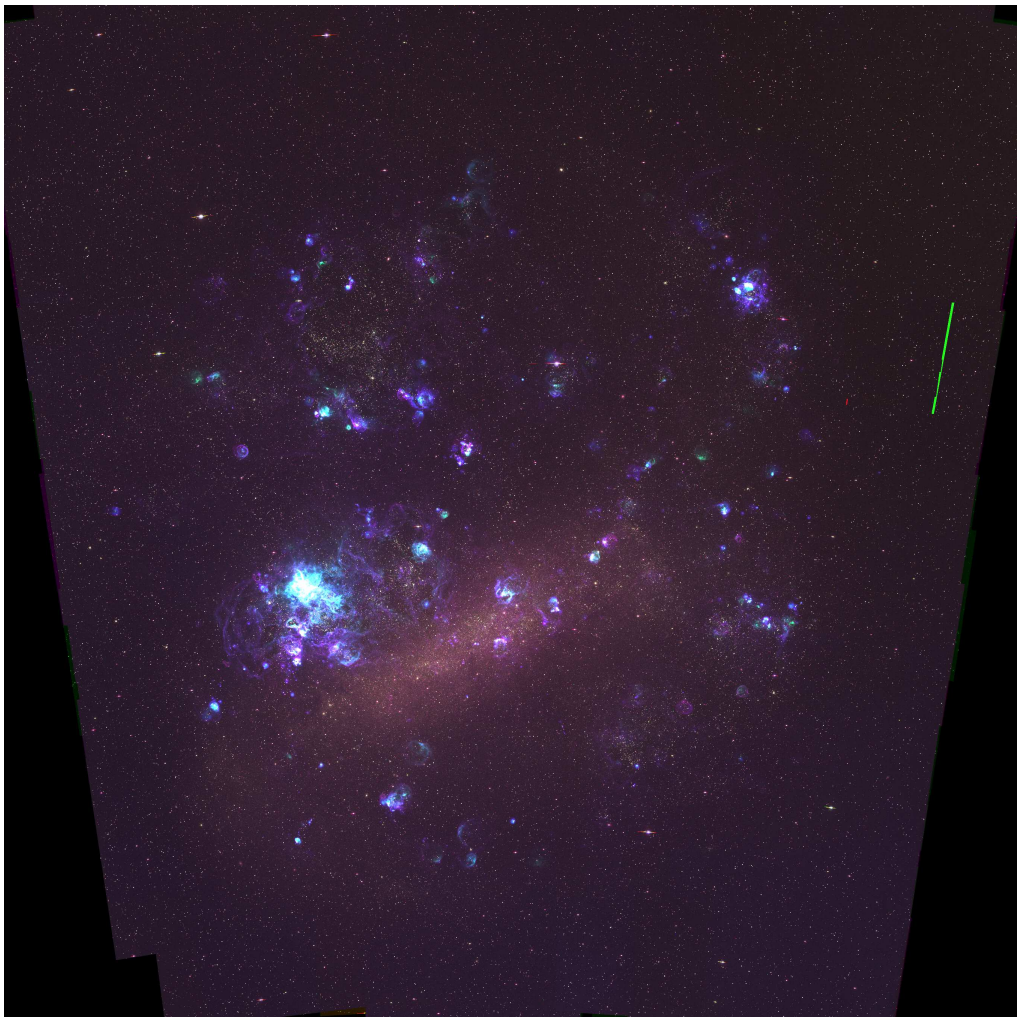

Figure 2.8: The Large Magellanic Cloud in Hα, [S II], and [O III] Light. The MCELS LMC image. North is up, east is to the left. From Smith et al. (2000), it consists of Hα (red), [S II] (green), and [O III] (blue) images.

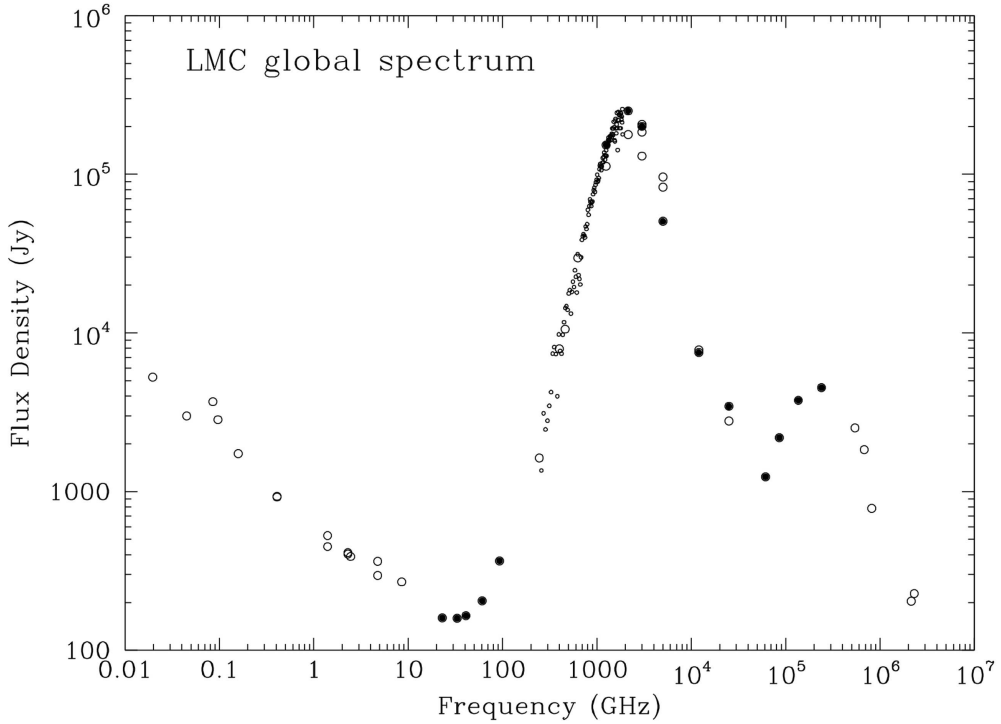

Figure 2.9: Large Magellanic Cloud Spectral Energy Distribution. From Israel et al. (2010).

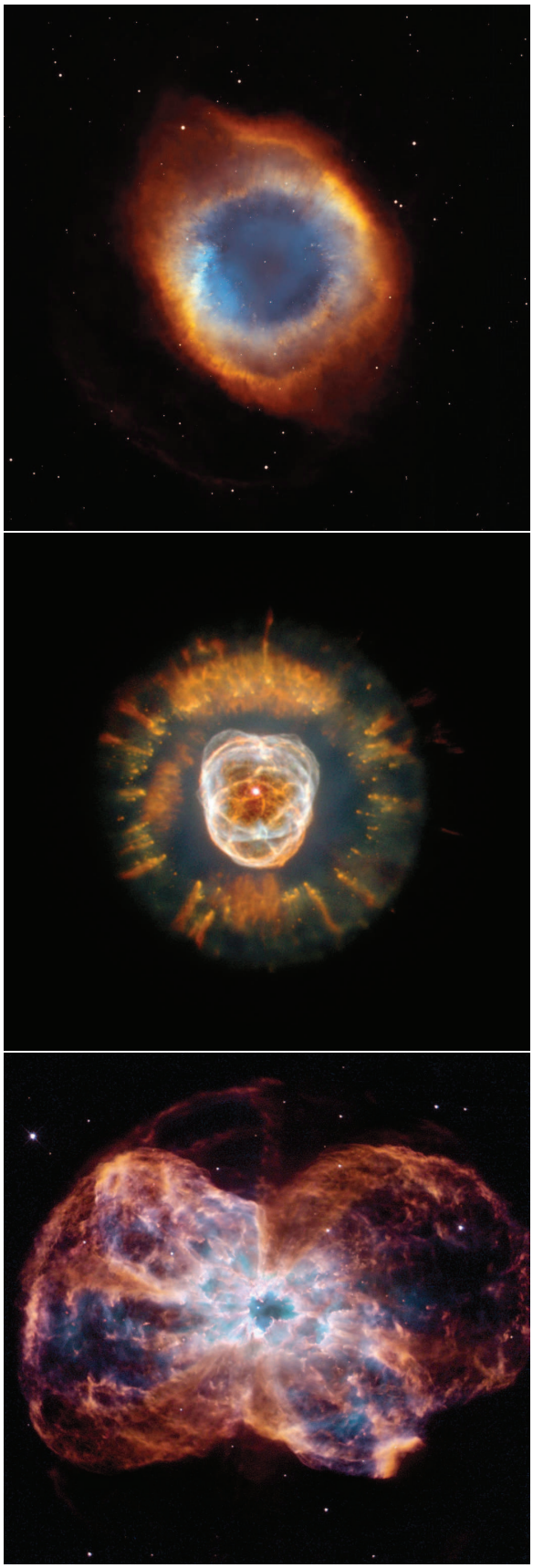

Figure 2.10: Planetary Nebulae Examples. From the HST. Top: Helix Nebula (NGC 7293), Credits: NASA, ESA, and K. Noll (STScI). Middle: Eskimo Nebula (NGC 2392), Credit: Andrew Fruchter (STScI). Bottom: NGC 2440, Credits: NASA, ESA, and K. Noll (STScI). Acknowledgment: The Hubble Heritage Team (STScI/AURA).

2.3.1 History of Planetary Nebulae Research

Galactic planetary nebulae have been recorded since the comet hunter Charles Messier in 1746 included M27 in his list of *faux* comets (Messier, 1781). This object and others that had visual appearances similar to planets were referred to as planetary nebulae in 1785 by William Herschel in a letter to Jerome Lalande in March of that year (Hoskin, 2014). The nature of these objects was quite a mystery until early spectroscopic observations were made by William Huggins (Huggins and Miller, 1864). The observations revealed emission lines, particularly the most prominent [OIII] line at λ5007. Near the end of the first quarter of the 20^{th} century, Menzel (1926) described the state of understanding of planetary nebulae at that time. Distance and motion measurements were not yet very precise. It was known that many of the planetary nebulae were associated with very hot "O" type stars but they had not yet grappled with the planetary nebula measurements which put them about 12 magnitudes fainter than average "O" type stars. The data gave them a result which required the central star to be much further away than the planetary nebula nebulosity and hence the two were not really considered parts of the same object. Observation of the LMC planetary nebulae led to the explanation that the LMC planetary nebulae were a different class of planetary nebulae, a "diffuse variety" of planetary nebulae. Masses were computed assuming that the diffuse material at the edges of the nebulae were orbiting their centres and resulted in very improbable and inconsistent views of planetary nebulae. Other major problems included understanding the spectra. There was some discussion about normal "O" stars and planetary nebula "O" stars but there was not enough evidence to come to clear conclusions. The possibility that the central star consisted of a "residue of refractory material" was discussed. It was noted that the central star of the planetary nebula could not be considered to be an ordinary "O" star.

Ambarzumian and Milne (1932) were among the first to attempt to explain the morphology of planetary nebulae theoretically and derive their basic properties. Perhaps the main advance made in their paper was the application of radiative equilibrium to the shaping of planetary nebulae and the ionisation of the nebular shell.

A great number of observations and theoretical results were published in the following decades. Osterbrock and O'dell (1968) and Osterbrock (1973) provided a good look at the evolution of observations and theories of the planetary nebulae up through 1973.

Kwok et al. (1978) extended the understanding by modeling the planetary nebula with a high speed wind from the central star interacting with the stellar wind from the precursor AGB star, the "Interacting Stellar Winds" model. By this time it was accepted that AGB stars are the progenitors of planetary nebulae but the details were not understood.

Frank et al. (1993) presented a paper on the shaping of planetary nebulae in which the

authors related that "Virtually the full range of PN morphologies are easily reproduced, as are the basic kinematics, ionization structures, and temperatures." This sentiment was soon shown to be overly optimistic. Kwok (1994) provided an overview of the evolving understanding of planetary nebulae wherein the origin and evolution of planetary nebulae are tightly coupled to their central star evolution.

When the first HST images were released by Harrington and Borkowski (1994), their Cat's Eye Nebula image (NGC 6543) shattered the predictions of planetary nebula structure and revealed that the formation history and resulting morphology of planetary nebulae were not understood (Balick and Frank, 2002). The predictions from Frank et al. (1993) included dense tori of material that would have been ejected early in the life of the central star, but there was no sign of this feature in the Cat's Eye Nebula image. The complexity of the image "mocked Frank et al.'s simple paradigm in several ways" (Balick and Frank, 2002) and the intricate knots and jet-like features were completely absent from the model predictions.

The images released by Harrington and Borkowski (1994) prompted an ongoing series of conferences on asymmetric planetary nebulae which were held to discuss their morphology. The earliest of these, APN I[11], was held in 1994 (Kahn, 1995). The most recent was APN VI[12] (De Marco, 2014). In the 2014 conference, it was concluded that asymmetric planetary nebulae had to be binary stars. This conclusion was announced by De Marco (2014) at the conference with the statement that "[d]uring this conference the last nails in the coffin of single star models for non spherical planetary nebulae have been put."

Evidence supporting the idea that most visible planetary nebulae have descended from binary stars was described by Moe and De Marco (2006); Moe and De Marco (2012). These papers described models of planetary nebula formation which suggest that a single progenitor star must have a mass greater than $\sim 2.3 \pm 0.3$ $M_{\odot}$ to produce a planetary nebula. Low mass progenitors could produce planetary nebulae only if they were part of a binary system. The primary idea behind this assertion is that close binaries provide a mechanism to enhance the AGB mass loss rate to the level required to create a planetary nebula in low mass stars.

RC measurements of the flux density from Galactic planetary nebulae were being made by the mid–1960s (e.g., Menon and Terzian, 1965). These single-dish measurements could not detect any structure because the beamwidths were much larger than the extent of the emission of the planetary nebulae.

By the 1970s RC measurements were becoming more available as technology improved. Higgs (1971) catalogued 121 RC Galactic planetary nebulae and Taylor et al. (1987) presented RC spectra for eighteen Galactic planetary nebulae. Kwok (1985) published 5 GHz images

[11] http://physics.technion.ac.il/ ips/volume11.html.
[12] http://www.astroscu.unam.mx/apn6/PROCEEDINGS/, id.122.

of ten compact planetary nebulae with a resolution of $\sim 0.4''$. Terzian (1989) published the emission spectrum of a Galactic planetary nebula, NGC 7027, from 100 cm to 300 nm. By this time RC interferometer techniques were being utilized to provide images of planetary nebulae with sub-arcsec resolution (Terzian, 1989).

The first three tentative extragalactic RC planetary nebula detections were published: Zijlstra et al. (1994) for SMP L58 in the LMC and Dudziak et al. (2000) for Wray 16-423 and He 2-436 in the Sagittarius dwarf galaxy. Then, Filipović et al. (2009) reported the first confirmed extragalactic RC detections of fifteen planetary nebulae in the MCs: four in the SMC and eleven in the LMC (one of which has recently been reclassified as a planetary nebula mimic, an H II region).

An early attempt to classify emission objects, including planetary nebulae, was published by Cohen and Green (2001). They examined a region of the Galactic plane centred on $l = 312°$. They used NIR data at $l = 8.3\,\mu$m from the Midcourse Space Experiment and RC data at 843 MHz from the Molonglo Observatory Synthesis Telescope. They classified the following types of objects with ratios of these two wavelengths:

1. $8\,\mu$m/1 GHz $RC \sim 25 \pm 5 \Rightarrow$ diffuse and compact H II regions,
2. $8\,\mu$m/1 GHz $RC \sim 42 \pm 5 \Rightarrow$ ultra-compact and hyper compact H II regions, and
3. $8\,\mu$m/1 GHz $RC \sim 4.7 \pm 1.1 \Rightarrow$ planetary nebulae.

The problem of classification was also addressed by Reid and Parker (2010) who published a paper examining the PNLF in the LMC.

In 2005, a series of papers presenting the Macquarie/AAO/Strasbourg Hα Planetary Nebula Catalogue (MASH) began with Parker et al. (2005). This paper examined the southern Galactic plane and the MCs using the UK Schmidt Telescope of the Anglo-Australian Observatory (AAO) with narrow band Hα plus [N II] $\lambda\lambda 6548, 6584$ images on Tech-Pan film. The task was to image 4000 deg^2 with a resolution of $\sim 1''$. The result was the scanned online digital atlas called the SuperCOSMOS Hα Survey. The next paper in the series was an application of this catalogue to planetary nebula discovery in the LMC (Parker et al., 2006). Additional images were taken to match the Hα plates. The short red maps of the entire 25 deg^2 field of the LMC were also digitized and co-added in order to detect planetary nebulae. A third paper added 460 planetary nebulae to the previous list of 169 known planetary nebulae (Reid and Parker, 2006b). A confirmation of Reid and Parker's technique was published in Shaw et al. (2007) with data from the HST images on six planetary nebulae that were discovered in the Reid and Parker catalogue: RP 265, RP 671, RP 723, RP 764, RP 885, and RP 1550.

Frew (2008), however, showed that since most planetary nebulae are very faint in visible wavelengths, they cannot be detected in the Galaxy at more than a few kpc distance. It is impossible to get a representative sample of planetary nebulae across the Galaxy due to variations in the extinction along different paths. Much of the Galaxy is masked from view by the obscuring gas and dust.

Frew and Parker (2010) discussed how planetary nebulae could be detected and addressed the planetary nebula mimic problem. They created techniques to eliminate contaminants by accessing new multi-wavelength surveys and spectroscopy to provide emission line ratios. This multi-wavelength approach to mimic detection was applied to pre-MASH detected planetary nebulae and 45% of the original population were shown to be planetary nebula mimics. This was a very important result since many existing planetary nebula catalogues were contaminated with planetary nebula mimics, rendering them essentially useless for any statistical studies of planetary nebulae.

Cohen et al. (2011) refined these techniques and came up with a MIR/RC ratio for planetary nebulae of 4.7 ± 1.1. This is important because these are both wavelengths that can penetrate dust and gas in the ISM.

Reid and Parker (2013) extended their planetary nebula survey of the LMC to include $\sim 64\,\mathrm{deg}^2$ of the outer limits of the LMC. Sixty-one new planetary nebulae were discovered. An additional 107 of 109 previously known outer region planetary nebulae were reconfirmed in this study.

The white paper by the IAU Planetary Working Group discussed current and future planetary nebula research (Kwitter et al., 2014). The earliest detection mechanism for planetary nebulae used [O III] λ5007. Unfortunately, this technique does not find planetary nebulae exclusively since H II regions will also be detected. This is clearly not adequate for planetary nebula identification. There have been several multi-wavelength approaches employed which utilized narrow band imaging and access to deep, multi-wavelength surveys including NIR, MIR, and RC wavelengths (Parker et al., 2005). This is an approach which appears to be very promising and needs to be extended to provide planetary nebula identification, location, and characterization.

Among the most critical determinations that need to be made in astronomy are the distances to objects under study. Recently there have been several approaches that use planetary nebulae to provide distance estimates. The most prevalent one is the PNLF at [O III] λ5007 (Kwitter et al., 2014) which is used primarily as a distance estimator to bright extragalactic planetary nebulae, although Frew (2008) has applied this to Galactic planetary nebulae. This estimator appears to be useful with an error $\sim$ 10% but current understanding of planetary

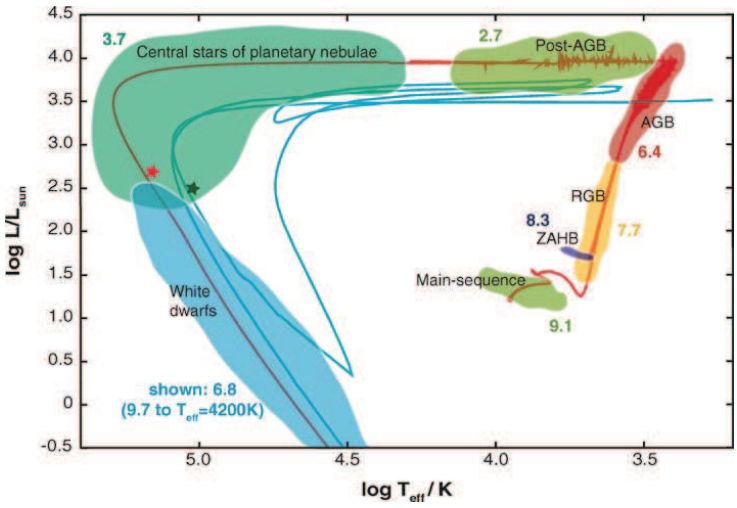

Figure 2.11: A Planetary Nebula Hertzsprung-Russell Diagram. This diagram is from Herwig (2005) showing the planetary nebula evolutionary track for 2 $M_{\odot}$ stars of solar composition. The numbers along the track are approximate times in log(years) for the accompanied segments. Broadening of the trace indicates numerical instability in the simulation. The blue line is the track of an H-deficient star. The track show the "born-again" AGB evolution scenario describing the result of a very late pulse which may occur in up to a quarter of AGB central stars (e.g., Iben and Renzini, 1983; Iben, I., 1995).

nebulae does not provide the mechanism for this distance estimation accuracy. Why it appears to work is not understood (Ciardullo, 2012). The use of 8 μm IR and planetary nebula diameters was examined by Ortiz (2013). The use of the IR provides access to some planetary nebulae that would otherwise be obscured by unknown extinction. This method was shown to have a an error of about 20%. The use of Hα fluxes and planetary nebula diameters was examined by Frew et al. (2016b) with an error of about 18%. The approach of using RC measurements and angular diameters to derive a (Σ–D) relation for statistical distance calibration was proposed by Vukotic et al. (2014), see section 2.3.3. This approach has been employed in this thesis, see sections 4.5 and 5.5. For a thorough discussion of distance measurements using planetary nebulae, see Smith (2014).

2.3.2 Planetary Nebula Evolution

Planetary nebulae are the end stage of the life of a moderate mass star ($\sim$1–10 $M_{\odot}$) that evolved through the red giant phase to become an AGB star and then a planetary nebula. A simplified Hertzsprung-Russell diagram shows the evolutionary path from a main sequence star to a white dwarf star in Figure 2.11.

The importance of planetary nebulae in determining the chemical, atomic, molecular, and solid-state galactic ISM enrichment was discussed in the paper by Kwok (2005) concerning the challenges of the 21^{st} century. It had been clear that planetary nebulae were easily observable in

the visible due to the strong recombination lines of H I and [He I] as well as collisionally excited lines of metals like [O III] λ5007. Kwok pointed out that infrared and mm/sub-mm observations have revealed a great deal of neutral material in the form of dust and molecules. The full tally of the components of a planetary nebula include ionised and neutral atoms, molecules, and various solid state forms of matter which appear in regions of very different densities, temperatures, and morphologies. The richness of the overall spectrum begins in the $\gamma-$ray regime and extends through the RC portion of the spectrum in the MHz range.

The process that creates the stunning images that planetary nebulae exhibit is far from understood. Balick and Frank (2002) presented a number of theories of post-AGB star evolution to a planetary nebula. Among the most developed were variations of the two-wind model from Kwok et al. (1978). This model was classified as a "Hydrodynamic Model of Intertial Confinement" by Balick and Frank (2002). Frank (1998) had a more complete review of hydrodynamic shaping, particularly the problem of asymmetric or "bipolar" outflows. Recently, De Marco (2014) posited that 80% of planetary nebulae have non-spherical shapes and no self-consistent model can explain them. Further, hydrodynamic models of binary interactions do not accurately describe the observed morphology of planetary nebulae. Simpler models based on one–dimensional simulations may need to be re-visited.

When the moderate mass star exhausts its supply of H, the core contracts and the temperature increases. This causes the upper layers of the star to expand. Although the core is getting hotter, the outer layers are expanding to the point where the surface cools to about the temperature of an M star, $\sim 3500\,\mathrm{K}$. The star moves towards becoming a first ascent red giant star on the giant horizontal branch, see Figure 2.11. Since the star has expanded so much, the outer layers are considerably less gravitationally bound to the core. This promotes significant mass loss. Convection becomes the major energy transport mechanism because of the cooler temperature of the outer regions of the star. This is due to H becoming increasingly opaque at the cooler temperatures. The convective region can extend down to the energy producing nuclear reaction depth and can end up with an increase in N and a decrease in C and O in the convection region. This is called the "first dredge-up", see Figure 2.12.

Stars with a mass of $< 2\,\mathrm{M}_\odot$ are expected to become red giant branch stars after experiencing a thermal runaway called an He flash. For stars with a mass $> 2\,\mathrm{M}_\odot$, the He is predicted to ignite in a more controlled fashion and the initial He flash does not occur. The star stabilizes with an He burning core and an H burning shell outside the core.

At this time, the triple alpha process is producing C in the He shell where most of the energy generated by the star is being produced. Further alpha process reactions will generate elements such as O and Ne. As the He shell is consumed it burns outward to the H shell. At

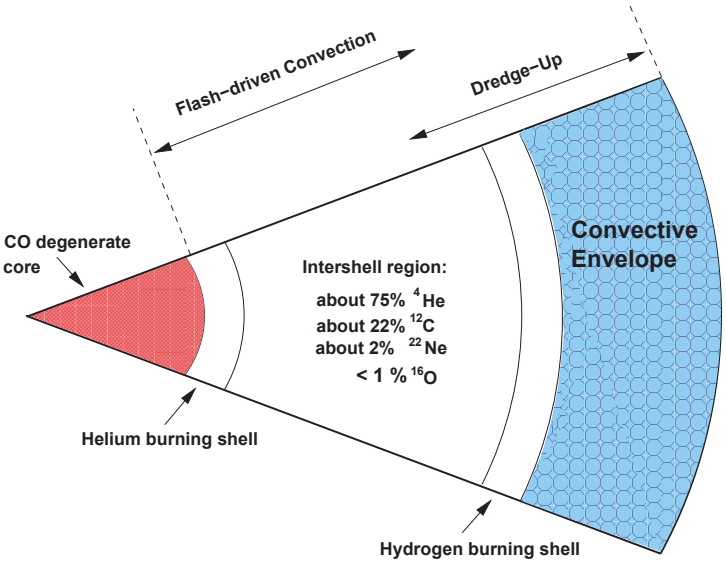

Figure 2.12: Asymptotic Giant Branch Star Structure. AGB Structure (Karakas, 2007).

that point the H burning again dominates and is then punctuated by a series of runaway He shell flash events as the H shell is consumed thus producing more He. These thermonuclear runaway events result in the mixing of core nuclear products with H and He and transporting the mixture out to the surface of the star in the dredge-up process. This process occurs during the AGB phase of the star. The gas of the star outside of the core is heated which causes the gas to expand. This expansion causes it to be less gravitationally bound and produces a strong wind carrying away material from the star. This cools the star and the cycle can repeat. The repetition causes the star to approach the red giant branch evolutionary track again and it becomes a second ascent red giant branch star. These evolutionary tracks approach the red giant branch track as if it were an asymptote, which leads to the star being designated as an "asymptotic giant branch" star. For details on this process, see Karakas and Lattanzio (2007) and references therein.

The evolution of AGB stars goes through two stages. The first is the early phase which is characterized by little dynamical activity followed by the thermally pulsing stage. The early stage is a relatively stable configuration, Figure 2.12, consisting of a degenerate carbon/oxygen (C/O) core with an He shell inside of an H shell with a convective volume extending to the extremes of the star's volume. The energy generation in the He shell provides the energy to make this configuration stable. When the He becomes depleted, the stability of this structure cannot be supported. The result is that H burning commences until the He shell can be replenished with the reaction products from the H burning. Then the He shell will be able again to provide the energy to stabilize the star. This alternation of He burning and H burning causes the

thermal pulsations seen with the two shells alternately providing the energy produced in the star. The period for this oscillation is $\sim 10^5$ years. During this stage of evolution, consisting of up to a few dozen pulses, the He burning ash in the form of C and O continues to build up in the core. These stars which started out with a mass > 2 $M_\odot$ are more luminous than the smaller red giant branch stars but the temperatures observed can be as low as an M8 star, 2500 K. The fusion products in each of the dredge-up events from the thermal pulses increase in mass so the surface of the star becomes enriched with He, C, N, O, and other s-process (slow neutron process) elements (Sterling and Dinerstein, 2008, and references therein). Repeated dredge-up events in high mass AGB stars, $\sim 2-4$ $M_\odot$, alter the surface composition with the dredged-up C so that they evolve into carbon stars.

In very massive AGB stars, in the range of $\sim 4-8$ $M_\odot$, nuclear burning can take place at the bottom of the convective zone. This is called hot-bottom burning and is the process by which these massive AGB stars develop very O-rich surfaces (Marigo, 2007, and references therein).

The most massive AGB stars have masses of $\sim 8-10$ $M_\odot$ and are called super AGB stars. These evolve into either neutron stars or O-Ne-Mg core stars (Herwig, 2005). The fate of this mass range is an open issue. They may not evolve into planetary nebulae.

All AGB stars eventually eject virtually all of their mass outside of the core. This mass loss phase is due to a super wind (Wachter et al., 2002). The mass loss can be up to $\dot{M} = 10^{-4}\,M_\odot\,\mathrm{yr}^{-1}$, (Zijlstra, 2006) with a relatively low velocity of $\sim 10-20\,\mathrm{km\,s}^{-1}$. The mass outside of the core, the envelope, slowly flows into the ISM near the AGB star which now can be called a "proto-planetary nebula" or a "pre-planetary nebula" or a "post-AGB star".

When the mass of the gas envelope around the core is reduced to $\sim 10^{-2}$ $M_\odot$, the super wind has effectively ended, and the core is slowly exposed while the density of the surrounding gas envelope decreases as it expands. AGB stars have two energy producing shells, Figure 2.12. One is an He burning shell close to the C/O degenerate core, and the other is an H burning shell further from the centre. The two burning shells cause the overall temperature of the core to increase. The He shell burning results in an increase of the core mass, and the core mass increase, in turn, causes a contraction in the size of the core (Paczyński, 1970). Interestingly, the core diameter decrease compensates for the increase in temperature and results in an almost constant luminosity. As the C/O core heats up from $T_{eff} = 5000\,\mathrm{K}$, the core moves to the left in the Hertzsprung-Russell diagram (Schoenberner, 1983), see Figure 2.11. The bolometric luminosity of the core is effectively a function only of its core mass, M_c (Kwok, 1994), so it is not affected by the increase in temperature,

$$\frac{L}{\mathrm{L}_\odot} \sim 59250 \times \left[\frac{M_c}{\mathrm{M}_\odot} - 0.52\right]. \tag{2.22}$$

The effective temperature of the AGB core climbs in temperature to $\sim 2.5 \times 10^5$ K. The mass that was ejected into the ISM is exposed to intense hard UV radiation and begins to ionise. Dust in the envelope near the central star that condensed from dredged up material will evaporate and contribute to the fast wind leaving the environs of the central star. The central star produces a fast wind which is not as dense but much more energetic than the previously ejected AGB slow wind: $v \sim 2000\,\mathrm{km\,s^{-1}}$ and $\dot{M} = 10^{-7}\,\mathrm{M_\odot\,yr^{-1}}$. This fast wind sculpts the ejected material from the AGB star slow wind and the result is the visible ionised gas referred to as a planetary nebula. The central star maximum temperature is approximated by Tylenda (1989) as

$$\log\left(T_{\max}\right) \sim 5.72 + 1.41 \times \log\left(\frac{M_c}{\mathrm{M}_\odot}\right). \tag{2.23}$$

The H burning eventually ends when there is no more H available to supply the H shell and the central star descends towards the white dwarf cooling track. The time for this transition, from emitting the super wind to reaching the white dwarf cooling track, is the lifetime of the planetary nebula and was approximated by Tylenda (1989) as

$$\log\left(\Delta t\right) \sim 1.0 - 4.96 \times \left(\frac{M_c}{\mathrm{M}_\odot} - 1.0\right) - \log\left(\frac{M_c}{\mathrm{M}_\odot} - 0.52\right). \tag{2.24}$$

This estimate in years is a very steep function, see Figure 2.13. It goes from 12000 yr for a $0.6\,\mathrm{M_\odot}$ core, to 1700 yr for a $0.7\,\mathrm{M_\odot}$ core, and to only 20 yr for a $1\,\mathrm{M_\odot}$ core. It is obvious that there is a strong bias towards finding planetary nebulae from moderate mass stars. A recent value of the peak of the core mass is $M \sim 0.680 \pm 0.130\,\mathrm{M_\odot}$ (Tremblay et al., 2016) taken from measurements of a Galactic white dwarf sample with distances of ≤ 20 pc. High mass stars are much less common than low mass stars and high mass stars have an inherently shorter time that they illuminate their ejected mass. High mass stars will not have time to develop a planetary nebula. White dwarf stars with mass up to $\sim 1.3\,\mathrm{M_\odot}$ have been detected (DeGennaro et al., 2008) but the observable characteristics displayed during their very brief post–AGB phase is not known.

Models of planetary nebulae really began to take form in studies by Kwok et al. (1978). He proposed the "Interacting Stellar Winds" model, which primarily applies to spherically symmetric morphologies. Over the years, many refinements have been seen (Kwok, 2012, and references therein). This theory is generally accepted but non-spherical morphologies are still a problem to be solved.

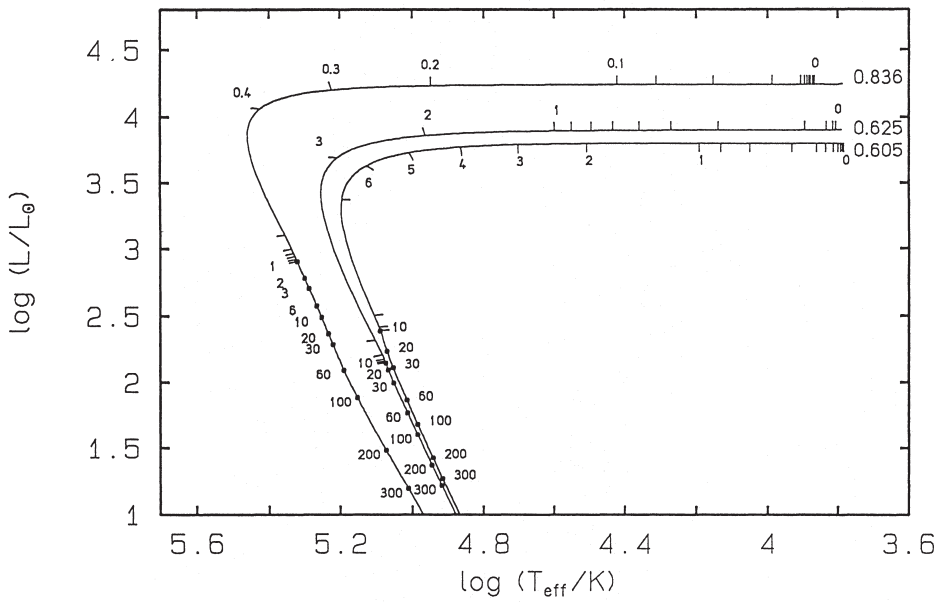

Figure 2.13: Post-Asymptotic Giant Branch Star Lifetime. Planetary nebula lifetime (Bloecker, 1995) showing lifetime of post-AGB stars. Central star masses of 0.605 $M_\odot$, 0.625 $M_\odot$, and 0.836 $M_\odot$ are shown. Time marks are in 10^3 years.

Regardless of the morphology, the physical process of FF radiation from a planetary nebula is similar to that of the ISM described in Section 2.1.1. The FF emission from a planetary nebula is that of a cloud of gas ionised by the central star. The following development for FF emission specifically describes planetary nebulae and follows closely that of Pottasch (1984).

The emission coefficient, j_ν, for FF emission in a strongly ionised gas can be written

$$4\pi j_\nu = 6.72 \times 10^{-38} g_{ff} \frac{n_p n_e}{T_e^{1/2}} e^{\left[\frac{-h\nu}{kT_e}\right]}, \tag{2.25}$$

where n_e is electrons cm^{-3}, n_p is protons cm^{-3}, T_e is in Kelvin, ν is frequency in Hz, h and k have their usual values, and g_{ff} is the FF Gaunt factor. The result has units of erg cm^{-3} s^{-1} Hz^{-1}. In the radio frequency domain, the Gaunt factor can be approximated by the following numerical result

$$g_{ff} = \frac{\sqrt{3}}{\pi} \ln\left(\frac{4.95 \times 10^{-2} T_e^{3/2}}{\nu z}\right), \tag{2.26}$$

with ν in GHz and z the ionic charge. To determine the optical depth, the absorption coefficient κ_ν can be determined by relating it through Kirchhoff's law

$$\frac{j_\nu}{\kappa_\nu} = B_\nu = \frac{2\nu^2 kT}{c^2}, \tag{2.27}$$

where the blackbody radiation is written in the Rayleigh-Jeans approximation[13] since $h\nu \ll kT$. Self absorption is the result of electrons absorbing energy from photons due to their interaction with hydrogen ions. This absorption coefficient can be approximated with

$$\kappa_\nu = 8.24 \times 10^{-2} {T_e}^{-1.35} \nu^{-2.1} n\left(H^+\right) n_e, \tag{2.28}$$

where ν is in GHz and κ_ν is in pc^{-1}.

With this, the optical depth is

$$\tau_\nu = \int \kappa_\nu dS = 8.24 \times 10^{-2} {T_e}^{-1.35} \nu^{-2.1} \int n\left(H^+\right) n_e dS. \tag{2.29}$$

For the simple case where there is no incident radiation and the emission is from an isothermal nebula, the emission flux density can be written as

$$S_\nu = \int I_\nu d\Omega = \frac{2\nu^2 kT_e}{c^2} \left(1 - e^{-\tau_\nu}\right) \Omega. \tag{2.30}$$

Considering an isothermal constant density nebula, for high frequencies

$$S_\nu = \frac{2\nu^2 kT_e}{c^2} \tau_\nu \Omega \propto \nu^{-0.1}, \tag{2.31}$$

the optical depth decreases as frequencies increase, $\tau_\nu \to 0$ and $S_\nu \propto \nu^{-0.1}$. This provides a slowly decreasing SED at increasing frequencies.

Considering an isothermal constant density nebula, for low frequencies the approximation can be written

$$S_\nu = \frac{2\nu^2 kT_e}{c^2} \Omega \propto \nu^2. \tag{2.32}$$

The optical depth increases as the frequencies increases, $\tau_\nu \to \infty$ and $S_\nu \propto \nu^2$, in this portion of the spectrum. This is applicable from very low frequencies to the frequency where the planetary nebula becomes thin and Equation 2.31 becomes applicable: the critical frequency. The critical frequency can be used to estimate quantities such as the FF luminosity and the electron density along the line of sight.

The characteristics described above provide an explanation for the SEDs of planetary nebulae (for example, Figure 2.14). A comparison of Figure 2.14 with Figure 2.15 suggests that NGC 7027 is $<$ 3000 yrs old. Figure 2.16 provides a much wider range of frequencies for NGC 7027. This shows the radio spectrum critical frequency at $\sim$ 5 GHz, above which the

[13] For typical RC emission frequencies of ~ 1 GHz , $h\nu \sim 10^{-25}$ J and for a typical T_e of 10^6 K, $kT_e \sim 10^{-19}$ J.

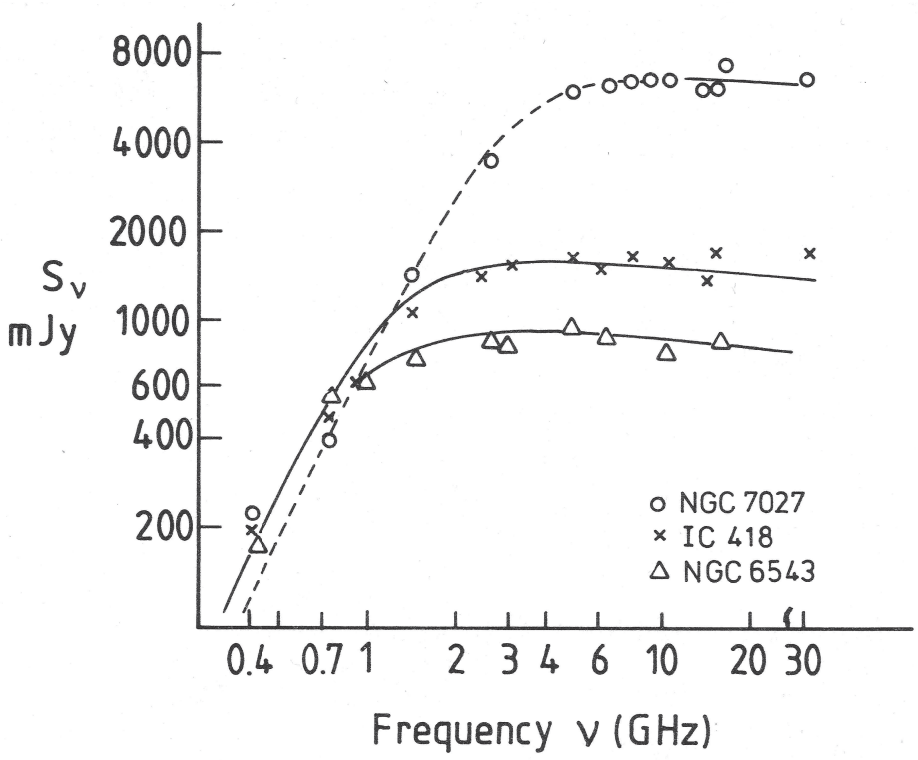

Figure 2.14: Observed Spectral Energy Distribution from Planetary Nebulae. (Pottasch, 1984).

planetary nebula is optically thin with the expected small negative slope. Below 5 GHz, the large positive slope clearly indicates that the planetary nebula is optically thick. The infrared portion of the frequency range shows the presence of warm dust in the envelope of material around the central star. A striking visible image of NGC 7027 is shown in Figure 2.17.

2.3.3 The Surface Brightness-Diameter Distance Model

Reliable distance measurements are essential to any statistical investigation of planetary nebula properties. There have been several attempts in recent decades to produce reliable distance estimates (Smith, 2014). The foundation for current efforts can be traced back to Shklovskii (1960) who examined RC emission from Galactic supernovae and derived a theory of RC emission from these discrete sources starting with the radiation flux from a synchrotron source

$$F_\nu \propto r^3 \cdot K \cdot H_\perp^{\frac{\gamma+1}{2}} \cdot \nu^{\frac{1-\gamma}{2}} \cdot \left(2.8 \times 10^8\right)^{\frac{\gamma-1}{2}}, \tag{2.33}$$

where r is the radius of the emission region, H is the magnetic field strength, K is the constant from the differential energy spectrum expressed as $dN\,(E) = KE^{-\gamma}dE$, ν is the frequency, and the equation $\alpha = (\gamma - 1)/2$ defines γ in terms of α, the spectral index for the emission.

In order to express changes in these parameters as the radius r changes, a base value is

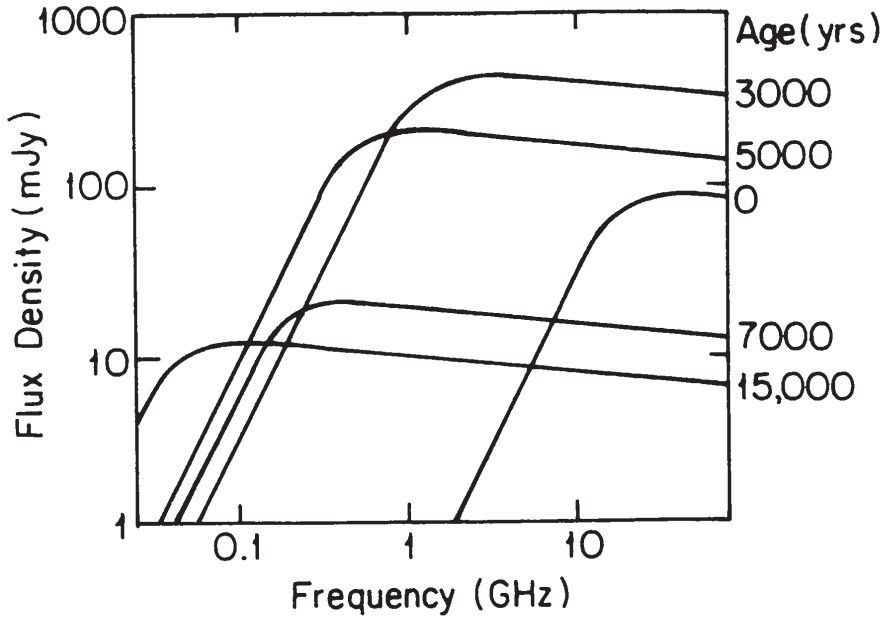

Figure 2.15: Modeled Planetary Nebulae Spectral Energy Distributions. Planetary nebulae at different ages from 0 to 15000 yr (Terzian, 1989).

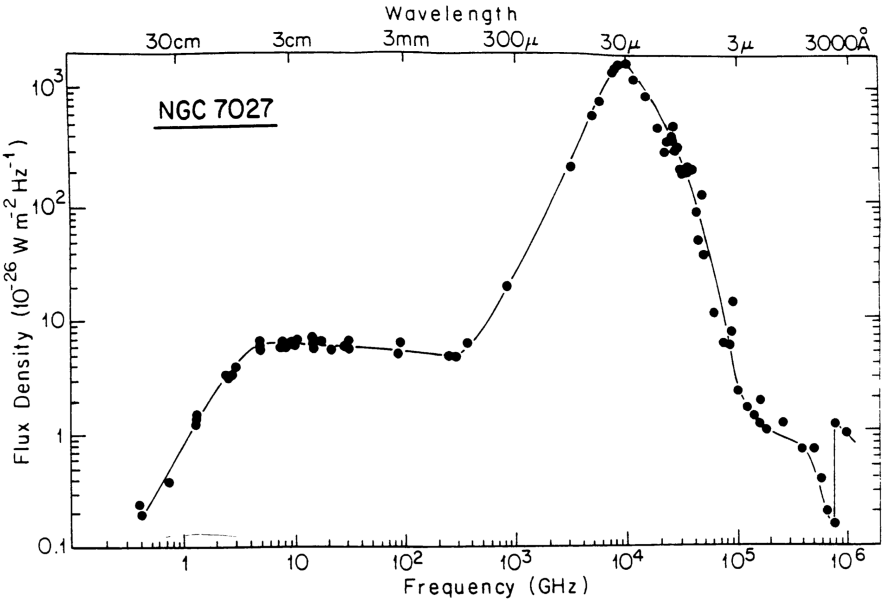

Figure 2.16: Measured Spectral Energy Distribution of NGC 7027. Measurements in the RC, IR, and optical frequencies for NGC 7027 (Terzian, 1989).

Figure 2.17: Image of NGC 7027. HST image of NGC 7027 from the Hubble Legacy Archive processed by Delio Tolivia Cadrecha. (https://apod.nasa.gov/apod/ap130826.html).

defined at r_0. Then, since this region is filled with plasma, the "frozen in theorem" from Alfvén (1942) can be applied and the magnetic field strength, H, can be expressed in terms of the field at r_0, H_0, in terms of r,

$$H = H_0\left(\frac{r_0}{r}\right)^2. \tag{2.34}$$

Shklovskii further defined $\beta = 2\gamma$ and derived for frequencies $\nu \sim 1\,\mathrm{GHz}$ expressions for flux and flux-density

$$\begin{aligned} F_\nu &\propto r_0^\beta r^{-\beta} K_0 H_{0\perp}^{\frac{\gamma+1}{2}} \propto r^{-\beta} \\ S_\nu &\propto r_0^\beta r^{-(\beta+2)} K_0 H_{0\perp}^{\frac{\gamma+1}{2}} \propto r^{-(\beta+2)} \end{aligned}, \tag{2.35}$$

where r refers to the emission region radius; K_0, the reference or maximum intensity of the emission; and $H_{0\perp}$, the magnetic field strength perpendicular to the motion of the relativistic electrons. Although Shklovskii's paper concerned itself with synchrotron radiation from supernovae remnants, the conclusion suggested that surface brightness in general could be used for distance determination.

For planetary nebulae, Amnuel et al. (1984) considered the relationship between Galactic planetary nebula diameters and surface brightness, Σ, of the RC emission from FF radiation,

in order to estimate the distances to planetary nebulae. They used the form $\Sigma \sim D^{\beta_D}$ for the relationship which is similar to that used for supernovae except that they used a power law index, β, dependent on diameter, D. Their measurements at 5 GHz were used to create a (Σ–D) curve for the Σ range of $5 \times 10^{-18} > \Sigma > 10^{-20}\,\mathrm{W\,m^{-2}\,Hz^{-1}\,sr^{-1}}$.

They expanded their model by combining the asymptotic results of Daub (1982) and Milne (1982) out to $10^{-16} > \Sigma > 10^{-22}\,\mathrm{W\,m^{-2}\,Hz^{-1}\,sr^{-1}}$.

Their asymptotic results were

$$\begin{aligned} \Sigma &> 3.6 \times 10^{-18}\,\mathrm{W\,m^{-2}\,Hz^{-1}\,sr^{-1}} \rightarrow \Sigma = 3.5 \times 10^{-21} D^{-2} \\ \Sigma &< 5.5 \times 10^{-21}\,\mathrm{W\,m^{-2}\,Hz^{-1}\,sr^{-1}} \rightarrow \Sigma = 5.5 \times 10^{-23} D^{-5} \end{aligned} . \tag{2.36}$$

Urosevic et al. (2007) derived a theoretical (Σ–D) relation for planetary nebulae. They started with the FF emission volume emissivity of a planetary nebula, ε_ν, which can be written (Rohlfs and Wilson, 2004) as follows

$$\varepsilon_\nu \propto n^2 T^{-1/2}, \tag{2.37}$$

with n the electron and ion density. The surface brightness can then be expressed as $\Sigma_\nu \propto \varepsilon_\nu D$ where D is the diameter of the planetary nebula. These can be combined to produce

$$\Sigma_\nu \propto n^2 T^{-1/2} D. \tag{2.38}$$

Assuming a constant mass flow out from the centre, the density is $n \propto D^{-2}$. With T a constant, putting the defined n into equation 2.38 results in the simple theoretical (Σ–D) relation

$$\Sigma_\nu \propto D^{-3}. \tag{2.39}$$

This led to the observation by Urosevic et al. (2007) that the standard power law form written

$$\Sigma = A \times D^{-\beta}, \tag{2.40}$$

with $\beta = 3$, is actually expressing the result using the lower limit of the slope. Measured slopes < 3 are posited to be due to data selection effects that mask low flux density measurements. In general, the value of β is expected to be ≥ 3.

In order to model the correct empirical (Σ–D) relation from a representative sample of planetary nebulae, the diameters and the fluxes must be accurately measured. There are a number of difficulties in the measurement of planetary nebula parameters considering the Malmquist bias effect. This causes a selection which produces a biased sample due to the fact

that the brightest objects will be detected but many of the dimmer objects will be missed.

Phillips (2002) created a planetary nebula distance scale with forty-four nearby sources ($< 0.7\,\mathrm{kpc}$) as calibrators and found that the (Σ–D) relationship could be described by

$$\Sigma_{5\,\mathrm{GHz}} = 2.33^{+0.88}_{-0.64} \times 10^{-22} D^{-2.07\pm0.19}. \tag{2.41}$$

Urosevic et al. (2007) analyzed these data and concluded that their (Σ–D) fitting could model the data used but it did not lead to a consistent luminosity-diameter (L–D) plot. The (L–D) plot was described by Arbutina et al. (2004) in a study of supernova (Σ–D) and (L–D) correlations. The assertion was that a good (L–D) correlation supported a valid (Σ–D) correlation. Urosevic et al. (2007) carried over this conclusion to planetary nebulae. The (L–D) data correlation coefficient was only -0.06 where a good correlation coefficient would be > -0.5. This suggested that the data did not produce a valid (Σ–D) correlation due to limits in sensitivity and resolution of the radio surveys used.

Urošević et al. (2009) developed an improved model of the (Σ–D) relation at 5 GHz, derived an empirical (Σ–D) relation, and validated RC planetary nebula distance calculations. The model is predicated on the idea that there are two shocks in the planetary nebula. The first is an inner shock at the interface between the central star wind and the inner boundary of the high density shell. The second shock is at the outer limit of the shell as the material plows into the previously ejected, slowly expanding AGB material.

The power law index, β, initially from the AGB star, has the value of 1, primarily due to the fast central star wind. After the fast wind has run its course, the remaining isothermal shock continues to propagate away from the central star in the AGB wind causing a steeply declining surface brightness with an evolution of β from 1 to ≥ 3.

Vukotić et al. (2009) analyzed a sample consisting of fifteen RC MC planetary nebula detections compiled from various radio surveys. Optical diameters were available for ten of the planetary nebulae. Five of the LMC planetary nebula flux densities were above the 3σ instrumental sensitivity, 1.5 mJy beam^{-1}. These planetary nebulae, plus one taken in "snapshot" mode with higher sensitivity, comprised the sample for this investigation. Most of the population from which this sample was drawn were likely to be below the sensitivity line of these observations and not detected. Hence, "the resulting values for β should not be taken seriously" (Vukotić et al., 2009). The value for β from the biased sample was likely to represent a slope that was too small. The SMC planetary nebulae were not used in this analysis since optical diameters were not available for them.

Vukotić et al. (2009) also applied a Monte Carlo sample simulation analysis to the MC RC planetary nebulae. The data making up the original sample are described in Filipović et al.

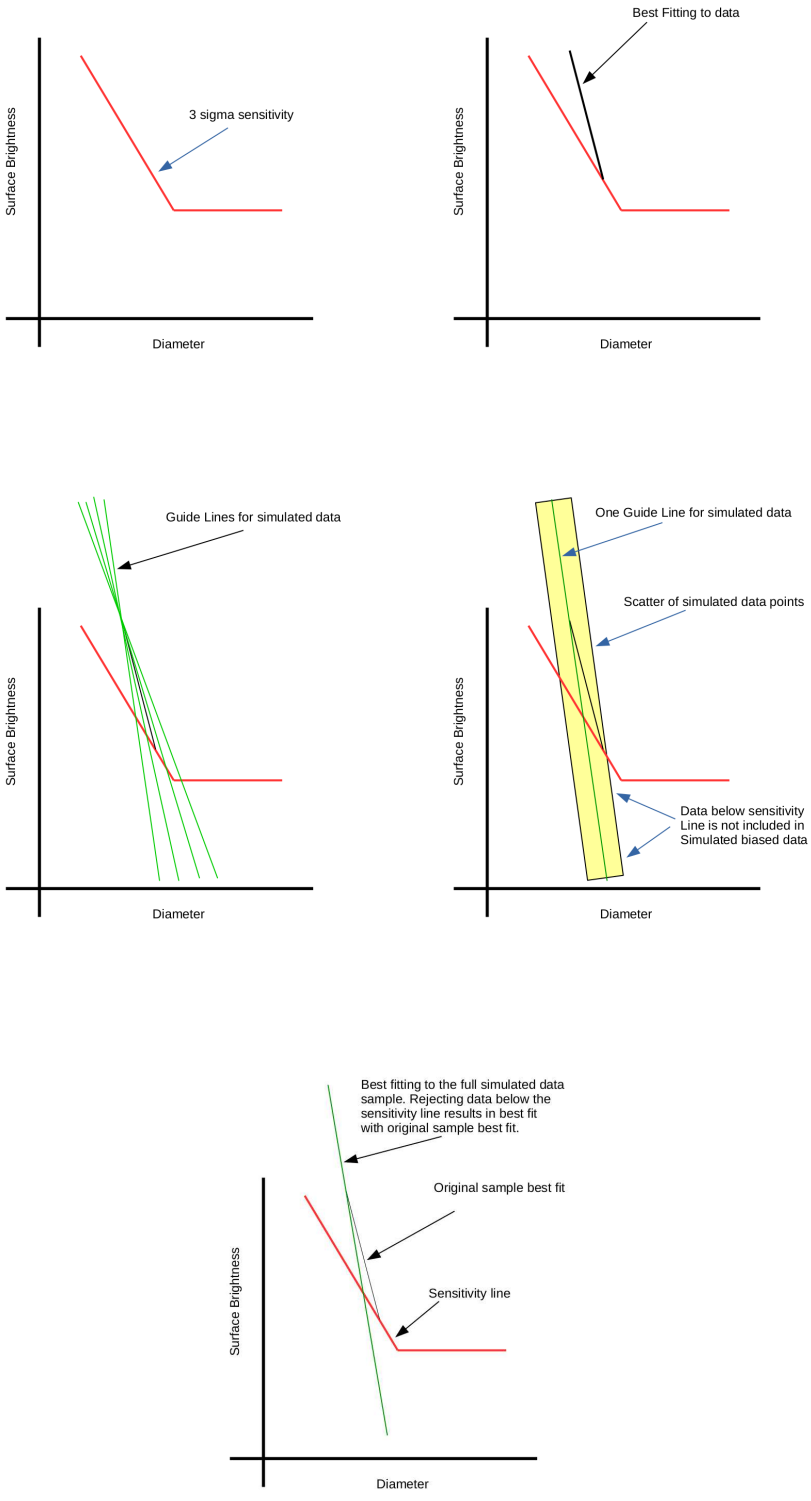

Figure 2.18: Surface Brightness–Diameter Sample Bias Analysis.

(2009). A brief description of this analysis is sketched in Figure 2.18, as follows:

1. Top left: The 3 σ sensitivity line for the measurements is established.

2. Top right: The best fitting of the sample is seen with respect to the sensitivity.

3. Middle left: Several guide lines with different slopes are defined. These will be the bases for several different simulated samples.

4. Middle right: One particular guide line of several is shown with its simulated sample created by randomly choosing points with D coordinates that exhibit the same sample density as the measured sample. Then these points are scattered away from the guide line with the same Gaussian distribution as seen in the measured sample. Only artificial data points that are above the sensitivity line are retained in the accumulated simulated sample in order to best approximate the biased measured sample. In order to create a better representation of the measured sample, this process is applied one hundred times creating a simulated sample with up to 100 times the number of measured samples. This is done independently on each guide line.

5. Bottom: The final artificial biased sample which generates a best fitting line closest to the original data represents the best approximation to the original sample. The unbiased sample from which this biased sample is derived represents the best approximation to the original unbiased sample.

Vukotić et al. (2009) applied the process outlined above and analyzed selection effects in the (Σ–D) relation using Monte Carlo simulations similar to those used by Urošević et al. (2005) in their study of the extragalactic (Σ–D) relation for supernovae. In detail, Vukotić et al. started with a calculation of the best fitting to the (Σ–D) sample with D as the independent variable. Then with an interval in log D which is 5 times longer than the interval defined by the sample, random points were scattered through the expanded interval with the same log D density as the measured sample. Guide lines were then created with slopes from 1.5 to 3 in steps of 0.1, all of which were anchored on the (Σ–D) best fitting line at the smallest value of the log D simulation interval. Simulated data points were defined on each of these guide lines at the random log D values calculated. At this stage of the algorithm, all of the simulated points were on the guide lines. In order to simulate the errors present in the real data, a multiplier was applied to the Σ value of the simulated data points moving the points off the guide lines. This multiplier consisted of simulated Gaussian noise with the same standard deviation value as the measured sample times a parameter called *Scatter*. *Scatter* allows a variation in noise to simulate various

scenarios. With a *Scatter* value of one the simulated sample standard deviation is the same as the measured sample.

To study sensitivity selection effects, a sensitivity cutoff was applied to the simulated sample. Data were removed from further analysis if the Σ value of a simulated point was below the sensitivity cutoff. This process of creating random data and applying sensitivity selection was repeated one hundred times with the same standard deviation for each guide line as long as there were at least five or more simulated data points remaining after the sensitivity cutoff. The remaining sample was then fitted to a (Σ–D) line. This line was compared to the (Σ–D) fitting of the sample without the sensitivity cutoff. Vukotić et al. (2009) showed that the sensitivity cutoff flattened the resulting (Σ–D) fitting line to a slope below that of the unbiased sample. This is particularly pertinent when considering MC planetary nebulae since only a small percentage of known planetary nebulae have been found with detectable RC emissions.

Vukotić and Urošević (2012) described a statistical distance calculation to planetary nebulae using the (Σ–D) relation. Since there were significant errors in the calibration data in both Σ and D, they chose to do the calibration with orthogonal offsets rather than vertical offsets.[14] They applied the principles of bootstrap resampled statistics from Efron and Tibshirani (1993) to the measured sample using Monte Carlo methods to create a much larger resampled sample. In this way no estimated sample measurement errors were needed to account for the fitting parameter uncertainty estimations.

Vukotic et al. (2014) described the details of the calculations discussed in Vukotić and Urošević (2012) with an improved approach to the statistical distance estimation. The specific analysis used in this paper started with the application of bootstrap resampled sample statistics. The driving force behind adopting this approach was that all of the information in the measured sample would be retained in the resampled sample with much better resolution. This was due to the fact that the resampled sample had many times the data point count compared to the measured sample but had the same statistical information with improved accuracy and consistency.

In this procedure, a grid of cells is created to contain the values of the PDF at each grid point coordinate for the resampled sample. This grid establishes the resolution of this discrete representation of the PDF. The centroid coordinates of the resampled sample are translated to match the coordinates of the measured sample on the grid of cells which approximates the actual PDF.

The PDF contained $\sim 10^6$ resampled samples distributed over a square grid of 100×100 cells

[14] Pavlovic et al. (2013) described fitting similar (Σ–D) data for supernovae. Six least squares fitting approaches were compared with the orthogonal fitting being selected for their (Σ–D) fitting because of significant scatter in their sample in both axes.

and one of 1000×1000 cells populated with the sample density in each cell. The results from these two grid sizes were compared to determine what changes in the best fitting parameters would be realized with the different grid densities. The low density grid representation varied insignificantly from the high density grid representation of the PDF, so the low density grid was chosen for the study.

The resampled sample is calculated from the measured sample by repeatedly creating resampled samples. The centroid is calculated for each repeated resampling cycle and the new resampled sample is added to the sample after the centroids of the resampled samples are aligned to the centroid of the measured sample. This is a repeated building up of a PDF representation of the measured sample until a smooth resampled sample distribution is created in this discrete PDF.

To determine the distance represented by this PDF, the value of the diameter, D, is first determined and then is used to calculate the value for the distance, d. The PDF is a grid of values which are indexed by discrete values of Σ and D. The values of the PDF across the PDF grid with a particular value of Σ provide a PDF from which the mean, mode, and median can be extracted. This can be done at every Σ value of interest.

The overall goodness of fit for the distance calculation (Vukotic et al., 2014) can be related to the average fractional error for distance

$$\overline{f} = \frac{1}{N} \sum_{i=1}^{N} \left| \frac{d_i - d_i^{\mathrm{s}}}{d_i} \right|, \tag{2.42}$$

where the d_i is the measured distance, d_i^{s} is the statistical distance calculated, and N is the number of samples for the average.

A combination of the previously mentioned (Σ–D) techniques and improvements on those techniques were used in this thesis for the statistical distance calibration by creating a continuous PDF which provided the (Σ–D) probability function at any value of Σ and D.

The surface brightness range of planetary nebulae is expected to be similar within a few dex regardless of their location. The measured surface brightness of Galactic planetary nebulae is from $\sim 10^{-24}$ to $\sim 10^{-16}$ $\mathrm{W\,m^2\,Hz^{-1}\,sr^{-1}}$ while MC planetary nebulae are only detected in the interval from $\sim 10^{-20}$ to $\sim 10^{-16}$ $\mathrm{W\,m^2\,Hz^{-1}\,sr^{-1}}$. This implies a very large selection bias whose effect is to remove a large population of lower surface brightness values from the measured sample.

With a biased selection of points making up the measured sample, a bootstrap resampled sample was calculated to be used in creating a continuous PDF representing the unbiased sample. Bootstrap based Gaussian kernel density smoothing (Bozzetto et al., 2017; Feigelson and Babu, 2012; Wasserman, 2005) was applied which uses the kernel function

$$K\left(\frac{x-x_i}{h}\right)=\frac{1}{\sqrt{2\pi}}\exp\frac{(x-x_i)^2}{2h^2}, \tag{2.43}$$

in each dimension where h is the kernel bandwidth and x_i are the resampled sample data. The PDF function in one dimension is

$$f_h(x)=\frac{1}{nh}\sum_{i=1}^{n}K\left(\frac{x-x_i}{h}\right). \tag{2.44}$$

Choosing the bandwidth, h, is perhaps the greatest challenge in this approach. Too small and the variance is excessively large creating a rough PDF whereas if h is too large there is undue smoothing and real features in the measured sample are averaged out. The selection of the optimal bandwidth can be done by minimizing the bootstrap integrated mean square error as shown in Bozzetto et al. (2017)

$$BIMSE(h)=B^{-1}\sum_{i=1}^{B}\int_{-\infty}^{\infty}\left(f_h^*(x)-f(x)\right)^2dx, \tag{2.45}$$

where B is the of number of smoothed bootstrap resamples from the measured sample. This process can give an unambiguous selection of the optimal bandwidth.

The (Σ–D) relation studied here is in two dimensions. Feigelson and Babu (2012) described the procedure for combining two separate Gaussian kernels to describe the two dimensional PDF

$$f_{h^xh^y}(x,y)=\frac{1}{nh^xh^y}\sum_{i=1}^{n}K\left(\frac{x-x_i}{h^x}\right)K\left(\frac{y-y_i}{h^y}\right). \tag{2.46}$$

This PDF contains all of the information about the data from which it was created in a useful representation where h^x, h^y are the values of h for the x and y axes. This quantity is a continuous function of the probabilities as a function of the observables Σ and D. Optimization consists of using the previous value of h^x, h^y as the initial value for the calculation of the optimized bandwidth until the previous value and the newly calculated value are within some small difference of the initial value for this iteration.

This is similar to the PDF calculated in Vukotic et al. (2014) except that the PDF calculated here is a continuous function of Σ and D rather than the approximation from a matrix of values at discrete points. Additional details for the creation of the PDFs are described in Bozzetto et al. (2017) and Pavlovic et al. (2013).

Chapter 3

The Far-Infrared / Radio Continuum Ratio in the Small Magellanic Cloud

This chapter is based on my publication, Leverenz and Filipović (2013). I would like to acknowledge the contributions made by Miroslav D. Filipović, for facilitating access to unpublished data, reviews of the text, and discussions about analysis procedures and results.

3.1 Data Sources

The data sources used for the FIR/RC ratio and other relations are listed in Table 3.1 and shown in Figure 3.1. Data from two radio telescopes were used in this study: the Parkes

Table 3.1: Data Sources for the FIR/RC Ratio Study. Data used in this study include IRAS and Spitzer satellite images, radio images from ATCA and Parkes radio telescopes, and Hα images from NFCCD/CTIO, and CO $J = (1 - 0)$ images.

Band	Telescope	Resolution (arcsec)	Resolution (pc)	Reference
60 μm	IRAS	120	35.3	(Miville-Deschênes and Lagache, 2005)
100 μm	IRAS	120	35.3	(Miville-Deschênes and Lagache, 2005)
70 μm	Spitzer	18	5.3	(Bolatto et al., 2007)
160 μm	Spitzer	40	11.8	(Bolatto et al., 2007)
3 cm RC	ATCA+Parkes	2	0.6	(Dickel et al., 2010) a
6 cm RC	ATCA+Parkes	3	0.9	(Dickel et al., 2010) a
6 cm RC	Parkes	162	48.6	(Filipovic et al., 1997) a
13 cm RC	ATCA+Parkes	60	17.6	(Staveley-Smith et al., 1997; Stanimirovic et al., 1999) a
21 cm RC	ATCA+Parkes	90	26.4	(Staveley-Smith et al., 1997; Filipovic et al., 1997) a
21 cm RC	Parkes	1128	338	(Filipovic et al., 1997) a
H I	ATCA+Parkes	98	28.8	(Staveley-Smith et al., 1997; Stanimirovic et al., 1999) a
Hα	NFCCD/CTIO	3	0.9	(Smith et al., 2000)
CO	NANTEN 4 m	156	45.8	(Mizuno et al., 2001)

(a)Also see Haynes et al. (1991); Xu et al. (1992); Klein et al. (1993); Filipovic et al. (1995, 1997, 1998a,b,c), Filipovic et al. (2002); Payne et al. (2004); Filipovic et al. (2005); Reid et al. (2006); Payne et al. (2007), and Crawford et al. (2011b); Wong et al. (2011c,d, 2012b).

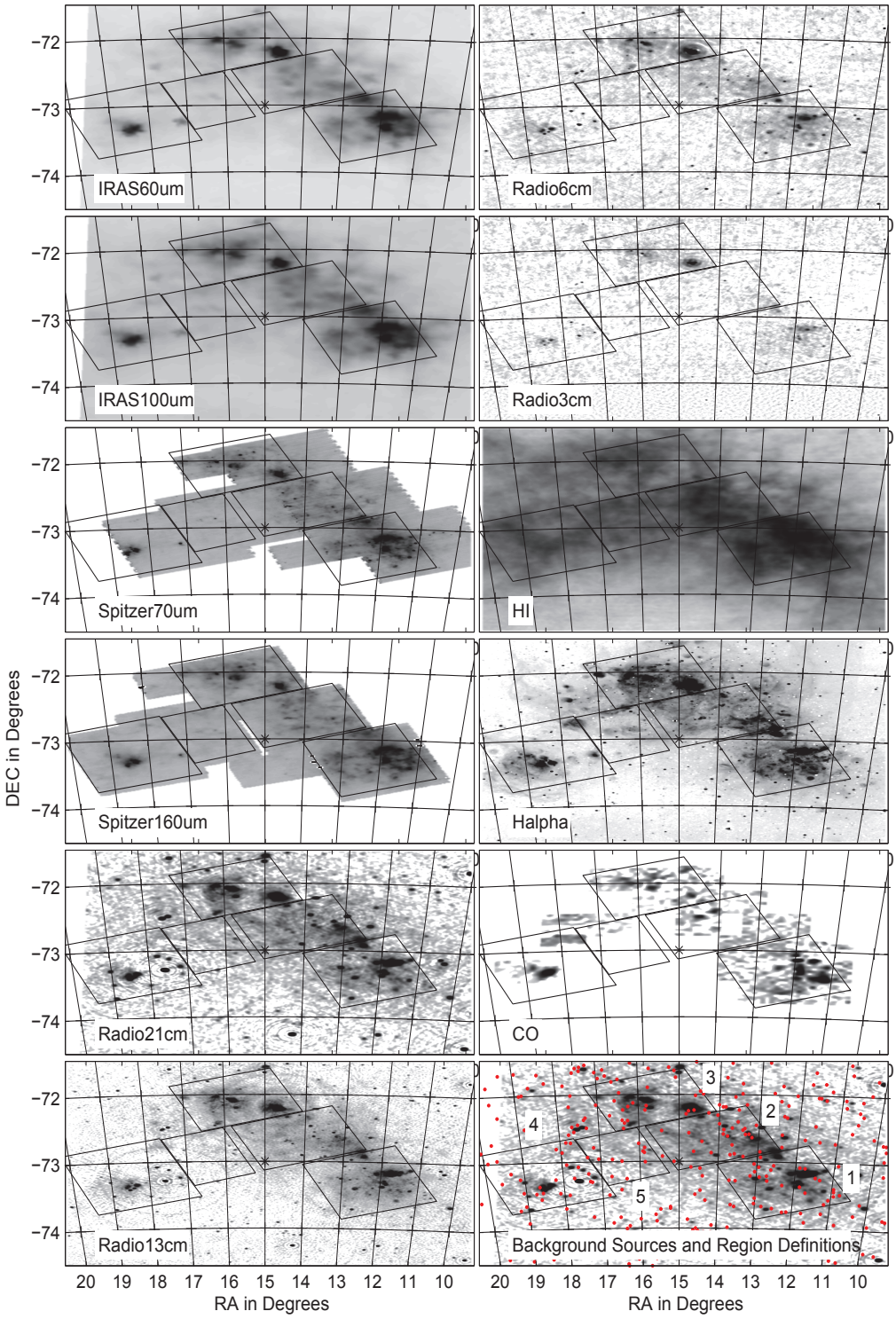

Figure 3.1: Small Magellanic Cloud Data for FIR/RC Correlations. All of the data sources used in this chapter are shown in this figure. The IRAS FIR data are the improved reprocessed data from the IRAS satellite survey (Miville-Deschênes and Lagache, 2005). Spitzer FIR data are from the Spitzer Survey of the Small Magellanic Cloud (S3MC) (Bolatto et al., 2007). The 160 μm Spitzer data provides the outline for the definition of the five regions used in this analysis which is shown in the background source panel. The four sources of RC data used in this thesis are shown in this figure. H I data from the ATCA and Parkes telescopes are combined to produce the data used here. Details of the data are found in Table 3.1. Data are displayed with North to the top and East to the left and J2000 coordinates in degrees. These plots are smoothed with a 25″ Gaussian kernel and scaled by the square root of the intensity.

Table 3.2: Regional Measured Flux Density Data and Derived Results. Flux functions per region, together with masses derived from H I and CO data, given as masses of H I and of H_2. The percentages refer to the portion of the total summed over all regions for each wavelength shown in this table. The SMC data refers to the whole SMC data set which includes data not contained in the regions.

Data	Region 1	Region 2	Region 3	Region 4	Region 5	SMC	Units
60 μm	24.9(39%)	13.1(20%)	16.0(25%)	7.33(11%)	2.88(4%)	92.6	10^2 Jy
100 μm	47.6(37%)	26.4(21%)	29.3(23%)	17.7(14%)	7.47(6%)	208.	10^2 Jy
70 μm	26.6(34%)	18.8(24%)	17.0(22%)	9.02(12%)	5.98(8%)	102.	10^2 Jy
160 μm	73.9(35%)	42.2(20%)	45.7(22%)	34.3(16%)	15.2(7%)	332.	10^2 Jy
H I	2.64(30%)	1.87(22%)	1.41(16%)	1.79(21%)	0.954(11%)	48.2	10^{27} H I /cm^2
H I	4.56(30%)	3.23(22%)	2.43(16%)	3.09(21%)	1.65(11%)	27.9	10^7 H I $M_\odot$
Hα	44.1(30%)	30.2(20%)	54.7(37%)	15.6(10%)	4.78(3%)	149.	10^{-11}ergs/cm^2/s
CO	494.(52%)	121.(13%)	179.(19%)	150.(16%)	4.72(0%)	82.6	10^2 K km/s
H_2	71.5(50%)	13.9(9.7%)	32.8(23%)	24.6(17%)	0.54(0.4%)	159.	10^5 $M_\odot$
3 cm	6.28(26%)	3.80(16%)	7.61(32%)	4.49(19%)	1.57(7%)	54.8	Jy
6 cm	5.80(29%)	3.87(19%)	6.47(32%)	2.91(15%)	0.861(4%)	33.5	Jy
13 cm	7.59(31%)	5.69(23%)	7.63(31%)	2.94(12%)	0.680(3%)	35.1	Jy
21 cm	7.55(29%)	6.46(24%)	7.59(29%)	3.69(14%)	1.17(4%)	40.0	Jy

Radio Telescope and the ATCA. For high resolution correlation investigations, the combined ATCA+Parkes data were used and, for the low resolution thermal fraction investigations, the Parkes data from Filipovic et al. (1997) were used exclusively due to the superior overall flux density accuracy of the data.

3.1.1 Radio Continuum Data

The high resolution RC data at 21 cm and 13 cm are from observations made with the ATCA telescope in 1992 from October 6^{th} to the 8^{th}. The observations were made using five antennas in the 375 m east-west array configuration (Wong et al., 2012b; Filipovic et al., 2005) at 1.42 GHz and at 2.37 GHz. The angular resolution was $\sim 98''$ full width half max (FWHM) and $\sim 49''$ FWHM, respectively. There were 320 pointings used to create a mosaic of data covering an area of $\sim 20\,\mathrm{deg}^2$. The "short spacing" low spatial frequency data fill was accomplished using Parkes survey data (Filipovic et al., 1997).

The 6 cm and 3 cm high resolution continuum data are from Dickel et al. (2010), at 4.8 GHz and 8.6 GHz, using the EW352 (February 2005) and EW367 (February and March 2006) configurations in 3564 individual pointing positions achieving resolutions of $35''$ and $22''$, respectively. The data were reprocessed to include data from the sixth antenna approximately 6 km from the centre of the ATCA that included the low spatial frequency data from the Parkes survey (Haynes et al., 1991). The addition of this incomplete, $2'' - 3''$ interference pattern provided greater resolution to the image for the evaluation of previously unresolved sources and was used here to enhance morphological studies using wavelet cross correlations. The additional data did not cover the full extent of the SMC but covered all of the areas examined in this study. (See Haynes et al. (1991); Xu et al. (1992); Klein et al. (1993); Filipovic et al. (1995,

1997, 1998a,b,c); Filipovic et al. (2002); Payne et al. (2004); Filipovic et al. (2005); Reid et al. (2006); Payne et al. (2007); and Crawford et al. (2011b); Wong et al. (2011c,d, 2012b)).

The H I 21 cm data are from observations made with the ATCA telescope in 1992 from October 6^{th} to the 14^{th} and August 2^{nd} to the 3^{rd}. The observations were made using five antennas in the 375 m east-west array configuration (Staveley-Smith et al., 1995, 1997) at 1.42 GHz. The angular resolution was $\sim 98''$ FWHM. There were 320 pointings used to create a mosaic of data covering an area of $\sim 20\,\mathrm{deg}^2$. The "short spacing" low spatial frequency data fill was accomplished using Parkes survey data (Stanimirovic et al., 1999) observed from 1996 March 14^{th} to 17^{th}.

The column densities were corrected for self–absorption using the correction factors from Stanimirovic et al. (1999). The H I mass was calculated for each region and the whole SMC and is shown in Table 3.2. Results reported here of 2.8×10^8 H I $M_\odot$ from a $3^\circ \times 3^\circ$ reduced data set compare favorably to a published value of 3.8×10^8 H I $M_\odot$ from Stanimirovic et al. (1999) for a $5^\circ \times 5^\circ$ image.

3.1.2 Far-Infrared Data

The IRAS data used in this thesis are the improved reprocessed data from the IRAS satellite survey (Miville-Deschênes and Lagache, 2005). The data are in two bands: 60 μm and 100 μm which have been corrected for zodiacal light, calibration, zero levels, and striping problems (see Figure 3.1).

The data used from the Spitzer satellite are from the MIPS instrument. They are from the Spitzer Survey of the SMC (S3MC) which covered most of the bar and wing in two bands: 70 μm and 160 μm (Bolatto et al., 2007). The data have been corrected for zodiacal light, Galactic foreground, and cosmic infrared background using Leroy's published data (Leroy et al., 2007) to adjust the final calibration.

3.1.3 Carbon Monoxide mm Data

CO data are from the NANTEN millimeter-sub-millimeter observatory on Pampa la Bola in the Atacama Desert, Chile (Mizuno et al., 2001). The NANTEN telescope was used at a wavelength of 2.6 mm and the observations had an angular resolution of $2.6'$ FWHM. Regions 1–3 were well covered by this data. Region 4 had coverage primarily around N84 and there was only incidental coverage of Region 5.

The conversion factors for the CO data to H_2 mass used in this thesis are from Leroy et al. (2011). Leroy calculated three different conversion factors for the SMC for different parts of the SMC which varied by 40%. (Leroy-West $\rightarrow$ Region 1; Leroy-North $\rightarrow$ Region 3; Leroy-

Table 3.3: CO Conversion Factors to H_2. From (Leroy et al., 2011) as assigned to the SMC regions and the calculated H_2 mass for each region.

Region	Conversion Factor $M_\odot(pc^{-2})(K\,km\,s^{-1})^{-1}$	H_2 $*10^5\,M_\odot$
1	67	71.5
2	53	13.9
3	85	32.8
4	67	24.6
5	53	0.54
SMC	69	159

East → Region 4; average of Leroy-West and Leroy-North → Region 2 and Region 5). This conversion was expected to detect only the most dense H_2 clouds. The conversion factors applied to the five regions and the overall average value applied to the entire SMC are shown in Table 3.3.

3.1.4 Hα Data

The Hα data are from the MCELS program using the UM/CTIO Curtis Schmidt telescope (Smith et al., 2000). The central $3.5^\circ \times 4.5^\circ$ of the SMC were imaged in overlapping $1^\circ \times 1^\circ$ fields with 2048^2 pixels per field to provide at least two samples of each pixel. The Hα filter was centred on 656.2 nm with a width of 3 nm. Two continuum channels were also imaged for stellar contribution subtraction: 685 nm, $\delta = 9.5$ nm, and 513 nm, $\delta = 3$ nm.

3.1.5 Background Sources

Since the SMC is essentially transparent to 1.42 GHz RC radiation and it presents a cross section of several deg^2, many background sources were expected to be visible in the SMC RC data. A total of 717 discrete RC sources were detected by Payne et al. (2004), Crawford et al. (2011b); Wong et al. (2011c,d, 2012b), of which 616 were identified as background sources. They are plotted in Figure 3.1 (bottom right panel) along with the numbers assigned to each of the five regions on an image of the 21 cm RC data.

3.2 Far-Infrared / Radio Continuum Ratios

The analysis of the FIR/RC ratios applied cross correlation calculations between several different wavelengths. This was done by employing traditional pixel by pixel correlations as well as wavelet correlations. The pixel by pixel correlation studies provided intensity correlations as a function of position. The wavelet cross correlation technique probed morphological correlations which were sensitive to changes over a range of spatial scales. FIR/RC correlation was studied over the entire SMC as well as the regions defined previously.

All of the correlation analysis with RC data were done excluding data at the coordinates of the background sources. The mask consisted of a Gaussian function with a FWHM of $2'$ applied to the coordinates of each background source. The data sets also had a median filter of $15'' \times 15''$ applied to remove zero pixels and to provide a slight smoothing.

Measurements of the FIR/RC correlations in the SMC were made down to scale factors of less than 1 kpc by considering each of the five regions in the SMC. Three of these regions cover the bar structure and two cover the portion of the wing structure that is closest to the bar. The structure of the correlations within the regions is shown in images which display the organization of the FIR and RC emissions giving rise to the measured values, see Figure 3.1. These correlations were compared to measurements from more distant galaxies and are shown in Figure 3.2.

Using the 60 μm IRAS IR flux and the 21 cm RC flux, a FIR/RC calculation was made for each of the five SMC regions and the whole SMC (defined as a $3^\circ \times 3^\circ$ region centred at RA 15° DEC -73°). These results were directly compared to the survey done by Yun et al. (2001). Yun's catalogue identified radio counterparts to the IRAS Redshift Survey galaxies with 60 μm IR fluxe densities of ≤ 2 Jy. The catalogue includes 1750 galaxies and contains radio positions and redshifts. Also tabulated were 1.4 GHz RC luminosities from the selected galaxies and their IRAS fluxes.

An ordinary least squares fitting (OLS) was performed on this data to determine the FIR/RC ratio as defined by the data from Yun et al. (2001). The fitting equation calculated in this thesis is

$$\log(\mathrm{L}_{1.4\,\mathrm{GHz}}) = \left(\frac{0.995\,W}{\mathrm{Hz}}\right) \cdot \log\left(\frac{L_{60\,\mu\mathrm{m}}}{\mathrm{L}_\odot}\right) + \left(\frac{12.377\,\mathrm{W}}{\mathrm{Hz}}\right). \tag{3.1}$$

For each $5'' \times 5''$ pixel of the SMC data, the values of the FIR/RC ratio were calculated. The sums of this ratio for each region are plotted on the graph with Yun's data set, see Figure 3.2. The line described by the best fitting equation is extended through the SMC data presented in this thesis to show how the fitted ratio of the data from Yun et al. (2001) corresponds with the SMC data. The correlation is evident in all five regions and for the whole SMC. The distances from Yun's regression best fitting line to the regional and complete SMC data are very small: from Δ=0.017 dex to Δ=0.115 dex. These differences change slightly depending on whether the background sources are included or not. The differences for each region and the whole SMC are shown in Table 3.4, including the change due to background sources.

For comparison, Figure 3.2 also plots the LMC correlation calculated here from data published on the LMC by Hughes et al. (2006). The distance to Yun's regression line for the LMC was calculated to be Δ=0.308 dex.

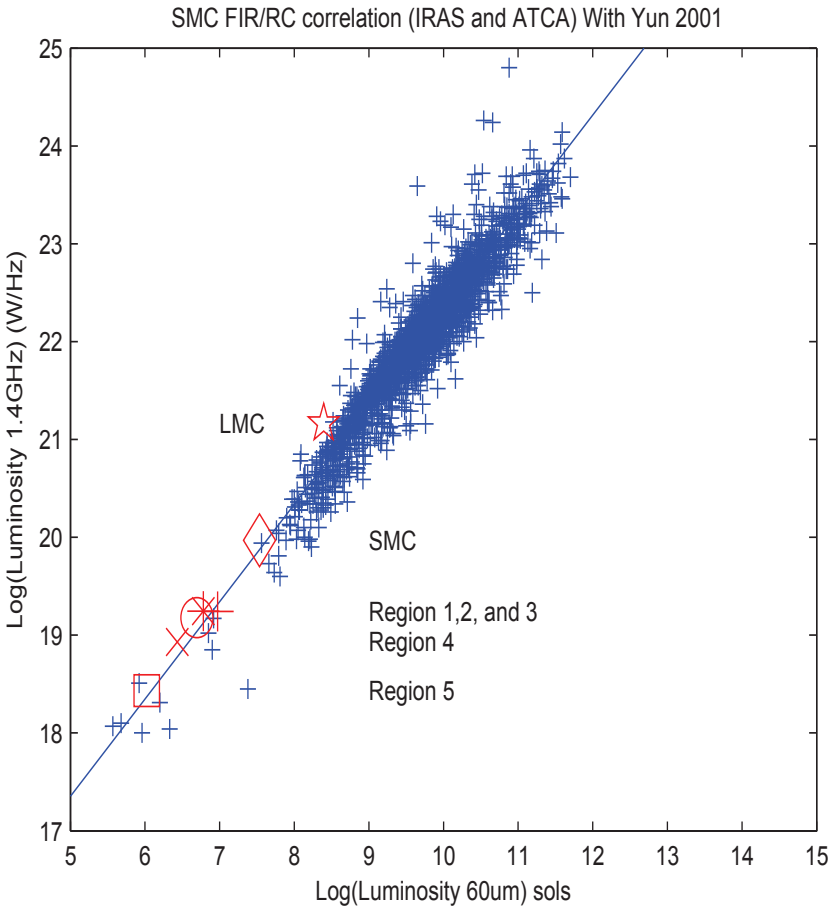

Figure 3.2: Small Magellanic Cloud FIR/RC Correlations. Correlations for the whole SMC (defined as a 2.5° x 2.5° region centred at RA 15° DEC −73°) and the regions defined in this chapter compared to the data from Yun et al. (2001). Regions 1-5 and whole SMC are plotted and labeled. (1-plus, 2-circle, 3-asterisk, 4-x, 5-square, and SMC-diamond). Additionally, the correlation calculated from data published on the LMC by Hughes et al. (2006) is plotted using the star marker. (Note: sols = $L_{\odot}$)

Table 3.4: Data Fitting Comparison to Yun's Luminosity Measurement Data. Comparison of the differences between the data fitting to data from Yun et al. (2001) and to the current measurements. The contribution to the fitting from the background sources is shown to be less than 10 percent of the fitting discrepancy.

Regions	Without BKG	With BKG	Difference
	dex	dex	%
1	0.1159	0.1153	-0.52
2	0.0431	0.0433	0.46
3	0.0465	0.0460	-1.08
4	0.0183	0.0172	-6.39
5	0.0297	0.0283	-4.94
SMC	0.0783	0.0783	0.00

3.3 Pixel by Pixel Analysis

Pearson's linear correlation coefficient calculation was performed between several pairs of data sets, Equation 3.2. For each pair of data sets, the data set with the smallest FWHM beamwidth was convolved with a Gaussian kernel to smooth it to the same FWHM as the lower resolution data. The sampling was then done at a spacing corresponding to the beamwidth of the lower resolution data to guarantee statistical independence of the samples. In this equation, f_N refers to the N^{th} image, f_{Ni} refers to the i^{th} pixel of the N^{th} image, and r_p is the Pearson's linear correlation coefficient

$$r_p = \frac{\sum \left(f_{1i} - \langle f_1 \rangle\right)\left(f_{2i} - \langle f_2 \rangle\right)}{\sqrt{\sum \left(f_{1i} - \langle f_1 \rangle\right)^2 \sum \left(f_{2i} - \langle f_2 \rangle\right)^2}}. \tag{3.2}$$

The error in this correlation is

$$\Delta r_p = \frac{\sqrt{1 - r_p^2}}{\sqrt{n^2 - 2}}. \tag{3.3}$$

The formal errors for these data sets are $\simeq$10% since n, the total number of points in a data set, is $\sim 10^3$ when the resolution of the data sets are considered. Of course, the real error is possibly larger due to calibration errors and other systematic errors in the data.

Perfectly correlated images would have a coefficient of 1 and perfectly anti-correlated images would have a coefficient of -1. Table 3.5 shows various pairs of data sets for the five regions and the correlations therein. Values above 0.7 in Table 3.5 indicate moderate to strong correlation. Those values are printed in bold face type. Pairs chosen for correlation are from different physical production mechanisms, for example, RC versus FIR or Hα versus CO.

Correlation for FIR with H I appears to be associated with the supernova count. Region 1 with nine supernovae and Region 5 with twelve supernovae have the highest correlation counts with all FIR bands showing excellent correlation with H I. Region 2 with two supernovae has excellent FIR correlation only with 160 μm emission. Other regions without supernova do not exhibit significant correlation for FIR with H I.

Other correlation patterns are also evident. Region 3 shows high correlations for some wavelengths of FIR with 21 cm and 13 cm. In Region 3, the strongest correlation of Hα is with 21 cm, 13 cm, 60 μm, and 100 μm. CO correlates well with FIR in Region 4.

Figure 3.3 shows the scatter plots of the 21 cm continuum and 60 μm IR data for the pixels from each of the five regions and from the whole SMC. For each pair of data sets, the data set with the smallest FWHM beamwidth was convolved with a Gaussian kernel to smooth it to the same FWHM as the lower resolution data. The sampling was performed at

Table 3.5: Correlations between Measured Data Sets. Pearson correlations for pairs of data sets. All results have a calculated error of $\simeq 10\%$. For each pair of data sets, the data set with the smallest FWHM beamwidth is convolved with a Gaussian kernel to smooth it to the same FWHM as the lower resolution data. The sampling is then done at a spacing corresponding to the beamwidth of the lower resolution data. Values above 0.7 are in **Boldface** to emphasize good correlation.

	Regions				
Data Sets	1	2	3	4	5
RC 21 cm with					
60 μm	0.620	0.686	**0.825**	0.444	0.263
70 μm	0.573	0.513	0.585	0.484	0.193
100 μm	0.574	0.607	**0.752**	0.410	0.201
160 μm	0.587	0.458	0.656	0.515	0.168
RC 13 cm with					
60 μm	0.609	**0.700**	**0.815**	0.501	0.304
70 μm	0.610	0.628	**0.752**	**0.720**	0.127
100 μm	0.569	0.638	**0.740**	0.461	0.244
160 μm	0.629	0.577	0.661	0.616	0.129
CO with					
RC 21 cm	0.272	0.059	0.311	0.422	–0.255
RC 13 cm	0.296	0.073	0.305	0.347	0.032
60 μm	0.531	0.130	0.318	**0.759**	0.116
70 μm	0.531	0.142	0.405	0.471	0.190
100 μm	0.554	0.170	0.378	**0.769**	0.146
160 μm	0.599	0.168	0.479	**0.896**	0.181
H I	0.304	0.205	0.173	0.444	0.293
Hα	0.312	0.018	0.307	0.291	–0.055
H I with					
RC 21 cm	0.404	0.255	0.059	0.092	0.137
RC 13 cm	0.443	0.307	0.044	0.137	0.109
60 μm	**0.762**	0.584	0.197	0.394	**0.748**
70 μm	**0.709**	0.545	0.209	0.226	**0.790**
100 μm	**0.810**	0.680	0.338	0.472	**0.833**
160 μm	**0.773**	**0.708**	0.401	0.506	**0.857**
Hα with					
RC 21 cm	0.377	0.659	**0.859**	0.563	0.329
RC 13 cm	0.273	0.597	**0.830**	**0.722**	0.237
60 μm	0.205	0.327	**0.816**	0.516	0.408
70 μm	0.387	0.290	0.638	0.535	0.018
100 μm	0.158	0.297	**0.731**	0.475	0.350
160 μm	0.438	0.247	0.661	0.179	0.020

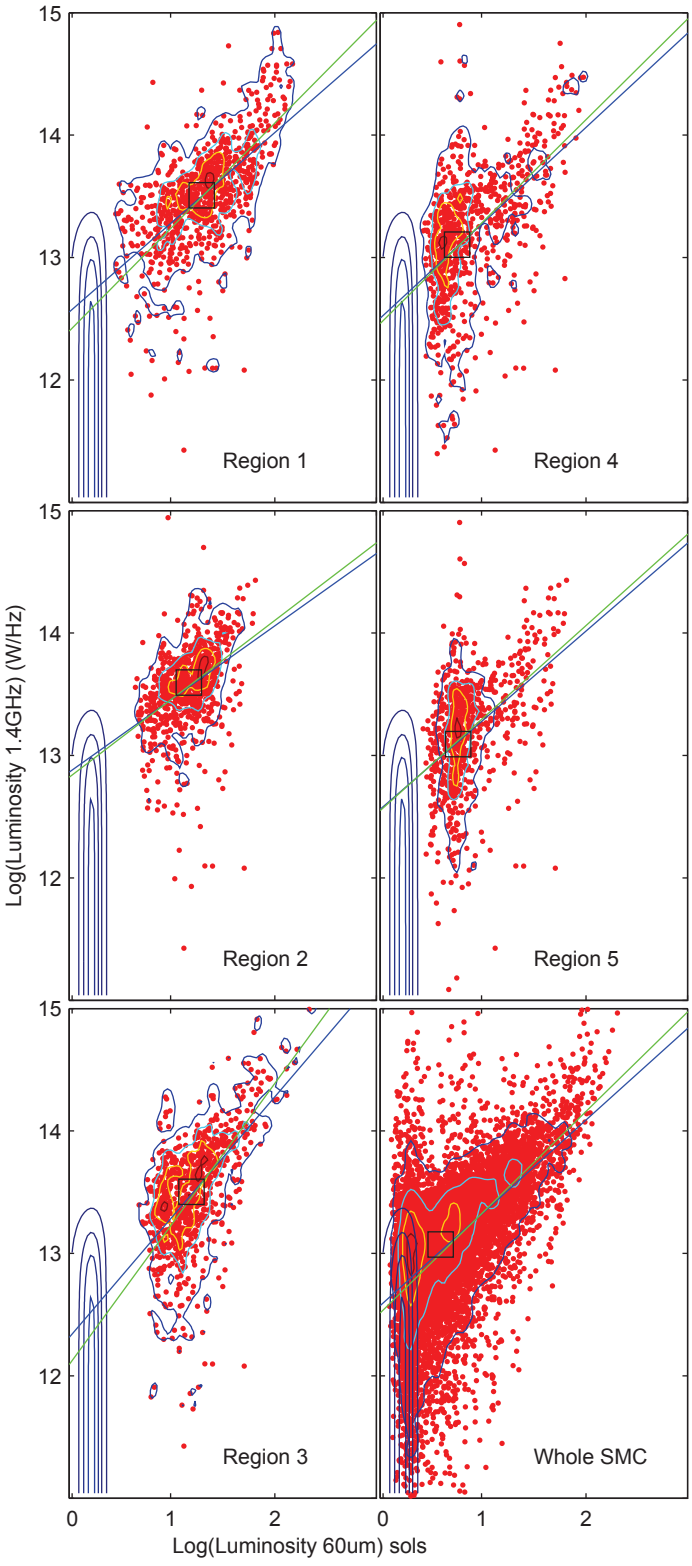

Figure 3.3: Small Magellanic Cloud FIR/RC Scatter Plots. Scatter plots for 21 cm with 60 μm for the regions and the whole SMC. For each pair of data sets, the data set with the smallest FWHM beamwidth is convolved with a Gaussian kernel to smooth it to the same FWHM as the lower resolution data. The sampling is then done at a spacing corresponding to the beamwidth of the lower resolution data. The two lines in each plot are the OLS and WLS fittings to the data. The WLS is in green, the OLS in blue. The contours in the data plot show the density of data points and the Gaussian distribution of the background noise. Those contours are at 5%, 30%, 60%, and 90% of the peak data density. The position of the square is the average of the data set. (Note: sols = $L_\odot$)

a spacing corresponding to the beamwidth of the lower resolution data to guarantee statistical independence. Figure 3.3 also shows two different least squares fittings to each data set. The blue line is the OLS and the green line is the weighted least square (WLS) calculated using the MATLAB LSCOV function (Matlab, 2010). The OLS assumes the error of each data point is the same and consequently weights every data point equally. The purpose of the WLS is to improve the fitting by reducing the effect of measurement error on the calculated parameters of the linear fitting. Each point is given a weighting which specifies its effective contribution to the resulting computations.

The weighting factors were calculated from an estimation of the measurement error for each data point. The weighting factors (equivalent to the inverse relative error) depend on the position of the point relative to the range of measured values present in the sample. For each coordinate, the data point with a value at the minimum of the range was assigned a weighting factor of 0.01 and the data point at the maximum of the range was assigned a weighting factor of 1. Intermediate values were assigned weights proportional to their position in the range from minimum to maximum value. This linear weighting was done independently on the 1.4 GHz axis and the 60 μm axis for every data point. The w values are the adopted weighting factors for the data points. For each data point, the aggregate weighting value is

$$w = \sqrt{w^2_{\mathrm{L}_\odot 1.4\,\mathrm{GHz}} + w^2_{\mathrm{L}_\odot 60\,\mu\mathrm{m}}}. \tag{3.4}$$

The LSCOV calculation inputs were three arrays: the 1.4 GHz values; the 60 μm values; and the calculated values for the aggregate data weighting, w.

The difference in the slope and offset of these fitting lines and the averages are shown in Table 3.6. The last row contains the differences in percent of the OLS slope and the WLS slope of the fitted lines. It is expected that the OLS would be a better representation of the entire data set whereas the WLS would describe the strongest data.

Strong to moderate Pearson correlations in FIR/RC, FIR/H I, and IR/Hα in Regions 1 and 3 as seen in Table 3.5 appear to show the effect of two populations of data in those regions. The range of OLS slopes in the regions is 0.594 to 0.978 while the WLS slopes range from 0.638 to 1.144 over the regions. In every region the OLS slope is flatter that the WLS slope. The set of contour lines to the left of the figures is from the background noise using measurements from the northeast corner of the whole SMC data set which are not considered to be part of the SMC. The measured average value and the root mean square (RMS) noise were used to calculate a background Gaussian noise distribution and the results of this distribution were used to create the noise contours for the background. Also shown are four contours which were created by organizing the luminosity data into a 100 $\times$ 100 bin array. The contours shown are at 5%, 30%,

Table 3.6: Fitting Values for Scatter Plots of 21 cm with 60 μm . Data set averages for 21 cm, RC, y = log (Luminosity 1.4 GHz)(W/Hz), FIR, x = log (luminosity 60 μm) $L_{\odot}$, and fitting parameters to $y = ax + b$ using OLS and WLS. These numerical values are shown graphically in Figure 3.3. The slope values are also shown with the WLS always larger than the OLS value. $\Delta a\%$ is the difference between the slope values, a, from the OLS and WLS fittings. For comparison, Yun et al. (2001) data as fitted here using OLS gives $a = 0.995$ and $b = 12.38$.

	Regions					
	1	2	3	4	5	SMC
RC	13.51	13.60	13.50	13.11	13.10	13.07
FIR	1.296	1.169	1.195	0.753	0.762	0.590
OLS a	0.730	0.594	0.978	0.776	0.725	0.755
WLS a	0.846	0.638	1.144	0.829	0.752	0.819
OLS b	12.55	12.86	12.31	12.50	12.56	12.57
WLS b	12.40	12.82	12.09	12.46	12.55	12.51
$\Delta a\%$	13.7	6.8	14.5	6.4	3.6	7.8

60%, and 90% of the maximum bin count. Visually examining these contours indicates that 90% of the data are found with values quite symmetric to the fitted lines, both OLS and WLS. With the application of the relative error weighting in the WLS fitting, it would be expected that the WLS fitting is a better representation of the data. The Gaussian noise distribution calculated for the measured background noise used the same scaling. It is clear that there is not a significant contribution by noise to the scatter plot for any of the five regions. The whole SMC plot includes portions of sky, however, which are not part of the SMC and contain only noise so that there is considerable overlap seen in the lower luminosity values of the scatter plot with the noise contours. The plotted square in each data set is the location of the average pixel value.

3.4 Far-Infrared / Radio Continuum Ratio Map

In order to relate particular physical structures in the SMC with variations in the FIR/RC ratio, Figure 3.4 was calculated showing the log ratio of FIR and 21 cm RC data. The q value map was calculated using the formula from Helou et al. (1988) with the IRAS 60 μm and 100 μm data sets. The FIR flux, F_{FIR}, is

$$\left(\frac{F_{FIR}}{\mathrm{Wm}^{-2}}\right) = 1.26 \cdot 10^{-14} \left(\frac{2.58 S_{60\mu\mathrm{m}} + S_{100\mu\mathrm{m}}}{\mathrm{Jy}}\right). \tag{3.5}$$

The q values of the pixels are

$$q = \log\left(\frac{F_{FIR}}{3.75 \cdot 10^{12}\,\mathrm{W\,m^{-2}}}\right) - \log\left(\frac{S_{RC}}{\mathrm{W\,m^{-2}\,Hz^{-1}}}\right) \ . \tag{3.6}$$

The average value of the ratio is q=2.65. This suggests that the SMC has a slight FIR excess when compared to the average figure of q=2.34 in Yun et al. (2001). Approximately 98% of

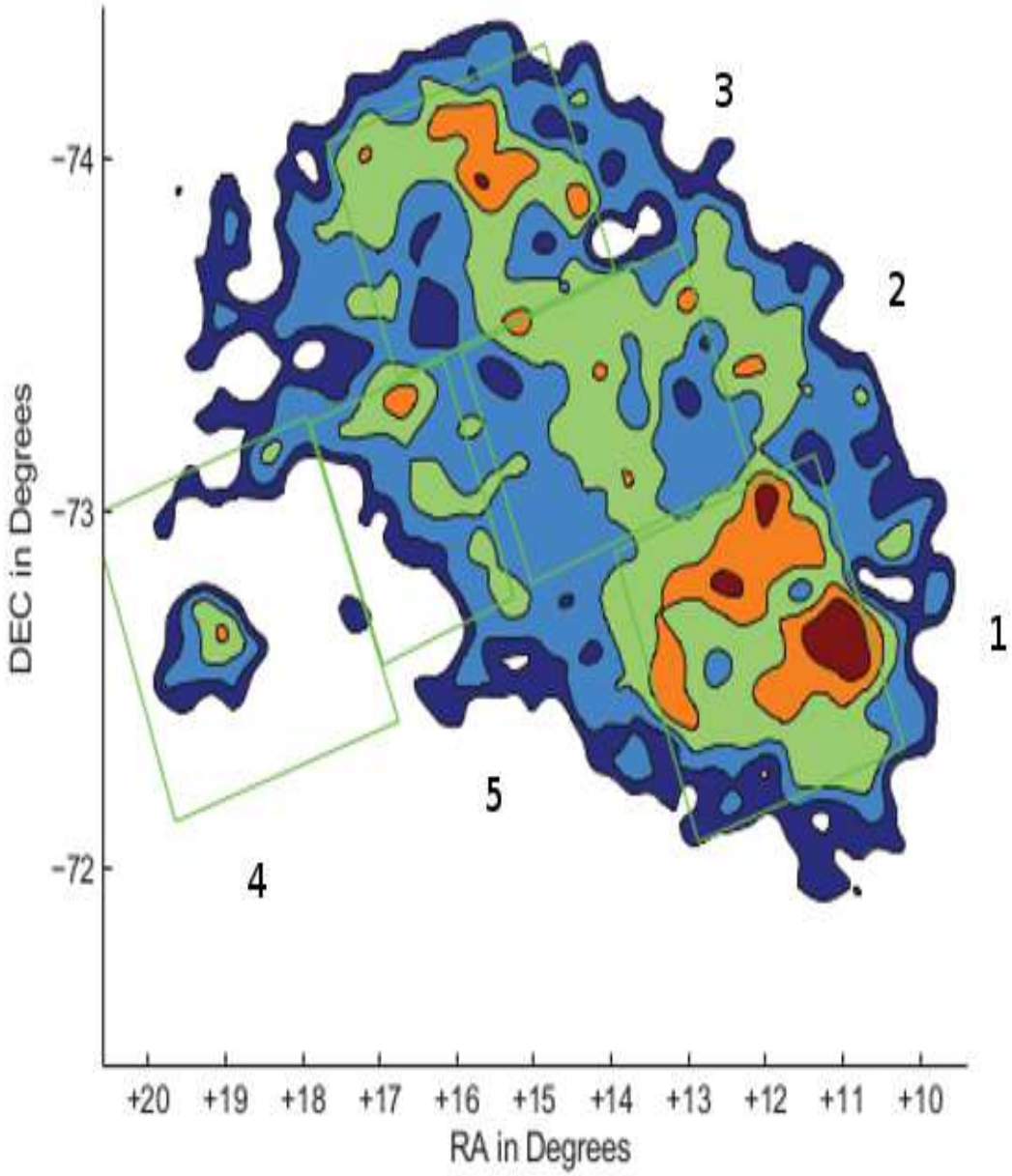

Figure 3.4: Small Magellanic Cloud q Value Plot. This figure shows the q value plot of the SMC which has been convolved with a Gaussian kernel of 108 pc FWHM. Red $>$ 2.95 $>$ orange $>$ 2.75 $>$ green $>$ 2.55 $>$ light blue $>$ 2.35 $>$ dark blue $>$ 2.15 $>$ white. Region numbers are shown in the figure.

Yun's galaxies are within a factor of 5 of 2.65: ∼1.6 to ∼3.0. Figure 3.4 shows the distribution of q values across the SMC from q <2.15 to q >2.95.

Region 1, with an average q of 2.80, has a large portion of its area with q ≥2.65. This suggests that there is abundant dust in the area. Relatively high Pearson correlations of FIR with H I are also seen in Table 3.5 for Region 1. There are nine supernova remnants in this region. The strongest RC feature in this region is N 19 containing SNR B0045-734 (Payne et al., 2004; Crawford et al., 2011b; Wong et al., 2011c,d, 2012b). The other regions have extended areas where the RC excess is present.

Region 2, with an average q of 2.58, has a large portion of its area with q ≤2.65. With two supernova remnants in this region, it could be inferred that there is not much star-forming activity here which suggests that the dust, as a result, is cooler.

Region 3, with an average q of 2.70, has twelve supernova remnants. It also has areas of q <2.65 and areas of q >2.65 with similar sizes. The high star formation rate leads to the very high Pearson correlation seen in all of the IR data maps with the 21 cm data. Hα correlates very well also with the RC data and the FIR data.

Region 4, with an average q of 2.75, is dominated by background radio source SMC B0109-7330. The eastern part of the region has significant dust and gas. It is the only region that has strong correlation of CO with the IR emission in the Pearson correlation results.

Region 5, with an average q of 2.73, has a very small total energy emission, 0.2 – 0.3 of the average of the other five regions. Scaled for area, it is $\sim 0.4-\sim 0.6$ of the average.

3.5 Wavelet Analysis

Wavelets can be used as a tool for scaling analysis (Frick et al., 2001). It is a technique that convolves the data with a family of self-similar analyzing functions that depend on scale and location. The family of analyzing functions is defined by dilations and translations of the analyzing function, also called the mother function. In two dimensions, the continuous wavelet transformation is

$$W(a,\vec{x}) = \frac{1}{a^{\kappa}} \int_{-\infty}^{\infty} \int_{-\infty}^{\infty} f(\vec{x}') \Psi^* \left(\frac{\vec{x}' - \vec{x}}{a} \right) d\vec{x}'. \tag{3.7}$$

In this expression, $\vec{x} = (x, y)$ and $f(\vec{x})$ is the two dimensional data set for which the Fourier transform exists, $\Psi^*(\vec{x})$ is the complex conjugate of the analyzing function, a is the scale factor, and κ is the normalizing parameter.

The analyzing function used here is the Pet Hat function (Frick et al., 2001). This function is defined in terms of its Fourier transform as

$$\hat{\Psi}\left(\vec{k}\right) = \cos^2\left(\frac{\pi}{2}\log_2\frac{k}{2\pi}\right) : \pi < \left|\vec{k}\right| < 4\pi$$
$$= 0 : \text{otherwise.} \tag{3.8}$$

This function specifies an annulus in Fourier space with a median radius of 2π and is non-zero only for the specified annulus.

3.6 Wavelet Cross Correlation

Given a two dimensional data set, the energy of the transformation as a function of scale factor, a, over the entire plane is

$$M(a) = \int_{-\infty}^{\infty}\int_{-\infty}^{\infty} |W(a,\vec{x})|^2 d\vec{x}. \tag{3.9}$$

The wavelet cross correlation coefficient as a function of a is

$$r_w(a) = \frac{\int\int W_1(a,\vec{x})\, W_2^*(a,\vec{x})\, d\vec{x}}{\sqrt{[M_1(a)\, M_2(a)]}}, \tag{3.10}$$

where the subscripts refer to the source data sets used in the cross correlation.
The error in the cross correlation is

$$\Delta r_w(a) = \frac{\sqrt{1 - r_w^2(a)}}{\sqrt{\left(\frac{L}{a}\right)^2 - 2}}, \tag{3.11}$$

where L is the linear size of the data set. For the data used here, $\Delta r_w(a)$ is $\leq 15\%$.

For each pair of data sets used in wavelet cross correlation, the data set with the smallest FWHM beamwidth was convolved with a Gaussian kernel to smooth it to the same FWHM as the lower resolution data. The sampling was performed at a spacing corresponding to the beamwidth of the lower resolution data. Figure 3.5 shows wavelet correlations of several data sets with the 21 cm RC in all five regions. The smallest scale that can be used to analyze the data is the resolution of the data. The largest scale is dependent on the overall size of the data set. The smallest linear dimension of the data set should be no less than four times the largest scale factor used in the analysis. The resolution of the 21 cm data was $90''$ (27 pc) and the finest resolution calculated was $80''$ (24 pc). The correlation was performed with IRAS 60 μm and 100 μm data with $120''$ (36 pc) resolution, and with Spitzer 70 μm and 160 μm data with $18''$ (5.4 pc) and $40''$ (12 pc) resolution, H I data with $98''$ (30 pc) resolution, Hα with $3''$ (1 pc) resolution, and CO data with $156''$ (46 pc) resolution. For the data sets used here, the maximum valid scale value for the wavelet cross correlation was $794''$ (238 pc) for Regions 1-4 and $501''$ (150 pc) for Region 5 except for the CO data.

Table 3.7: Smallest Excellent 21 cm RC Wavelet Cross Correlation Scale Factors. Scale factors in pc for Region 1 through 5 with data from several other data sets. Listed are the minimum scale factors in pc for which the wavelet cross correlations are considered excellent, which is taken to be ≥ 0.75. **BoldFace** values are limited by the beamwidth of one of the data sets.

	Regions				
	1	2	3	4	5
IRAS 60 μm	53.2	**35.3**	**35.3**	51.5	129.8
IRAS 100 μm	57.3	**35.3**	**35.3**	55.9	136.1
Spitzer 70 μm	52.4	**28.3**	**24.0**	50.6	50.3
Spitzer 160 μm	54.5	33.4	**24.0**	52.6	53.2
H I	129.8	—	170.1	88.7	83.6
Hα	30.6	**25.3**	**24.0**	45.9	53.2
CO	97.0	—	229.0	—	—

The CO map is much more irregular than the other data sets. Region 1 has nearly complete coverage with the cross correlation results beginning at 125″. Region 2 is not well covered and has a large hole in the coverage in the centre of that region. The only scale factors that satisfiy validity requirements are at 125″ and 200″, both of which are shown. Region 3 also has nearly complete coverage with the cross correlation results beginning at 125″. Region 4 is split into two smaller areas. Interpreting the wavelet cross correlation in that region was problematic. Region 5 has just a sliver of data that is too small and irregular to use in a wavelet correlation. Wavelet correlations of Regions 4 and 5 were not calculated.

3.7 Wavelet Cross Correlation: Far-Infrared with Radio Continuum

Table 3.7 shows the smallest scale factors for which excellent wavelet cross correlation was measured. Frick et al. (2001) regarded 0.75 or above as representing an excellent correlation between images and that value has been adopted here as the correlation threshold. The scale factors were extracted from the data in Figure 3.5. The data clearly exhibits strong morphological correlation of dust emission in the FIR with the 21 cm continuous emission from the defined regions of the SMC down to the beamwidth limited minimum scale factor, ~ 35 pc. In Regions 2 and 3, the limit of the correlations is primarily due to the data resolution. Table 3.7 presents the wavelet correlations extracted from Figure 3.5 which correlates the Spitzer IR data with the higher resolution 3 cm and 6 cm data, (Dickel et al., 2010). The wavelet cross correlation with the Spitzer data demonstrates that the FIR/RC wavelet correlation scale factors extend down to $\sim$15 pc. Within each region, all of the FIR bands show similar correlation patterns with RC data with respect to scale factor. The coverage of the regions was quite good for the Spitzer 160 μm data but less so for the Spitzer 70 μm data, particularly in Regions 1, 3, and 4. There are also some unexpected differences between the 3 cm and 6 cm correlations

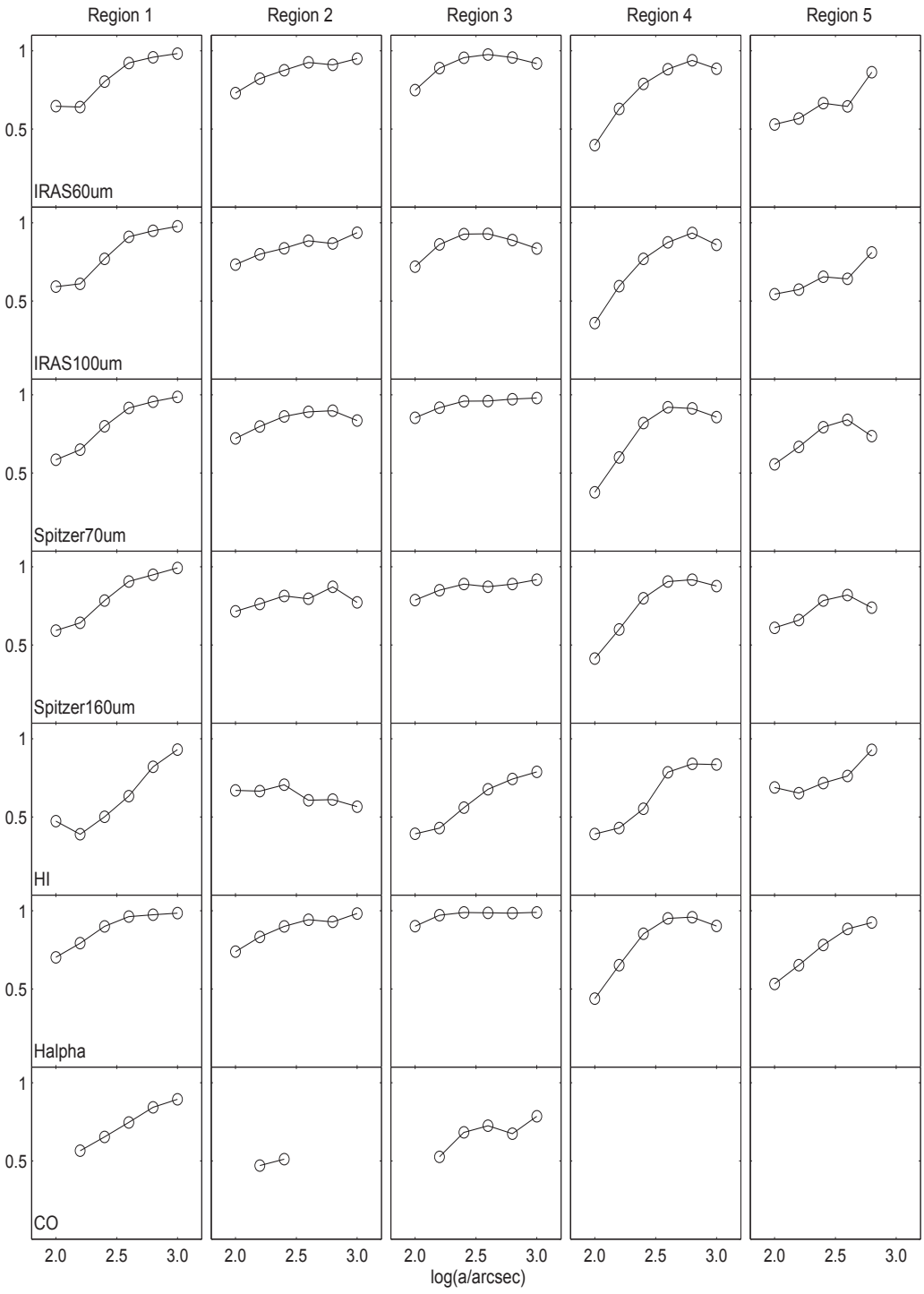

Figure 3.5: Small Magellanic Cloud 21 cm Wavelet Cross Correlations. Plots for Region 1 through 5 with data from several other data sets. The data points for Regions 1-4 are calculated at scale factors of 80″, 125″, 200″, 316″, 501″, and 794″ which correspond to 24 pc, 37 pc, 60 pc, 95 pc, 150 pc, and 238 pc respectively. The data set from Region 5 is too small to support wavelet cross correlations of 794″ so correlations are only shown up to 501″, 150 pc. Coverage over the map of CO data is not complete except for Regions 1 and 3.

Table 3.8: 6 cm and 3 cm RC High Resolution Wavelet Cross Correlations. Scale factors in pc for Region 1 through 5 with data from Spitzer and $H\alpha$ data sets. Listed are the minimum scale factors in pc for which the wavelet cross correlations are considered excellent, which is taken to be ≥ 0.75.

6 cm RC					
Region	1	2	3	4	5
Spitzer 70 μm	43.2	19.8	14.7	23.1	137.3
Spitzer 160 μm	45.2	22.7	17.7	17.6	114.1
Hα	9.0	14.0	10.4	9.1	87.5
3 cm RC					
Spitzer 70 μm	37.9	27.6	16.4	33.3	129.4
Spitzer 160 μm	39.7	36.8	17.6	35.5	80.6
Hα	12.6	32.1	17.10	33.8	—-

with the FIR data.

3.8 Wavelet Cross Correlation: Other Bands with Radio Continuum

H I cross correlation is seen in Figure 3.5 with 21 cm RC in Region 1. The correlation initially dips before beginning a slow rise to the correlation threshold at ∼130 pc. Region 2 never achieves correlation threshold and Region 3 does not until ∼170 pc. Regions 4 and 5 have the same scale factor of ∼85 pc.

Hα correlations with 21 cm RC (Table 3.7) are essentially at the resolution of the H I data at ∼25 pc for Regions 1 through 3. Regions 4 and 5 have correlation thresholds at larger scale factors of ∼85 pc. High resolution Hα correlations from Figure 3.6 with 3 cm and 6 cm (Table 3.8) show that the Hα wavelet cross correlation extends down to much smaller scale factors from 9 pc to 33 pc for Regions 1 through 4.

The CO correlations are very sparse since the map of the data is rather incomplete. Region 1 has a correlation threshold at 97 pc and above. No significant correlation is detected in Region 2. Region 3 has a correlation threshold at 229 pc. No other correlations are possible.

3.9 Discussion of Far-Infrared / Radio Continuum Correlations

The FIR/RC correlation coefficient, q, determined in this study is very close to the expected value for normal galaxies even though the SMC is structurally different from the spiral galaxies which constitute most of the population on which the correlation is based. Spirals generally have a thick underlying non-thermal disk. The expected thermal fraction for the disk of a spiral

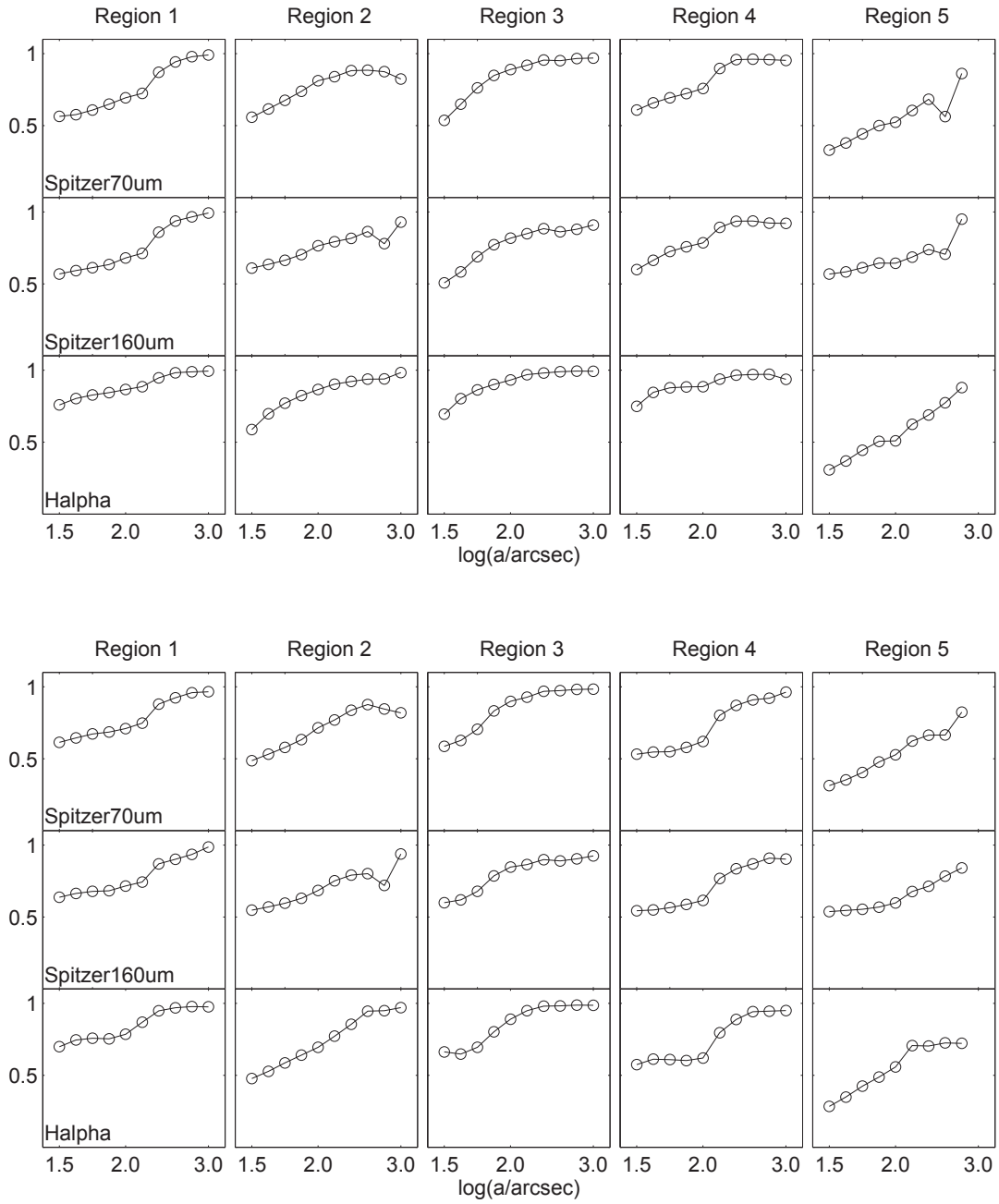

Figure 3.6: Small Magellanic Cloud 6 and 3 cm Wavelet Cross Correlations. 6 cm (top) and 3 cm (bottom) wavelet cross correlation plots for Regions 1 through 5 with the Spitzer FIR data sets and Hα data. These graphs extend the cross correlation calculations down to 9 pc. The data points are calculated at scale factors of 31″, 40″, 50″, 63″, 80″, 125″, 200″, 316″, 501″, and 794″ which correspond to 9 pc, 12 pc, 15 pc, 19 pc, 24 pc, 37 pc, 60 pc, 95 pc, 150 pc, and 238 pc respectively. Region 5 scale factors are limited to a maximum of 501″, 150 pc, due to the small size of the region.

galaxy is ∼0.1 (Condon, 1992). The three regions that cover the SMC bar all have high thermal fractions of ∼0.54 to ∼0.95, see Figure 3.7. The existence of the bar, however, was questioned by Zaritsky et al. (2000). Their argument centred around the hydrodynamic interaction between gaseous components providing the physical mechanism for the SMC morphology. They further suggested that the SMC was actually spheroidal with highly irregular recent star formation. The overall thermal fraction for the SMC was measured in this thesis and found to have a value of ∼0.43 using 1.4 GHz and 4.8 GHz data. This is higher than previously published values of 0.15-0.40 for the SMC by Loiseau et al. (1987) using 1.4 GHz and 2.3 GHz data but is lower than the value of 0.71 measured by Israel et al. (2010) using 5 GHz and 10 GHz data. Each of the SMC regions measured here except Region 2, however, has a thermal fraction of >0.71.

The triggers for star formation events in massive spirals are believed to be density waves (Beck, 2000). In the SMC, there is not enough mass to support such a mechanism so that the trigger in the SMC is likely to be stochastic which leads to a discontinuous formation history with bursts of star formation lasting short periods of time (Klein and Graeve, 1986). With only two supernova remnants detected in Region 2, there is clearly no evidence of a galactic nucleus with its traditional high star formation rate. Figure 3.4 shows the distribution of q values in the SMC and there is no indication of the q value decreasing from a "nucleus" to the edge of the galaxy as Helou and Bicay (1993) expected in their "Leaky Bucket" FIR/RC model. Figure 3.4 does show that most of the SMC bar is consistent with q values within the expected limits of Yun et al. (2001). The depth of the SMC extends 5–10 kpc along the line of sight (Martin et al., 1989). The measured thermal fraction leads to the conclusion that there are not enough cosmic ray electrons to generate higher non-thermal emissions and/or that the magnetic field strength is too low in most regions. The published values of the magnetic field are $5 - 10$ μG along the bar (Ye and Turtle, 1991). Sreekumar and Fichtel (1991) concluded that the cosmic ray energy density level in the SMC is three to five times too low to be in equilibrium with the cosmic ray sources. This low cosmic ray density was described by Klein et al. (1984) as being a result of the internal pressure from the cosmic ray electrons. This causes rapid diffusion of the cosmic ray electrons out of the star–forming regions. This is consistent with the observation here that the bar has primarily thermal RC emission in Region 1 and Region 3 where there is high density H I and star formation activity. Region 2 may be populated primarily with cosmic ray electrons which have diffused out of the two star–forming regions in Region 1 and Region 3.

3.10 Far-Infrared / Radio Continuum Correlation Models

The FIR/RC correlation models examined here start with the assumption that the source of relativistic electrons and ionising photons is the supernova rate. UV photons from massive stars are absorbed by dust which re-emit the energy in the FIR. The relativistic electrons from the supernova remnants interact with magnetic fields or interact with ionised gas to produce RC radiation.

Voelk (1989) proposed a calorimeter theory which assumed that all of the ionising photons are absorbed by dust and that all of the energy of the cosmic ray electrons is dissipated by RC emission within the galaxy. This does not appear to be consistent with the SMC since Sreekumar and Fichtel (1991) determined that most of the cosmic ray electrons escape the SMC.

Applying the "Leaky Bucket" model of Helou and Bicay (1993) to the SMC would result in most of the ionising photons and cosmic ray electrons escaping the SMC. The observational prediction of the model is that q decreases radially from the centre of the galaxy to the edges of the galaxy. Regions 1 and 3 are the main star–forming regions in the SMC at the present time. Star formation in Region 2 must be suppressed since the H_2 content is the lowest of any region except for Region 5, see Table 3.2. Due to the irregular nature of the SMC, different position angles from these star–forming areas point towards very different environments as seen in Figure 3.4. This does not appear to match the gradual decrease in q modeled by Helou and Bicay, particularly since neither a nucleus nor a disk can be identified in the SMC.

Hoernes et al. (1998) published a model which decomposes both the RC emission and FIR emission into two parts. Hoernes selected M 31 as a test case with these four criteria:

1. M 31 is close to the Galaxy and well resolved in both radio and in the FIR.
2. The radio emission is dominated by the non-thermal component.
3. The FIR is dominated by cool dust emission.
4. M 31 has a low star formation rate of about an order of magnitude below the Galaxy.

Of these criteria, the SMC is also close enough to be well resolved in the RC and FIR. But the RC emissions from the SMC are not dominated by the non-thermal RC component with the overall SMC non-thermal emission at 57% and a minimum non-thermal emission of only 5% in Region 3, see Figure 3.7.

The supernova rate, R_s, for the SMC is about 1/350 years, $\mathrm{Rs_{SMC}} = 2.8 \cdot 10^{-3}\,\mathrm{SN\,yr^{-1}}$ (Filipovic et al., 1998a) whereas the Galaxy has a supernova rate of about 1/50 years, $\mathrm{Rs_{Galaxy}} =$

$20 \cdot 10^{-3}\,\mathrm{SN} \cdot \mathrm{yr}^{-1}$ (Diehl et al., 2006). Dividing these rates by the galaxies' respective volumes shows that the supernova rate per unit volume is higher in the SMC than in the Galaxy

$$\frac{\mathrm{Rs}_{\mathrm{SMC}}}{\mathrm{V}_{\mathrm{SMC}}} \approx \frac{2.8 \cdot 10^{-3}\mathrm{SN\,yr}^{-1}}{15\,\mathrm{kpc}^3} \approx 0.19 \frac{\mathrm{SN}}{\mathrm{kpc}^3\,\mathrm{kyr}}, \tag{3.12}$$

$$\frac{\mathrm{Rs}_{\mathrm{Galaxy}}}{\mathrm{V}_{\mathrm{Galaxy}}} \approx \frac{20 \cdot 10^{-3}\mathrm{SN\,yr}^{-1}}{1200\,\mathrm{kpc}^3} \approx 0.017 \frac{\mathrm{SN}}{\mathrm{kpc}^3\,\mathrm{kyr}}. \tag{3.13}$$

Whereas M 31 has a star formation rate of an order of magnitude below the Galaxy with those two galaxies having approximately the same volume, the SMC has a volumetric supernova rate an order of magnitude above the Galaxy or two orders of magnitude above M 31. The SMC does not appear to be described by the Hoernes decomposition model.

3.11 Radio Continuum Decomposition into Thermal and Non-Thermal Emissions

Data from the Parkes single dish telescope were used for the RC thermal fraction calculations (Filipovic et al., 1997) due to their superior overall flux-density accuracy. The Parkes data were converted to a data map with $5''$ resolution using the MIRIAD REGRID program to match the 6 cm data set. The thermal fraction of the emissions at 21 cm was calculated using equation 3.14 from Niklas et al. (1997). $S_{6\,\mathrm{cm}}$ and $S_{21\,\mathrm{cm}}$ are the measured flux densities of the regions

$$\frac{S_{6\,\mathrm{cm}}}{S_{21\,\mathrm{cm}}} = f_{th}\left(\frac{\nu_{6\,\mathrm{cm}}}{\nu_{21\,\mathrm{cm}}}\right)^{-\alpha_{th}} + f_{nth}\left(\frac{\nu_{6\,\mathrm{cm}}}{\nu_{21\,\mathrm{cm}}}\right)^{-\alpha_{nth}}. \tag{3.14}$$

In this equation, f_{th} is the thermal fraction and f_{nth} is the non-thermal fraction defined as $f_{nth} = (1 - f_{th})$. The thermal spectral index used is $\alpha_{th} = 0.1$. The non-thermal spectral index is assigned a value of $\alpha_{nth} = 1.09$ after Bot et al. (2010). The thermal fractions calculated are 0.81, 0.54, 0.95, 0.84, and 0.76 for Regions 1 through 5, respectively, and 0.43 for the full SMC, see Figure 3.7. The thermal fraction calculation assumes that the synchrotron emission spectrum can be described by a single power law and that the ISM is optically thin. These assumptions can introduce a bias into the calculated thermal fraction if the spectral index is not constant. The index is expected to steepen in locations that are increasingly remote from the area where the cosmic ray electrons are initially accelerated since the energy loss of cosmic ray electrons is $\sim E^2$. Conversely, in star-forming regions, the thermal fraction would likely be overestimated as the spectral index is flatter than in other regions. The entire SMC as well as each region, however, shows approximately four to nine times the expected thermal fraction of

0.1 (Condon, 1992) which suggests that cosmic ray electrons are not necessarily the source of the RC energy that makes the FIR/RC correlation so consistent.

3.12 Regional Decomposition of the Small Magellanic Cloud

The top panel of Figure 3.7 shows the relationship of the slope of the WLS of 21 cm RC versus 60 μm emissions from Table 3.6 plotted against the estimated thermal fractions. The regions show a strong tendency towards increasing WLS slope with increasing thermal fraction. The comments below all refer to Table 3.5.

Region 3 has the highest WLS slope, ∼1.14, the highest thermal fraction, ∼0.95, and the highest 21 cm flux density of the five regions. It has the best Pearson correlation of any region for RC 21 cm emission with all of the IR data sets. Region 3 has excellent Pearson correlation of the 13 cm RC with the higher temperature IR emissions of 60 μm and 70 μm and it also has excellent Pearson correlation of Hα with RC 21 cm, 13 cm, IR 60 μm, 70 μm, and 160 μm, covering cold dust to warm dust emitters. The locations of the high H I concentration corresponds to the IR emissions by way of the high Pearson correlation indicating that the H I and dust are co-located. It has excellent wavelet cross correlation of the 21 cm with 60 μm down to the resolution limit of 35 pc. Figure 3.6 shows the wavelet cross correlation of the higher resolution FIR and RC data (70 μm and 160 μm Spitzer data with 6 cm and 3 cm RC data), indicating that the correlation extends down to 15 pc.

The next two regions in terms of WLS slope and thermal fraction are Regions 1 and 4. They have WLS slope values and thermal fractions very similar to each other with WLS slope values, ~ 0.85, and thermal fractions, ~ 0.82. Region 1 contains N 19 and NGC 267 while Region 4 contains NGC 456. All three of these are H II regions with embedded stellar associations (Bica and Dutra, 2000). Region 1 has nine supernova remnants and high Pearson correlation values for H I with 60 μm, 100 μm, and 160 μm. The excellent wavelet cross correlation of the 21 cm RC with 60 μm extends down to 50 pc. Region 4 has excellent Pearson correlation of CO with IR emissions at 60 μm, 100 μm, and 160 μm with the correlation increasing as the temperature of the dust emission decreases. Interestingly, the 21 cm flux density for Region 1 is only slightly below Region 3 but Region 4 has the second lowest flux density at approximately half of the flux density of Region 1. The CO data in Region 4 contains NGC 456 but much of the remainder of the region is not covered in the CO data.

Region 5 has a WLS slope of 0.72 and a thermal fraction of 0.76. The region contains the open cluster, NGC 419, which has been examined by Rubele et al. (2010) who suggested that the star formation history of the cluster displayed continuous star formation over 1.2 to 1.9 Gyr.

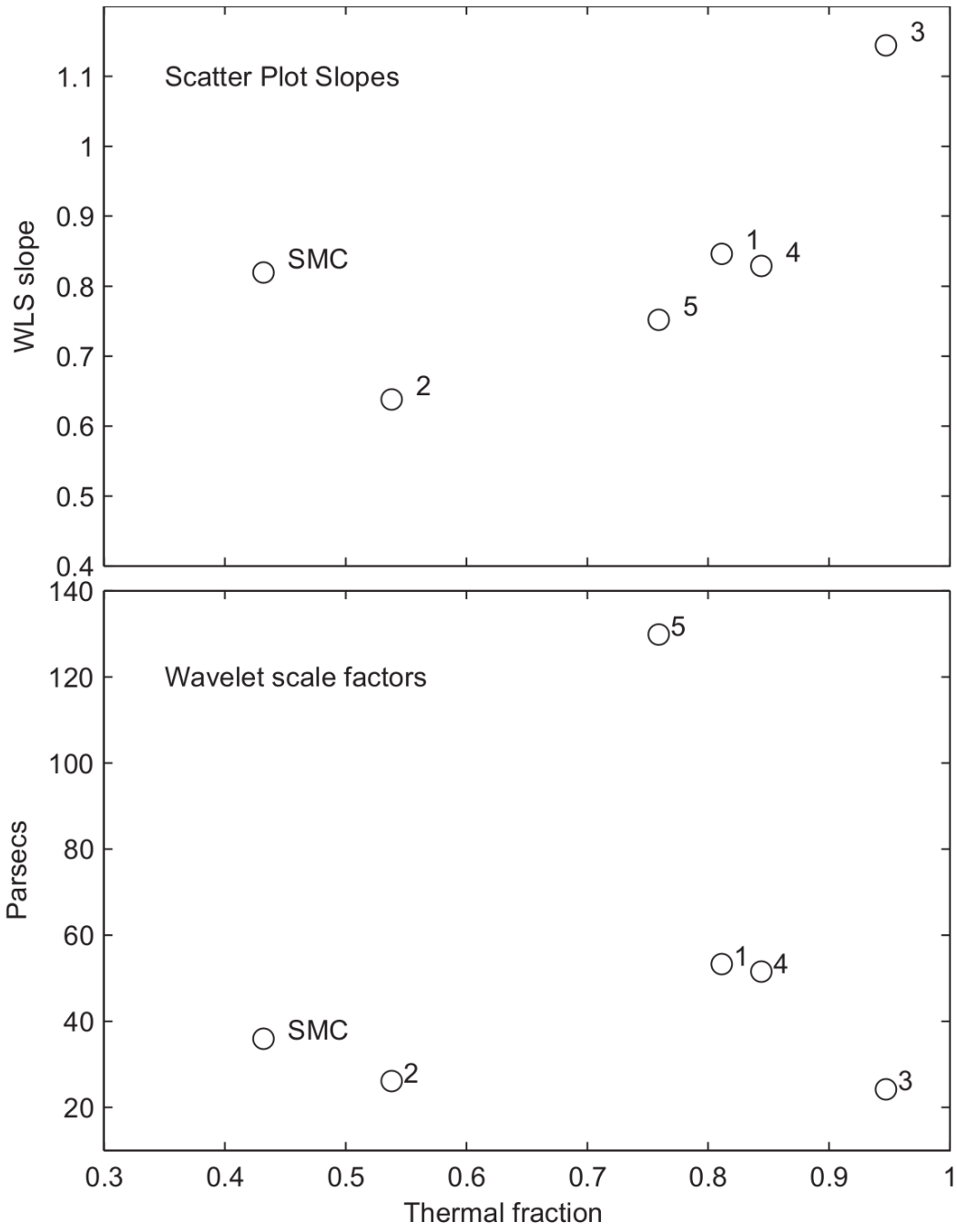

Figure 3.7: Small Magellanic Cloud Scatter Plot Slopes and Thermal Fractions. Top: WLS slope of 21 cm RC versus 60 μm data plotted against the thermal fraction. The thermal fractions plotted are 0.81, 0.54, 0.95, 0.84, and 0.76 for Regions 1 through 5. The SMC estimate is 0.43. Bottom: Minimum wavelet cross correlation scale factor for 21 cm RC with 60 μm that had excellent correlation. For Regions 1 through 5, those scale factors are 53.2 pc, 28.3 pc, 24.0 pc, 51.5 pc, and 129.8 pc. The Region 2 and 3 are from the higher resolution Spitzer 70 μm data. For the $3^\circ \times 3^\circ$ central portion of the SMC, excellent wavelet correlation is seen down to a scale factor of 36 pc.

This region exhibits no strong Pearson correlations in any data set pairs investigated here, see Table 3.5. There is excellent wavelet correlation down to 130 pc which is the largest measured by this study of the SMC. Oddly, the Spitzer 70 μm wavelet correlation with 6 cm RC gives a much smaller correlation threshold, 50 pc, but the Spitzer 70 μm is consistent with the 60 μm correlation threshold when correlated to 6 cm and 3 cm RC data.

Region 2 has the smallest WLS slope of the regions with a value of 0.62. It also displays the smallest thermal fraction of 0.54. It contains the open cluster, NGC 330, as well as two supernova remnants. It exhibits no strong Pearson correlations. The wavelet correlation threshold is at the resolution limit of 35 pc. The higher resolution wavelet correlation graphs, see Figure 3.6, show the correlation actually goes down to 19 pc.

The thermal fraction of the SMC is estimated here to be 0.43. This is higher than the typical value of ~ 0.1 given by Condon (1992) for spiral galaxies. It is very close to the value of 0.45 for the LMC measured by Hughes et al. (2006). The average value of the thermal fraction of the five regions is 0.78 over an area of 2.9 deg^2 whereas the SMC measurement is over 9 deg^2. This suggests that the regions, primarily in the bar, emit mostly thermal RC energy but that the larger area contains significant non-thermal emission from a large population of cosmic ray electrons that have diffused out of the bar. The star formation activity is in the bar where the H I has high density. The non-thermal emission is taking place where the H I has low density outside of the bar. The small size of the SMC suggests that the cosmic ray leakage into the nearby areas would be substantial. The total 21 cm flux density from the regions is 26.5 Jy and the total flux density in the $3^\circ \times 3^\circ$ data set used for these thermal fraction calculations is 36 Jy.

The q values that were calculated including only the thermal portion of the RC emission satisfy the range of q values for normal galaxies from Yun et al. (2001) for each of the five regions: 1) 2.90, 2) 2.85, 3) 2.72, 4) 2.83, 5) 2.85. Even the "greater" SMC, which has a q value of 3.02, is at the 98% q value consistent with Yun's correlation study.

3.13 Summary of Far-Infrared / Radio Continuum Correlations

This study demonstrated that the FIR/RC correlations for the SMC and for each of the five regions defined here were consistent with the regression calculated on 1750 galaxies by Yun et al. (2001). Both the "greater" SMC and the sub-regions of the bar and wing were examined and correlated as well.

Pearson correlation coefficients of RC 21 cm emissions with 60 μm and 100 μm emissions

had positive correlation only in Region 3 which was the region with the highest star formation rate. Not surprisingly, Region 3 also had positive Pearson correlation of Hα with RC and FIR emissions. Interestingly, Region 1 had twice as much H I and Hα as Region 3 and had the second highest star formation rate in the SMC. Its strongest Pearson correlations were in terms of H I with FIR emissions. Since the star formation rate in the SMC is predicted to be stochastic, Region 1 may have a suppressed supernova rate at this time.

Pixel by pixel scatter plots indicated two populations of correlations in terms of 21 cm RC and 60 μm emissions. The highest slope was from Region 3 which also had the largest difference between the WLS and OLS slope values, 1.14–0.98, 14.5%. Region 1 had the second largest slope and the second largest difference of slopes of 0.85–0.73, 13.7%. These differences suggested that regions with the highest star formation rate also have the strongest indication of two distinct emission populations. The other regions and the SMC had smaller slopes and less significant differences of 7.8% to 3.6%.

The wavelet cross correlation scale factors for the FIR with the RC for the five regions were all within 20 to 60 pc except for Region 5 which was $\sim$130 pc and which may have had few features at small scale factors. There was no clear trend displayed in this correlation. The region with the highest thermal fraction, Region 3, and the region with the lowest thermal fraction, Region 2, had the the smallest wavelet correlation scale factors. Hα had wavelet cross correlation scale factors with the 6 cm RC emission between 9 and 14 pc for all of the regions except for Region 5 which was 87 pc.

The five regions had q values of: 1) 2.80, 2) 2.58, 3) 2.70, 4) 2.75, 5) 2.73. The measured value of q for the SMC was 2.65 which included portions of the greater SMC that were not included in regions comprising the bar and wing. The SMC and all of the regions had q values above the correlation value of 2.34 but well within the values of 1.64 to 3.04 between which 98% of the q values for the galaxies measured by Yun et al. (2001) were found. This suggested that the RC emission in the SMC is slightly deficient compared to the FIR emission. It could be due to cosmic ray electrons escaping the bar or wing of the SMC without losing much of their energy. Since the non-thermal fraction of the RC emission was so small, the non-thermal RC emission was significantly under-luminous considering that the non-thermal fraction is expected to be dominant. This may be due to the small physical size of the SMC and a low magnetic field density.

The SMC displayed a thermal fraction that was much higher than is common for disk galaxies. Disk galaxies typically have a thermal fraction of 0.1 (Condon, 1992) while the SMC was measured here to have a value of 0.43. The regions had even higher measured values of the thermal fraction: 1) 0.81, 2) 0.54, 3) 0.95, 4) 0.84, and 5) 0.76. This suggested that galaxies

could have most of their RC radiation derived from thermal sources powered by the radiation field from high mass stars in H II regions rather than by supernova remnants. There appeared to be a weak correlation between the thermal fraction and the q values. The thermal fraction values above 0.5 corresponded to q values above 2.7 and thermal fraction values below ~ 0.5 had q values of below 2.7. The SMC and all five of the defined regions had FIR/RC correlations consistent with q values in Yun et al. (2001) when only thermal RC radiation was considered. Thermal radiation can thus be the major source of RC emission from a galaxy with little or no contribution by non-thermal emissions. This suggests that measurements of the RC emission of galaxies could lead to over-estimating the supernova rate by assuming the 0.1 ratio of thermal to non-thermal radiation.

Chapter 4

Radio Detection of Planetary Nebulae: The Small Magellanic Cloud

This section is based on my publication, Leverenz et al. (2016). I would like to acknowledge the contributions made by I. S. Bojičić in detecting planetary nebula mimics and discussions about analysis procedures, and by Miroslav D. Filipović, E. J. Crawford, J. D. Collier, K. Grieve, D. Drašković, and W. A. Reid for access to unpublished data, reviews of the text, and discussions about procedures and results.

The SIMBAD database (Wenger et al., 2000) contains entries for 105 SMC planetary nebulae. The coordinates for these entries were used as the source catalogue for planetary nebula detection. Several processed RC images have been published for the SMC and are available at various wavelengths. Also available are raw data from the ATOA. This archive facilitates access to the Australia Telescope National Facility unprocessed radio telescope data. The data available were obtained with the ATCA and other Australian facilities managed by CSIRO. A significant difficulty in working with the SIMBAD defined data set was determining which of the putative 105 planetary nebulae were really planetary nebulae and not mimics.

Previous examinations of planetary nebulae in the SMC have used data with resolutions of $\sim$ 16″ to 30″ and with sensitivities of $\sim$ 0.5 to 0.7 mJy beam^{-1}, see Table 4.1. The improvements that the Compact Array Broadband Backend (CABB) brings to the ATCA's sensitivity enable an examination of planetary nebulae with almost an order of magnitude improvement in resolution and sensitivity. This has led to the radio detection of ten SMC planetary nebulae previously undetected at radio frequencies with $\sigma \geq 3$ above the noise.

In the search for SMC planetary nebula radio counterparts, several archival ATCA data sets were used together with targeted observations of a sample of SMC planetary nebulae. Table 4.1 presents compiled information on RC imagery used in this study.

Wong et al. (2011a) described the creation of a new high resolution image at 20 cm for the SMC. This was done by combining three archived images from ATCA projects (C159, C1288, and C1197) plus the Parkes image from Filipovic et al. (1997). Those images included array configurations of 375-m, 6A, H214, and H75. The new image is identified as the 20 cm^a image in Table 4.1.

Wong et al. (2012a) studied compact H II regions in the SMC. Archive images were used at 3, 6, 13, 20, and 36 cm (Wong et al., 2011b; Filipovic et al., 2002; Turtle et al., 1998) plus images from the area near LHA 115-N 77 from Ye et al. (1995). Additional images from near LHA 115-N 19 were used including ATCA images from array configurations of 375-m, 1.5D, 6C, 6B, and 750A. The 20 cm image produced by their study was employed here and is identified as the 20 cm^b image.

Bojicic et al. (2010) created a new high resolution image from data originally acquired by Ye et al. (1995), ATCA project C281. He reprocessed the C281 data using a different cleaning technique and careful flagging of the noisy observational data which resulted in the new high resolution, high sensitivity image used here. This image is identified as the 20 cm^c image.

The 13 cm^a (ν=2.1 GHz) image used here is from ATCA project C2521 (PI: Jacco van Loon). These observations were obtained with the CABB in January 2012 with the ATCA configured in the 6A array. The 13 cm^b (ν=2.1 GHz) image used here is from the new, December 2014, CABB observations, project CX310, (PI: Andrew O'Brian) with the ATCA configured in the 6A array configuration.

Crawford et al. (2011b) applied a "peeling" technique employing joint deconvolution to 6 and 3 cm images from the SMC. Images from five ATCA projects (C1604, C1207, C882, C859, and C634) were combined. These are identified as the 3 cm^a and 6 cm^a images.

The new ATCA observations from project C2367 (PI: I. Bojičić) were targeted to examine the bright end of the radio planetary nebula luminosity function, to understand the quantitative differences in the multi-wavelength characteristics of Galactic and MC planetary nebulae, and to relate these to planetary nebula age and luminosity (Bojičić et al. in preparation). The SMC observations consisted of ten objects over a large range of [O III] magnitudes. These were studied to determine their general radio properties and to resolve some of the dubious detections and/or planetary nebula identifications. The SMC data were acquired on 28^{th} and 29^{th} of November 2010 using the "snapshot" mode with $\sim$ 1 hour integration for each pointing over the twelve hour observing session. These images created for this study employed MIRIAD

Table 4.1: RC Data for the Small Magellanic Cloud Planetary Nebula Study. Details of the characteristics for the sources of the radio frequency data investigated here.

Radio Band	Frequency (GHz)	Sensitivity (mJy beam^{-1})	Resolution ($''$)	Ref
3 cm^a	8.640	0.6	20	1
3 cm^b	9.000	0.027	1.27 × 0.97	2
6 cm^a	4.800	0.7	30	1
6 cm^b	5.500	0.022	2.06 × 1.59	2
6 cm^c	5.466	0.07	2.74 × 2.22	3
13 cm^a	2.100	0.015	1.7	4
13 cm^b	2.100	0.06	1.7	5
20 cm^a	1.420	0.5	16.33 × 9.45	6
20 cm^b	1.420	0.1	5.3 × 5	7
20 cm^c	1.370	0.05	7.05 × 6.58	8

References: 1: Crawford et al. (2011a), 2: Crawford et al. (2012) CABB, 3: ATCA C2768 (PI: Jordan Collier) CABB, 4: ATCA C2521 (PI: Jacco van Loon) CABB, 5: ATCA CX310 (PI: Andrew O'Brian) CABB, 6: Wong et al. (2011a), 7: Wong et al. (2012a), 8: Bojicic et al. (2010)

(Sault et al., 1995), KARMA (Gooch, 1996), and SCILAB (Scilab, 2013) software packages. These are identified as the 3 cm^b and 6 cm^b images.

The 6 cm^c image used in this study is from ATCA project C2768 (PI: Jordan Collier; observation from 6th February 2013, J. D. Collier et al. in preparation), obtained with the CABB. This image was acquired with the ATCA 6A antenna configuration.

4.1 Base Catalogue and Detection Method

In order to create the base catalogue for this study, the SIMBAD database was queried for objects with planetary nebula as the primary object type and within the approximate boundaries of the 20 cm^a image from Wong et al. (2011a) which extends approximately 3° from the centre of the SMC: RA (J2000)=$00^h52^m38^s$ and DEC (J2000)=–72°48′01″ (see Figure 4.1). Within the 3° boundary, 105 catalogued SMC planetary nebulae were found. Also searched was literature which could identify any other planetary nebulae or planetary nebula candidates not listed in SIMBAD. No other objects, however, which fell into this category were found. The radio images listed in Table 4.1 had variable coverage of the SMC. If planetary nebula coordinates were contained in an image, the location was then examined for radio emissions.

To confirm the radio detection, the Hα cutout images from *Magellanic Cloud Emission-line Survey* (MCELS: Smith et al., 2000) and MIR images from *Surveying the Agents of Galaxy Evolution in the Tidally Stripped, Low Metallicity Small Magellanic Cloud* (SAGE-SMC) Spitzer Legacy program (Gordon et al., 2011) were examined and were overlaid with contours from the corresponding radio map for each planetary nebula, see Figure 4.2. A positive detection was considered for objects with peak flux over 3 σ, where σ is the measured noise level. The

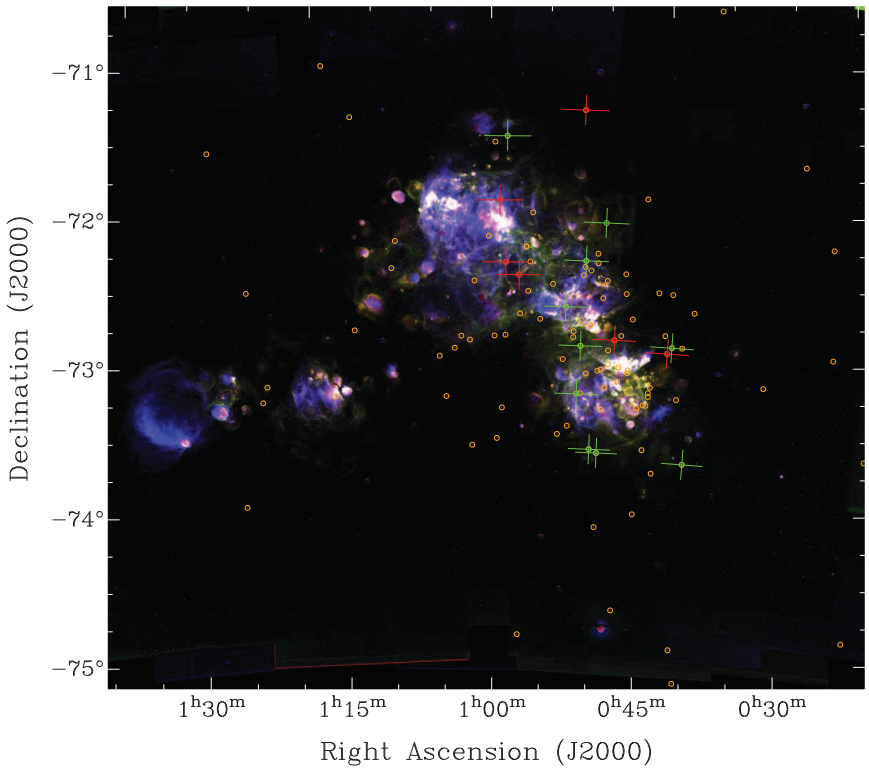

Figure 4.1: Locations of Small Magellanic Cloud Planetary Nebulae. Distribution of the 105 catalogued planetary nebulae in the SMC examined here (small orange circles). The background SMC image (MCELS: Smith et al., 2000) consists of Hα (red), [S II] (green), and [O III] (blue) images. The ten locations highlighted with the green crosses are at the coordinates of the new radio planetary nebulae. The six red crosses are locations of previously detected radio planetary nebulae.

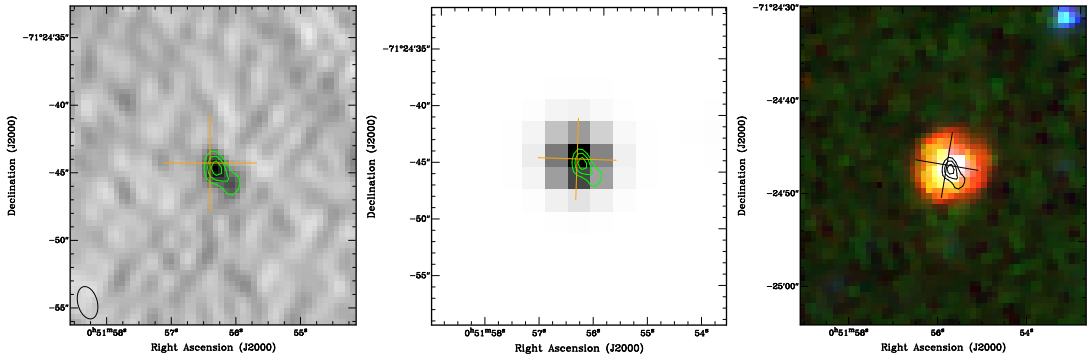

Figure 4.2: Example of Finding Charts for Small Magellanic Cloud Planetary Nebulae. These images are constructed as follows: Left: total intensity radio image, Middle: Hα cutout image from MCELS data, and Right: colour composite images from the IRAC (SAGE-SMC) data with RGB = 8.0, 5.8, and 4.5 μm. All images are overlaid with radio contours (green/black full lines) and catalogued SIMBAD position (orange/black cross). The resolving beam in the radio image is shown in the lower left corner. Field sizes are approximately the same. The object shown in this example is SMP S17.

positional uncertainty was adopted as the limit of the FWHM fitting to the data convolved with the ATCA maximum absolute positional uncertainty of 5″ (Stevens et al., 2014). It was also required that the distance from the catalogued position to the radio peak be within the positional uncertainties of the radio peak. The measured positional uncertainties for all of the objects presented in this thesis meet these requirements.

4.2 Manual Examination of Planetary Nebula Locations

For references to SMC planetary nebulae catalogued as "SMP SMC xx", "SMP Sxx" was used as a shorthand. For references to "Jacoby SMC xx", "J xx" was used. In general, SMP catalogue numbers were used where possible.

After careful examination of all available data, ten new RC detections were made of objects in the base catalogue: SMP S6, LIN 41, LIN 142, SMP S13, SMP S14, SMP S16, J 18, SMP S18, SMP S19, and SMP S22. Also, for six previously detected objects (Payne et al., 2008; Filipović et al., 2009; Bojicic et al., 2010): LIN 45, SMP S11, SMP S17, LIN 321, LIN 339, and SMP S24, measurements of flux density were recorded in at least one frequency, confirming the previous detection.

In the targeted observations of SMC planetary nebulae (images 3 cm^b and 6 cm^b) six out of the ten observed objects were detected. There were no radio counterparts found for: SMP S10, SMP S25, SMP S7, or SMP S9.

Except for one (LIN 45 at 6 cm, see Figure 4.3) all detected radio counterparts appeared to be unresolved in the radio maps. Therefore, in order to estimate integrated flux densities and positions, the radio image at each planetary nebula position was fitted with a Gaussian model

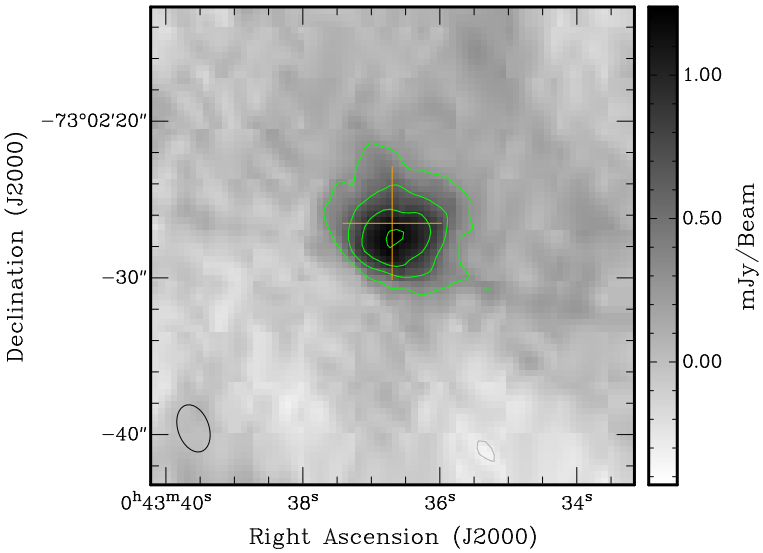

Figure 4.3: The RC Image at 6 cm of LIN 45. This image is overlaid with contours at 3, 6, 9, and $12 \times \sigma$ where σ=0.1 mJy/beam is the RMS noise measured in the vicinity of the detection. The resolving beam is shown in the lower left corner. The orange cross represents the catalogued position for this object. Note that this object is clearly resolved at 3 and $6 \times \sigma$ with an angular extension of about $7''$.

using the MIRIAD IMFIT task. The noise for each radio map was estimated by applying the MIRIAD SIGEST task to an empty part of the image with a minimum area of 10 arcmin^2.

The SIMBAD coordinates and the measured integrated radio flux densities for detected objects are presented in Table 4.3. Since none of the detected objects appeared to be resolved, the uncertainties in flux density estimates were determined from the RMS noise. Finding charts for newly detected SMC planetary nebulae (excluding the six objects previously detected) are shown in Figures 4.4 and 4.5. These images were constructed as total intensity radio maps with at least one of the detection frequencies overlaid with contours at multiples of the estimated RMS noise. Orange crosses represent previously catalogued positions found in SIMBAD.

As can be seen from the finding charts presented, in most cases the radio detections were of isolated sources well correlated with their optical counterparts. Only one object (J 18) showed a relatively large offset ($\sim 4''$) and appeared to be associated with a large and complex radio structure. In combination with the overall brightness in optical and infrared bands, J 18 was flagged as a doubtful detection.

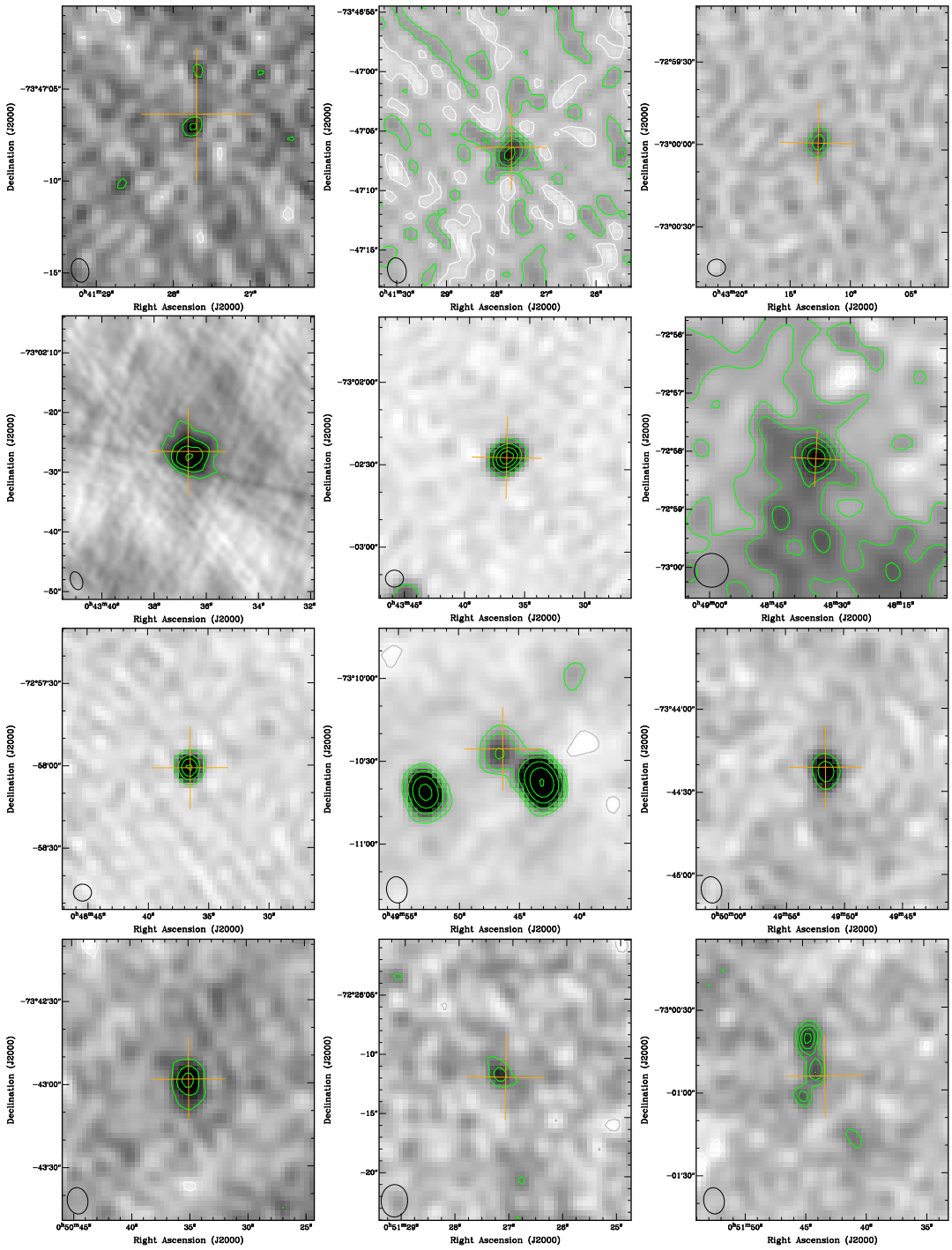

Figure 4.4: Radio Planetary Nebulae: SMP S6, S11, S13, S14, S16; LIN 41, 45, 142; J 18. New radio detections of SMC Planetary Nebulae. Images are constructed as total intensity radio maps. Contours are integral multiples of the measured RMS noise. First row: SMP S6 (at 3 cm), SMP S6 (at 6 cm), LIN 41 (at 20 cm); Second row: LIN 45 (at 6 cm), LIN 45 (at 20 cm), SMP S11 (at 6 cm); Third row: SMP S11 (at 20 cm), LIN 142 (at 13 cm), SMP S13 (at 13 cm); Fourth row: SMP S14 (at 13 cm), SMP S16 (at 6 cm), J 18 (at 13 cm). The beam size of each image is shown in the bottom left corner.

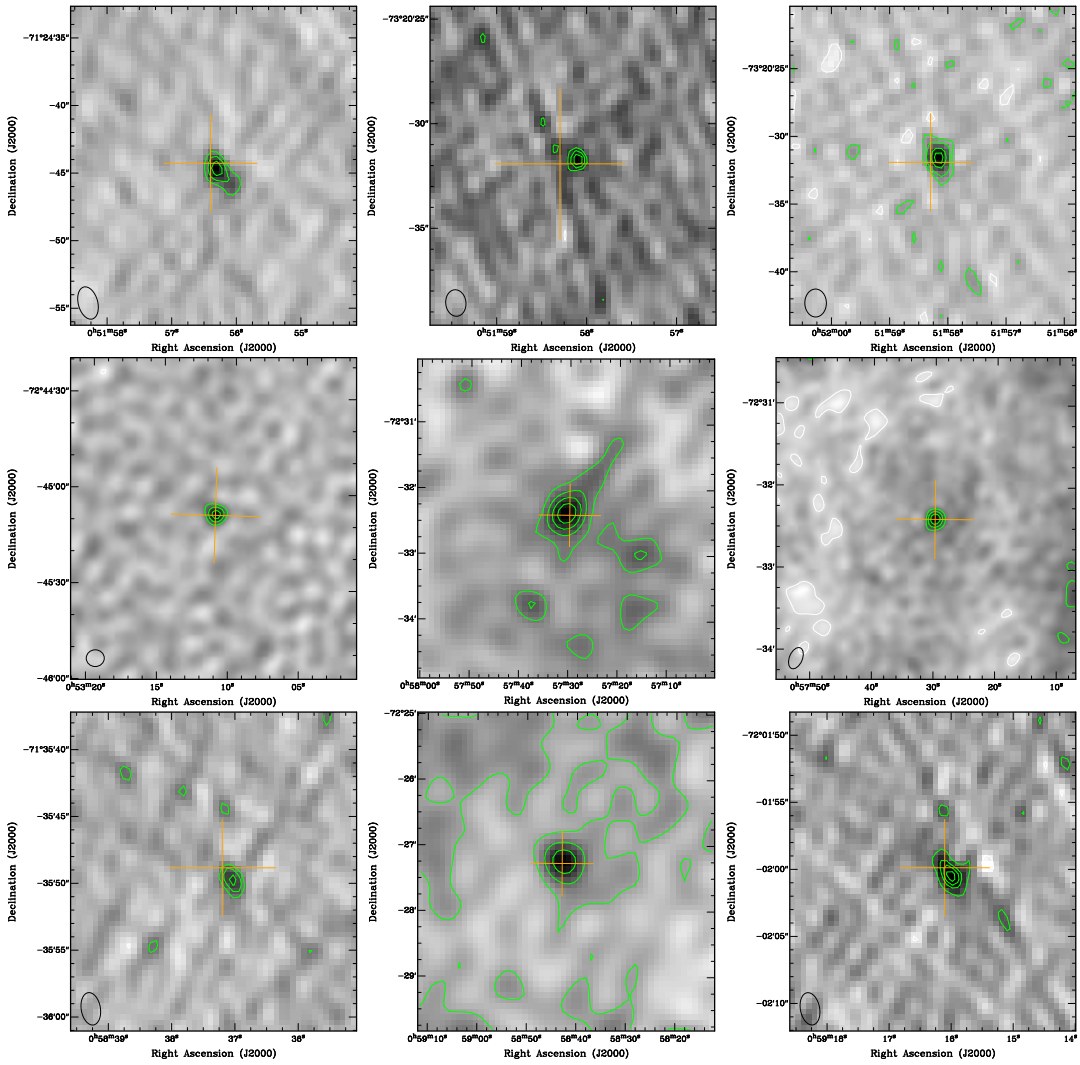

Figure 4.5: Radio Planetary Nebulae: SMP S17, S18, S19, S22, S24; LIN 321, 339. New radio detections of SMC Planetary Nebulae. Images are constructed as total intensity radio maps. Contours are integral multiples of the measured RMS noise. First row: SMP S17 (at 6 cm), SMP S18 (at 3 cm), SMP S18 (at 6 cm); Second row: SMP S19 (at 13 cm), LIN 321 (at 6 cm), LIN 321 (at 20 cm); Third row: SMP S22 (at 6 cm), LIN 339 (at 6 cm), SMP S24 (at 6 cm). The beam size of each image is shown in the bottom left corner.

Table 4.2: Small Magellanic Cloud RC Planetary Nebula Parameters. This includes measured and calculated parameters. The photometric angular diameters in Col. 2 are from the sources referenced in Col. 3. The spectral indices, α, are shown in Col. 4. The adopted flux densities at 6 cm are shown in Col. 5. The radii in pc are shown in Col. 7. Values for brightness temperatures, T_b; the electron densities, log n_e; and ionised masses, M_i; are calculated from the adopted 6 cm flux densities and presented in Cols. 6, 8, and 9, respectively. Note that SMP S11, and LIN 41, 45, 142, 321, and 339 are likely planetary nebula mimics and not true planetary nebulae.

PN	θ (")	ref$_\theta$	α	S_{6cm} (mJy)	T_b (K)	r (pc)	log n_e (cm^{-3})	M_i (M$_\odot$)
(1)	(2)	(3)	(4)	(5)	(6)	(7)	(8)	(9)
SMP S6	0.4	2	–0.3	1.3±0.1	620	0.057	4.2	0.12
LIN 41	...	...	...	0.5±0.2	...	...	...	...
LIN 45	9.0	1	–0.15	4.6±0.4	<10	2.7	2.4	22.30
SMP S11	0.7^w	2	0.16	2.7±0.4	420	0.105	3.2	1.54
LIN 142	14	1	...	:0.29	<10	4.2	1.5	10.56
SMP S13	0.4	2	...	0.6±0.2	290	0.057	4.0	0.08
SMP S14	0.9	2	...	0.35±0.15	40	0.126	3.4	0.17
SMP S16	0.4	3	...	0.5±0.2	240	0.054	3.9	0.06
J 18	0.4	2	...	:0.22	:110	0.051	:3.8	:0.05
SMP S17	0.5	2	–0.13	1.2±0.3	370	0.075	4.0	0.15
SMP S18	0.3	2	0.19	0.80±0.15	680	0.045	4.2	0.05
SMP S19	0.6	2	...	0.6±0.2	130	0.09	3.6	0.10
LIN 321	3.3	4	–0.18	3.5±1.5	30	0.5	3.0	4.37
SMP S22	0.8	2	...	0.4±0.2	50	0.12	3.5	0.20
LIN 339	2.7	4	0.26	4.3±1.1	50	0.4	3.2	3.80
SMP S24	0.4	2	0	0.7±0.2	350	0.06	4.0	0.08

References 1: Bica and Dutra (2000), 2: Stanghellini et al. (2003), 3: Meynadier and Heydari-Malayeri (2007), 4: Shaw et al. (2010).

Table 4.3: Coordinates and Flux Density Measurements of Detected Objects. The new flux density measurements are shown in the columns titled "new" and previous detections from Payne et al. (2008); Filipović et al. (2009); Bojicic et al. (2010) are listed in the columns titled "F09". A colon in front of a radio flux density represents an uncertain radio detection. A ">" indicates that the number is the lower limit for a flux density. Superscripts *a*, *b*, and *c* refer to specific data sources referenced in the "Radio Band" column of Table 4.1. Note that SMP S11, and LIN 41, 45, 142, 321, and 339 are likely planetary nebula mimics and not true planetary nebulae.

No.	PN	RA J2000	DEC J2000	$S_{3\,cm}$ (mJy)		$S_{6\,cm}$ (mJy)		$S_{13\,cm}$ (mJy)		$S_{20\,cm}$ (mJy)	
				new	F09	new	F09	new	F09	new	F09
	(1)	(2)	(3)	(4)	(5)	(6)	(7)	(8)	(9)	(10)	(11)
1	SMP S6	00:41:27.8	–73:47:06	1.1 ± 0.5^b	...	1.3 ± 0.1^b	...	...	...	$>0.2^b$	...
2	LIN 41	00:43:12.9	–72:59:58	...	...	...	...	...	...	0.6 ± 0.2^b	...
3	LIN 45	00:43:36.7	–73:02:27	...	3.1	4.8 ± 0.3^b	4.4	...	5.0	4.4 ± 0.5^b	5.1
4	SMP S11	00:48:36.5	–72:58:01	...	2.4	2.9 ± 0.5^a	2.6	...	2.0	2.0 ± 0.2^b	1.9
5	LIN 142	00:49:46.4	–73:10:26	...	...	...	...	$:0.32\pm0.12^a$	...	...	...
6	SMP S13	00:49:51.6	–73:44:23	...	...	...	...	0.6 ± 0.2^a	...	...	...
7	SMP S14	00:50:35.1	–73:42:58	...	...	...	...	0.4 ± 0.1^a	...	...	...
8	SMP S16	00:51:27.2	–72:26:11	...	...	0.5 ± 0.2^c	...	...	...	...	...
9	J 18	00:51:43.7	–73:00:53	...	...	...	...	$:0.24^a$	...	...	...
10	SMP S17	00:51:56.3	–71:24:45	...	...	0.9 ± 0.3^b	1.5	...	...	$:1.0^a$	1.4
11	SMP S18	00:51:58.3	–73:20:32	0.9 ± 0.5^b	...	0.8 ± 0.15^b	...	...	...	...	...
12	SMP S19	00:53:11.1	–72:45:08	...	...	...	...	0.6 ± 0.2^b	...	...	...
13	LIN 321	00:57:29.9	–72:32:24	$:1.5^a$	...	3.5 ± 1.5^a	3.0‡	...	...	4.4 ± 1.5^a	...
14	SMP S22	00:58:37.1	–71:35:50	...	...	0.4 ± 0.2^b	...	...	...	...	...
15	LIN 339	00:58:42.9	–72:27:17	$:1.3^a$	4.2	4.4 ± 0.9^a	4.1	...	3.5	$>1.1^c$	2.3
16	SMP S24	00:59:16.1	–72:02:00	$:0.5^{\ b}$	...	0.7 ± 0.2^b	...	...	...	...	0.7†

‡ Payne et al. (2008);† Bojicic et al. (2010)

4.3 Radio Continuum Properties of the Detected Planetary Nebulae

In order to make additional estimates of physical properties from the objects in the planetary nebula sample, the RC SED and brightness temperatures, T_b, were investigated for each object as good proxies for planetary nebula evolutionary status (Kwok, 1985; Zijlstra, 1990; Gruenwald and Aleman, 2007). The estimated spectral indices for objects having measurements of flux density on at least two frequencies are presented in Table 4.2. Two objects from the planetary nebula sample showed possible self–absorption effects at lower frequencies (SMP S11 and LIN 339). The SEDs of these two objects were further examined by fitting radio SED models from Siódmiak and Tylenda (2001) with assumed spherical symmetry and a constant density distribution. The results are shown in Figure 4.6 (left). Although there is an indication that the emission in the $\nu < 1.5$ GHz could be affected by self–absorption, the emission at 5 GHz appears to be optically thin. The conclusion is that none of the investigated objects show optical thickness effects in the high frequency region ($\nu > 2$ GHz) and the measurements are applicable to further calculation of physical parameters. Table 4.2 (Col. 5) presents the adopted flux densities at 5 GHz for all of the detected objects. If direct measurement at 5 GHz was not available, an estimate of the flux density from a neighboring band was made assuming optically–thin emission ($\alpha = -0.1$).

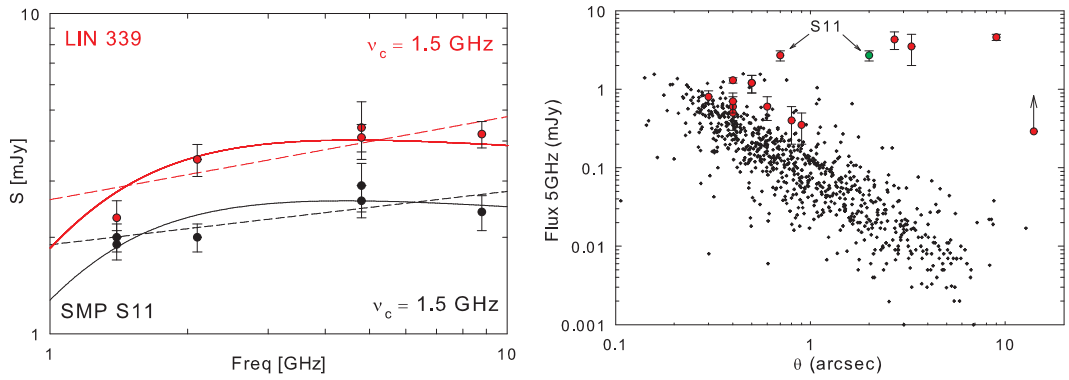

Figure 4.6: Radio Spectral Energy Distribution Model and Planetary Nebula Data Plot. Left: Radio SED model fits from Siódmiak and Tylenda (2001) of LIN 339 and SMP S11. Right: $S - \theta$ plot (flux density versus angular diameter) of Galactic planetary nebulae data from Bojičić 2010 (PhD Thesis) and Frew et al. (2016b) scaled to the SMC distance (black dots) and the new SMC measurements (red markers).

Finally, the derived parameters in Table 4.2 for all planetary nebulae were calculated using available, optically determined, angular diameters. This is defined as the diameter of a circle which encloses 85% of the total measured flux. The angular diameters were adopted from Bica and Dutra (2000), Stanghellini et al. (2003), Meynadier and Heydari-Malayeri (2007), and

Shaw et al. (2010). From Stanghellini et al. (2003), photometric radii were used except for SMP S11 where the measured angular dimension is at 10% of peak brightness. Radio brightness temperatures for this object at 1.4 GHz, calculated from $\theta = 2''$ and $\theta = 0.7''$, were 350 K and 3700 K, respectively. Since the former T_b was in better agreement with the indicated self–absorption effects at $\nu < 1.5$ GHz, the value adopted was $\theta = 0.7''$ as the better estimate of this object's angular size. Low brightness temperatures for all objects confirmed optically–thin emission in the observed frequency range.

The results obtained here were compared with a sample of known Galactic planetary nebulae. Recently, Frew et al. (2016b) published well determined distances for over 1200 Galactic planetary nebulae. These results were used to scale angular diameters and integrated flux densities for ∼750 Galactic planetary nebulae to the distance of the SMC. The radio flux densities were adopted from Bojičić 2010 (PhD Thesis) and references therein. In Figure 4.6 (right) the distribution of flux densities versus angular diameters ($S - \theta$) is shown for a sample of Galactic planetary nebulae (black crosshairs) and radio detected SMC planetary nebulae (red filled circles). J 18 was excluded because of its doubtful detection and LIN 41 because no published angular diameter was available. An additional data point for SMP S11, using the photometric diameter of $2.0''$, is over-plotted with a green filled circle. Here it can be seen clearly that nine planetary nebulae from this sample (SMP S6, SMP S13, SMP S14, SMP S16, SMP S17, SMP S18, SMP S19, SMP S22, and SMP S24) follow the $S-\theta$ distribution of Galactic planetary nebulae.

Five objects (LIN 45, SMP S11, LIN 142, LIN 321, and LIN 339) show a large separation from the Galactic planetary nebula $S - \theta$ distribution. The distinct, and possibly systematic, offset of these five objects in the region of high flux density in the Galactic planetary nebula $S - \theta$ distribution could be caused by uncertainties in angular sizes and flux densities. It could also point to different evolutionary pathways for planetary nebulae in low metallicity environments such as the MCs. More sensitive observations of a larger sample of SMC planetary nebulae are needed in order to examine this possibility. In the literature describing observations of these five objects, however, there are suggestions regarding the nature of these purported planetary nebulae, see Section 4.4. Based on those previous results and these new findings which include the MIR morphologies (see Figure 4.7), the conclusion is that none of these five objects are *bona fide* planetary nebulae.

4.4 Small Magellanic Cloud Planetary Nebula Mimics

LIN 41 was first identified as an emission star and an emission nebula in Henize (1956). Lindsay

(1961) proposed that it was a possible planetary nebula. This conclusion was disputed (Barlow, 1987; Monk et al., 1988; Oliveira et al., 2012) with the suggestion that LIN 41 was very likely an H II region powered by an early B-type main sequence star. In IRAC images, it appears as a resolved source with colours typical for H II regions and faint halo-like structures including a faint extension northeast from the bright core. Based on the relatively low radio brightness (the radio flux density is 0.6 mJy), it is likely that this object belongs to the population of ultra-compact H II regions.

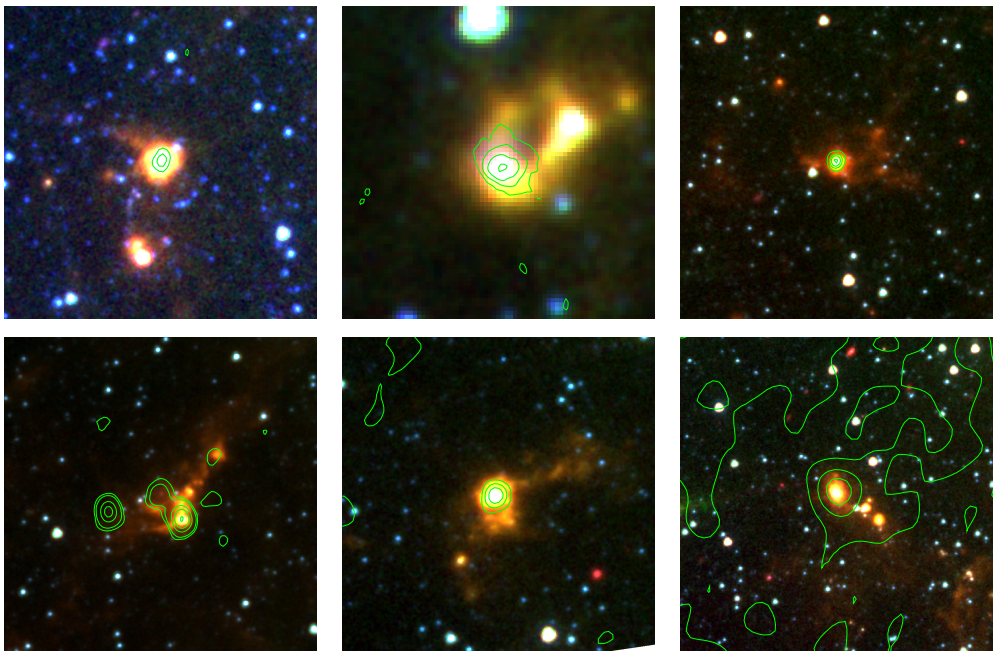

Figure 4.7: Colour Composite Images from IRAC: SMP S11; LIN 41, 45, 142, 321, 339. These composite images are from the IRAC (SAGE-SMC) data with RGB = 8.0, 5.8 and 4.5 μm overlaid with radio contours. Top row: LIN 41, LIN 45, and SMP S11. Bottom row: LIN 142, LIN 321, and LIN 339.

LIN 45 was classified as a planetary nebula candidate by Lindsay (1961) and as an H II region by Henize and Westerlund (1963). Spectral line ratios (Dufour and Killen, 1977) and overall morphology in Hα (McCall et al., 1990; Oey et al., 2013) suggested a compact H II region with bright core or ridge, surrounding a late O or early B type star. Jacoby and De Marco (2002), however, noted that in the low metallicity environment of the SMC, the [O III]/Hα ratio of a planetary nebula would be similar to that of an H II region and they re-considered LIN 45 as a planetary nebula. Finally, Hajduk et al. (2014) listed it as a planetary nebula mimic with photometric variability. The MIR morphology, the estimates of the ionised mass, and its angular size at 6 cm clearly suggest that this object is unlikely to be a planetary nebula.

SMP S11 was classified as a bipolar planetary nebula with a bright compact core and extended lobes (up to 2″ from the centre: Stanghellini et al., 2003). Bernard-Salas et al. (2009) reported an unusual "bump" in the MIR continuum of this source with a peak of around 30-

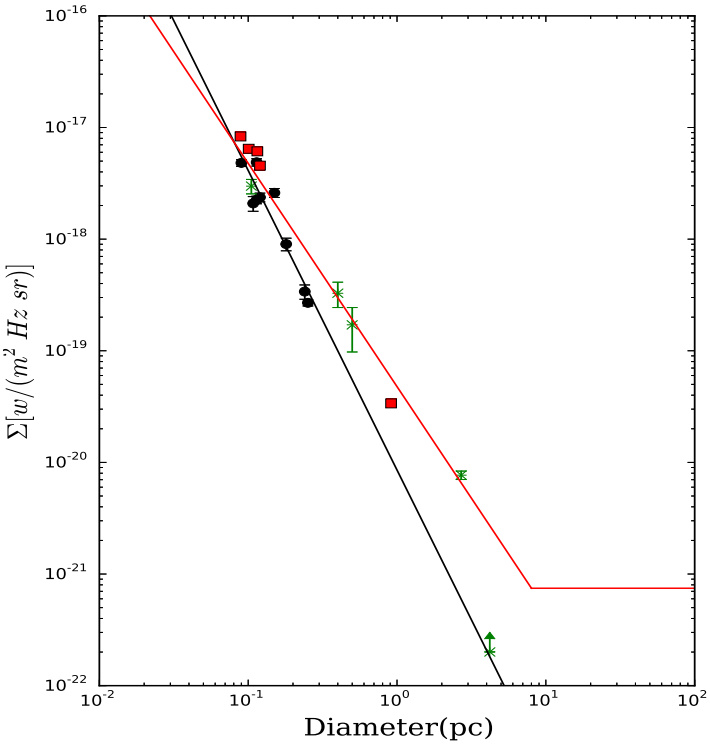

Figure 4.8: Small Magellanic Cloud Planetary Nebulae 6 cm Radio Surface Brightness. Measurements of Σ for the SMC planetary nebulae are shown here as round black markers with error bars. The square red markers are the five LMC planetary nebulae plotted by Vukotić et al. (2009) from data presented in Filipović et al. (2009). The red slanted line with the horizontal section at the bottom is the LMC 3σ sensitivity plot for the LMC observations made by Filipović et al. (2009). The black slanted line is a fitting of the SMC radio planetary nebula data to a power law function with an index of 2.7±0.4. The correlation coefficient is –0.94. The green x markers are the plots of the five planetary nebula mimics for which diameter data is available. This figure re-plots a portion of Figure 1 from Vukotić et al. (2009) to include the new SMC data.

35 μm indicating cold dust. It showed the largest offset from the expected sulfur abundance in a sample of 6 SMC planetary nebulae examined by Henry et al. (2012). Finally, Shaw et al. (2010) noted that its metallicity was typical of an SMC H II region and atypical of a bipolar planetary nebula suggesting that this object was not a planetary nebula. The separation from the Galactic planetary nebula population in the $S - \theta$ diagram and its unusually high ionised mass could be attributed to uncertainties in the angular size and radio flux density. The MIR image, however, shows complex structures around a bright core, much larger than for typical planetary nebulae. All of this suggests that this object is a planetary nebula mimic.

LIN 142 was originally classified as a planetary nebula by Henize (1956). It was later classified by de Oliveira et al. (2000) as a pair or multiple in a star cluster. Bica et al. (2008) classified it as a nebula, likely with an embedded cluster, and as one of a pair of stars. The sep-

aration from the Galactic planetary nebula population in the $S-\theta$ diagram, its unusually high ionised mass, and large angular size suggest that this object is part of an H II region (DEM S50) and not a planetary nebula.

LIN 321 and *LIN 339* were listed as planetary nebulae in Henize (1956). LIN 321, however, was characterized as a low excitation blob by Meynadier and Heydari-Malayeri (2007). LIN 339 was classified as a compact H II region by Charmandaris et al. (2008). The separation from the Galactic planetary nebula population in the $S-\theta$ diagram, their unusually high ionised masses, their large angular sizes, and their morphologies in the MIR composite images suggest that both of these objects are very likely compact H II regions.

4.5 Small Magellanic Cloud Surface Brightness-Diameter Model

Surface brightness measurements are independent of distances and have been applied to supernovae for over fifty years (Shklovskii, 1960). Amnuel et al. (1984) applied this measure to planetary nebulae and derived a basic (Σ–D) relationship for planetary nebulae: $\Sigma \sim D^{-2}$. Urosevic et al. (2007) used forty-four Galactic planetary nebula calibrators with distances of less than 0.7 kpc to determine the multiplier, A, and the exponent, β, in the equation $\Sigma = A \times D^{-\beta}$ ($\beta = 2.07 \pm 0.19$) with a strong correlation coefficient r of 0.86.

Urošević et al. (2009) applied the "Interacting Stellar Winds" model of Kwok (1994) to derive a theoretical (Σ–D) model for optically-thin planetary nebulae. They noted that the majority of planetary nebulae will evolve from optically thick to optically thin, with the time it takes for this to occur dependent on many factors. In their model the fast wind from the central star sweeps up the slow wind from the previous evolutionary stage AGB star. This "piling up" creates the nebular shell. The optically–thin planetary nebula model predicts a decreasing radio surface brightness from the enclosed volume as the nebular shell diameter increases. Early phases of evolution of the planetary nebula are shown to have a $\beta = 1$. Later in the evolution of planetary nebulae, the surface brightness, Σ, declines as β tends towards a value of 3. Their empirical fits to various Galactic data sets from the literature with 5 GHz RC surface brightness and optically measured diameters resulted in values of β from approximately 1.4 to 2.6. The data set they employed with the best correlation coefficient was Galactic data from planetary nebulae at a distance of < 1 kpc. With this data they found $\beta = 2.61 \pm 0.21$ with $r = -0.97$. With this maximum distance there should be no Malmquist bias in their results. They suggested that the (Σ–D) relation they derived should be used to indicate only general trends in surface brightness. The new SMC estimate presented in this thesis of $\beta = 2.7 \pm 0.4$

with $r = -0.94$ is in excellent agreement with their Galactic results. Therefore, the new SMC sample of planetary nebulae appear to be in a similar state of evolution.

The definition adopted for the radio surface brightness is that of Vukotić et al. (2009),

$$\Sigma \left[\mathrm{W\,m^{-2}\,Hz^{-1}\,sr^{-1}}\right] = 1.505 \cdot 10^{-19}\, S\ [\mathrm{Jy}]/\theta^2\ [']. \tag{4.1}$$

This form was used in order to make direct comparisons between the SMC data presented here and their LMC data.

The radio detected SMC planetary nebulae are plotted in Figure 4.8 which is modeled after the (Σ–D) plot from Vukotić et al. (2009). The black round points are the SMC planetary nebula measurements reported here which were used to calculate the power law index. The surface brightness sensitivity of the new SMC measurements allow plotting of these measurements of the planetary nebulae at lower Σ values than the LMC planetary nebulae plotted by Vukotić et al. (2009). They found β (for their fitting to the 6 cm data) to be 0.9±0.5 with a correlation coefficient of 0.64. They suggested, however, that the sensitivity selection effect and small number of data points above the sensitivity line likely resulted in a value that "should not be taken seriously." The SMC planetary nebula data would also be expected to be under the influence of the sensitivity selection effect since only 17% of the SMC planetary nebulae examined here were detectable at the sensitivity of these observations and virtually all planetary nebulae are expected to be radio emitters until they disperse (Gurzadyan, 1997). Vukotić et al. (2009) indicated that the flattening of β due to a cutoff at lower flux densities is expected. From simulations by Vukotić et al. (2009), however, for values of β below 2 there should be little influence on the measured slope. For larger values of slope, the sensitivity effect should force the measured slope to be only slightly more than 2. The measured value shown here of β is expected to be subject to the flattening effect. As measured here, $\beta = 2.7 \pm 0.4$, which is consistent with the Galactic data analysed by Urošević et al. (2009).

The data set displayed here indicates the difficulty of separating true planetary nebulae from mimics. Figure 4.8 includes the SMC planetary nebulae and five objects which have been excluded from consideration. All five of these objects have been classified previously in the literature as planetary nebulae. The critical examination presented here indicates that these five objects are actually planetary nebula mimics. The exclusion of the identified mimics results in an excellent agreement with the Galactic measurements that Urošević et al. (2009) reported.

4.6 Small Magellanic Cloud Planetary Nebulae Summary

The positions of the 105 catalogued SMC planetary nebulae that are listed in the SIMBAD database were examined. These locations were analyzed using all available radio maps at 3, 6, 13, and 20 cm. From these locations, sixteen sources were found to have detectable radio emissions in at least one of these radio bands with a flux density which was $\geq 3\sigma$ above the noise. Ten of these were new radio detections reported here for the first time. Six were previously detected radio planetary nebulae. From this list, two of the new detections and four remeasured objects were found to be likely mimics rather than planetary nebulae.

The improvements that the CABB brought to the ATCA observations of the SMC enabled a more than doubling of the population of known radio planetary nebulae in the SMC. The low noise and high resolution characteristics of ATCA were well suited for this research. These improvements also enabled measurements for the (Σ–D) relation of the planetary nebulae in the SMC. This (Σ–D) relation result was consistent with previous results in the LMC and the Galaxy.

Chapter 5

Radio Detection of Planetary Nebulae: The Large Magellanic Cloud

This section is based on my publication, Leverenz et al. (2017). I would like to acknowledge the contributions made by B. Vukotić and D. Urošević for applying their new (Σ–D) PDF algorithms to the data presented and by Miroslav D. Filipović and Kevin Grieve for access to unpublished data, reviews of the text, and discussions regarding the procedures and results.

The definitive list of LMC planetary nebulae from Reid and Parker (2006a,b, 2010), collectively referred to here as the "RP" catalogue, was used to establish the search coordinates for the LMC planetary nebulae. The RP catalogue of the LMC was constructed from a portion of the AAO/UKST Hα survey of the Southern Galactic Plane (Parker et al., 2005).

The ATOA was the source of all of the RC data used for this study. All projects were searched which included data at 3, 6, 13, or 20 cm. Only data that were obtained using a 6 km configuration of the ATCA antenna array were accepted in order to select projects with the best possible resolution. Typically, these projects contained raw data for multiple images with different central coordinates. A project was selected for processing if an LMC planetary nebula was located within a 10 arcmin radius of any central coordinate contained therein. Most of these ATCA projects were intended to image LMC objects that were not planetary nebulae.

Filipović et al. (2009) reported the first confirmed extragalactic RC detection of fifteen planetary nebulae in the MCs of which eleven are located in the LMC. Prior to that study, a tentative RC detection of only three extragalactic planetary nebulae had been reported in the literature (Zijlstra et al., 1994; Dudziak et al., 2000). Bojicic et al. (2010) and Leverenz et al.

(2016) reported detection results and RC data measurements for a total of sixteen planetary nebula positions in the SMC. The RC detection of LMC planetary nebulae was re-examined and extended in Leverenz et al. (2017) with a total of thirty-one RC detections. These consisted of twenty-one new RC detections reported for the first time as well as re-measurements of seven previously reported RC detections (Filipović et al., 2009). Three planetary nebulae that had been detected in surveys and reported in Filipović et al. (2009) were also included in that total.

5.1 Planetary Nebula Detection in the Australia Telescope Online Archive

A manual search was conducted to identify projects that contained data that could potentially result in a planetary nebula RC detection. Each central coordinate and each frequency from all of the identified projects found in this way were manually processed to create images from the data. Then the images were examined at the coordinates of known (optical) planetary nebulae for detectable RC emission.

One project, ATCA C2367, which operated in 2010, was executed specifically to study RC planetary nebulae detection in the MCs. This project yielded most (26 out of 29) of the 3 cm and 6 cm detections in this study.

Seventeen ATCA projects were found which met the selection criteria as explained above. All of the raw data at the frequencies of interest from these projects were examined. Each project contained data from two to four frequencies. All of the data were manually processed to produce images at each frequency. Each image was examined for RC detections at the planetary nebula coordinates. Due to differences in sensitivity (RMS noise level) and primary beam coverage from one image/frequency to another, planetary nebula RC detection at one frequency did not mean that detection at another frequency was to be expected. Only nine projects had data that led to a planetary nebula RC detection, see Table 5.1. Four of those projects had planetary nebula RC detections at only one frequency.

A total of sixty-one images, which were produced from the downloaded data, did not contain any planetary nebula RC detections. Table 5.2 lists the projects which contained the raw data that yielded those images. The pointing centres of each of those images are listed. Since reliable measurements can be made at positions up to approximately two-thirds of the radius of the image, only RP catalogue references of planetary nebulae within this radius were accepted (see Section 5.2).

The ATCA data were processed using MIRIAD software (Sault et al., 2011). The MIRIAD SIGEST task was used to determine the 1σ RMS noise level in a region essentially devoid of any strong

point sources near each planetary nebula examined. For unresolved sources, the MIRIAD IMFIT task was used to determine the integrated flux density from the planetary nebula using a Gaussian fitting. For resolved sources, the pixels within a $1\,\sigma$ Jy beam^{-1} contour encompassing the planetary nebula were used to estimate the planetary nebula integrated flux density. A positive RC detection with either method was defined as a flux density estimate $\geq 3\sigma$ above the RMS noise.

5.2 Raw Data Download and Processing into Radio Continuum Images

The planetary nebula catalogue used as the base list for this study is from Reid and Parker (2006a,b, 2010), collectively referred to here as RP. The RP catalogue of the LMC was constructed from a portion of the AAO/UKST Hα survey of the Southern Galactic Plane (Parker et al., 2005). The catalogue covers ~ 25 deg^2 centred on the LMC and contains 629 planetary nebulae found using deep Hα and "Short Red" images. Each planetary nebula was then verified using spectroscopic measurements and classified as "Known", "True", "Likely", or "Possible". This catalogue was further refined with an extensive re-examination of the "Likely" and "Possible" categories using a multiwavelength analysis of the catalogue in Reid (2014). The subset of the RP catalogue used in the current study contains coordinates only from planetary nebulae classified as "Known" or "True".

The RP catalogue numbers are written as "RPxxxx" to stand for "[RP2006] xxxx". LMC catalogue references from Sanduleak et al. (1978), which have the form "SMP LMC xx", are referred to as "SMP Lxx". For references to SMC planetary nebulae catalogued as "SMP SMC xx", "SMP Sxx" is used as a shorthand. In general, SMP catalogue numbers are used where possible but, for planetary nebulae that do not appear in the SMP catalogue, the RP catalogue numbers are used.

Planetary nebulae that are resolved at any observational wavelength are frequently found to have an irregular shape (Kwok, 2010). This is easily seen in high resolution images of planetary nebulae at optical wavelengths and in some of the resolved RC images, for example, see Figures 5.1–5.5 (SMP L13, SMP L21, SMP L37, SMP L38, and SMP L58). As the dimensions of the synthesised beam increase, approaching the overall size of the planetary nebula, the detected shape becomes more indistinct, approaching a Gaussian intensity distribution defined only by the source intensity and the synthesised beam parameters. For unresolved planetary nebulae, the coordinates can be approximated as the position of the peak of a Gaussian fitting to the intensity. For resolved images, however, there is no consistent point of the typically asymmetric

Table 5.1: RC Data for the Large Magellanic Cloud Planetary Nebula Study. RC data used in this study are identified with the ATCA project numbers. Data using the CABB configuration were acquired using the 2 GHz receiver bandwidth capability of the ATCA. Project C2908 is a MOSAIC survey of the LMC Supershell 4.

ATCA Project No.	ν (GHz)	λ (cm)	Beam ($'' \times ''$)	RMS (mJy/beam)
C256	1.376	20	2.4×7.0	0.1
C256	2.378	13	7.7×4.2	0.1
C308	5.824	6	2.5×1.1	0.1
C308	8.640	3	1.6×0.7	0.1
C354	1.376	20	8.5×7.9	0.15
C395	1.376	20	6.6×6.3	0.13
C395	2.378	13	3.8×3.5	0.14
C479	1.344	20	7.4×6.9	0.12
C479	2.378	13	4.1×3.9	0.12
C520	1.384	20	10.0×6.0	0.15
C1973 CABB	5.500	6	2.4×2.0	0.03
C2367 CABB	5.500	6	2.0×1.6	0.01
C2367 CABB	9.000	3	1.2×1.0	0.1
C2908 CABB	2.162	13	5.3×3.9	0.3

image to unambiguously define as its coordinates since only a portion of the planetary nebula may be detected. The RP catalogue positions are in the visible portion of the spectrum which may image different parts of the planetary nebula than the RC data. The position of the central star is likely the best definition if it can be detected but RC imaging cannot detect the central star.

The synthesised telescope beam for each RC detection is shown in the images of the planetary nebulae, see Figures 5.1–5.5. The synthesised beam is a two-dimensional Gaussian distribution dependent on the wavelength, the ATCA telescope array configuration, and the coordinates of the image. The optical diameters of the planetary nebulae that were studied here range over an order of magnitude: from 0.24 arcsec to 2.53 arcsec. The synthesised radio beam sizes are typically not symmetric and vary widely as seen in Table 5.1 (Col. 4) from 0.7 arcsec to 10.0 arcsec. As well as meeting the requirement that the intensity measured is $\geq 3\sigma$ above the RMS noise, one of two additional conditions for a planetary nebula RC detection was required: 1) for unresolved sources, the peak of the RC intensity must be <5 arcsec from the RP planetary nebula coordinates; or 2) the apparent centre of a resolved source must be <5 arcsec from the RP planetary nebula coordinates. Five arcsec was chosen since the maximum absolute positional uncertainty of the ATCA is 5 arcsec (Stevens et al., 2014).

5.3 Detection Results

After careful examination of all of the available data, twenty-one new RC detections of planetary nebulae in the base catalogue were identified: SMP L13, SMP L15, SMP L21, SMP L23,

Table 5.2: RC Data Sets Downloaded that Did Not Yield Planetary Nebula Detections. ATCA projects that contained planetary nebula coordinates but did not yield planetary nebula RC detections. The listed coordinates represent the centre of the pointing.

ATCA Project	λ (cm)	RA (J2000) (h m s)	DEC (J2000) (° ′ ″)	RP Catalogued PNe* not detected
C015	6	05:35:27.90	–69:16:21.59	365 395
	3	–	–	395
C148	6	05:08:59.00	–68:43:34.09	1395 1396 1399 1426 1443 1444 1446 1456 1550
	3	–	–	1444 1550
C256	20	05:18:51.40	–69:37:31.70	1223 1225 1228 1229 1230 1231 1232 1234 1235 1338 1341 1352 1353 1354 1357 1358 1371 2194
	13	–	–	1225 1228 1229 1230 1338 1341
C282	20	04:53:29.70	–67:23:20.20	1078 1081 1092 1095 1554 1555 1556 1558 1580 1584 1595
	13	–	–	1092 1095
	20	05:22:41.10	–66:40:56.30	1801 1895
	13	–	–	1895
C354	20	05:09:53.00	–68:53:15.00	1218 1219 1310 1313 1314 1315 1317 1323 1324 1395 1396 1399 1400 1402 1408 1416 1418 1426 1443 1444 1446 1456 1550 1823 1835
	13	–	–	1218 1323 1324 1395 1399 1418 1426 1443 1444 1446 1550
	20	05:35:24.00	–67:34:50.00	366 1053
	13	–	–	366 1053
C394	20	05:05:54.00	–68:01:46.00	1397 1409 1532 1798 1802 1878
	13	–	–	1802 1878
C395	20	04:59:42.00	–70:09:10.00	1602 1605 1608 1609 1660 1679 1697 1771
C479	20	05:05:30.00	–67:52:00.00	1397 1532 1802 1878 1886
	13	–	–	1878
C520	20	05:13:50.80	–69:51:47.00	1225 1237 1267 1288
C634	20	05:13:50.80	–69:51:47.00	1636
	13	–	–	1636
C663	6	05:31:55.82	–71:00:18.86	1012
C1074	20	04:53:40.00	–68:29:40.00	1800
	13	–	–	1800
C2044	6	05:23:33.02	–69:37:03.73	757 875 889
	3	–	–	757 875 889
	6	05:27:41.04	–67:27:15.60	1047
	6	05:39:07.52	–69:30:25.44	243
	6	05:39:57.98	–71:10:18.05	44 46
	3	–	–	44 46
	6	05:19:11.78	–69:12:23.84	1227
	3	–	–	1227
	6	05:22:08.68	–67:58:12.87	979 980 1534
	3	–	–	980 979
C2367	6	05:03:41.30	–70:14:13.60	1605
	3	–	–	1605

RP Catalogued PNe* This catalogue is a general inventory of LMC planetary nebulae known at time of publication and also contains planetary nebulae found by Henize (1956), Lindsay (1961), Lindsay and Mullan (1963), Lindsay (1963), Westerlund and Smith (1964), Sanduleak et al. (1978), Jacoby (1980), Morgan and Good (1992), and Morgan (1994).

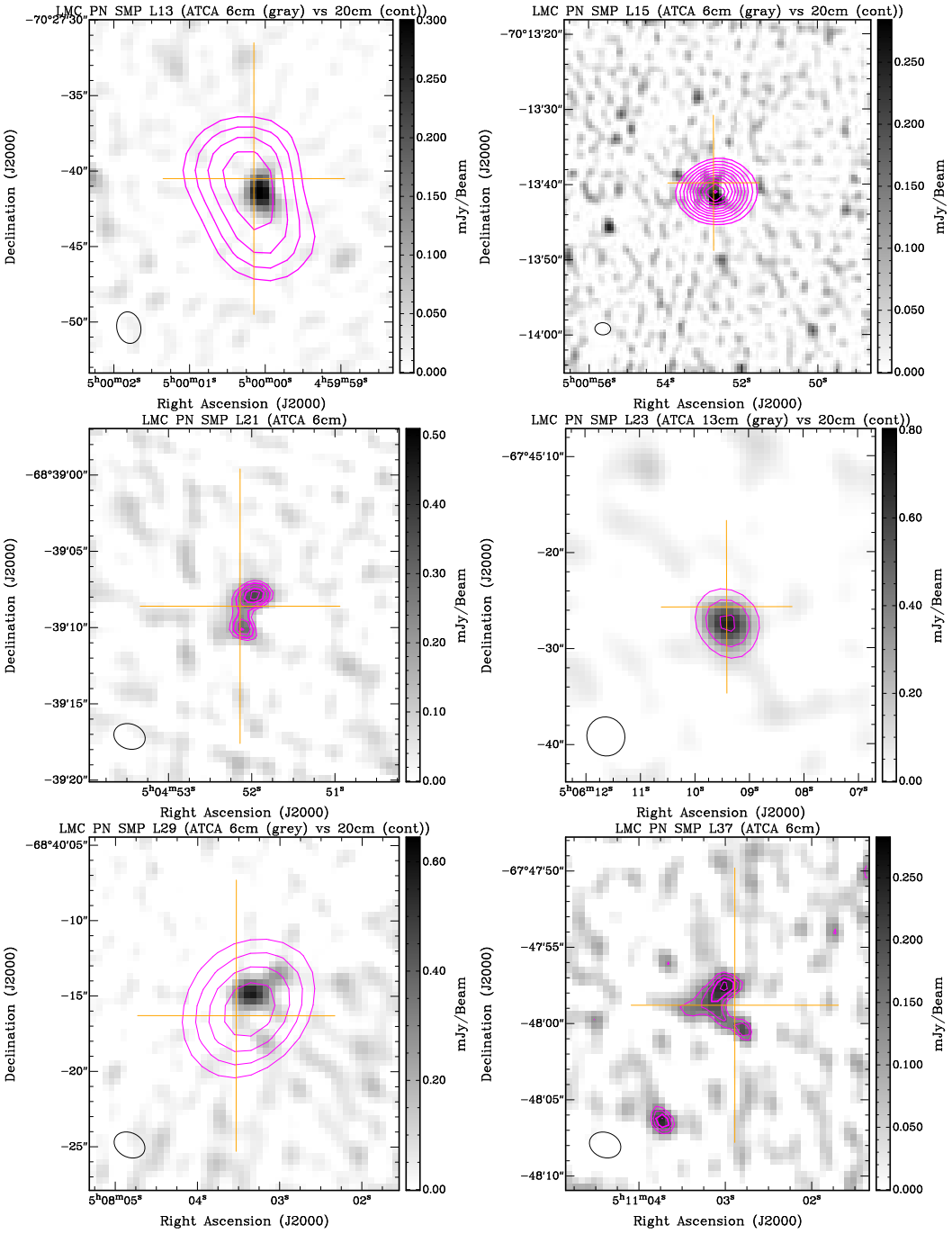

Figure 5.1: Radio Planetary Nebulae: SMP L13, L15, L21, L23, L29, L37. New and previous RC detections of LMC planetary nebulae. Images are constructed as total intensity RC maps. Contours are integral multiples of the measured RMS noise starting at 3σ with spacings of 1σ. Top row: SMP L13 at 6 cm (grey scale) with 20 cm contours and SMP L15 at 6 cm (grey scale) with 20 cm contours; Second row: SMP L21 at 6 cm and SMP L23 at 13 cm (grey scale) with 20 cm contours; Third row: SMP L29 at 6 cm (grey scale) with 20 cm contours and SMP L37 at 6 cm. The beam size of each image is shown in the bottom left corner. The orange crosses represent the planetary nebula positions from the RP catalogue.

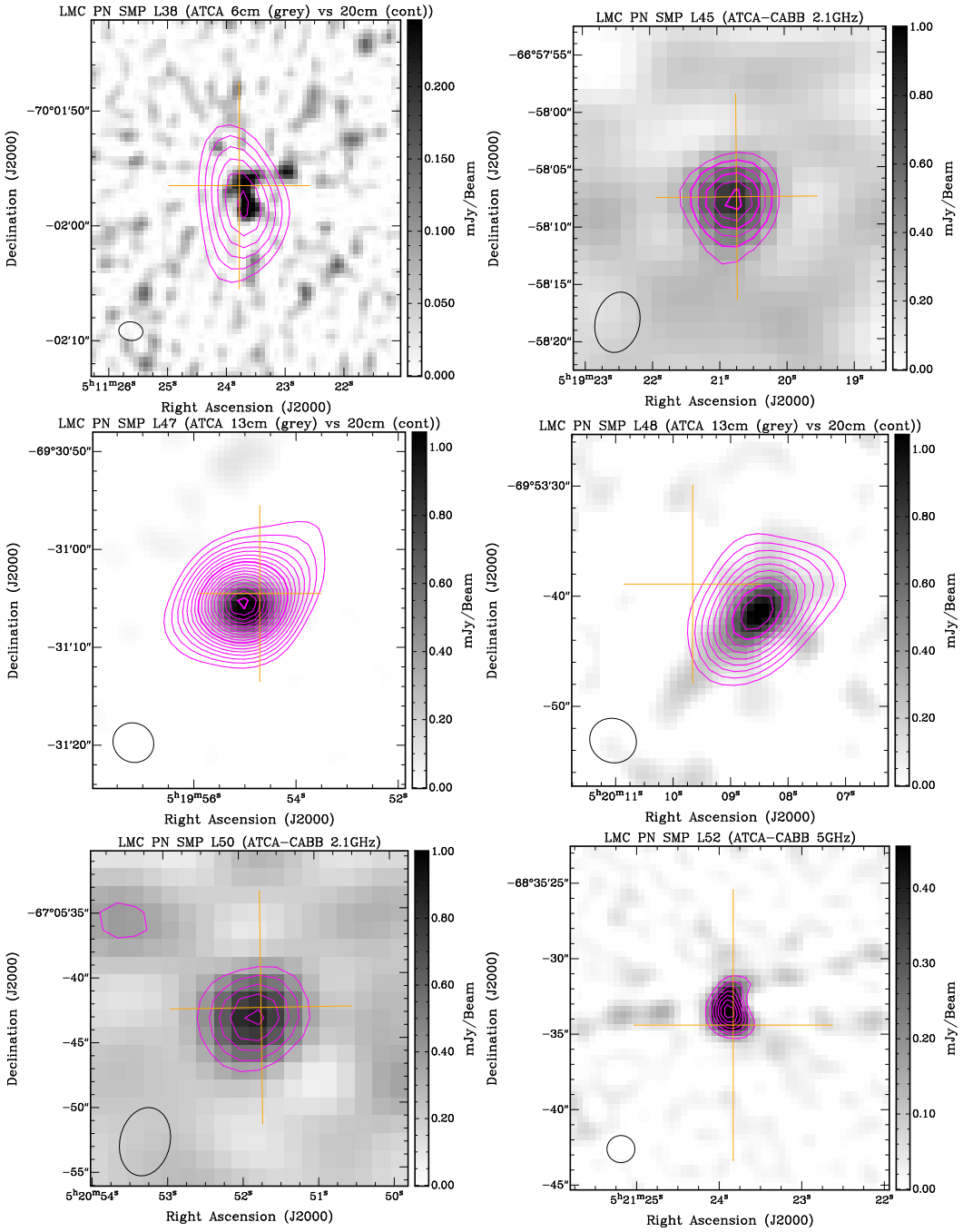

Figure 5.2: Radio Planetary Nebulae: SMP L38, L45, L47, L48, L50, L52. New and previous RC detections of LMC planetary nebulae. Images are constructed as total intensity RC maps. Contours are integral multiples of the measured RMS noise starting at 3σ with spacings of 1σ. Top row: SMP L38 at 6 cm (grey scale) with 20 cm contours and SMP L45 at 2.1 GHz; Second row: SMP L47 and SMP 48 at 13 cm (grey scale) with 20 cm contour; Third row: SMP L50 at 2.1 GHz and SMP L52 at 5 GHz. The beam size of each image is shown in the bottom left corner. The orange crosses represent the planetary nebula positions from the RP catalogue.

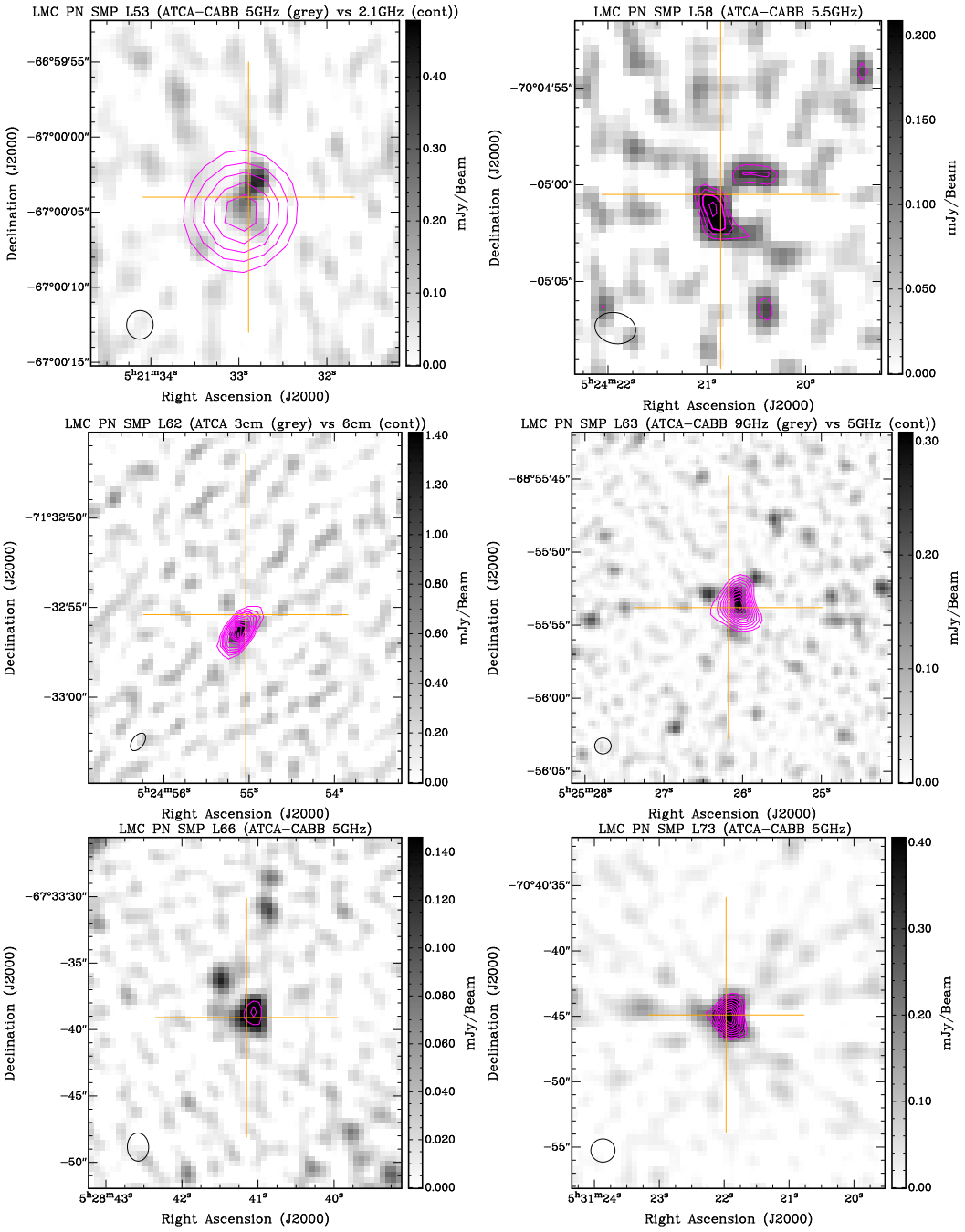

Figure 5.3: Radio Planetary Nebulae: SMP L53, L58, L62, L63, L66, L73. New and previous RC detections of LMC planetary nebulae. Images are constructed as total intensity RC maps. Contours are integral multiples of the measured RMS noise starting at 3σ with spacings of 1σ. Top row: SMP L53 at 5 GHz (grey scale) with 2.1 GHz contours and SMP L58 at 5.5 GHz; Second row: SMP L62 at 3 cm (grey scale) with 6 cm contours and SMP L63 at 9 GHz (grey scale) with 5 GHz contours; Third row: SMP L66 at 5 GHz and SMP L73 at 5 GHz. The beam size of each image is shown in the bottom left corner. The orange crosses represent the planetary nebula positions from the RP catalogue.

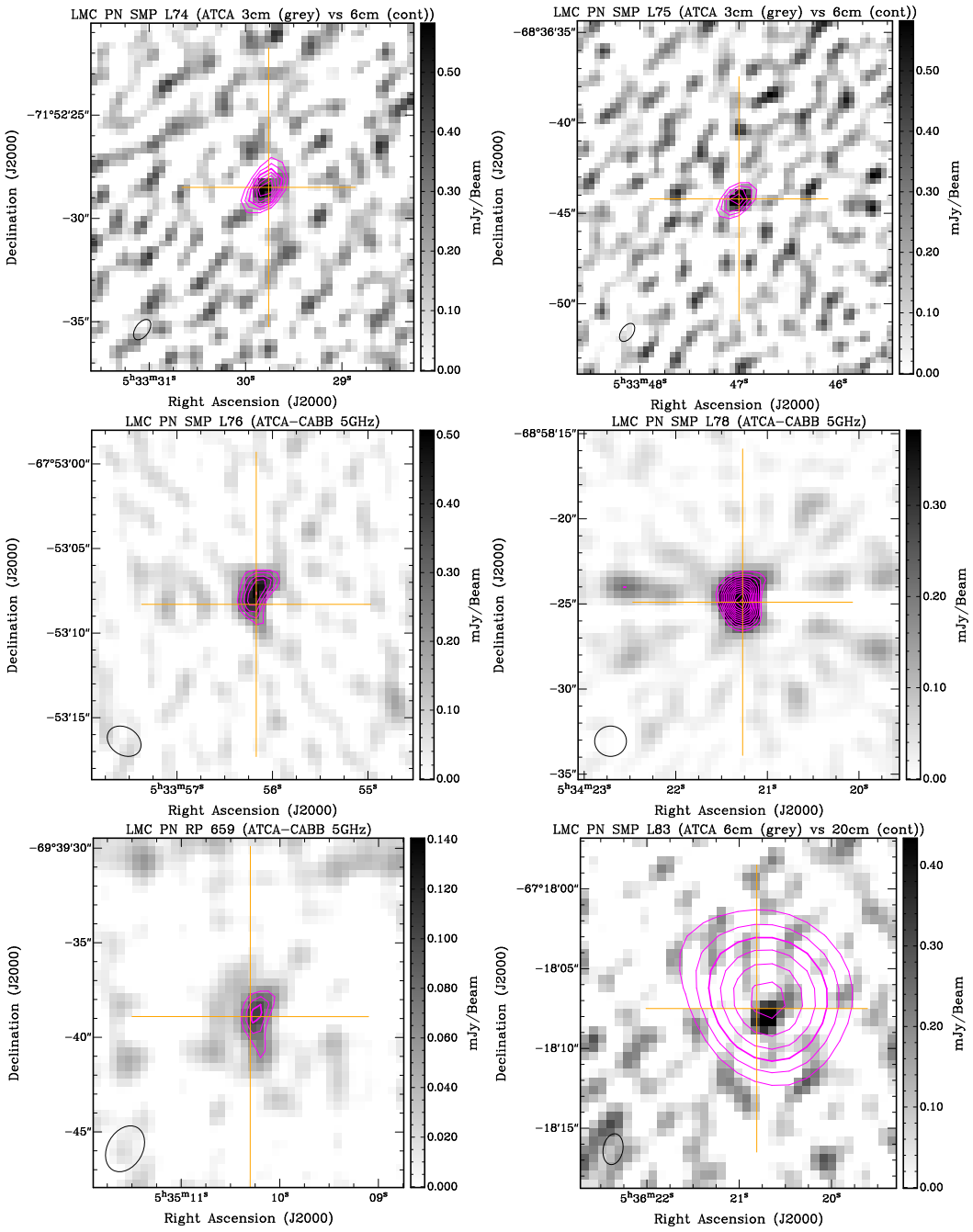

Figure 5.4: Radio Planetary Nebulae: SMP L74, L75, L76, L78, L83; RP659. New and previous RC detections of LMC planetary nebulae. Images are constructed as total intensity RC maps. Contours are integral multiples of the measured RMS noise starting at 3σ with spacings of 1σ. Top row: SMP L74 at 3 cm (grey scale) with 6 cm contours and SMP L75 at 3 cm (grey scale) with 6 cm contours; Second row: SMP L76 at 5 GHz and SMP L78 at 5 GHz; Third row: RP 659 at 5 GHz and SMP L83 at 6 cm (grey scale) with 20 cm contours. The beam size of each image is shown in the bottom left corner. The orange crosses represent the planetary nebula positions from the RP catalogue.

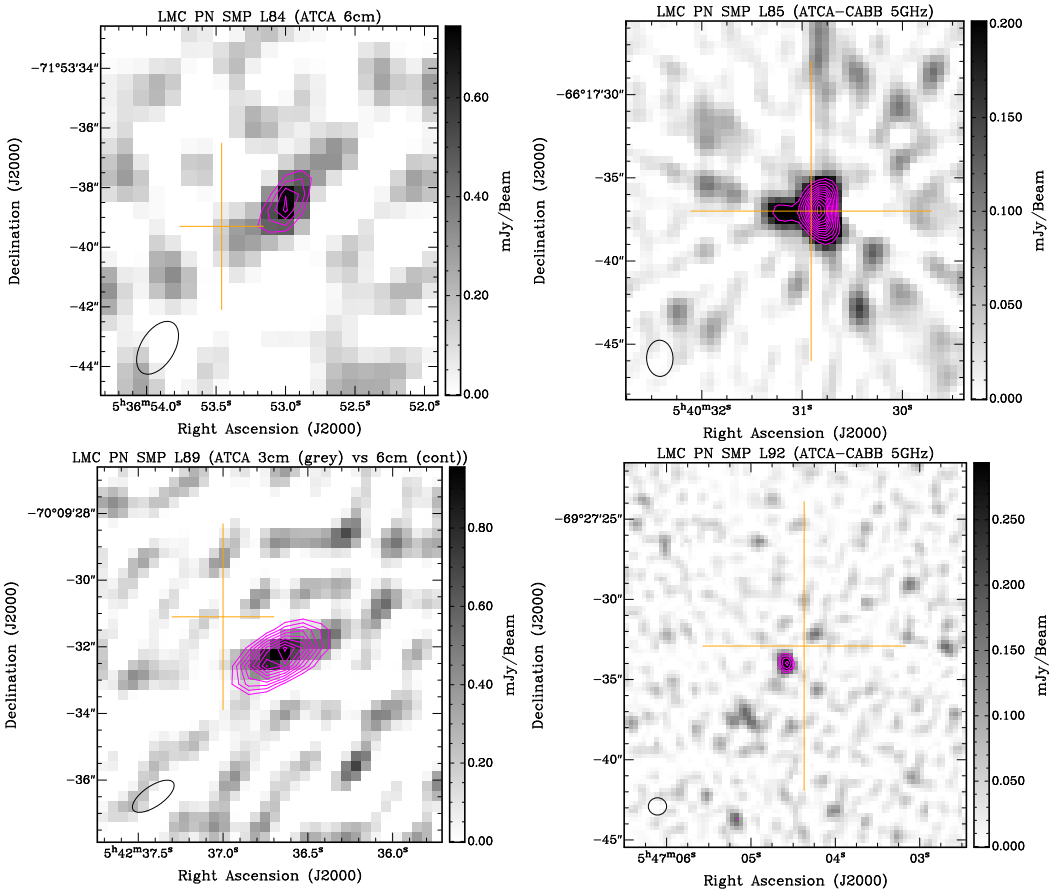

Figure 5.5: Radio Planetary Nebulae: SMP L84, L85, L89, L92. New and previous RC detections of LMC planetary nebulae. Images are constructed as total intensity RC maps. Contours are integral multiples of the measured RMS noise starting at 3σ with spacings of 1σ. Top row: SMP L84 at 6 cm and SMP L85 at 5 GHz; Bottom row: SMP L89 at 3 cm (grey scale) with 6 cm contours and SMP L92 at 5 GHz. The beam size of each image is shown in the bottom left corner. The orange crosses represent the planetary nebula positions from the RP catalogue.

SMP L29, SMP L37, SMP L38, SMP L45, SMP L50, SMP L52, SMP L53, SMP L58, SMP L63, SMP L66, SMP L73, SMP L75, SMP L76, SMP L78, RP 659, SMP L85, and SMP L92.

For seven previously detected radio planetary nebulae: SMP L47, SMP L48, SMP L62, SMP L74, SMP L83, SMP L84, and SMP L89 (Filipović et al., 2009), a flux density was measured on at least one frequency, confirming previous detections. The data for these planetary nebula detections came from the various ATCA projects listed in Table 5.1.[1] All of these LMC RC planetary nebulae have been listed in the RP catalogue with a classification of "Known" or "True".

Four LMC planetary nebulae listed in Filipović et al. (2009) had no new reliable detections: SMP L8, SMP L25, SMP L33, and SMP L39. SMP L8 had been reclassified as a compact H II region and was not listed in the RP catalogue. Therefore, it is not included in the study presented here. RC emission was detected from the positions of two other previously known RC planetary nebulae: SMP L25 and SMP L33 in 20 cm data from ATCA project C354. Unfortunately, both planetary nebulae were far from the centre of the primary beam ($\sim$25 arcmin at 20 cm) and, therefore, their flux density measurements were very uncertain even after the image had been corrected for the primary beam (MIRIAD LINMOS task). SMP L39 was not contained in any of the projects which met the requirements for inclusion.

The RP coordinates and the measured integrated RC flux densities for the detected planetary nebulae are shown in Table 5.3. The flux densities of the three previously detected planetary nebulae that could not be measured (SMP L25, SMP L33, SMP L39) are included in Table 5.3 with intensities from Filipović et al. (2009) for completeness of the LMC planetary nebula sample. The finding charts for all LMC planetary nebula RC detections are shown in Figures 5.1 through 5.5. These images were constructed as total intensity RC maps at the detection frequencies overlaid with contours at integral multiples of the estimated RMS noise. The orange crosses represent the planetary nebula coordinates from the RP catalogue.

As can be seen from the finding charts presented, Figures 5.1–5.5, in most cases, the RC detections were of isolated sources well correlated with their RP catalogue optical counterparts. Most detections of a planetary nebula were at one or two frequencies with only two detections at three frequencies and none at four frequencies. This resulted from either a lack of data at the other frequencies or an absence of measured flux values below the 3σ noise level required for detection.

[1] Also refer to Shaw et al. (2006) for a detailed description of the optical characteristics for many of these planetary nebulae.

Table 5.3: Coordinates and Flux Density Measurements of Detected Planetary Nebulae. The new flux density measurements are shown in the columns titled "new" and previous detections (Filipović et al., 2009) are listed in the columns titled "F09". The symbol "<" indicates that the actual value is less than the indicated value. Col. 12 is the MIR/$S_{20\,cm}$ ratio using 8 μm data from the VizieR Online Data Catalog: SAGE LMC and SMC IRAC Source Catalog (IPAC 2009). Col. 13 is the calculated Hα flux density using tabulated Hβ and extinction values cHβ from (Reid and Parker, 2010). Col. 14 is from Table 4.2. The "Source Ref.", Col. 15, refers to the sources of the RC data used for our measurements from the ATCA project database references found at the bottom of this table.

No.	PN	RA	DEC	$S_{3\,cm}$ (mJy)		$S_{6\,cm}$ (mJy)		$S_{13\,cm}$ (mJy)		$S_{20\,cm}$ (mJy)		MIR/	Hα flux (10^{-13})	θ	Source
		(J2000)	(J2000)	new	F09	new	F09	new	F09	new	F09	$S_{20\,cm}$	erg cm^{-2} s^{-1}	($''$)	Ref.
	(1)	(2)	(3)	(4)	(5)	(6)	(7)	(8)	(9)	(10)	(11)	(12)	(13)	(14)	(15)
1	SMP L13	04:59:59.99	–70:27:40.8	...	...	0.40±0.04	...	...	...	0.45±0.04	...	18.0	5.8	0.94	8
2	SMP L15	05:00:52.71	–70:13:41.1	...	...	0.64±0.05	...	0.98±0.05	...	0.90±0.06	...	24.4	6.5	0.82	4,8
3	SMP L21	05:04:51.99	–68:39:09.7	...	...	0.62±0.05	...	...	...	...	...	...	6.9	0.24	8
4	SMP L23	05:06:09.45	–67:45:27.8	...	...	...	...	0.67±0.04	...	0.66±0.04	...	4.4	6.7	0.39	5
5	SMP L25	05:06:23.91	–69:03:19.0	...	2.4±0.24	...	2.1 ±0.21	...	...	...	1.8±0.2	10.5	14.7	0.46	...
6	SMP L29	05:08:03.32	–68:40:16.6	...	...	0.65±0.06	...	...	...	0.70±0.07	...	17.9	5.9	0.54	3,8
7	SMP L33	05:10:09.41	–68:29:54.5	...	1.8±0.2	...	<1.5	...	...	...	<1	...	5.1	0.62	...
8	SMP L37	05:11:02.92	–67:47:59.4	...	...	0.52±0.04	...	...	...	...	...	...	3.3	0.50	8
9	SMP L38	05:11:23.69	–70:01:57.4	...	...	0.58±0.05	...	...	...	0.58±0.05	...	87.9	7.0	0.50	6,8
10	SMP L39	05:11:42.11	–68:34:59.1	...	<1.5	...	<1.5	...	...	...	2.3 ±0.23	3.0	2.2	0.46	...
11	SMP L45	05:19:20.71	–66:58:06.9	...	...	...	...	1.00±0.10	...	...	...	...	3.6	1.44	9
12	SMP L47	05:19:54.65	–69:31:05.1	...	2.3±0.23	...	2.1±0.21	1.50±0.05	...	1.30±0.05	2.2±0.22	17.1	11.3	0.50	1
13	SMP L48	05:20:09.48	–69:53:39.1	...	<1	1.4±0.2	1.5±0.2	1.50±0.10	...	1.00±0.05	1.6±0.2	18.0	10.2	0.40	1
14	SMP L50	05:20:51.73	–67:05:43.4	...	...	...	...	1.00±0.15	...	...	...	...	6.5	0.70	9
15	SMP L52	05:21:23.96	–68:35:33.8	...	...	1.00±0.05	...	...	...	...	...	...	11.1	0.40	8
16	SMP L53	05:21:32.83	–67:00:04.6	...	...	0.61±0.06	...	0.92±0.15	...	...	...	...	20.7	0.80	8,9
17	SMP L58	05:24:20.77	–70:05:01.5	...	...	0.31±0.05	..	...	...	...	...	...	9.0	0.26	8
18	SMP L62	05:24:55.08	–71:32:56.3	2.1±0.2	1.8±0.2	2.6±0.1	2.1±0.21	...	...	...	2.5 ±0.3	3.0	18.8	0.54	2
19	SMP L63	05:25:26.02	–68:55:54.0	0.5±0.1	...	1.2±0.1	...	...	...	...	...	...	12.7	0.52	8
20	SMP L66	05:28:41.00	–67:33:39.3	...	...	0.25±0.05	...	...	...	...	...	...	8.3	1.08	8
21	SMP L73	05:31:21.89	–70:40:45.5	...	...	1.01±0.06	...	...	...	...	...	...	13.7	0.50	8
22	SMP L74	05:33:29.76	–71:52:28.5	0.97±0.15	<1.5	1.06±0.15	<1.5	...	...	...	3.0±0.3	5.2	...	0.70	8
23	SMP L75	05:33:47.00	–68:36:44.2	1.14±0.15	...	1.45±0.15	...	...	...	...	...	...	10.2	0.40	8
24	SMP L76	05:33:56.10	–67:53:09.2	...	...	0.61±0.07	...	...	...	...	...	...	13.7	...	8
25	SMP L78	05:34:21.19	–68:58:25.3	...	...	1.28±0.06	...	...	...	...	...	...	12.5	0.56	8
26	RP 659	05:35:10.19	–69 39 39.3	...	...	0.12±0.02	...	...	...	...	...	...	1.2	...	7
27	SMP L83	05:36:20.81	–67:18:07.5	...	0.7±0.07	0.74±0.10	0.9±0.1	...	...	0.9±0.1	1.6 ±0.2	1.4	4.9	2.52	3
28	SMP L84	05:36:53.46	–71:53:39.3	...	<1.5	0.80±0.11	<1.5	...	...	...	1.6±0.2	1.7	...	0.58	8
29	SMP L85	05:40:30.80	–66:17:37.4	...	...	1.15±0.06	...	...	...	...	...	...	6.5	...	8
30	SMP L89	05:42:37.17	–70:09:30.4	1.60±0.15	1.8±0.2	1.49±0.10	1.6±0.2	...	...	...	2.1±0.21	13.3	7.9	0.46	8
31	SMP L92	05:47:04.80	–69:27:32.1	...	...	0.41±0.06	...	...	...	...	...	...	6.6	0.52	8

ATCA project numbers as in Table 5.1 - 1: C256, 2: C308, 3: C354, 4: C395, 5: C479, 6: C520, 7: C1973, 8: C2367, 9: C2908.

5.4 Radio Continuum Properties of the Detected Planetary Nebulae

From the measurements made here and data from the literature, additional physical properties of the detected planetary nebulae were determined. In Table 5.3 (Col. 12) the ratios of MIR and 20 cm flux densities were calculated using 8 μm MIR data from the Sage LMC and SMC IRAC Source Catalog (IPAC 2009)[2] containing LMC data from Meixner et al. (2006). This data were downloaded from the VizieR Online Data Catalog collection. Cohen et al. (2007b), using Galactic data from Cohen and Green (2001) and other sources referenced therein, examined the MIR/RC ratio, $S_{8.3\,\mu\mathrm{m}}/S_{843\,\mathrm{MHz}}$, for planetary nebulae in the Galactic plane and calculated a median ratio of 12. The median ratio for the population of the LMC planetary nebulae presented in this thesis is 11.9, using $S_{8\,\mu\mathrm{m}}/S_{1.4\,\mathrm{GHz}}$. The largest deviation from this median in the sample is calculated to be 87.9 for SMP L38. This, however, is likely due to unusual dust emissions from PAHs emitted by this planetary nebula as discussed in Bernard-Salas et al. (2009) who included this planetary nebula in their study of the MC planetary nebulae.

The RC SED was calculated for each planetary nebula for which measurements of flux density had been made on at least two frequencies (Table 5.4). The fitting equation is

$$S_\nu = \beta\nu^\alpha, \tag{5.1}$$

where α is the spectral index and S_ν is the flux density at frequency ν. The spectral indices are shown in Cols. 4a and 4b of Table 5.4.

Planetary nebula RC emission is primarily thermal radiation from FF interactions between electrons and ions within the nebular shell (Kwok, 2000). The SED is dependent on the metallicity, electron density, and temperature. Typically, at higher frequencies, >5 GHz, the nebula is optically thin and the spectral index, α, is expected to be ~ -0.1. At lower frequencies, <5 GHz, young planetary nebulae are most likely optically thick with an expected spectral index of $\sim$2 (Pottasch, 1984). Different density profile models, however, can produce very different SEDs. For example, if the density profile is from a constant mass loss, the spectral index for the planetary nebula would be optically thin and observed to be inverted with $\alpha \sim$0.6 (Panagia and Felli, 1975). Gruenwald and Aleman (2007) cautioned that RC SED observations from planetary nebulae cannot uniquely determine their density profiles.

The critical frequency of a planetary nebula is defined as the transition frequency from optically thick with a positive spectral index to optically thin with a negative spectral index. Most Galactic planetary nebulae exhibit a critical frequency of less than 5 GHz

[2]http://adsabs.harvard.edu/abs/2012yCat.2305....0G

Table 5.4: Large Magellanic Cloud RC Planetary Nebula Parameters. Measured and calculated LMC planetary nebula RC parameters. Col. 2 contains the photometric angular diameters. The references used for the diameters are listed in Col. 3 and they refer to the list at the bottom of the table. The spectral indices (α) are listed in Col. 4a and 4b. The adopted flux densities at 6 cm are in Col. 5. Those which are in brackets were estimated from other band measurements. The angular diameters in arcseconds in Col. 2 were used to calculate the radii in pc shown in Col. 7. Values for brightness temperatures, T_b; the electron densities, n_e; and ionised masses, M_i; were calculated from the adopted 6 cm flux densities and the radii. These are presented in Cols. 6, 8, and 9, respectively.

PN	θ	Ref	α		$S_{6\,cm}$	T_b	r	$\log(n_e)$	M_i
	($''$)		>5 GHz	< 5 GHz	(mJy)	(K)	(pc)	(cm^{-3})	($M_\odot$)
(1)	(2)	(3)	(4a)	(4b)	(5)	(6)	(7)	(8)	(9)
SMP L13	0.94	1	...	–0.09±0.10	0.40±0.04	25±3	0.11	3.19	0.225
SMP L15	0.82	1	...	–0.27±0.10	0.64±0.05	68±5	0.10	3.38	0.236
SMP L21	0.24	4	...	...	0.62±0.05	594±48	0.03	4.17	0.036
SMP L23	0.40	3	...	0.28±0.20	[0.68±0.04]	302±18	0.05	3.87	0.075
SMP L25	0.46	1	0.27±0.40	0.11±0.20	2.1±0.21	559±56	0.06	4.02	0.167
SMP L29	0.54	2	...	–0.05±0.13	0.65±0.06	124±11	0.07	3.65	0.128
SMP L33	0.62	1	...	...	[1.9±0.2]	339±36	0.07	3.80	0.252
SMP L37	0.50	2	...	...	0.52±0.04	116±9	0.06	3.66	0.096
SMP L38	0.50	1	...	0.00±0.13	0.58±0.05	130±11	0.06	3.68	0.103
SMP L39	0.46	2	...	...	[2.0±0.2]	645±65	0.06	4.00	0.168
SMP L45	1.44	2	...	...	[0.88±0.09]	29±3	0.17	3.09	0.612
SMP L47	0.50	2	...	0.26±0.13	2.1±0.21	493±49	0.06	3.96	0.203
SMP L48	0.40	2	...	0.22±0.08	1.4±0.2	596±85	0.05	4.02	0.116
SMP L50	0.70	1	...	...	[0.93±0.14]	128±19	0.08	3.56	0.216
SMP L52	0.40	2	...	...	1.0±0.05	349±17	0.05	3.94	0.096
SMP L53	0.80	1	...	–0.44±0.30	0.61±0.06	53±5	0.10	3.39	0.211
SMP L58	0.26	1	...	...	0.31±0.05	260±42	0.03	3.98	0.028
SMP L62	0.54	2	–0.43±0.30	...	2.6±0.1	496±19	0.07	3.95	0.251
SMP L63	0.52	2	–1.80±0.60	...	1.2±0.1	251±21	0.06	3.84	0.160
SMP L66	1.10	4	...	...	0.25±0.05	12±2	0.13	2.99	0.214
SMP L73	0.50	2	...	...	1.01±0.06	226±13	0.06	3.80	0.135
SMP L74	0.70	2	–0.18±0.60	...	1.06±0.15	121±17	0.08	3.59	0.236
SMP L75	0.40	2	–0.50±0.50	...	1.45±0.15	507±52	0.05	4.03	0.115
SMP L76	...	...	...	...	0.61±0.07	...	...	...	...
SMP L78	0.56	1	...	...	1.28±0.06	230±11	0.07	3.78	0.179
RP 659	...	...	...	...	0.12±0.02	...	....	....	...
SMP L83	2.53	2	...	–0.14±0.20	0.74±0.10	7±1	0.30	2.68	1.337
SMP L84	0.50	2	...	...	0.80±0.11	132±18	0.07	3.65	0.150
SMP L85	...	...	...	...	1.15±0.06	...	...	...	...
SMP L89	0.46	2	0.14±0.30	...	1.49±0.10	397±27	0.06	3.94	0.143
SMP L92	0.52	2	...	...	0.41±0.06	86±13	0.06	3.58	0.090

1: Shaw et al. (2001), 2: Shaw et al. (2006), 3: Vassiliadis et al. (1998), 4: Stanghellini et al. (1999).

(Gruenwald and Aleman, 2007). The critical frequencies for the planetary nebulae, however, depend on gas density and can range from ∼0.4 GHz to >15 GHz (Gruenwald and Aleman, 2007). Young and compact planetary nebulae have been observed with critical frequencies of ∼5 GHz to 28 GHz (Aaquist and Kwok, 1991). These young planetary nebulae most likely have very high electron densities which make the critical frequency much higher than 5 GHz (Kwok, 1982; Pazderska et al., 2009). The spectral indices, α, were calculated above and below 5 GHz with Equation 5.1 as a proxy of the evolutionary state of the planetary nebulae.

Non-thermal RC radiation has been proposed for some planetary nebula emissions (Dgani and Soker, 1998). This mechanism requires fast winds from the central star of the planetary nebula to create an inner region where strong magnetic fields interact with the central star wind. A non-thermal SED would be expected to have a spectral index $\alpha \ll -0.1$ (Gurzadyan, 1997). Cohen et al. (2006) reported non-thermal emissions from a very unusual AGB star. This star was measured to have $\alpha \sim -0.9$ and contained shocked interactions between a cold, planetary nebula–like shell and the hot, fast stellar wind from the AGB star. The source, however, of most apparent non-thermal RC detections is more likely to be a supernova remnant or an active galactic nucleus coincident with the position of the planetary nebula.

In Table 5.4 (Col. 5) the adopted flux densities at 6 cm for all of the detected RC planetary nebulae are presented. If a direct measurement at 6 cm was not available, the estimated flux density from neighbouring bands was used to calculate the 6 cm value. This was necessary for SMP L23, SMP L33, SMP L39, and SMP L45. The entries which were estimated are indicated in Table 5.4 with brackets around the 6 cm values.

The adopted 6 cm flux densities were compared with a sample of well-measured Galactic planetary nebulae. This sample is a database of optical diameters and 6 cm integrated flux density measurements from Siódmiak and Tylenda (2001) consisting primarily of planetary nebulae from the Galactic bulge. Their diameter measurements were calculated using the 10% peak contour approach. They used only optical data from photographic plates since they judged that newer CCD images were too sensitive and could not be directly compared to extant diameter measurements derived from photographic plates. Their data were re-scaled here to the distance of the LMC (50 kpc; Pietrzyński et al. (2013)). Both the LMC data and the re-scaled Galactic data are plotted on Figure 5.6.

Additionally, nine SMC planetary nebulae from Leverenz et al. (2016): SMP S6, SMP S13, SMP S14, SMP S16, SMP S17, SMP S18, SMP S19, SMP S22, and SMP S24 are also plotted on Figure 5.6. These SMC planetary nebulae were determined unambiguously to not be planetary nebula mimics and were also re-scaled to the distance of the LMC. The green star markers on Figure 5.6 represent the SMC data.

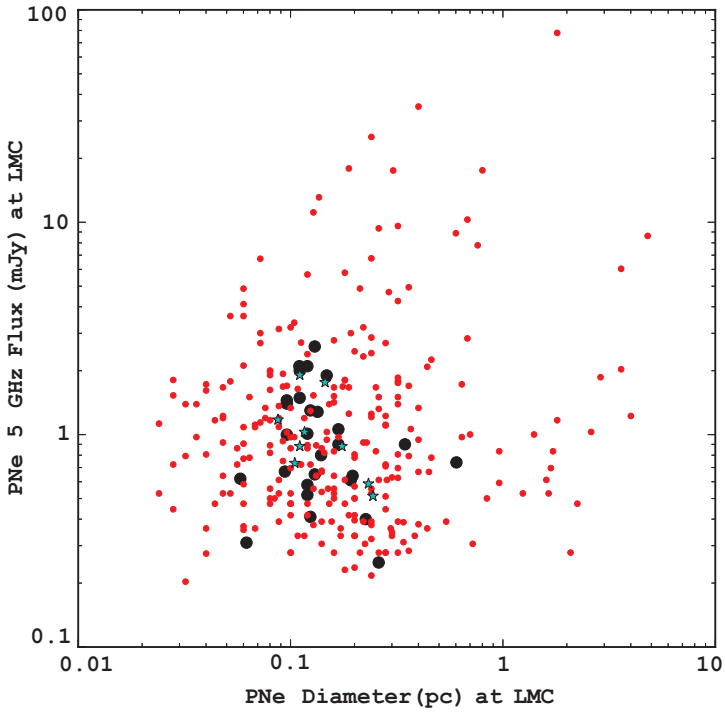

Figure 5.6: Galactic and Magellanic Cloud Planetary Nebulae Comparison. Data from Siódmiak and Tylenda (2001) (small red dots) are shown with SMC planetary nebula data from Leverenz et al. (2016) (green stars), both scaled to the distance of the LMC. New LMC measurements are shown as large black dots.

The LMC RC planetary nebula measurements were consistent with the scaled flux densities and diameters from both the Galactic and SMC samples. The angular diameters in Table 5.4 (Col. 2) were adopted from Shaw et al. (2001); Shaw et al. (2006), Vassiliadis et al. (1998), and Stanghellini et al. (1999). For consistency, only photometric radii were used, defined as the radius containing 85% of the total emitted flux (Shaw et al., 2001), since measurements based on this method were available from all of the sources consulted for the radius data which were adopted. The differences in the techniques for the diameter measurements for this comparison were not estimated to be significant (the 10% peak flux density for the Galactic planetary nebulae used by Siódmiak and Tylenda (2001) compared to the 85% flux density employed for the MC planetary nebulae).

The adopted 6 cm flux densities and the angular diameters from the literature were used to estimate the electron densities, n_e, and ionised masses, M_i, for all detected RC planetary nebulae which are shown in Table 5.4 (Cols. 8 and 9). The n_e and M_i were calculated from equations (1) and (2) in Gathier (1987), respectively. The electron temperature, T_e, for all planetary nebulae was chosen to be the canonical temperature of 10000 K. The solar metallicity parameter and the consensus filling factors were both assigned a numerical value of 0.3 (Boffi and Stanghellini, 1994; Frew et al., 2016a). The helium abundance for SMP L13 was taken from de Freitas Pacheco et al. (1993). SMP L39, SMP L52, and RP 659 were assigned the default value of 0.1 per Gathier (1987) since measured values for those planetary nebulae were not available. Calculations for the remaining planetary nebulae used helium abundances from Chiappini et al. (2009). No values for the fraction of doubly ionised helium were available so the default value of 0.33, as used by Gathier (1987), was adopted. The uncertainties in n_e and M_i were estimated to be on the order of 40%.

Thermal brightness, T_b, at 6 cm is shown in Table 5.4 (Col. 6). It is a good proxy for planetary nebula evolutionary status (Kwok, 1985; Zijlstra, 1990; Gruenwald and Aleman, 2007) and is also an indication of self–absorption. The conventional RC T_b was calculated assuming an isothermal nebula, from Wilson et al. (2009)

$$T_b = \frac{c^2}{2\,k\,\nu^2} \cdot \frac{S_\nu}{\Delta\Omega}. \tag{5.2}$$

To determine the self–absorption correction for the results, the two component model of self–absorption from Siódmiak and Tylenda (2001) was applied. Values of $\xi = 0.27$ and $\varepsilon = 0.19$ were adopted for this comparison. This model provided a correction factor based on the ratio of the measured T_b with T_e. The canonical value of 10000 K for T_e was adopted. The highest T_b calculated from the data was for SMP L39 at 645 K. For this value of T_b, the model provided a correction factor of 1.8 at 20 cm and 1.01 at 6 cm. The value of 339 K for T_b from SMP L33

was determined to have a correction factor of 1.4 at 20 cm. At 6 cm, there was essentially no self–absorption. The conclusion was that there was significant self–absorption in some of the results at 20 cm but at shorter wavelengths the self–absorption was negligible.

Table 5.5: Results of the Surface Brightness-Diameter Analysis at 6 cm. Col. 1 lists the sample designation with the number of data points in Col. 2 and the calculated correlation coefficient in Col. 3. Cols. 4-7 list the values for the parameters of the fitting from the Σ offsets and their estimated uncertainties. The average fractional error for the calculated distances are in Col. 8. Cols. 9-13 present the values for the orthogonal-offset-fitting and the corresponding average distance fractional errors. In Cols. 14-16 the average fractional errors are presented for the PDF distance estimators: mean, mode, and median.

Sample			Σ offsets					Orthogonal offsets					$f(\%)$		
	N	r	A	ΔA	β	$\Delta\beta$	$f(\%)$	A	ΔA	β	$\Delta\beta$	$f(\%)$	mean	mode	median
(1)	(2)	(3)	(4)	(5)	(6)	(7)	(8)	(9)	(10)	(11)	(12)	(13)	(14)	(15)	(16)
LMC	28	–0.87	–19.7	0.3	2.2	0.4	22.97	–20.3	0.4	2.9	0.5	19.58	18.29	17.28	18.37
SMC†	9	–0.94	–20.1	...	2.7	...	9.99	–20.4	...	3.0	...	9.52	...	...	...
LMC+SMC	37	–0.88	–19.9	0.3	2.3	0.3	20.17	–20.3	0.3	2.9	0.4	17.00	16.05	14.64	16.02

† Presented results are not reliable due to the small number of data points and are given only for the sake of completeness. Unlike the other two samples, these fitting parameters were not determined with the bootstrap procedure described in this thesis but from a simple linear regression fitting to the data sample. The 2 dimensional density smoothing did not yield convergent results and no fractional errors were calculated.

5.5 Magellanic Clouds Surface Brightness-Diameter Model

The RC flux density measurements at 6 cm and radius measurements in parsecs from Table 5.4 were used to calculate the surface brightness and diameter values for the (Σ–D) relation study of the MC planetary nebulae.

Recently, Leverenz et al. (2016) described the (Σ–D) relation for a sample of SMC planetary nebulae. That work is extended here by analyzing the RC detected planetary nebulae in terms of the (Σ–D) relation for both the LMC and the SMC. The model for the RC surface brightness adopted from Vukotić et al. (2009) is

$$\Sigma \left[\mathrm{W\,m^{-2}\,Hz^{-1}\,sr^{-1}}\right] = 1.505 \cdot 10^{-19}\, S\,[\mathrm{Jy}]/\theta^2\,[']\tag{5.3}$$

and the form of the (Σ–D) model equation adopted for these surface brightnesses from Vukotic et al. (2014) is

$$\Sigma = A \times D^{-\beta}.\tag{5.4}$$

There are 715 observed planetary nebulae in the LMC (Reid and Parker, 2013; Reid, 2014) but only thirty-one of them have been detected at radio frequencies. This is indicative of a strong observational bias suggesting that only the "tip of the iceberg" was observed at radio frequencies (Vukotić et al., 2009). Indeed, while the measured surface brightness of Galactic planetary nebulae extends from $\sim 10^{-24}$ to $\sim 10^{-16}$ $\mathrm{W\,m^{-2}\,Hz^{-1}\,sr^{-1}}$, the planetary nebulae from the MCs were detected only in the high brightness half of this interval from $\sim 10^{-20}$ to $\sim 10^{-16}$ $\mathrm{W\,m^{-2}\,Hz^{-1}\,sr^{-1}}$. Similar selection effects could be seen in D as well. The largest planetary nebula in the RC LMC sample is smaller than 1 pc, unlike the largest planetary nebula used for Hα statistical distance calibration (Frew et al., 2016a) which is > 2 pc in size.

With such a strong selection effect in play, a Monte Carlo simulation was constructed (described in Section 5.9) to quantify the influence of sensitivity related selection effects on the (Σ–D) samples. Utilizing bootstrap statistics (Efron and Tibshirani, 1993), the prior distribution of the (Σ–D) relation parameters was constructed. For each (Σ–D) data sample, both Σ offset and orthogonal offset analyses were applied. In addition, the (Σ–D) probability density function (PDF) was reconstructed by using bootstrap based kernel density smoothing (for details, see Bozzetto et al., 2017, and references therein). The reconstruction of the (Σ–D) PDF provided a better insight into observational biases and evolutionary features of each sample (see also Vukotic et al., 2014, and references therein). Unlike Vukotic et al. (2014), the PDF calculation was improved here with the use of bootstrap based kernel density smoothing instead of bootstrap based centroid offset smoothing. A standard Gaussian kernel was applied

in order to calculate optimal smoothing bandwidths. For data in two dimensions, a Gaussian product kernel was used. The optimal smoothing bandwidths, h, were selected by minimizing the bootstrap integrated mean squared error (BIMSE) (for details, see Bozzetto et al., 2017).

From planetary data available from the LMC and SMC, three samples were defined:

1. The sample of twenty-eight LMC planetary nebulae,
2. The sample of nine SMC planetary nebulae with reliable flux density estimates, and
3. The sample consisting of the combined LMC + SMC planetary nebulae with thirty-seven total planetary nebulae.

As a measure of the sample spread and reliability, the correlation coefficient, r, and the average fractional error, f, were calculated. The values of the best fitting (Σ–D) parameters were used to calculate the (Σ–D) statistical distances to the MCs (for a detailed description of statistical distance calculation, see Vukotic et al. (2014)). The results are shown in Table 5.5 and Figure 5.7.

The average fractional error for distance is

$$f = \frac{1}{N} \sum_{i=1}^{N} \left| \frac{d_{\rm i} - d_{\rm i}^{\rm s}}{d_{\rm i}} \right|, \tag{5.5}$$

where N is the number of data points in the sample, $d_{\rm i}$ is the measured distance to the object of the $\rm i^{th}$ data point, and $d_{\rm i}^{\rm s}$ is a statistical distance to that object determined either from the parameters of an empirical fitting or from the PDF method. The PDF method for a fixed Σ value gives a probability density over D. The values of D for the mean, mode, and median were used to calculate the corresponding statistical distances, see Table 5.5.

5.6 Small Magellanic Cloud Sample

With the highest r value and the smallest values for f, the SMC sample appeared to be very compact and reliable, see Table 5.5. The kernel density smoothing, however, did not give convergent results for optimal smoothing bandwidths. This was caused by the small number of data points. The optimal smoothing bandwidths were calculated to be ~ 0.14 and ~ 0.40, but repeated calculations did not give consistent results.

It was noted that the SMC sample consisted of a small number of data points that were difficult to measure accurately in that they were very close to the survey sensitivity line. This suggested that the quality of this sample could be weaker than it would first appear from a simple linear regression. Applying the bootstrap procedure could provide erroneous values

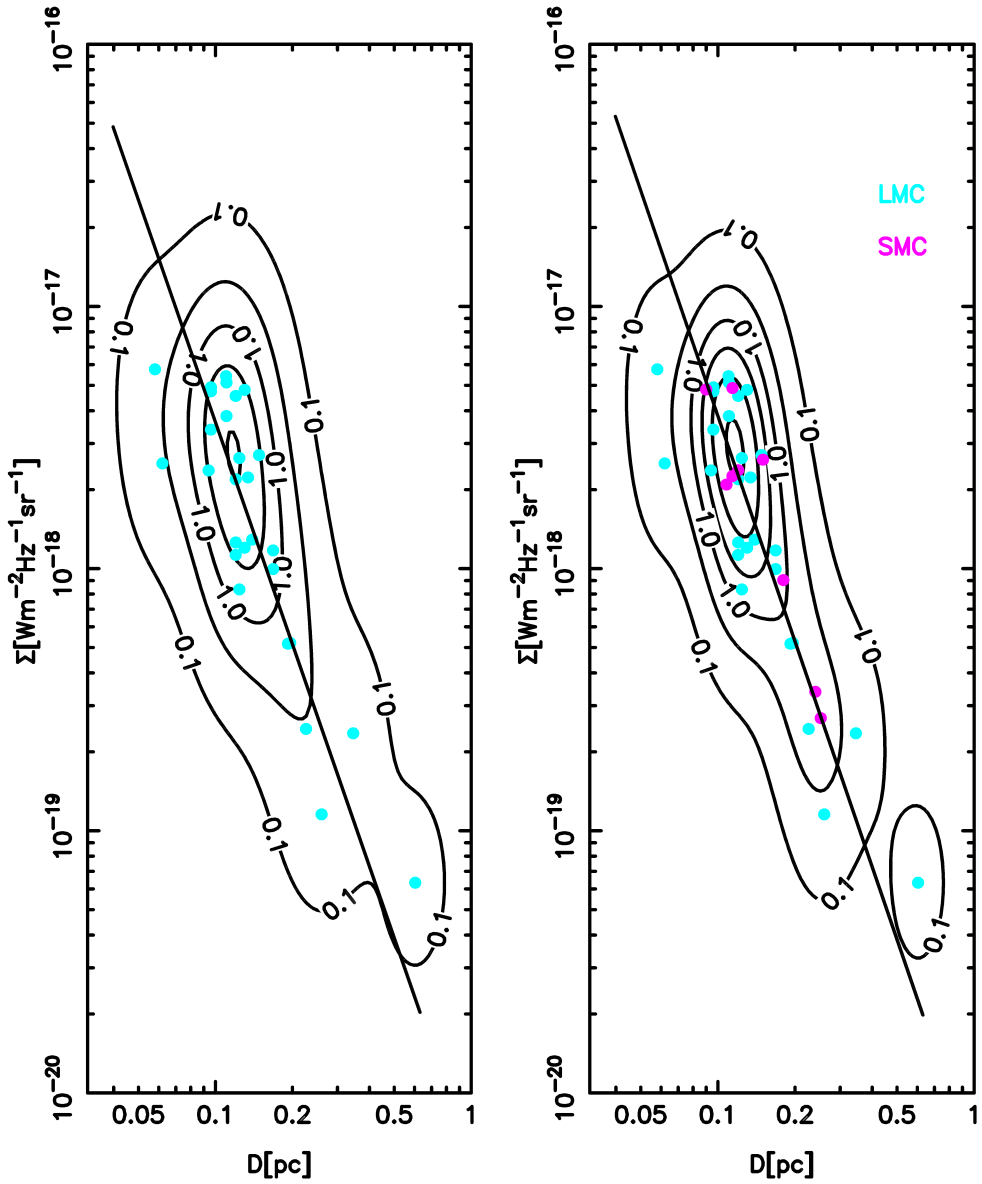

Figure 5.7: Surface Brightness-Diameter Probability Density Distributions. These plots are derived from 6 cm data with the reconstructed probability density distribution and orthogonal regression best fitting line: LMC (left) and LMC+SMC (right). The PDF contour plot is calculated on the 100×100 grid mapped on the plotted variables range. Contours levels are at 0.1, 0.5, 1.0, 1.5, 2.0, and 2.5. Optimal smoothing bandwidths are found at $h_{\log D} = 0.11$ and $h_{\log \Sigma} = 0.30$ for the LMC sample and $h_{\log D} = 0.09$ and $h_{\log \Sigma} = 0.26$ for the LMC+SMC sample.

for A and β and the calculated uncertainties for each. The small number of data points, even with the high correlation value, gave non-physical values for A and β when fitting the resampled samples. This resampling with repetition is the essence of the bootstrap analysis (see Vukotic et al. (2014) and references therein).

Instead of presenting these erroneous data, values from a simple empirical fitting of a single line to the SMC sample without the application of the bootstrap analysis are shown in Table 5.5. Even though these fitted parameter values are not considered reliable, the SMC sample was utilized to form a more complete combined MC planetary nebula sample.

5.7 Large Magellanic Cloud and Combined Sample

The larger LMC sample appeared to be more complete and reliable than the SMC sample although it was also very close to the survey sensitivity line, see Figures 5.7 and 5.9. An interesting feature of these plots was that the PDF contours in the (Σ–D) plots (Figure 5.7) at ≥ 1 levels appeared to be more symmetric about a line of a steeper slope than the slope of the orthogonal offset best fitting line for both the LMC and the combined sample. This (a)symmetric discrepancy was evident over a large part of the plotted variables range, $D \leq 0.3$ pc. This is in agreement with the Figure 5 plot from Frew et al. (2016b) where the authors plotted similar quantities (Hα brightness versus radius) along with the evolutionary paths for planetary nebulae of different masses. The plotted paths significantly deviated from a straight line in the $D \leq 0.3$ pc range. This revealed the need for developing new statistical tools for future empirical studies of planetary nebula evolution in order to quantify the subtleties of that evolution. With the larger data spread, the LMC sample was certainly less sensitivity biased than the SMC sample but the somewhat large uncertainties, especially $\Delta\beta \sim 0.4-0.5$, indicated a possible reduced sample quality. Although less extreme than the SMC sample bias, the LMC sample bias could cause peculiar values for the fitting of the parameters for the resampled sample.

Combining the SMC and LMC samples into one sample yielded the best results. The combined sample had smaller values for ΔA and $\Delta\beta$ compared to the LMC sample alone, see Table 5.5. It was also found that the average fractional distance error calculated with the PDF method for the combined sample was $f \sim 16\%$ which was lower than that of the LMC sample alone which was $f \sim 18\%$. This demonstrated the potential of RC MC planetary nebula samples to be used for statistical distance estimate calibration. Eighteen percent of the LMC's 50 kpc distance, however, is still $\sim$9 kpc. The LMC depth is reported to be approximately 1 kpc (Pietrzyński et al., 2013); (Frew et al., 2016b). This value suggests that there is significant

room for improvement in the statistical distance calculation. This is likely to be achieved by more sensitive and more accurate RC surveys with larger samples.

5.8 Magellanic Clouds Surface Brightness-Diameter Slope

The value of β in the (Σ–D) relation is theoretically expected to change from $\sim$1 to 3 over the lifetime of a planetary nebula (Urošević et al., 2009). Using a Galactic planetary nebula sample, they found an empirical slope of $\beta \simeq 2.3 \pm 0.4$ by fitting the Σ offsets. The β values from Σ offsets in this thesis, 2.3 for combined sample and 2.2 for the LMC sample alone, may imply a similar age for the MC planetary nebula population compared to their selected Galactic planetary nebula sample. The more robust orthogonal slope, however, of 2.9 could give the impression that the MC planetary nebulae might be in a late stage of their evolution, see Table 5.5.

Vukotić et al. (2009) argued that the MC planetary nebula samples were biased with sensitivity selection effects and consequently the empirical slopes should be steeper than that estimated from the (Σ–D) empirical data fittings.

Applying the bootstrap procedure to a sample of Galactic planetary nebulae with reliable distances, Vukotić and Urošević (2012) obtained an orthogonal offset, $\beta = 3.1 \pm 0.4$, which is consistent with the MC results presented in Table 5.5. The Σ offset slope for a Galactic planetary nebula sample was calculated by Urošević et al. (2009) and was compared to the orthogonal offset slope calculation from a Galactic planetary nebula sample by Vukotić and Urošević (2012). The results overlap within the estimated uncertainties of the slopes from Table 5.5.

5.9 Magellanic Clouds Surface Brightness-Diameter Sensitivity Analysis

To estimate the accuracy of the results related to the (Σ–D) slope, the influence of sensitivity related selection effects was simulated. This method is from Vukotić et al. (2009) who applied this technique to a very small sample of five planetary nebulae from the MCs. A similar simulation was performed here (although more advanced in some technical details) by applying this method to the current MC sample of thirty-one planetary nebulae. The great improvement in the number of RC MC planetary nebula detections was expected to result in a significantly more complete planetary nebula sample.

To estimate the influence of the sensitivity selection effects, artificial planetary nebula (Σ–D) samples were generated using a Monte Carlo simulation from the properties of the 6 cm

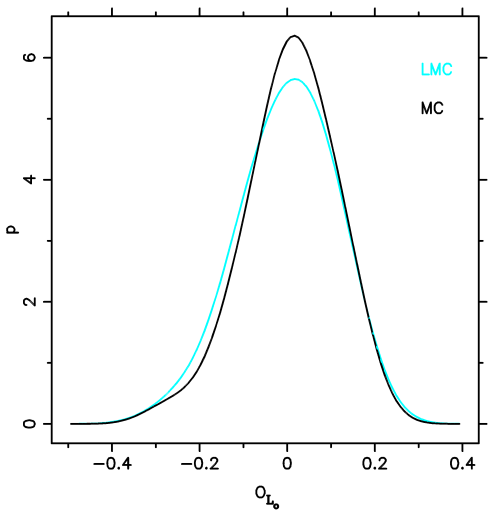

Figure 5.8: 6 cm Sample Probability Density Distributions. The initial findings for the 6 cm data sample probability density distributions of the orthogonal distances from the orthogonal offset best fitting lines $L_{\rm o}$ for the LMC and the combined sample.

data. The sample parameters were compared before and after the sensitivity selection. The simulation diameter interval, $[D_{\rm min}, D_{\rm max}]$, was chosen using $D_{\rm min} = 0.058$ pc from the minimum diameter value in Table 5.4. The maximum value, $D_{\rm max} \sim 2$ pc, was chosen because the largest planetary nebulae swell up to $D_{\rm max} \sim 2$ pc. Then artificial points were randomly generated and distributed in the $[D_{\rm min}, D_{\rm max}]$ interval using the random number generator of Saito and Matsumoto (2008) with a uniform density on the $\log D$ scale equal to the density of the adopted 6 cm data. This resulted in a total of fifty-five artificial points for the combined sample, LMC + SMC, and forty-two artificial points for the LMC sample per generated sample in a given $[\log D_{\rm min}, \log D_{\rm max}]$ interval. These points were then projected onto a series of lines with β ranging from 1.5 to 3.6. All of these lines intersected the orthogonal offset best fitting line at the 6 cm adopted data ($L_{\rm o}$) at $D_{\rm min}$. The next step was to disperse the points from the lines upon which they were projected in such a way as to simulate the dispersion of the adopted 6 cm data. This was achieved by applying the kernel density smoothing in one dimension from Bozzetto et al. (2017). From the adopted 6 cm data the smooth probability density distribution was constructed using the orthogonal distances (offsets) from the $L_{\rm o}$ line, see Figure 5.8.

It is reasonable to assume that the data do not have the same scatter along the simulated interval. (*Scatter* is a value used in the simulation.) The empirical data for the input of the sensitivity simulation modeled the sensitivity line in such a way that it passed through the data point that gave the lowest Σ value. There is no empirical knowledge of the data spread at the faint end. Even for the part above the sensitivity line, the PDF contours from Figure 5.7 did not appear to have much variability in spread. In this way the uniform dispersion model was simulated for the whole simulated data interval. This was sufficient to demonstrate the

influence of the sensitivity selection on the (Σ–D) slope. Even if a different *Scatter* value were selected at the faint end, most of it would get a sensitivity cut off and would not influence the results. The initial findings showed no significant difference for the overall scatter in the case of the LMC and the combined sample, see Figure 5.8. Both distributions were rather symmetric around the peak which was close to a value of zero. Each point was randomly dispersed in the orthogonal direction from the simulated slope line according to the probability density distribution from Figure 5.8. The dispersion for the simulation was controlled by *Scatter* multiplied by the dispersion obtained from the distributions in Figure 5.8. The orthogonal offset fitting parameters were generated and the fittings were then calculated for dispersing the artificial sample. For each simulated slope, one hundred artificial samples were generated. The mean values of the fitting parameters after selection and their estimated uncertainties (calculated as the standard deviation of the given array of elements) are presented in Table 5.6. In Figure 5.9 one artificial sample for $Scatter = 2.0$ is plotted with a simulated β of 3.5 along with the combined MC planetary nebula sample and sensitivity line. Since the present LMC survey was not uniform in terms of sensitivity, the sensitivity line was selected in such a way that it passed through the data point of the combined sample that gave the lowest Σ value at the horizontal part of the sensitivity line. For the break point of the sensitivity line, the average equivalent of the circular beam size calculated was selected from the beam sizes of each particular reduced image. At the adopted LMC distance, this translated to $D = 1.017$ pc.

The results reported in Table 5.6 do not appear to be significantly dependent on *Scatter*. For each given *Scatter* the $\Delta\beta$ became larger than $\sigma_{<\beta>}$ when the simulated β became as large as $\sim 2.5 - 2.7$. This corresponded to $< \beta > \sim 2.5$ ($Scatter = 1.0$) and, although within the estimated uncertainty, reduced to $< \beta > \sim 2.3$ for a larger value of *Scatter*. Hence the steeper slopes, such as ~ 2.9 (as obtained in this thesis), were significantly influenced by the sensitivity selection effect. For $< \beta > \sim 2.9$ the simulated slope was ~ 3.4 and was even greater for larger *Scatter*. Since the MC planetary nebula samples appear to be significantly influenced by sensitivity selection it is likely that only the brightest part of the sample was detected. Any strong claims, however, should be avoided since the results may depend on the simulation algorithm and the selected sensitivity line.

5.10 Large Magellanic Cloud Planetary Nebulae Summary

The ATOA was searched for projects with high resolution data at 3, 6, 13, or 20 cm which had pointing centres within 10 arcmin of planetary nebula coordinates from the RP database. Seventeen projects met those requirements and were processed in order to search for planetary

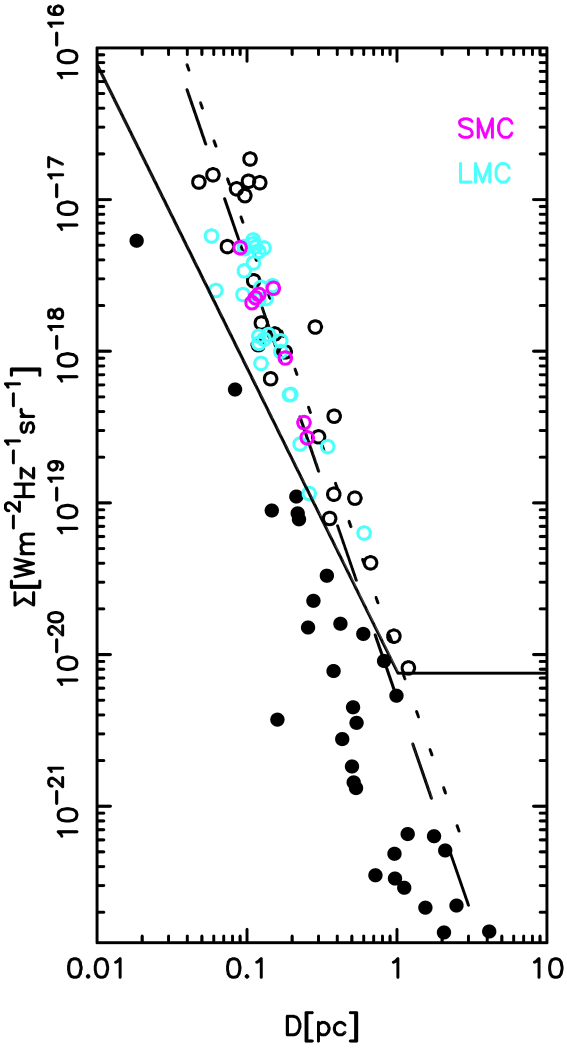

Figure 5.9: Surface Brightness-Diameter Comparison of Measured to Simulated Sample. An example of an artificial sample generated from the combined sample orthogonal offsets for the simulated β of 3.5 and a *Scatter* of 2.0. After selection the slope flattens to 2.8 (short-dashed line fitting). The solid line is the sensitivity line with the horizontal part at $\Sigma = 7.54 \times 10^{-21}\mathrm{W\,m^{-2}Hz^{-1}sr^{-1}}$ with the break point at $D = 1.017$ pc. The long-dashed line is the orthogonal offset best fitting to the combined MC planetary nebula sample. Data points in black are the simulated sample with the points below the sensitivity line plotted as filled circles.

Table 5.6: Simulated Samples for the Planetary Nebula Detection Sensitivity Analysis. Parameters of the simulated samples and results of the sensitivity simulations for the LMC sample and the combined sample. Cols. 1-2 are the parameters from Equation 5.4 of the simulated (Σ–D) evolution lines. While Cols. 3-7 present the results for the LMC sample, Cols. 8-12 in the same way present the results for the combined sample. In Cols. 3 and 5 are the mean values of (Σ–D) parameters calculated from the orthogonal offset fits after the selection has been applied and their estimated uncertainties are in Cols. 4 and 6, respectively. Col. 7 gives the difference between the mean slope after selection and the simulated slope. For all simulated slopes, a fitting to 100 artificially generated samples was used.

Simulated		LMC sample After selection					Combined sample After selection				
$\log A$	β	$< \log A >$	$\sigma_{<\log A>}$	$< \beta >$	$\sigma_{<\beta>}$	$\Delta\beta$	$< \log A >$	$\sigma_{<\log A>}$	$< \beta >$	$\sigma_{<\beta>}$	$\Delta\beta$
(1)	(2)	(3)	(4)	(5)	(6)	(7)	(8)	(9)	(10)	(11)	(12)
$Scatter$ = 1.0											
-18.62	1.50	-18.63	0.049	1.49	0.080	0.01	-18.56	0.035	1.48	0.054	0.02
-18.74	1.60	-18.75	0.054	1.59	0.083	0.01	-18.70	0.033	1.59	0.053	0.01
-18.87	1.70	-18.87	0.053	1.68	0.077	0.02	-18.82	0.037	1.69	0.060	0.01
-18.99	1.80	-19.00	0.057	1.79	0.093	0.01	-18.94	0.040	1.79	0.065	0.01
-19.11	1.90	-19.12	0.054	1.90	0.089	0.00	-19.07	0.045	1.89	0.062	0.01
-19.24	2.00	-19.24	0.070	2.00	0.112	0.00	-19.19	0.048	1.98	0.069	0.02
-19.36	2.10	-19.36	0.057	2.09	0.098	0.01	-19.31	0.049	2.09	0.075	0.01
-19.48	2.20	-19.48	0.064	2.20	0.107	-0.00	-19.44	0.048	2.19	0.071	0.01
-19.61	2.30	-19.59	0.061	2.26	0.098	0.04	-19.55	0.051	2.27	0.076	0.03
-19.73	2.40	-19.68	0.065	2.35	0.116	0.05	-19.66	0.049	2.36	0.084	0.04
-19.86	2.50	-19.78	0.078	2.40	0.120	0.10	-19.76	0.064	2.44	0.099	0.06
-19.98	2.60	-19.86	0.077	2.46	0.120	0.14	-19.85	0.063	2.50	0.102	0.10
-20.10	2.70	-19.94	0.097	2.53	0.159	0.17	-19.93	0.066	2.56	0.107	0.14
-20.23	2.80	-20.00	0.102	2.53	0.152	0.27	-20.01	0.075	2.61	0.110	0.19
-20.35	2.90	-20.07	0.136	2.61	0.167	0.29	-20.09	0.089	2.68	0.127	0.22
-20.47	3.00	-20.17	0.163	2.71	0.227	0.29	-20.16	0.099	2.72	0.132	0.28
-20.60	3.10	-20.18	0.144	2.71	0.197	0.39	-20.22	0.137	2.78	0.176	0.32
-20.72	3.20	-20.27	0.183	2.77	0.244	0.43	-20.28	0.128	2.81	0.168	0.39
-20.85	3.30	-20.32	0.262	2.79	0.323	0.51	-20.39	0.183	2.91	0.219	0.39
-20.97	3.40	-20.37	0.224	2.84	0.277	0.56	-20.45	0.169	2.96	0.209	0.44
-21.09	3.50	-20.46	0.433	2.92	0.444	0.58	-20.58	0.294	3.05	0.338	0.45
-21.22	3.60	-20.55	0.392	3.00	0.413	0.60	-20.61	0.281	3.08	0.308	0.52
$Scatter$ = 2.0											
-18.62	1.50	-18.62	0.091	1.50	0.144	-0.00	-18.56	0.069	1.48	0.115	0.02
-18.74	1.60	-18.73	0.099	1.59	0.145	0.01	-18.70	0.074	1.60	0.123	0.00
-18.87	1.70	-18.87	0.107	1.71	0.182	-0.01	-18.80	0.077	1.68	0.115	0.02
-18.99	1.80	-18.96	0.095	1.80	0.153	-0.00	-18.92	0.065	1.77	0.105	0.03
-19.11	1.90	-19.09	0.101	1.90	0.165	0.00	-19.05	0.082	1.88	0.131	0.02
-19.24	2.00	-19.17	0.099	1.97	0.146	0.03	-19.17	0.083	1.99	0.125	0.01
-19.36	2.10	-19.29	0.100	2.09	0.151	0.01	-19.27	0.075	2.08	0.136	0.02
-19.48	2.20	-19.34	0.116	2.10	0.198	0.10	-19.36	0.084	2.14	0.141	0.06
-19.61	2.30	-19.42	0.111	2.17	0.173	0.13	-19.43	0.073	2.18	0.122	0.12
-19.73	2.40	-19.48	0.137	2.20	0.215	0.20	-19.52	0.078	2.26	0.129	0.14
-19.86	2.50	-19.56	0.129	2.29	0.212	0.21	-19.59	0.101	2.33	0.174	0.17
-19.98	2.60	-19.62	0.140	2.30	0.223	0.30	-19.66	0.106	2.36	0.182	0.24
-20.10	2.70	-19.68	0.145	2.37	0.225	0.33	-19.72	0.110	2.42	0.184	0.28
-20.23	2.80	-19.74	0.166	2.44	0.237	0.36	-19.80	0.129	2.48	0.196	0.32
-20.35	2.90	-19.77	0.156	2.46	0.259	0.44	-19.84	0.142	2.50	0.210	0.40
-20.47	3.00	-19.79	0.184	2.45	0.321	0.55	-19.88	0.169	2.53	0.230	0.47
-20.60	3.10	-19.85	0.198	2.48	0.278	0.62	-19.95	0.141	2.60	0.193	0.50
-20.72	3.20	-19.90	0.216	2.54	0.311	0.66	-19.97	0.180	2.58	0.252	0.62
-20.85	3.30	-19.95	0.227	2.59	0.329	0.71	-20.02	0.226	2.62	0.308	0.68
-20.97	3.40	-20.02	0.302	2.67	0.440	0.73	-20.01	0.212	2.62	0.260	0.78
-21.09	3.50	-20.09	0.397	2.72	0.541	0.78	-20.10	0.290	2.71	0.388	0.79
-21.22	3.60	-20.06	0.343	2.65	0.479	0.95	-20.18	0.290	2.79	0.346	0.81
$Scatter$ = 3.0											
-18.62	1.50	-18.54	0.127	1.49	0.233	0.01	-18.51	0.091	1.47	0.167	0.03
-18.74	1.60	-18.67	0.129	1.59	0.217	0.01	-18.66	0.119	1.60	0.187	-0.00
-18.87	1.70	-18.78	0.135	1.72	0.243	-0.02	-18.76	0.104	1.70	0.173	-0.00
-18.99	1.80	-18.86	0.149	1.78	0.254	0.02	-18.88	0.105	1.81	0.182	-0.01
-19.11	1.90	-18.98	0.137	1.92	0.233	-0.02	-18.96	0.119	1.87	0.209	0.03
-19.24	2.00	-19.07	0.128	1.99	0.206	0.01	-19.06	0.105	1.97	0.169	0.03
-19.36	2.10	-19.14	0.158	2.01	0.298	0.09	-19.18	0.122	2.10	0.176	-0.00
-19.48	2.20	-19.18	0.130	2.07	0.191	0.13	-19.25	0.102	2.14	0.170	0.06
-19.61	2.30	-19.22	0.137	2.08	0.230	0.22	-19.31	0.116	2.19	0.208	0.11
-19.73	2.40	-19.30	0.153	2.21	0.287	0.19	-19.36	0.128	2.25	0.199	0.15
-19.86	2.50	-19.35	0.165	2.25	0.280	0.25	-19.43	0.130	2.24	0.214	0.26
-19.98	2.60	-19.37	0.159	2.26	0.338	0.34	-19.47	0.131	2.28	0.249	0.32
-20.10	2.70	-19.44	0.198	2.35	0.378	0.35	-19.53	0.132	2.35	0.210	0.35
-20.23	2.80	-19.51	0.190	2.35	0.357	0.45	-19.56	0.145	2.36	0.234	0.44
-20.35	2.90	-19.55	0.221	2.44	0.394	0.46	-19.58	0.156	2.37	0.246	0.53
-20.47	3.00	-19.57	0.266	2.41	0.448	0.59	-19.66	0.184	2.47	0.273	0.53
-20.60	3.10	-19.57	0.251	2.40	0.438	0.70	-19.70	0.166	2.49	0.286	0.61
-20.72	3.20	-19.69	0.266	2.58	0.438	0.62	-19.72	0.204	2.51	0.317	0.69
-20.85	3.30	-19.66	0.244	2.46	0.433	0.84	-19.78	0.283	2.58	0.410	0.72
-20.97	3.40	-19.71	0.310	2.60	0.529	0.80	-19.78	0.203	2.52	0.328	0.88
-21.09	3.50	-19.73	0.275	2.59	0.499	0.91	-19.83	0.250	2.58	0.382	0.92
-21.22	3.60	-19.76	0.313	2.60	0.493	1.00	-19.87	0.326	2.63	0.504	0.97

nebulae at established RP catalogue coordinates. Twenty-eight sources were found with detectable RC emissions in at least one of these RC bands with a flux density $\geq 3\sigma$ above the noise. Of these twenty-eight planetary nebulae, twenty-one were new RC detections reported here for the first time.

This RC detection count was only ∼5% of the known population of planetary nebulae in the LMC. The likely reasons for this very small detection ratio were the relatively low flux densities from the planetary nebulae at the distance to the LMC and the lack of complete (and uniform) area coverage of the LMC with high sensitivity observations.

These measurements along with data from the literature were used to calculate additional RC properties of the detected planetary nebulae. The MIR/20 cm flux density ratios were calculated resulting in a median value of 11.9 compared to the Cohen et al. (2007a) value for the Galactic bulge of 12. Further calculations revealed essentially no self–absorption effect for the 6 cm measurements. In addition, the adopted 6 cm flux densities and diameters compared very well with the Galactic bulge distance-scaled planetary nebula data set from Siódmiak and Tylenda (2001).

The combined sample of thirty-seven RC planetary nebulae (from the LMC and the SMC (Leverenz et al., 2016)) was used with available reliable data to examine the 6 cm radio (Σ–D) relation. Two sample sets were analyzed: the LMC sample and the combined LMC+SMC sample. The reconstruction of the PDF showed that the rather complex planetary nebula evolutionary paths were not likely to be well represented by a single linear best fitting line but that more complex statistical tools should be used. The rather incomplete SMC sample well complemented the more numerous LMC sample. Selected (Σ–D) data with both Σ offsets and orthogonal offsets were fitted to obtain the fitting parameters. The value of β in the (Σ–D) relation is theoretically expected to change from ∼1 to 3 over the lifetime of a planetary nebula (Urošević et al., 2009). For the combined sample, the orthogonal offsets, $\beta = 2.9 \pm 0.4$, and the Σ offsets, $\beta = 2.3 \pm 0.3$, were obtained. Both values were comparable to the previously obtained values for Galactic planetary nebula samples.

The RC MC data were very close to the measurement sensitivity limit which weakened its quality and Σ was only detected in the high range of values expected from measurements taken of Galactic planetary nebulae. Sensitivity selection effects were examined by simulating an artificial random sample with values of β from 1.5 to 3.6 and values of D extending over a range from the minimum observed diameter in the sample to 2 pc. A strong selection effect was seen in MC data. The results of the Monte Carlo sensitivity simulation suggested that selection effects were significant for values larger than $\beta \sim 2.6$. It was noted that a measured slope of $\beta = 2.9$ should correspond to a sensitivity free value of ~ 3.4. By creating an artificial

sample from the combined sample, it was shown that a large portion of the data in the artificial sample could not be detected with the sensitivity available for the measurements of the RC in the MCs.

For the LMC and combined LMC+SMC samples, the PDF statistical distance calibration was performed. Then the average fractional error was calculated for the statistical distance measurement. For the mean, mode, and median PDF estimators the average fractional distance error was $\sim 16\%$ for the combined sample and $\sim 18\%$ for the LMC sample alone. At the LMC distance ($\sim$ 50 kpc) this $\sim 18\%$ translated to $\sim$ 9 kpc average distance error which was still significantly larger than the 1 kpc LMC depth.

This study demonstrated the potential for using extended RC MC planetary nebula samples as statistical distance estimators. Still, much can be improved, including the understanding of observational biases, especially sensitivity selection effects. Next generation multi-frequency RC surveys with greater sensitivity and accuracy should lead to improved planetary nebula classification and to a better understanding of PDF evolutionary features.

Chapter 6

Summary and Observations

This thesis has investigated the ISM of the SMC and produced new planetary nebula RC detections in both the SMC and the LMC. The ISM of the SMC was examined for correlations among the FIR, RC, and other available wavelengths. The ubiquity of the value of the FIR/RC ratio for virtually all measured galaxies was confirmed over the entire SMC and in the five regions of the SMC. The sizes of these regions ranged from $\sim$ 3 kpc to $\sim$ 0.4 kpc with pixel correlations down to 15 pc. There were also ten new planetary nebula radio detections in the SMC reported in this thesis with six previously detected radio planetary nebulae remeasured. In the LMC, twenty-one new radio detections of planetary nebulae were made. Ten previously detected planetary nebulae were also examined with seven of those remeasured and verified in the LMC.

Measurements of radio planetary nebulae can inform theories of the ISM and provide data for a potentially powerful distance estimator using the (Σ–D) relation. With a total of thirty-one radio planetary nebulae available as statistical distance calibrators, the (Σ–D) relation was used to calculate a PDF with the latest techniques and produced a calibration with a statistical error of 16–17%.

The following observations were made in this investigation:

1. FIR/RC ratio studies of the SMC were conducted at several wavelengths. The 20 cm emission line of H I and optical emission lines for Hα and CO were also used. Maps of the SMC at 3, 6, 13, 21 cm, and H I emission were created from ATCA+Parkes radio telescope archival data. IRAS data at 60 μm and 100 μm and Spitzer 70 μm and 160 μm data were employed to examine dust content at different temperatures. Spitzer 160 μm data were used as the template for the five regions defined. The Hα image was used to map H II density and the CO image used to estimate H_2 density. All of the images used for the FIR/RC correlation studies here were re-gridded to 5″ corresponding to 15 pc, and

aligned to ICRS (J2000) on a pixel by pixel basis. The resulting images were smoothed with a 25″ Gaussian kernel. Additionally, data at the locations of 717 RC background sources were masked by applying a Gaussian kernel with a FWHM of 2′ to each image at the positions of the background sources. (See Figure 3.)

2. The FIR/RC ratio was analyzed and plotted for each defined SMC region. A published result for the FIR/RC ratio from the LMC was also plotted for comparison. The best fitting data results were compared to published values from a collection of 1750 galaxies with excellent correspondence seen. (See Figure 3.2 and Table 3.6.) Correlations between the data sets at the pixel level within each region are shown in Figure 3.3.

3. A q value plot (the log of FIR/RC ratio) of the data was calculated. This plot was used to reveal the activity and content of the regions. (See Figure 3.4.) The q coefficient for the SMC was shown to be slightly higher than the q value for normal spiral galaxies suggesting an excess of FIR emission.[1]

4. A much higher thermal fraction was seen in the SMC than in normal galaxies by a factor of between 5 and 10.[2] This suggested that the thermal emission alone was adequate to provide the RC flux necessary to meet the FIR/RC ratio in normal galaxies. This implied that a lower cosmic ray electron density or a lower magnetic field intensity compared to ordinary spiral galaxies was present. The morphology of the SMC, in particular the small size of the regions, was posited to be another reason why some regions may not be able to contain cosmic ray electrons, allowing them to leak out of the region before cooling. Tentative conclusions were presented considering the nature of each region and the characteristics of the data sets. (See Section 3.11.)

5. Wavelet cross correlation was performed on RC data sets paired with other data sets to extract morphological correlations between the different constituents of the SMC in the range of 9 to 238 pc. (See Figures 3.5 and 3.6.) This calculation revealed correlations at different spatial scale lengths in two dimensions and generally peaked at the larger scale factors between 60 to 238 pc.

6. Various FIR/RC models were compared to the SMC results and pointed to the conclusion that cosmic ray electrons do not provide the energy for the RC emission. (See Section 3.10.) The slope of the FIR/RC fitting was compared to the estimated thermal fractions for each region. Region 3 had the highest values of several parameters correlating 21 cm radiation

[1] Measured here, q(SMC)=2.65 and for 1750 measured galaxies q(average)=2.34 (Yun et al., 2001).

[2] The 5GHz thermal ratio presented in this thesis for the entire SMC is 0.43 and the average value of the five regions, which arguably comprise the "actual" SMC, is 0.78. This is consistent with Israel et al. (2010) who measured a thermal fraction of 0.71 in their work on the SMC.

with H I and dust concentration. The q value for the SMC, 2.65, was shown to be within $\sim 10\%$ of the average value from the original FIR/RC study of 1750 galaxies for which 98% had q values between 1.64 and 3.04 (Yun et al., 2001).

7. The SMC was examined for detectable radio emissions from planetary nebulae. The known distance to the SMC and its relative proximity to the Galaxy were key considerations for its selection. Ten new radio detected planetary nebulae were identified in the SMC. Six radio planetary nebulae previously detected were also remeasured. A total of six from this combined catalogue of sixteen, however, were shown to have characteristics suggesting that they were more likely planetary nebulae mimics.

8. Maps of the SMC at 3, 6, 13, and 20 cm as well as targeted radio observations were created from ATCA archives. (See Table 4.1.) New technology provided higher sensitivity and resolution for radio detection than previously available. SIMBAD online database classifications were used to provide an initial set of coordinates for SMC planetary nebulae. The presence of planetary nebula mimics in established catalogues required a careful examination of all available data for these planetary nebula detections. Hα images were used with IRAC 8.0, 5.8, and 4.5 μm data to detect planetary nebula mimics. Further mimic elimination was conducted by considering the calculated thermal brightness and the related self–absorption at the detection frequencies along with an examination of the literature for previous observations of these objects.

9. Targeted observations were much more successful at detecting the SMC radio planetary nebulae than using the general survey maps. Six out of ten detections at 3 and 6 cm came from targeted observations.

10. Finding charts were created for all of the radio detections of the SMC planetary nebulae. (See Figures 4.4 and 4.5.) Additional results from the data obtained were calculated including the planetary nebula electron density, ionised mass, and brightness temperature with an analysis of possible self–absorption effects. (See Tables 4.2 and 4.3.)

11. The data from the radio detected SMC planetary nebulae were used to calculate the (Σ–D) relation power law parameters. (See Figure 4.8.) The new detections were only possible with the new technology available at the time of the present work. The power law indices for these planetary nebulae were comparable to those calculated for the Galaxy and to previous work on the SMC. The expected flattening of the power law index calculated from the measured sample due to selection effects was discussed.

12. The LMC was examined for detectable RC emissions from planetary nebulae. The ATCA

archive was searched for RC projects (with a 6 km antenna configuration to provide the best possible resolution) which contained any coordinates from a list of 629 confirmed planetary nebulae in the LMC. The raw data for all matching projects were downloaded and processed in order to check for detectable emissions at the planetary nebula coordinates. In addition to one project done specifically to detect planetary nebulae in the MCs, seventeen projects downloaded had data at coordinates of interest. A total of sixty-one images were extracted from the downloaded projects that did not contain detectable radio planetary nebulae. (See Tables 5.1 and 5.2.)

13. Thirty-one new radio detections of LMC planetary nebulae were catalogued using new RC observations and data from the ATCA archives. Finder charts were created for the planetary nebula detections. (See Figures 5.1 - 5.5.) Additional results from the measured data were calculated including the planetary nebula electron density, ionised mass, and brightness temperature with an analysis of possible self–absorption effects. All known radio planetary nebulae in the LMC were catalogued in Table 5.3.

14. A (Σ–D) relation analysis was performed with the new set of twenty-eight LMC planetary nebulae and the SMC sample of nine planetary nebulae. The combined sample composed of the SMC and LMC planetary nebulae consisted of thirty-seven planetary nebulae. (See Section 5.7.)

15. Statistical distance calibrations were performed with each sample: the SMC sample, the LMC sample, and the LMC+SMC sample. Since only the brightest half of the known log range of planetary nebula brightness values were seen in the MC samples, it was obvious that a strong selection effect was in play. A Monte Carlo simulation was created using bootstrap statistics for each sample and the resulting resampled samples were used to calculate the fitting parameters of the (Σ–D) power law model for the LMC+SMC sample and for the LMC sample. (See Section 5.9.)

16. The first statistical distance calibration method used conventional vertical value fitting with Σ offsets minimized. The distance error calculation for the LMC+SMC sample was 20.17%. For the LMC sample, it was 22.97%. (See Table 5.5.)

17. The second statistical distance calibration method used orthogonal fitting which showed a significant improvement in the distance calculation error when going from Σ offset to orthogonal offset fitting. The result was a LMC+SMC distance error of 17.00%. For the LMC sample, it was 19.58%. (See Table 5.5.)

18. The third statistical distance calibration method used a PDF function calculated from

the bootstrap resampled sample which provided a continuous function from which the highest probability value of D could be extracted for a given Σ value. This provided an even better distance calibration error of 16.05% for the LMC+SMC sample and 18.29% for the LMC sample. (See Table 5.5.) This error was comparable to a study by Frew et al. (2016b) which used the ($S_{H\alpha}$ -r) relation and reported a distance measurement error of 18% with a calibration sample of 1100 planetary nebulae.

19. An examination of the plots of the PDF surface and the (Σ–D) contours of the samples showed that the best fitting value did not appear to coincide with the contour plots. Sensitivity selection effects were investigated which led to a change in the most likely slope of the (Σ–D) relation that properly represented the unbiased sample. The slope parameter calculated changed from the original measured $\beta = 2.9 \pm 0.4$ to a sensitivity free value of $\beta \sim 3.4$ using the simulated sample. (See Figures 5.7 and 5.9.)

Chapter 7

Future Work

A key issue in the understanding of galaxy formation and evolution is how galaxies obtain the gas they need to form stars (Leitner and Kravtsov, 2011). The mechanism for replenishment after initial star formation has been a puzzle. Gas clouds near galaxies can provide some of the material but gas accretion rates from gas clouds appear to be too low to sustain the star formation rates observed. There is a considerable amount of hot gas surrounding many galaxies but this gas must be cooled before it can contribute to star formation. An important source of material for star formation is suspected to be the gas and dust shed by AGB stars as they become planetary nebulae. Fontaine et al. (2001) suggested that $\sim 10-90\%$ of the initial mass of $\sim 1-10\,M_{\odot}$ main sequence stars is returned to the ISM through AGB winds. AGB winds are ideal sources of mass for star formation because the mass is injected directly into the ISM which is relatively dense and cool (Leitner and Kravtsov, 2011, and references therein). Investigating planetary nebulae and their distribution in galaxies is crucial to understanding their role in star formation.

At least three major problems need to be solved before planetary nebula distributions in galaxies can be determined. The first is simply the detection of planetary nebulae at distances beyond which obscuring dust, as in the Galactic disk, prevents optical means of discovery. The second is validating the identity of each such object as a planetary nebula. The third is determining the distances to the planetary nebulae.

Optical wavelength exploration has been the standard approach for planetary nebula studies since planetary nebulae were discovered. Now, with the dawn of true multi–wavelength astronomy, longer wavelengths are becoming available to discover and study planetary nebulae. This region of the electromagnetic spectrum is very desirable for research since it is much less susceptible to extinction from intervening gas and dust than are optical wavelengths.

New IR methods of detection are now being explored. For example, Froebrich et al. (2011)

described a survey of the northern Galactic plane in which they explored the H_2 molecular line 1-0 S(1) at 2.122 μm for which post-AGB stars and planetary nebulae are bright emitters. This emission line was also used by Gledhill et al. (2018) in another survey of the northern Galactic plane which was devised to detect planetary nebula candidates. Gledhill used MIR colour-colour diagnostics to validate 183 new detections from 291 planetary nebula candidates. Many of these were not visible in Hα surveys of the same area of the sky.

Another example of experimental detection is the use of H I recombination lines which are in the IR from 55 to 680 μm (Aleman et al., 2018). They focused on planetary nebula Mz 3, which was expected to provide particularly strong measurements because of the predicted laser amplification of these lines. This may not prove to be a good method to discover or validate planetary nebulae but it is an interesting new approach which could stimulate the development of other techniques in the future.

In this thesis, RC wavelengths, which have minimal extinction through gas and dust, were used to detect planetary nebulae in the MCs. This resulted in thirty-one new RC planetary nebula detections. There is, however, no known method of validating planetary nebula identity using only RC data. Thus, catalogues based on optical identification of planetary nebulae were used as the starting point for this RC detection study.

Since the unambiguous identification of planetary nebulae has, in general, only been possible using optical spectroscopic studies, there is the question: Can planetary nebula candidates be validated using only IR measurements? Cohen et al. (2011) suggested that IR colour-colour graphs could provide that discrimination and further suggested specific IR to RC ratios that could be used to validate the identification of planetary nebulae. There is not enough data, however, to more than tentatively support this. Parker et al. (2012) used MIR wavelengths to find four new Galactic planetary nebulae in the MIR data from the GLIMPSE (Galactic Legacy Infrared Mid-Plane Survey Extraordinaire) archive. For this study, six colour-colour criteria were determined from 136 known planetary nebulae in the GLIMPSE-I archive. Then 49 million archived GLIMPSE-I measurements were compared to these six colour-colour criteria, from which seventy planetary nebula candidates were selected. The search found only 80% of the known planetary nebulae in the GLIMPSE-I archive. Surprisingly, it did not find many of the planetary nebulae from which the selection criteria were calculated. This was attributed to the fact that most Galactic planetary nebulae are extended objects and do not appear in the GLIMPSE-I point-source archive. Additionally, not all of the planetary nebulae observed had good photometric measurements by which they could be separated from their local background. Nonetheless, four new planetary nebula candidates were extracted from the archive. It is possible that additional refinement could make this an important technique for discovery.

With detection and validation, planetary nebula distance determination is still necessary to provide crucial position data for the planetary nebulae within a galaxy. The distance issue is particularly a problem for obscured planetary nebulae which cannot be detected optically through the dust, but remains difficult even for non-obscured planetary nebulae.

Distance measurements to planetary nebulae were explored in this thesis using RC flux density and diameter measurements. Since the distances to the MCs are known, the planetary nebulae in the MCs were a good choice for this study. The method undertaken involved the creation of a statistical distance relation based on a (Σ–D) distance calibration. Specifically, 5 GHz RC flux densities for the planetary nebulae were measured or calculated from available measurements at other RC frequencies. Diameters from HST [O III] images of those planetary nebulae were then used to create a (Σ–D) sample. Bootstrap resampling was applied to model the entire range of the sample including the missing low flux density measurements. This created a more complete (Σ–D) sample which removed the sensitivity bias and provided a very good distance calibration from flux density measurements at 5 GHz. The (Σ–D) statistical distance calibration requires only the RC flux density, a consistent diameter measurement, and known distances to the calibrating sample.

The (Σ–D) approach appears to show great promise in solving the problem of accurately measuring distances to planetary nebulae. Among remaining questions are: What is the best frequency to use for the (Σ–D) distance calibration? Is it 5 GHz? Which wavelength can best penetrate galactic dust to produce the most consistent diameter measurements? Is it in the NIR or MIR or FIR?

These are important questions that need to be explored, along with the basic problem of unambiguous planetary nebula identification without optical observations. This research will require a significant investment. The results, however, could supply the locations of a significant proportion of the missing $\sim 85\%$ of the expected planetary nebula population in the Galaxy.

References

Aaquist, O. B. and Kwok, S. (1991). High-resolution radio continuum observations of compact planetary nebulae. *The Astrophysical Journal*, 378:599.

Abbe, C. (1867). On the Distribution of the Nebulæ in Space. *Monthly Notices of the Royal Astronomical Society*, 27(7):257–257.

Adams, S. M., Kochanek, C. S., Beacom, J. F., Vagins, M. R., and Stanek, K. Z. (2013). Observing the Next Galactic Supernova. *The Astrophysical Journal*, 778(2):15.

Aleman, I., Exter, K., Ueta, T., Walton, S., Tielens, A. G. G. M., Zijlstra, A., Montez, R., Abraham, Z., Otsuka, M., Beaklini, P. P. B., van Hoof, P. A. M., Villaver, E., Leal-Ferreira, M. L., Mendoza, E., and Lépine, J. D. R. (2018). Herschel Planetary Nebula Survey (HerPlaNS). hydrogen recombination laser lines in Mz 3. *Monthly Notices of the Royal Astronomical Society*, 477:4499–4510.

Alfvén, H. (1942). Existence of Electromagnetic-Hydrodynamic Waves. *Nature*, 150(3805):405–406.

Alfvén, H. and Herlofson, N. (1950). Cosmic Radiation and Radio Stars. *Physical Review*, 78(5):616–616.

Ambarzumian, V. A. and Milne, E. A. (1932). The Radiative Equilibrium of a Planetary Nebula. *Monthly Notices of the Royal Astronomical Society*, 93(1):50–60.

Amnuel, P. R., Guseinov, O. H., Novruzova, H. I., and Rustamov, Y. S. (1984). Statistical survey of planetary nebulae: Distances, masses, and distribution in the galaxy. *Astrophysics and Space Science*, 107(1):19–50.

Arbutina, B., Urošević, D., Stanković, M., and Tešić, L. (2004). L - D dependence for supernova remnants and its connection with the Σ- D relation. *Monthly Notices of the Royal Astronomical Society*, 350(1):346–350.

Arp, H. C. (1958). Southern hamisphere photometry .5 The color-magnitude diagram of NGC361 and the adjoining field in the Small Magellanic Cloud. *The Astronomical Journal*, 63:487.

Balick, B. and Frank, A. (2002). Shapes and Shaping of Planetary Nebulae. *Annual Review of Astronomy and Astrophysics*, 40(1):439–486.

Barlow, M. J. (1987). The determination of the masses of Magellanic Cloud planetary nebulae using forbidden O II doublet ratio electron densities. *Monthly Notices of the Royal Astronomical Society*, 227:161–183.

Beck, R. (2000). Magnetic Fields in Normal Galaxies. *Philosophical Transactions: Mathematical, Physical and Engineering Sciences*, 358(1767):777–796.

Beck, R., Brandenburg, A., Moss, D., Shukurov, A., and Sokoloff, D. (1996). GALACTIC MAGNETISM: Recent Developments and Perspectives. *Annual Review of Astronomy and Astrophysics*, 34(1):155–206.

Bernard-Salas, J., Peeters, E., Sloan, G. C., Gutenkunst, S., Matsuura, M., Tielens, A. G. G. M., Zijlstra, A. A., and Houck, J. R. (2009). Unusual Dust Emission from Planetary Nebulae in the Magellanic Clouds. *The Astrophysical Journal*, 699(2):1541–1552.

Biajaoui, A., Slezak, E., and Mars, G. (1989). The Wavelet Transform A new tool for Signal, Image and Data Processing. *Bulletin d'Information du Centre de Donnees Stellaires*, 36:193.

Bica, E., Bonatto, C., Dutra, C. M., and Santos, J. F. C. (2008). A general catalogue of extended objects in the Magellanic System. *Monthly Notices of the Royal Astronomical Society*, 389(2):678–690.

Bica, E. and Dutra, C. M. (2000). Updating the Census of Star Clusters in the Small Magellanic Cloud. *The Astronomical Journal*, 119:1214–1224.

Bicay, M. D. and Helou, G. (1990). The 60 micron to 20 centimeter infrared-to-radio ratio within spiral galaxies. *The Astrophysical Journal*, 362:59–73.

Blackburn, J. K. (1995). FTOOLS: A FITS Data Processing and Analysis Software Package. In Shaw, R. A., Payne, H. E., and Hayes, J. J. E., editors, *Astronomical Data Analysis Software and Systems IV*, volume 77 of *Astronomical Society of the Pacific Conference Series*, page 367.

Bloecker, T. (1995). Stellar evolution of low- and intermediate-mass stars. II. Post-AGB evolution. *Astronomy and Astrophysics*, 299:755.

Boffi, F. R. and Stanghellini, L. (1994). Filling factors and ionized masses in planetary nebulae. *Astronomy and Astrophysics*, 284:248–258.

Bojicic, I. S., Filipovic, M. D., and Crawford, E. J. (2010). SMC SMP 24: A Newly Radio-Detected Planetary Nebula in the Small Magellanic Cloud. *Serbian Astronomical Journal*, 181:63–68.

Bolatto, A. D., Simon, J. D., Stanimirovic, S., van Loon, J. T., Shah, R. Y., Venn, K., Leroy, A. K., Sandstrom, K., Jackson, J. M., Israel, F. P., Li, A., Staveley-Smith, L., Bot, C., Boulanger, F., and Rubio, M. (2006). The Spitzer Survey of the Small Magellanic Cloud: S3MC Imaging and Photometry in the Mid- and Far-Infrared Wavebands. August 1, 2006 Accepted for publication in The Astrophysical Journal. Given the draconian figure file-size limits implemented in astro-ph, readers are encouraged to download the manuscript with full quality images from http://celestial.berkeley.edu/spitzer/publications/s3mcsurvey.pdf.

Bolatto, A. D., Simon, J. D., Stanimirović, S., van Loon, J. T., Shah, R. Y., Venn, K., Leroy, A. K., Sandstrom, K., Jackson, J. M., Israel, F. P., Li, A., Staveley-Smith, L., Bot, C., Boulanger, F., and Rubio, M. (2007). The Spitzer Survey of the Small Magellanic Cloud: S3MC Imaging and Photometry in the Mid- and Far-Infrared Wave Bands. *The Astrophysical Journal*, 655:212–232.

Bot, C., Ysard, N., Paradis, D., Bernard, J. P., Lagache, G., Israel, F. P., and Wall, W. F. (2010). Submillimeter to centimeter excess emission from the Magellanic Clouds. II. On the nature of the excess. *Astronomy and Astrophysics*, 523:20.

Boyer, M. L., Srinivasan, S., van Loon, J. T., McDonald, I., Meixner, M., Zaritsky, D., Gordon, K. D., Kemper, F., Babler, B., Block, M., Bracker, S., Engelbracht, C. W., Hora, J., Indebetouw, R., Meade, M., Misselt, K., Robitaille, T., Sewiło, M., Shiao, B., and Whitney, B. (2011). Surveying the Agents of Galaxy Evolution in the Tidally Stripped, Low Metallicity Small Magellanic Cloud (SAGE-SMC). II. Cool Evolved Stars. *The Astronomical Journal*, 142:103.

Bozzetto, L. M., Filipović, M. D., Vukotić, B., Pavlović, M. Z., Urosević, D., Kavanagh, P. J., Arbutina, B., Maggi, P., Sasaki, M., Haberl, F., Crawford, E. J., Roper, Q., Grieve, K., and Points, S. D. (2017). Statistical Analysis of Supernova Remnants in the Large Magellanic Cloud. *The Astrophysical Journal Supplement Series*, 230(1):30.

Burke, B. F. and Graham-Smith, F. (2002). *An introduction to radio astronomy*. Cambridge University Press, Cambridge [England] ; New York, 2nd edition. Bernard F. Burke and Francis Graham-Smith. ill. ; 26 cm.

Cane, H. V. (1979). Spectra of the non-thermal radio radiation from the galactic polar regions. *Monthly Notices of the Royal Astronomical Society*, 189:465–478.

Carlstrom, J. E. and Kronberg, P. P. (1991). H II regions in M82 - High-resolution Millimeter Continuum Observations. *The Astrophysical Journal*, 366:422–431.

Charmandaris, V., Heydari-Malayeri, M., and Chatzopoulos, E. (2008). Spitzer mid-infrared study of compact H II regions in the Magellanic Clouds. *Astronomy and Astrophysics*, 487(2):567–573.

Chiappini, C., Gorny, S., Stasinska, G., and Barbuy, B. (2009). Abundances in the Galactic bulge: results from planetary nebulae and giant stars. *Astronomy and Astrophysics*, 494(2):591–610.

Chyzy, K. T., Sridhar, S. S., and Jurusik, W. (2017). What drives galactic magnetism? *Astronomy and Astrophysics*, 603:9.

Ciardullo, R. (2012). The Planetary Nebula Luminosity Function at the Dawn of Gaia. *Astrophysics and Space Science*, 341(1):151–161.

Ciardullo, R., Bond, H. E., Sipior, M. S., Fullton, L. K., Zhang, C. Y., and Schaefer, K. G. (1999). A Hubble Space Telescope Survey for Resolved Companions of Planetary-Nebula Nuclei. *The Astronomical Journal, Volume 118, Issue 1, pp. 488-508.*, 118:488–508.

Ciardullo, R., Jacoby, G. H., and Ford, H. C. (1989). Planetary nebulae as standard candles. IV - A test in the Leo I group. *The Astrophysical Journal*, 344:715.

Cioni, M.-R., Clementini, G., Girardi, L., Guandalini, R., Gullieuszik, M., Miszalski, B., Moretti, M.-I., Ripepi, V., Rubele, S., Bagheri, G., Bekki, K., Cross, N., de Blok, W. J. G., de Grijs, R., Emerson, J. P., Evans, C. J., Gibson, B., Gonzales-Solares, E., Groenewegen, M. A. T., Irwin, M., Ivanov, V. D., Lewis, J., Marconi, M., Marquette, J.-B., Mastropietro, C., Moore, B., Napiwotzki, R., Naylor, T., Oliveira, J. M., Read, M., Sutorius, E., van Loon, J. T., Wilkinson, M. I., and Wood, P. R. (2011). The VMC survey. *Astronomy and Astrophysics*, 527:A116.

Cioni, M. R. L., Habing, H. J., and Israel, F. P. (2000). The morphology of the Magellanic Clouds revealed by stars of different age: results from the DENIS survey. *Astronomy and Astrophysics*, 358:L9–L12.

Cohen, M., Chapman, J. M., Deacon, R. M., Sault, R. J., Parker, Q. A., and Green, A. J. (2006). Radio observations of the planetary nebula around the OH/IR star OH 354.88-0.54 (V1018 Sco). *Monthly Notices of the Royal Astronomical Society*, 369(1):189–196.

Cohen, M. and Green, A. J. (2001). Extended Galactic emission at l=312o: a comparison of mid-infrared and radio continuum (843 MHz) images. *Monthly Notices of the Royal Astronomical Society*, 325(2):531–544.

Cohen, M., Green, A. J., Meade, M. R., Babler, B., Indebetouw, R., Whitney, B. A., Watson, C., Wolfire, M., Wolff, M. J., Mathis, J. S., and Churchwell, E. B. (2007a). Absolute diffuse calibration of IRAC through mid-infrared and radio study of H II regions. *Monthly Notices of the Royal Astronomical Society*, 374(3):979–998.

Cohen, M., Parker, Q. A., Green, A. J., Miszalski, B., Frew, D. J., and Murphy, T. (2011). Multi-wavelength diagnostic properties of Galactic Planetary Nebulae detected by GLIMPSE-I. *Monthly Notices of the Royal Astronomical Society*, 413(1):514–542.

Cohen, M., Parker, Q. A., Green, A. J., Murphy, T., Miszalski, B., Frew, D. J., Meade, M. R., Babler, B., Indebetouw, R., Whitney, B. A., Watson, C., Churchwell, E. B., and Watson, D. F. (2007b). Spitzer IRAC Observations of Newly Discovered Planetary Nebulae from the Macquarie-AAO-Strasbourg Hα Planetary Nebula Project. *The Astrophysical Journal*, 669(1):343–362.

Condon, J. J. (1992). Radio emission from normal galaxies. *Annual Review of Astronomy and Astrophysics*, 30:575–611.

Condon, J. J., Cotton, W. D., Greisen, E. W., Yin, Q. F., Perley, R. A., Taylor, G. B., and Broderick, J. J. (1998). The NRAO VLA Sky Survey. *The Astronomical Journal*, 115(5):1693–1716.

Condon, J. J. and Yin, Q. F. (1990). A new starburst model applied to the clumpy irregular galaxy markarian 325. *The Astrophysical Journal*, 357:97–104.

Crawford, E., Filipovic, M., De, H., Wong, G., Tothill, N., Draskovic, D., Collier, J., and Galvin, T. (2011a). New 6 and 3-cm radio-continuum maps of the Small Magellanic Cloud, Part I: The maps. *Serbian Astronomical Journal*, 183(183):95–102.

Crawford, E. J., Filipović, M. D., Bojičić, I. S., Cohen, M., Payne, J. L., De Horta, A. Y., and Reid, W. (2012). Radio planetary nebulae in the Magellanic Clouds. In *IAU Symposium*, volume 283, pages 334–335.

Crawford, E. J., Filipovic, M. D., de Horta, A. Y., Wong, G. F., Tothill, N. F. H., Draskovic, D., Collier, J. D., and Galvin, T. J. (2011b). New 6 and 3-cm Radio-Continuum Maps of the Small Magellanic Cloud. Part I - The Maps. *Serbian Astronomical Journal*, 183:95–102.

Daub, C. T. (1982). A statistical survey of local planetary nebulae. *The Astrophysical Journal*, 260:612.

de Freitas Pacheco, J. A., Costa, R. D. D., and Maciel, W. J. (1993). Abundances of non-type I planetary nebulae in the LMC. *Astronomy and Astrophysics*, 279:567–571.

De Marco, O. (2014). Asymmetric Planetary Nebulae VI: the conference summary. In *Asymmetrical Planetary Nebulae VI Conference*, page 122.

de Oliveira, M. R., Dutra, C. M., Bica, E., and Dottori, H. (2000). Morphologies and ages of star cluster pairs and multiplets in the Small Magellanic Cloud. *Astronomy and Astrophysics Supplement Series*, 146(1):57–72.

DeGennaro, S., von Hippel, T., Winget, D. E., Kepler, S. O., Nitta, A., Koester, D., and Althaus, L. (2008). White Dwarf Luminosity and Mass Functions from Sloan Digital Sky Survey Spectra. *The Astronomical Journal*, 135:1–9.

Dgani, R. and Soker, N. (1998). Nonthermal Radio Emission from Planetary Nebulae. *The Astrophysical Journal Letters*, 499:L83.

Dickel, J. R., Gruendl, R. A., McIntyre, V. J., and Amy, S. W. (2010). A 4.8 and 8.6 GHz Survey of the Small Magellanic Cloud: The Images. *The Astronomical Journal*, 140:1511–1518.

Dickey, J. M., Marx-Zimmer, M., Düsterberg, C., Meb, U., Stanimirovic, S., Staveley-Smith, L., and Kobulnicky, H. A. (1999). Interstellar Phases in the Magellanic Clouds. In *New Views of the Magellanic Clouds*, page 588. Published on behalf of the International Astronomical Union by Astronomical Society of the Pacific.

Dickey, J. M., Mebold, U., Stanimirovic, S., and Staveley-Smith, L. (2000). Cold Atomic Gas in the Small Magellanic Cloud. *The Astrophysical Journal*, 536:756–772.

Diehl, R., Halloin, H., Kretschmer, K., Lichti, G. G., Schönfelder, V., Strong, A. W., von Kienlin, A., Wang, W., Jean, P., Knödlseder, J., Roques, J.-P., Weidenspointner, G., Schanne, S., Hartmann, D. H., Winkler, C., and Wunderer, C. (2006). Radioactive 26Al from massive stars in the Galaxy. *Nature*, 439:45–47.

Downes, D., Wilson, T. L., Bieging, J., and Wink, J. (1980). H110-alpha and h2co survey of galactic radio sources. *Astronomy and Astrophysics Supplement Series*, 40:379–394.

Draine, B. T. (2011). *Physics of the Interstellar and Intergalactic Medium*.

Dreyer, J. L. E. (1888). A New General Catalogue of Nebulæ and Clusters of Stars, being the Catalogue of the late Sir John F. W. Herschel, Bart, revised, corrected, and enlarged. *Memoirs of the Royal Astronomical Society*, 49:1.

Dudziak, G., Péquignot, D., Zijlstra, A. A., and Walsh, J. R. (2000). A radio-continuum and photoionization-model study of the two planetary nebulae in the Sagittarius dwarf galaxy. *Astronomy and Astrophysics*, 363:717–732.

Dufour, R. J. and Killen, R. M. (1977). The chemical composition of three planetary nebulae in the Magellanic Clouds. *The Astrophysical Journal*, 211:68–76.

Dumas, G., Schinnerer, E., Tabatabaei, F. S., Beck, R., Velusamy, T., and Murphy, E. (2011). The local radio-IR correlation in M51. *The Astronomical Journal*, 141(2):19.

Dunlop, J. (1828). A Catalogue of Nebulae and Clusters of Stars in the Southern Hemisphere, Observed at Paramatta in New South Wales. *Philosophical Transactions of the Royal Society of London*, 118:113–151.

Efron, B. and Tibshirani, R. J. (1993). *An Introduction to the Bootstrap*. Chapman & Hall, New York, NY.

Emerson, J. and Sutherland, W. (2010). The Visible and Infrared Survey Telescope for Astronomy (VISTA): Looking Back at Commissioning. *The Messenger*, 139:2–5.

Feast, M. W., Thackeray, A. D., and Wesselink, A. J. (1960). The Brightest Stars in the Magellanic Clouds. *Monthly Notices of the Royal Astronomical Society*, 121(4):337–385.

Feigelson, E. D. and Babu, G. J. (2012). Statistical Methods for Astronomy. *Modern Statistical Methods for Astronomy*.

Filipovic, M. D., Bohlsen, T., Reid, W., Staveley-Smith, L., Jones, P. A., Nohejl, K., and Goldstein, G. (2002). An ATCA radio-continuum study of the Small Magellanic Cloud - I. Source catalogues at 1.42, 2.37, 4.80 and 8.64 GHz. *Monthly Notices of the Royal Astronomical Society*, 335:1085–1090.

Filipović, M. D., Cohen, M., Reid, W. A., Payne, J. L., Parker, Q. A., Crawford, E. J., Bojičić, I. S., de Horta, A. Y., Hughes, A., Dickel, J., and Stootman, F. (2009). Radio planetary nebulae in the Magellanic Clouds. *Monthly Notices of the Royal Astronomical Society*, 399:769–777.

Filipovic, M. D., Haynes, R. F., White, G. L., and Jones, P. A. (1998a). A radio continuum study of the Magellanic Clouds. VII. Discrete radio sources in the Magellanic Clouds. *Astronomy and Astrophysics Supplement Series*, 130:421–440.

Filipovic, M. D., Haynes, R. F., White, G. L., Jones, P. A., Klein, U., and Wielebinski, R. (1995). A radio continuum study of the Magellanic Clouds. IV. Catalogues of radio sources

in the Large Magellanic Cloud at 1.40, 2.45, 4.75, 4.85 and 8.55 GHz. *Astronomy and Astrophysics Supplement Series*, 111:311.

Filipovic, M. D., Jones, P. A., White, G. L., and Haynes, R. F. (1998b). A radio continuum study of the Magellanic Clouds. VIII. Discrete sources common to radio and infrared surveys of the Magellanic Clouds. *Astronomy and Astrophysics Supplement Series*, 130:441–448.

Filipovic, M. D., Jones, P. A., White, G. L., Haynes, R. F., Klein, U., and Wielebinski, R. (1997). A radio continuum study of the Magellanic Clouds V. Catalogues of radio sources in the Small Magellanic Cloud at 1.42, 2.45, 4.75, 4.85 and 8.55 GHz. *Astronomy and Astrophysics Supplement Series*, 121:321–326.

Filipovic, M. D., Payne, J. L., Reid, W., Danforth, C. W., Staveley-Smith, L., Jones, P. A., and White, G. L. (2005). An ATCA radio-continuum study of the Small Magellanic Cloud - III. Supernova remnants and their environments. *Monthly Notices of the Royal Astronomical Society*, 364:217–236.

Filipovic, M. D., Pietsch, W., Haynes, R. F., White, G. L., Jones, P. A., Wielebinski, R., Klein, U., Dennerl, K., Kahabka, P., and Lazendic, J. S. (1998c). A radio continuum study of the Magellanic Clouds. VI. Discrete sources common to radio and X-ray surveys of the Magellanic Clouds. *Astronomy and Astrophysics Supplement Series*, 127:119–138.

Filipovic, M. D., White, G. L., Jones, P. A., Haynes, R. F., Pietsch, W. N., Wielebinski, R., and Klein, U. (1996). The Magellanic Clouds: Overview of their History, Structure, Chemical Composition and Surveys. In Burkert, A., Hartmann, D. H., and Majewski, S. R., editors, *The History of the Milky Way and Its Satellite System*, volume 112, page 91. ASP Conference Series.

Fontaine, G., Brassard, P., and Bergeron, P. (2001). The Potential of White Dwarf Cosmochronology. *Publications of the Astronomical Society of the Pacific*, 113(782):409–435.

Frank, A. (1998). Bipolar Outflows and the Evolution of Stars. *New Astronomy Reviews*, 43(1):31–65.

Frank, A., Balick, B., Icke, V., and Mellema, G. (1993). Astrophysical gasdynamics confronts reality - The shaping of planetary nebulae. *The Astrophysical Journal*, 404:L25.

Frew, D. J. (2008). *Planetary Nebulae in the Solar Neighbourhood: Statistics, Distance Scale and Luminosity Function*. Doctor of philosophy, Macquarie University.

Frew, D. J., Bojičić, I. S., and Parker, Q. A. (2016a). The H α surface brightness radius plane as a diagnostic tool for photoionized nebulae. In *11th Pacific Rim Conference on Stellar*

Astrophysics, pages 2–5. 11th Pacific Rim Conference on Stellar Astrophysics: Physics and Chemistry of the Late Stages of Stellar Evolution.

Frew, D. J. and Parker, Q. A. (2010). Planetary Nebulae: Observational Properties, Mimics and Diagnostics. *Publications of the Astronomical Society of Australia*, 27(02):129–148.

Frew, D. J., Parker, Q. A., and Bojičić, I. S. (2016b). The H surface brightness-radius relation: a robust statistical distance indicator for planetary nebulae. *Monthly Notices of the Royal Astronomical Society*, 455(2):1459–1488.

Frick, P., Beck, R., Berkhuijsen, E. M., and Patrickeyev, I. (2001). Scaling and correlation analysis of galactic images. *Monthly Notices of the Royal Astronomical Society*, 327:1145–1157.

Froebrich, D., Davis, C. J., Ioannidis, G., Gledhill, T. M., Takami, M., Chrysostomou, A., Drew, J., Eislöffel, J., Gosling, A., Gredel, R., Hatchell, J., Hodapp, K. W., Kumar, M. S. N., Lucas, P. W., Matthews, H., Rawlings, M. G., Smith, M. D., Stecklum, B., Varricatt, W. P., Lee, H. T., Teixeira, P. S., Aspin, C., Khanzadyan, T., Karr, J., Kim, H.-J., Koo, B.-C., Lee, J. J., Lee, Y.-H., Magakian, T. Y., Movsessian, T. A., Nikogossian, E. H., Pyo, T. S., and Stanke, T. (2011). UWISH2 - the UKIRT Widefield Infrared Survey for H_2. *Monthly Notices of the Royal Astronomical Society*, 413:480–492.

Gascoigne, S. C. B. and Kron, G. E. (1953). Population Types and the Magellanic Clouds. *Publications of the Astronomical Society of the Pacific*, 65:32.

Gathier, R. (1987). Properties of planetary nebulae. I - Nebular parameters and distance scales. *Astronomy and Astrophysics, Supplement*, 71:245–253.

Gioia, I. M., Gregorini, L., and Klein, U. (1982). High frequency radio continuum observations of bright spiral galaxies. *Astronomy and Astrophysics*, 116:164–174.

Gledhill, T. M., Froebrich, D., Campbell-White, J., and Jones, A. M. (2018). Planetary Nebulae in the UWISH2 survey. *Monthly Notices of the Royal Astronomical Society, Advance Access*.

Gooch, R. (1996). Karma: a visualization test-bed. In Jacoby, G. H. and Barnes, J., editors, *Astronomical Data Analysis Software and Systems V*, volume 101 of *Astronomical Society of the Pacific Conference Series*, page 80.

Gordon, K. D., Meixner, M., Meade, M. R., Whitney, B., Engelbracht, C., Bot, C., Boyer, M. L., Lawton, B., Sewiło, M., Babler, B., Bernard, J.-P., Bracker, S., Block, M., Blum, R., Bolatto, A., Bonanos, A., Harris, J., Hora, J. L., Indebetouw, R., Misselt, K., Reach, W.,

Shiao, B., Tielens, X., Carlson, L., Churchwell, E., Clayton, G. C., Chen, C.-H. R., Cohen, M., Fukui, Y., Gorjian, V., Hony, S., Israel, F. P., Kawamura, A., Kemper, F., Leroy, A., Li, A., Madden, S., Marble, a. R., McDonald, I., Mizuno, A., Mizuno, N., Muller, E., Oliveira, J. M., Olsen, K., Onishi, T., Paladini, R., Paradis, D., Points, S., Robitaille, T., Rubin, D., Sandstrom, K., Sato, S., Shibai, H., Simon, J. D., Smith, L. J., Srinivasan, S., Vijh, U., Van Dyk, S., van Loon, J. T., and Zaritsky, D. (2011). Surveying the Agents of Galaxy Evolution in the Tidally Stripped, Low Metallicity Small Magellanic Cloud (Sage-Smc). I. Overview. *The Astronomical Journal*, 142(4):102.

Gould, B. A. (1889). On the comparison of the photographic, with the instrumental, determinations of star-places. *The Astronomical Journal*, 9:36.

Gruenwald, R. and Aleman, A. (2007). Radio-continuum spectrum, brightness temperature, and planetary nebulae properties. *Astronomy and Astrophysics*, 461(3):1019–1025.

Gurzadyan, G. A. (1997). *The Physics and Dynamics of Planetary Nebulae*. Springer.

Hajduk, M., Gadkowski, M., and Soszyski, I. (2014). Search for binary central stars of the SMC PNe. *Astronomy and Astrophysics*, 561:A8.

Hajian, A. R. (2006). Distances to Planetary Nebulae. *Proceedings of the International Astronomical Union*, 2(S234):41.

Harrington, J. P. and Borkowski, K. J. (1994). WFPC2 imaging of NGC 6543: closing in on bubbles, shocks, and precessing jets. *American Astronomical Society, 185th AAS Meeting, id.90.03; Bulletin of the American Astronomical Society, Vol. 26, p.1469*, 26:1469.

Harwit, M. and Pacini, F. (1975). Infrared galaxies - evolutionary stages of massive star formation. *The Astrophysical Journal*, 200:L127–L129.

Haslam, C. G. T. and Osborne, J. L. (1987). The infrared and radio-continuum emission of the galactic disk. *Nature*, 327:211–214.

Haynes, R. F., Klein, U., Wayte, S. R., Wielebinski, R., Murray, J. D., Bajaja, E., Meinert, D., Buczilowski, U. R., Harnett, J. I., Hunt, A. J., Wark, R., and Sciacca, L. (1991). A radio continuum study of the magellanic clouds. i - complete multi-frequency maps. *Astronomy and Astrophysics*, 252:475–486.

Helou, G. and Bicay, M. D. (1993). A physical model of the infrared-to-radio correlation in galaxies. *The Astrophysical Journal*, 415:93–100.

Helou, G., Khan, I. R., Malek, L., and Boehmer, L. (1988). Iras observations of galaxies in the virgo cluster area. *The Astrophysical Journal Supplement Series*, 68:151–172.

Henize, K. G. (1956). Catalogues of Hα-EMISSION Stars and Nebulae in the Magellanic Clouds. *The Astrophysical Journal Supplement Series*, 2:315.

Henize, K. G. and Westerlund, B. E. (1963). Dimensions of Diffuse and Planetary Nebulae in the Small Magellanic Cloud. *The Astrophysical Journal*, 137:747.

Henry, R. B. C., Speck, A., Karakas, A. I., Ferland, G. J., and Maguire, M. (2012). The curious conundrum regarding sulfur abundances in planetary nebulae. *The Astrophysical Journal*, 749(1):61.

Herbig, G. H. (1977). Summary of the Conference: Observations. In *Star Formation*, volume 75, page 283.

Herschel, J. F. (1864). A General Catalogue of Nebulae and Clusters of Stars. *Philosophical Transactions of the Royal Society of London*, 154:1–137.

Herwig, F. (2005). Evolution of Asymptotic Giant Branch Stars. *Annual Review of Astronomy and Astrophysics*, 43(1):435–479.

Higgs, L. A. (1971). A Survey of Microwave Radiation from Planetary Nebulae. *Monthly Notices of the Royal Astronomical Society*, 153(3):315–336.

Hilditch, R. W., Howarth, I. D., and Harries, T. J. (2005). Forty eclipsing binaries in the small magellanic cloud: fundamental parameters and cloud distance. *Monthly Notices of the Royal Astronomical Society*, 357:304–324.

Hodge, P. (1999). Magellanic Cloud Studies, Past and Future. In Chu, Y.-H., Suntzeff, N., Hesser, J., and Bohlender, D., editors, *New views of the Magellanic Clouds : proceedings of the 190th Symposium of the International Astronomical Union*, page 588. Published on behalf of the International Astronomical Union by Astronomical Society of the Pacific.

Hoernes, P., Berkhuijsen, E. M., and Xu, C. (1998). Radio-fir correlations within m 31. *Astronomy and Astrophysics*, 334:57–70.

Hoskin, M. (2014). William Herschel and The Planetary Nebulae. *Journal for the History of Astronomy*, 45(2):209–225.

Huggins, W. and Miller, A. W. (1864). On the Spectra of Some of the Nebulae. *Philosophical Transactions of the Royal Society of London*, 154:437–444.

Hughes, A., Wong, T., Ekers, R., Staveley-Smith, L., Filipovic, M., Maddison, S., Fukui, Y., and Mizuno, N. (2006). A multiresolution analysis of the radio-FIR correlation in the Large Magellanic Cloud. *Monthly Notices of the Royal Astronomical Society*, 370:363–379.

Hummel, E. (1981). The radio continuum properties of spiral galaxies. *Astronomy and Astrophysics*, 93:93–105.

Iben, I. and Renzini, A. (1983). Asymptotic Giant Branch Evolution and Beyond. *Annual Review of Astronomy and Astrophysics*, 21(1):271–342.

Iben, I. J. (1999). AGB Theory — A Retrospective. In Bertre, T. L., Lebre, A., and Waelkens., C., editors, *Asymptotic Giant Branch Stars IAU Symposium #191*.

Iben, I., J. (1995). Planetary nebulae and their central stars - origin and evolution. *Physics Reports*, 250(1-2):2–94.

Israel, F. P., Wall, W. F., Raban, D., Reach, W. T., Bot, C., Oonk, J. B. R., Ysard, N., and Bernard, J. P. (2010). Submillimeter to centimeter excess emission from the Magellanic Clouds. I. Global spectral energy distribution. *Astronomy and Astrophysics*, 519:67.

Jacoby, G. H. (1980). The luminosity function for planetary nebulae and the number of planetary nebulae in local group galaxies. *The Astrophysical Journal Supplement*, 42:1.

Jacoby, G. H. (1989). Planetary nebulae as standard candles. I - Evolutionary models. *The Astrophysical Journal*, 339:39.

Jacoby, G. H., Ciardullo, R., and Walker, A. R. (1990). Planetary nebulae as standard candles. VI - A test in the Magellanic Clouds. *The Astrophysical Journal*, 365:471.

Jacoby, G. H. and De Marco, O. (2002). A Survey for Very Faint Planetary Nebulae in the SMC. I. Identification, Confirmation, and Preliminary Analysis. *The Astronomical Journal*, 123:269–278.

Jolliffe, I. T. (2002). *Principal component analysis, Second Edition*. Springer-Verlag New York Berlin Heidelberg, New York Berlin Heidelberg, 2nd edition.

Joye, W. A., Mandel, E., Jedrzejewski, R. I., and Hook, R. N. (2003). New features of saoimage ds9.

Kahn, F. D. (1995). Closing Summary. In *Annals of the Israel Physical Society, Asymmetrical planetary nebulae*.

Karakas, A. (2007). Yields from single AGB stars. In *Asymmetrical Planetary Nebulae IV*, page 8, La Palma. http://www.iac.es/proyect/apn4, article #63.

Karakas, A. I. and Lattanzio, J. C. (2007). Stellar Models and Yields of Asymptotic Giant Branch Stars. *Publications of the Astronomical Society of Australia*, 24:103–117.

Kennicutt, R. C., J. (1983). The rate of star formation in normal disk galaxies. *The Astrophysical Journal*, 272:54–67.

Kennicutt, Robert C., J. and Pogge, R. W. (1990). Forbidden S III emission and extinction in extragalactic H II regions. *Astronomical Journal*, 99:61–70.

Kerr, F., Hindman, J., and Robinson, B. (1954). Observations of the 21 cm Line from the Magellanic Clouds. *Australian Journal of Physics*, 7(2):297.

Klein, U. and Emerson, D. T. (1981). A Survey of the Distributions of 2.8-CM Radio Continuum in Nearby Galaxies - Part One - Observations of 16 Spiral. *Astronomy and Astrophysics*, 94:29.

Klein, U. and Graeve, R. (1986). Multi-frequency radio continuum observations of dwarf irregular galaxies. *Astronomy and Astrophysics*, 161:155–168.

Klein, U., Graeve, R., and Wielebinski, R. (1983). A survey of the distribution of wavelength 2.8 CM radio continuum in nearby galaxies. III - A small sample of irregular and blue compact galaxies. *Astronomy and Astrophysics*, 117(2):332–342.

Klein, U., Grave, R., and Beck, R. (1984). Radio Continuum Emission from Magellanic-Type and Dwarf Irregular Galaxies. In *IAU Symp. 108: Structure and Evolution of the Magellanic Clouds*, volume 108, page 313.

Klein, U., Haynes, R. F., Wielebinski, R., and Meinert, D. (1993). A radio continuum study of the Magellanic Clouds III. The magnetic field in the Large Magellanic Cloud. *Astronomy and Astrophysics*, 271:402.

Klein, U., Wielebinski, R., and Morsi, H. W. (1988). Radio continuum observations of M82. *Astronomy and Astrophysics*, 190:41–46.

Klessen, R. S. (2011). Star Formation in Molecular Clouds. *EAS Publications Series*, 51:133–167.

Klessen, R. S. and Glover, S. C. O. (2016). Physical Processes in the Interstellar Medium. *ArXiv e-prints*, 43.

Kwitter, K. B., Mendez, R. H., Pena, M., Stanghellini, L., Corradi, R. L. M., De Marco, O., Fang, X., Henry, R. B. C., Karakas, A. I., Liu, X. W., Lopez, J. A., Manchado, A., and Parker, Q. A. (2014). The present and future of planetary nebula research. A white paper by the IAU planetary nebula working group. *Revista Mexicana de Astronomia y Astrofisica*, 50(2).

Kwok, S. (1982). From red giants to planetary nebulae. *The Astrophysical Journal*, 258:280.

Kwok, S. (1985). High-resolution radio observations of compact planetary nebulae. *The Astronomical Journal*, 90:49.

Kwok, S. (1994). Planetary nebulae: A modern view. *Publications of the Astronomical Society of the Pacific*, 106:344–355.

Kwok, S. (2000). *The Origin and Evolution of Planetary Nebulae*. Cambridge University Press, 2000, Cambridge ; New York.

Kwok, S. (2005). Planetary Nebulae: New Challenges in the 21st Century. *Journal of the Korean Astronomical Society*, 38:271–278.

Kwok, S. (2010). Morphological Structures of Planetary Nebulae. *PASA*, 27(02):174–179.

Kwok, S. (2012). Historical overview of planetary nebulae research. *Proceedings of the International Astronomical Union*, 7(S283):1–8.

Kwok, S., Purton, C. R., and Fitzgerald, P. M. (1978). On the origin of planetary nebulae. *The Astrophysical Journal*, 219:L125.

Leitner, S. N. and Kravtsov, A. V. (2011). Fuel Efficient Galaxies: Sustaining Star Formation with Stellar Mass Loss. *The Astrophysical Journal*, 734:48.

Lequeux, J. (2005). *The Interstellar Medium (Astronomy and Astrophysics Library)*. Springer.

Leroy, A., Bolatto, A., Stanimirovic, S., Mizuno, N., Israel, F., and Bot, C. (2007). The Spitzer Survey of the Small Magellanic Cloud: Far-Infrared Emission and Cold Gas in the Small Magellanic Cloud. *The Astrophysical Journal*, 658:1027–1046.

Leroy, A. K., Bolatto, A., Gordon, K., Sandstrom, K., Gratier, P., Rosolowsky, E., Engelbracht, C. W., Mizuno, N., Corbelli, E., Fukui, Y., and Kawamura, A. (2011). The CO-to-H2 Conversion Factor from Infrared Dust Emission across the Local Group. *The Astrophysical Journal*, 737:12.

Leverenz, H. and Filipović, M. D. (2013). An analysis of the FIR/RADIO continuum correlation in the small Magellanic cloud. *Astrophysics and Space Science*, 343(1):301–317.

Leverenz, H., Filipović, M. D., Bojičić, I. S., Crawford, E. J., Collier, J. D., Grieve, K., Drašković, D., and Reid, W. A. (2016). Radio planetary nebulae in the Small Magellanic Cloud. *Astrophysics and Space Science*, 361(3):108.

Leverenz, H., Filipovic, M. D., Vukotić, B., Urošević, D., and Grieve, K. (2017). Radio Planetary Nebulae in the Large Magellanic Cloud. *Monthly Notices of the Royal Astronomical Society*, 1811:1794–1811.

Li, A. and Draine, B. T. (2002). Infrared Emission from Interstellar Dust. III. The Small Magellanic Cloud. *The Astrophysical Journal*, 576:762–772.

Lindsay, E. M. (1961). A new catalogue of emission-line stars and planetary nebulae in the Small Magellanic Cloud. *The Astronomical Journal*, 66:169–185.

Lindsay, E. M. (1963). Second List of Emission-Line Objects in the Large Magellanic Cloud. *Irish Astronomical Journal*, 6:127.

Lindsay, E. M. and Mullan, D. J. (1963). First List of Emission Objects in the LMC. *Irish Astronomical Journal*, 6:51.

Loiseau, N., Klein, U., Greybe, A., Wielebinski, R., and Haynes, R. F. (1987). Thermal and nonthermal radio emission from the Small Magellanic Cloud. *Astronomy and Astrophysics*, 178:62–76.

Longair, M. S. (1992). *High energy astrophysics*. Cambridge University Press, Cambridge [England] ; New York, 2nd edition. M.S. Longair. ill. (some col.) ; 26 cm. v. 1. Particles, photons and their detection – v. 2. Stars, the galaxy and the interstellar medium.

Luck, R. E., Moffett, T. J., Barnes III, T. G., and Gieren, W. P. (1998). Magellanic Cloud Cepheids: Abundances. *The Astronomical Journal*, 115(2):605–634.

Maragoudaki, F., Kontizas, M., Morgan, D. H., Kontizas, E., Dapergolas, A., and Livanou, E. (2001). The recent structural evolution of the SMC. *Astronomy and Astrophysics*, 379:864–869.

Marigo, P. (2007). Can the third dredge-up extinguish hot-bottom burning in massive AGB stars? *Astronomy and Astrophysics*, 467(3):1139–1146.

Martin, N., Maurice, E., and Lequeux, J. (1989). The structure of the Small Magellanic Cloud. *Astronomy and Astrophysics*, 215:219–242.

Mathewson, D. S., Cleary, M. N., and Murray, J. D. (1974). The Magellanic stream. *The Astrophysical Journal,*, 190:291–296.

Mathewson, D. S., Ford, V. L., and Visvanathan, N. (1986). The structure of the Small Magellanic Cloud. *The Astrophysical Journal*, 301:664.

Matlab (2010). Matlab 7.10.0. The MathWorks Inc. https://www.mathworks.com/products/matlab.html.

McCall, M. L., Hill, R., and English, J. (1990). Small-scale star formation at low metallicity. *The Astronomical Journal*, 100:193–203.

McKee, C. F. (1995). The Multiphase Interstellar Medium. In A. Ferrara, McKee, C., Heiles, C., and Shapiro., P., editors, *The physics of the interstellar medium and intergalactic medium, ASP Conference Series, Volume 80.*, page 593, San Francisco,. Astronomical Society of the Pacific.

Meixner, M., Gordon, K. D., Indebetouw, R., Hora, J. L., Whitney, B., Blum, R., Reach, W., Bernard, J., Meade, M., Babler, B., Engelbracht, C. W., For, B., Misselt, K., Vijh, U., Leitherer, C., Cohen, M., Churchwell, E. B., Boulanger, F., Frogel, J. A., Fukui, Y., Gallagher, J., Gorjian, V., Harris, J., Kelly, D., Kawamura, A., Kim, S., Latter, W. B., Madden, S., MarkwickKemper, C., Mizuno, A., Mizuno, N., Mould, J., Nota, A., Oey, M., Olsen, K., Onishi, T., Paladini, R., Panagia, N., PerezGonzalez, P., Shibai, H., Sato, S., Smith, L., StaveleySmith, L., Tielens, A. G. G. M., Ueta, T., Dyk, S. V., Volk, K., Werner, M., and Zaritsky, D. (2006). Spitzer Survey of the Large Magellanic Cloud: Surveying the Agents of a Galaxy?s Evolution (SAGE). I. Overview and Initial Results. *AJ*, 132(6):2268–2288.

Menon, T. K. and Terzian, Y. (1965). Radio Observations of Planetary Nebulae. *The Astrophysical Journal*, 141:745.

Menzel, D. H. (1926). The Planetary Nebulae. *Publications of the Astronomical Society of the Pacific*, 38:295.

Messier, C. (1781). Catalogue des Nebuleuses & des amas d'Etoiles. *Connoissance des Temp.*

Meynadier, F. and Heydari-Malayeri, M. (2007). Low-excitation blobs in the Magellanic Clouds. *Astronomy and Astrophysics*, 461:565–569.

Milne, D. K. (1982). On the radio distance scale for planetary nebulae. *Monthly Notices of the Royal Astronomical Society*, 200(1):51P–54P.

Miville-Deschênes, M.-A. and Lagache, G. (2005). IRIS: A New Generation of IRAS Maps. *The Astrophysical Journal Supplement Series*, 157:302–323.

Mizuno, N., Rubio, M., Mizuno, A., Yamaguchi, R., Onishi, T., and Fukui, Y. (2001). First results of a co survey of the small magellanic cloud with nanten. *Publications of the Astronomical Society of Japan*, 53:L45–L49.

Moe, M. and De Marco, O. (2006). Do Most Planetary Nebulae Derive from Binaries? I. Population Synthesis Model of the Galactic Planetary Nebula Population Produced by Single Stars and Binaries. *The Astrophysical Journal*, 650(2):916–932.

Moe, M. and De Marco, O. (2012). Population synthesis of planetary nebulae from binaries. In *IAU Symposium*, volume 283 of *IAU Symposium*, pages 111–114.

Monk, D. J., Barlow, M. J., and Clegg, R. E. S. (1988). An optical spectrophotometric survey of abundances in Magellanic Cloud planetary nebulae. *Monthly Notices of the Royal Astronomical Society*, 234:583–624.

Morgan, D. H. (1994). The UKST Survey of planetary nebulae in the Large Magellanic Cloud. *Astronomy and Astrophysics Suppl. 103, 235-344 (1994)*, 103.

Morgan, D. H. and Good, A. R. (1992). New planetary nebulae in the Large Magellanic Cloud. *Astronomy and Astrophysics Supplement Series*, 92:571–582.

Murai, T. and Fujimoto, M. (1980). The magellanic stream and the galaxy with a massive halo. *Publications of the Astronomical Society of Japan*, 32:581.

Murphy, E. J. (2009). The Far-Infrared–Radio Correlation at High Redshifts: Physical Considerations and Prospects for the Square Kilometer Array. *The Astrophysical Journal*, 706(1):482–496.

Murphy, E. J., Helou, G., Kenney, J. D. P., Armus, L., and Braun, R. (2008). Connecting Far-Infrared and Radio Morphologies of Disk Galaxies: Cosmic-Ray Electron Diffusion After Star Formation Episodes. *The Astrophysical Journal*, 678(2):828–850.

Neugebauer, G., Habing, H. J., van Duinen, R., Aumann, H. H., Baud, B., Beichman, C. A., Beintema, D. A., Boggess, N., Clegg, P. E., de Jong, T., Emerson, J. P., Gautier, T. N., Gillett, F. C., Harris, S., Hauser, M. G., Houck, J. R., Jennings, R. E., Low, F. J., Marsden, P. L., Miley, G., Olnon, F. M., Pottasch, S. R., Raimond, E., Rowan-Robinson, M., Soifer, B. T., Walker, R. G., Wesselius, P. R., and Young, E. (1984). The Infrared Astronomical Satellite (IRAS) mission. *The Astrophysical Journal*, 278:L1.

Niklas, S. and Beck, R. (1997). A new approach to the radio-far infrared correlation for non-calorimeter galaxies. *Astronomy and Astrophysics*, 320:54–64.

Niklas, S., Klein, U., and Wielebinski, R. (1997). A radio continuum survey of Shapley-Ames galaxies at λ 2.8cm. II. Separation of thermal and non-thermal radio emission. *Astronomy and Astrophysics*, 322:19–28.

Oey, M. S., Lamb, J. B., Kushner, C. T., Pellegrini, E. W., and Graus, A. S. (2013). A sample of ob stars that formed in the field. *The Astrophysical Journal*, 768(1):66.

Oey, M. S., Suntzeff, N., Hesser, J., and Bohlender, D. (1999). Superbubbles in the Magellanic Clouds. In Chu, Y. H., editor, *New Views of the Magellanic Clouds*, volume 190, page 78.

Oliveira, J. M., van Loon, J. T., Sloan, G. C., Sewilo, M., Kraemer, K. E., Wood, P. R., Indebetouw, R., Filipovic, M. D., Crawford, E. J., Wong, G. F., Hora, J. L., Meixner, M., Robitaille, T. P., Shiao, B., and Simon, J. D. (2012). Early-stage young stellar objects in the Small Magellanic Cloud. *Monthly Notices of the Royal Astronomical Society*, 428(4):3001–3033.

Ortiz, R. (2013). A revised distance scale of planetary nebulae. *Astronomy and Astrophysics*, 560:A85.

Osterbrock, D. E. (1973). Introductory report: The origin and evolution of planetary nebulae. In Remy-Battiau, L., Vreux, J. M., and Menzel, D. H., editors, *Liege International Astrophysical Colloquia*, volume 18 of *Liege International Astrophysical Colloquia*, pages 391–402.

Osterbrock, D. E. and O'dell, C. R. (1968). Planetary Nebulae. In Osterbrock, D. E. and O'dell, C. R., editors, *Planetary nebulae, proceedings from IAU Symposium no. 34.*, volume 34.

Paczyński, B. (1970). Evolution of Single Stars. I. Stellar Evolution from Main Sequence to White Dwarf or Carbon Ignition. *Acta Astronomica*, 20:47.

Panagia, N. and Felli, M. (1975). The spectrum of the free-free radiation from extended envelopes. *Astronomy and Astrophysics*, 39:1–5.

Parker, Q. A., Acker, A., Frew, D. J., Hartley, M., Peyaud, A. E. J., Ochsenbein, F., Phillipps, S., Russeil, D., Beaulieu, S. F., Cohen, M., Koppen, J., Miszalski, B., Morgan, D. H., Morris, R. A. H., Pierce, M. J., and Vaughan, A. E. (2006). The Macquarie/AAO/Strasbourg H Planetary Nebula Catalogue: MASH. *Monthly Notices of the Royal Astronomical Society*, 373(1):79–94.

Parker, Q. A., Bojicic, I., and Frew, D. J. (2016). HASH: the Hong Kong/AAO/Strasbourg H-alpha planetary nebula database. 11th Pacific Rim Conference held in Hong-kong in Dec 2015 Subjects: Solar and Stellar Astrophysics (astro-ph.SR).

Parker, Q. A., Cohen, M., Stupar, M., Frew, D. J., Green, A. J., Bojicic, I., Guzman-Ramirez, L., Sabin, L., and Vogt, F. (2012). Discovery of planetary nebulae using predictive mid-infrared diagnostics. *Monthly Notices of the Royal Astronomical Society*, 427:3016–3028.

Parker, Q. A., Phillipps, S., Pierce, M. J., Hartley, M., Hambly, N. C., Read, M. A., MacGillivray, H. T., Tritton, S. B., Cass, C. P., Cannon, R. D., Cohen, M., Drew, J. E., Frew, D. J., Hopewell, E., Mader, S., Malin, D. F., Masheder, M. R. W., Morgan, D. H., Morris, R. A. H., Russeil, D., Russell, K. S., and Walker, R. N. F. (2005). The AAO/UKST

SuperCOSMOS Hα survey. *Monthly Notices of the Royal Astronomical Society*, 362(2):689–710.

Pavlovic, M. Z., Urosevic, D., Vukotic, B., Arbutina, B., and Goker, U. D. (2013). The radio surface brightness to diameter relation for galactic supernova remnants: sample selection and robust analysis with various fitting offsets. *The Astrophysical Journal Supplement*, 204(1):16.

Payne, J. L., Filipovic, M. D., Crawford, E. J., de Horta, A. Y., White, G. L., and Stootman, F. H. (2008). Optical Spectra of Radio Planetary Nebulae in the Small Magellanic Cloud. *Serbian Astronomical Journal*, 176:65–70.

Payne, J. L., Filipovic, M. D., Reid, W., Jones, P. A., Staveley-Smith, L., and White, G. L. (2004). An ATCA radio-continuum study of the Small Magellanic Cloud - II. Source identification and classification. *Monthly Notices of the Royal Astronomical Society*, 355:44–50.

Payne, J. L., White, G. L., Filipovic, M. D., and Pannuti, T. G. (2007). An ATCA radio-continuum study of the Small Magellanic Cloud - V. Long-slit optical spectroscopy of supernova remnants and confirmation of a new candidate supernova remnant. *Monthly Notices of the Royal Astronomical Society*, 376:1793–1804.

Payne-Gaposchkin, C. H. (1971). The variable stars of the Large Magellanic Cloud. *Smithson. Contrib. Astrophys*, 13.

Pazderska, B. M., Gawroski, M. P., Feiler, R., Birkinshaw, M., Browne, I. W. A., Davis, R., Kus, A. J., Lancaster, K., Lowe, S. R., Pazderski, E., Peel, M., and Wilkinson, P. N. (2009). Survey of planetary nebulae at 30 GHz with OCRA-p. *Astronomy and Astrophysics*, 498(2):463–470.

Phillips, J. P. (2002). The Distances of Planetary Nebulae: A Scale Based upon Nearby Sources. *The Astrophysical Journal Supplement Series*, 139(1):199–217.

Pietrzyński, G., Graczyk, D., Gieren, W., Thompson, I. B., Pilecki, B., Udalski, A., Soszyński, I., Kozłowski, S., Konorski, P., Suchomska, K., Bono, G., Moroni, P. G. P., Villanova, S., Nardetto, N., Bresolin, F., Kudritzki, R. P., Storm, J., Gallenne, A., Smolec, R., Minniti, D., Kubiak, M., Szymański, M. K., Poleski, R., Wyrzykowski, L., Ulaczyk, K., Pietrukowicz, P., Górski, M., and Karczmarek, P. (2013). An eclipsing-binary distance to the Large Magellanic Cloud accurate to two per cent. *Nature*, 495(7439):76–9.

Pottasch, S. R. (1984). *Planetary nebulae*, volume 107 of *Astrophysics and space science library ;*. D. Reidel ;Distributed in the U.S. by Kluwer Academic,, Dordrecht ;Boston :Hingham, Mass.

Powell, J., Gossan, S. E., Logue, J., and Heng, I. S. (2016). Inferring the core-collapse supernova explosion mechanism with gravitational waves. *Physical Review D*, 94:12–15.

Prialnik, D. (2010). *An introduction to the theory of stellar structure and evolution.* Cambridge University Press, Cambridge New York, 2 edition.

Reid, W. and Parker, Q. (2008). Spectral Diagnostics, Kinematics and Abundances Based on a New Population of Planetary Nebulae Discovered in the LMC. In Koribalski, B. and Jerjen, H., editors, *Galaxies in the Local Volume, Astrophysics and Space Science Proceedings*, volume 5, pages 325–326. Springer Netherlands.

Reid, W. A. (2014). A multiwavelength analysis of planetary nebulae in the Large Magellanic Cloud. *Monthly Notices of the Royal Astronomical Society*, 438:2642–2663.

Reid, W. A. and Parker, Q. A. (2006a). A new population of planetary nebulae discovered in the Large Magellanic Cloud - I. Preliminary sample. *Monthly Notices of the Royal Astronomical Society*, 365(2):401–413.

Reid, W. A. and Parker, Q. A. (2006b). A new population of planetary nebulae discovered in the Large Magellanic Cloud - II. Complete PN catalogue. *Monthly Notices of the Royal Astronomical Society*, 373(2):521–550.

Reid, W. A. and Parker, Q. A. (2010). A new population of planetary nebulae discovered in the Large Magellanic Cloud - III. The luminosity function. *Monthly Notices of the Royal Astronomical Society*, 405:1349–1374.

Reid, W. A. and Parker, Q. A. (2013). A new population of planetary nebulae discovered in the Large Magellanic Cloud (IV): the outer LMC. *Monthly Notices of the Royal Astronomical Society*, 436(1):604–624.

Reid, W. A., Payne, J. L., Filipovic, M. D., Danforth, C. W., Jones, P. A., White, G. L., and Staveley-Smith, L. (2006). An ATCA radio-continuum study of the Small Magellanic Cloud - IV. A multifrequency analysis of the N66 region. *Monthly Notices of the Royal Astronomical Society*, 367:1379–1393. DOI: 10.1111/j.1365-2966.2006.10017.x.

Rohlfs, K. and Wilson, T. L. (2004). *Tools of radio astronomy.* Astronomy and astrophysics library,. Springer, Berlin ; New York, 4th rev. and enl. edition.

Rubele, S., Girardi, L., Kerber, L., Cioni, M.-R. L., Piatti, A. E., Zaggia, S., Bekki, K., Bressan, A., Clementini, G., de Grijs, R., Emerson, J. P., Groenewegen, M. A. T., Ivanov, V. D., Marconi, M., Marigo, P., Moretti, M.-I., Ripepi, V., Subramanian, S., Tatton, B. L.,

and van Loon, J. T. (2015). The VMC survey - XIV. First results on the look-back time star formation rate tomography of the Small Magellanic Cloud. *Monthly Notices of the Royal Astronomical Society*, 449(1):639–661.

Rubele, S., Kerber, L., and Girardi, L. (2010). The star-formation history of the Small Magellanic Cloud star cluster NGC 419. *Monthly Notices of the Royal Astronomical Society*, 403:1156–1164.

Saito, M. and Matsumoto, M. (2008). SIMD-oriented fast Mersenne Twister: a 128-bit pseudorandom number generator. *Monte Carlo and Quasi-Monte Carlo Methods . . .*, (18654021):1–15.

Salpeter, E. E. (1955). The Luminosity Function and Stellar Evolution. *The Astrophysical Journal*, 121:161.

Sandage, A. and Tammann, G. A. (1981). *A revised Shapley-Ames catalog of bright galaxies*. Carnegie Institution of Washington publication ; 635. Carnegie Institution of Washington, Washington, D.C. Allan Sandage and G.A. Tammann. ill. ; 32 cm.

Sanduleak, N., MacConnell, D. J., and Davis Philip, A. G. (1978). The planetary nebula systems of the Magellanic Clouds. *Publications of the Astronomical Society of the Pacific*, 90:621.

Sault, R. J., Teuben, P., and Wright, M. C. H. (2011). MIRIAD: Multi-channel Image Reconstruction, Image Analysis, and Display. Astrophysics Source Code Library.

Sault, R. J., Teuben, P. J., and Wright, M. C. H. (1995). A Retrospective View of MIRIAD. *ASP Conf. Ser. 77: Astronomical Data Analysis Software and Systems IV*, 77:433.

Schlegel, D. J., Finkbeiner, D. P., and Davis, M. (1998). Maps of dust infrared emission for use in estimation of reddening and cosmic microwave background radiation foregrounds. *The Astrophysical Journal*, 500:525.

Schleicher, D. R. G. and Beck, R. (2013). A new interpretation of the far-infrared - radio correlation and the expected breakdown at high redshift. *Astronomy and Astrophysics*, 556:12.

Schmidt, M. (1959). The rate of star formation. *The Astrophysical Journal*, 129:243.

Schoenberner, D. (1983). Late stages of stellar evolution. II - Mass loss and the transition of asymptotic giant branch stars into hot remnants. *The Astrophysical Journal*, 272:708.

Schwering, P. B. W. and Israel, F. P. (1993). *IR sources in Magellanic Clouds (Schwering+ 1990)*, volume 2181 of *VizieR Online Data Catalog*. Machine readable data available in Downloads directory.

Scilab (2013). Scilab. Open source software from https://www.scilab.org/.

Scowen, P., Jansen, R., Beasley, M., and Calzetti, D. (2010). The Magellanic Clouds Survey: a Bridge to Nearby Galaxies (2010).

Shapley, H. (1957). *The inner metagalaxy.*

Shapley, H. (1961). *Galaxies.*

Shaw, R. a., Lee, T.-H., Stanghellini, L., Davies, J. E., García-Hernández, D. a., García-Lario, P., Perea-Calderón, J. V., Villaver, E., Manchado, A., Palen, S., and Balick, B. (2010). A Detailed Look At Chemical Abundances in Magellanic Cloud Planetary Nebulae. I. the Small Magellanic Cloud. *The Astrophysical Journal*, 717(1):562–576.

Shaw, R. A., Reid, W. A., and Parker, Q. A. (2007). Confirmation of New Planetary Nebulae in the Large Magellanic Cloud. *Publications of the Astronomical Society of the Pacific*, 119(851):19–29.

Shaw, R. A., Stanghellini, L., Mutchler, M., Balick, B., and Blades, J. C. (2001). Morphology and Evolution of the Large Magellanic Cloud Planetary Nebulae. *The Astrophysical Journal*, 548(2):727–748.

Shaw, R. A., Stanghellini, L., Villaver, E., and Mutchler, M. (2006). Hubble Space Telescope Images of Magellanic Cloud Planetary Nebulae. *The Astrophysical Journal, Supplement*, 167:201–229.

Shklovskii, I. S. (1960). Secular Variation of the Flux and Intensity of Radio Emission from Discrete Sources. *Astronomicheskii Zhurnal*, 37.

Siódmiak, N. and Tylenda, R. (2001). An analysis of the observed radio emission from planetary nebulae. *Astronomy and Astrophysics*, 373:1032–1042.

Smith, C., Leiton, R., and Pizarro, S. (2000). The UM/CTIO Magellanic Cloud Emission Line Survey (MCELS). In Alloin, D., Knut, O., and Galaz, G., editors, *Stars, Gas and Dust in Galaxies: Exploring the Links*, volume 221, page 83, San Francisco. Astronomical Society of the Pacific.

Smith, H. (2014). On the distances of planetary nebulae. *Monthly Notices of the Royal Astronomical Society*, 449(3):2980–3005.

Sreekumar, P. and Fichtel, C. E. (1991). Cosmic rays in the Small Magellanic Cloud. *Astronomy and Astrophysics*, 251:447–453.

Stanghellini, L., Blades, J. C., Osmer, S. J., Barlow, M. J., and Liu, X.-W. (1999). Hubble Space Telescope Images of Magellanic Cloud Planetary Nebulae: Data and Correlations across Morphological Classes. *ApJ*, 510:687–702.

Stanghellini, L., Shaw, R. A., Balick, B., Mutchler, M., Blades, J. C., and Villaver, E. (2003). Space Telescope Imaging Spectrograph Slitless Observations of Small Magellanic Cloud Planetary Nebulae: A Study on Morphology, EmissionLine Intensity, and Evolution. *The Astrophysical Journal*, 596(2):997–1014.

Stanimirovic, S., Staveley-Smith, L., Dickey, J. M., Sault, R. J., and Snowden, S. L. (1999). The large-scale HI structure of the Small Magellanic Cloud . *Monthly Notices of the Royal Astronomical Society*, 302:417–436.

Stark, J. L., Murtagh, F., and Bijaoui, A. (1998). *Image Processing and Data Analysis: The Multiscale Approach*. Cambridge University Press, 1 edition.

Staveley-Smith, L., Sault, R. J., Hatzidimitriou, D., Kesteven, M. J., and McConnell, D. (1997). An HI aperture synthesis mosaic of the Small Magellanic Cloud. *Monthly Notices of the Royal Astronomical Society*, 289:225–252.

Staveley-Smith, L., Sault, R. J., McConnell, D., Kesteven, M. J., Hatzidimitriou, D., Freeman, K. C., and Dopita, M. A. (1995). An HI Mosaic of the Small Magellanic Cloud. *Publications of the Astronomical Society of Australia*, 12:13.

Sterling, N. C. and Dinerstein, H. L. (2008). The Abundances of Light NeutronCapture Elements in Planetary Nebulae. II. s Process Enrichments and Interpretation1. *The Astrophysical Journal Supplement Series*, 174(1):158–201.

Stevens, J., Wark, R., and Edwards, P. (2014). ATCA Users Guide. Technical Report October, CSIRO.

Strauss, M. A., Davis, M., Yahil, A., and Huchra, J. P. (1990). A redshift survey of IRAS galaxies. I - Sample selection. *The Astrophysical Journal*, 361:49.

Strauss, M. A., Huchra, J. P., Davis, M., Yahil, A., Fisher, K. B., and Tonry, J. (1992). A redshift survey of IRAS galaxies. VII - The infrared and redshift data for the 1.936 Jansky sample. *The Astrophysical Journal Supplement Series*, 83:29.

Subramanian, S. and Subramaniam, A. (2009). Depth estimation of the Large and Small Magellanic Clouds. *Astronomy and Astrophysics*, 496(2):399–412.

Taylor, A. R., Pottasch, S. R., and Zhang, C. Y. (1987). Radio continuum spectra of compact planetary nebulae - A wind-shell model. *Astronomy and Astrophysics*, 171:178–188.

Terzian, Y. (1989). Radio images of planetary nebulae. In *IAU Symposium No. 131: Planetary nebulae*, volume 131, pages 17–28.

Thackeray, A. D. and Wesselink, A. J. (1953). The Distances of the Magellanic Clouds. *Monthly Notes of the Astronomical Society of South Africa*, 12:33.

Thompson, T. A., Quataert, E., Waxman, E., Murray, N., and Martin, C. L. (2006). Magnetic fields in starburst galaxies and the origin of the fir-radio correlation. *The Astrophysical Journal*, 645:186–198.

Tremblay, P. E., Cummings, J., Kalirai, J. S., Gaensicke, B. T., Gentile-Fusillo, N., and Raddi, R. (2016). The Field White Dwarf Mass Distribution. *Monthly Notices of the Royal Astronomical Society*, 461(2):2100–2114.

Turtle, A. J., Ye, T., Amy, S., and Nicholls, J. (1998). A Radio Survey of the SMC at 843 MHz with the MOST: I. The Survey. *Publications of the Astronomical Society of Australia*, 15(03):280–298.

Tylenda, R. (1989). Planetary nebulae with massive central stars. In *IAU Symposium*, volume 131, pages 531–537. Cambridge University Press.

Udalski, A., Szymanski, M., Kubiak, M., Pietrzynski, G., Soszynski, I., Wozniak, P., and Zebrun, K. (2000). The Optical Gravitational Lensing Experiment. BVI Maps of Dense Stellar Regions. II. The Large Magellanic Cloud. *Acta Astronomica*, 50:307–335.

Udalski, A., Szymanski, M., Kubiak, M., Pietrzynski, G., Wozniak, P., and Zebrun, K. (1998). The Optical Gravitational Lensing Experiment. BVI Maps of Dense Stellar Regions. I. The Small Magellanic Cloud. *Acta Astronomica*, 48:147–174.

Urošević, D., Pannuti, T. G., Duric, N., and Theodorou, A. (2005). The Σ D relation for supernova remnants in nearby galaxies. *Astronomy and Astrophysics*, 435(2):437–447.

Urošević, D., Pavlović, M. Z., and Arbutina, B. (2018). On the foundation of equipartition in supernova remnants. *The Astrophysical Journal, Volume 855, Issue 1, article id. 59, 8 pp. (2018).*, 855(59):8.

Urosevic, D., Vukotic, B., Arbutina, B., and Ilic, D. (2007). The Σ D relation for planetary nebulae: Preliminary analysis. *Serbian Astronomical Journal*, 174(174):73–77.

Urošević, D., Vukotić, B., Arbutina, B., Ilić, D., Filipović, M., Bojičić, I., Segan, S., and Vidojević, S. (2009). The Σ-D relation for planetary nebulae. *Astronomy and Astrophysics*, 495:537–546.

van den Berg, J. C., editor (2004). *Wavelets in Physics*. Cambridge University Press.

Van den Bergh, S. (2000). *The galaxies of the Local Group*. Cambridge University Press, Cambridge, UK.

van der Kruit, P. C. (1971). Observations of core sources in seyfert and normal galaxies with the westerbork synthesis radio telescope at 1415 mhz. *Astronomy and Astrophysics*, 15:110–122.

van der Marel, R. P. and Kallivayalil, N. (2014). Third-Epoch Magellanic Cloud Proper Motions II: The Large Magellanic Cloud Rotation Field in Three Dimensions. *The Astrophysical Journal*, 781(2):20.

Vassiliadis, E., Dopita, M. A., Meatheringham, S. J., Bohlin, R. C., Ford, H. C., Harrington, J. P., Wood, P. R., Stecher, T. P., and Maran, S. P. (1998). Hubble Space Telescope Observations of Planetary Nebulae in the Magellanic Clouds. VII. Cycle 3 and Archive Narrowband [O III] 500.7 nanometer Imaging. *ApJ*, 503:253–277.

Verter, F. (1987). Systematic properties of CO emission from galaxies. I - Luminosity function. *The Astrophysical Journal Supplement Series*, 65:555–580.

Voelk, H. J. (1989). The correlation between radio and far-infrared emission for disk galaxies - A calorimeter theory. *Astronomy and Astrophysics*, 218:67–70.

von Humboldt, A. (1866). *Cosmos*. Harper & Brothers, New York, Vol. II. edition.

Vukotic, B., Jurkovic, M., Urosevic, D., and Arbutina, B. (2014). On calibration of some distance scales in astrophysics. *Monthly Notices of the Royal Astronomical Society*, 440(3):2026–2035.

Vukotić, B. and Urošević, D. (2012). The Σ D relation for Galactic planetary nebulae: Application of orthogonal fitting procedure. *Proceedings of the International Astronomical Union*, 7(S283):522–523.

Vukotić, B., Urošević, D., Filipović, M. D., and Payne, J. L. (2009). The Σ-D analysis of recently detected radio planetary nebulae in the Magellanic Clouds. *Astronomy and Astrophysics*, 503:855–858.

Wachter, A., Schröder, K.-P., Winters, J. M., Arndt, T. U., and Sedlmayr, E. (2002). An improved mass-loss description for dust-driven superwinds and tip-AGB evolution models. *Astronomy and Astrophysics*, 384(2):452–459.

Wasserman, L. (2005). *All of Statistics : A Concise Course in Statistical Inference Brief Contents*.

Weingartner, J. C. and Draine, B. T. (2001). Dust grain-size distributions and extinction in the milky way, large magellanic cloud, and small magellanic cloud. *The Astrophysical Journal*, 548:296–309.

Welch, D. L., McLaren, R. A., Madore, B. F., and McAlary, C. W. (1987). Distance moduli and structure of the Magellanic Clouds from near-infrared photometry of classical Cepheids. *The Astrophysical Journal*, 321:162.

Wenger, M., Ochsenbein, F., Egret, D., Dubois, P., Bonnarel, F., Borde, S., Genova, F., Jasniewicz, G., Lalo, S., Lesteven, S., and Monier, R. (2000). The SIMBAD astronomical database. *Astronomy and Astrophysics Supplement Series*, 143(1):9–22.

Westerlund, B. (1961). Population I in the Large Magellanic Cloud. *Uppsala Astronomical Observatory Annals*, 5:1.

Westerlund, B. E. (1997). *The Magellanic Clouds*. Cambridge astrophysics series ; 29. Cambridge University Press, New York.

Westerlund, B. E. and Smith, L. F. (1964). Planetary nebulae in the Large Magellanic Cloud. *Monthly Notices of the Royal Astronomical Society*, 127:449.

Whittet, D. (2002). *Dust in the Galactic Environment, 2nd Edition (Series in Astronomy and Astrophysics)*. CRC Press.

Wilcots, E. M. (2008). The Evolution of the ISM in Star Forming Galaxies. In Koribalski, B. and Jerjen, H., editors, *Galaxies in the Local Volume, Astrophysics and Space Science Proceedings*, volume 5, pages 69–72. Springer Netherlands.

Wilson, T. L., Rohlfs, K., and Huettemeister, S. (2009). *Tools of radio astronomy*. Springer, Berlin ; New York, 5 edition.

Wong, G., Filipovic, M., Crawford, E., De, H., Galvin, T., Draskovic, D., and Payne, J. (2011a). New 20-cm radio-continuum study of the small Magellanic cloud: Part I. Images. *Serbian Astronomical Journal*, 182(182):43–52.

Wong, G., Filipovic, M., Crawford, E., Tothill, N., De, H., Draskovic, D., Galvin, T., Collier, J., and Payne, J. (2011b). New 20-cm radio-continuum study of the Small Magellanic Cloud, part II: Point sources. *Serbian Astronomical Journal*, 183(183):103–106.

Wong, G., Filipovic, M., Crawford, E., Tothill, N., De, H., and Galvin, T. (2012a). New 20-cm radio-continuum study of the small Magellanic cloud - part III: Compact Hii regions. *Serbian Astronomical Journal*, 185(185):53–64.

Wong, G. F., Crawford, E. J., Filipović, M. D., De Horta, A. Y., Tothill, N. F. H., Collier, J. D., Drasković, D., Galvin, T. J., and Payne, J. L. (2012b). New 6 and 3-cm radio-continuum maps of the Small Magellanic Cloud: Part II - Point source catalogue. *ArXiv e-prints*, 1203:4310.

Wong, G. F., Filipovic, M. D., Crawford, E. J., de Horta, A. Y., Galvin, T., Draskovic, D., and Payne, J. L. (2011c). New 20-cm Radio-Continuum Study of the Small Magellanic Cloud: Part I - Images. *Serbian Astronomical Journal*, 182:43–52.

Wong, G. F., Filipovic, M. D., Crawford, E. J., Tothill, N. F. H., de Horta, A. Y., Draskovic, D., Galvin, T. J., Collier, J. D., and Payne, J. L. (2011d). New 20-cm Radio-Continuum Study of the Small Magellanic Cloud: Part II - Point Sources. *Serbian Astronomical Journal*, 183:103–106.

Xu, C., Klein, U., Meinert, D., Wielebinski, R., and Haynes, R. F. (1992). A radio continuum study of the Magellanic Clouds. II - The far-infrared/radio correlation in the Large Magellanic Cloud. *Astronomy and Astrophysics*, 257:47–62.

Ye, T. and Turtle, A. J. (1991). The extended non-thermal radio emission from the Small Magellanic Cloud. *Monthly Notices of the Royal Astronomical Society*, 249:693–697.

Ye, T. S., Amy, S. W., Wang, Q. D., Ball, L., and Dickel, J. (1995). SNR:0101-7226 - a Shell-Type Supernova Remnant in the Small Magellanic Cloud with no X-Ray Emission. *Monthly Notices of the Royal Astronomical Society*, 275.

Young, J. S. and Scoville, N. Z. (1991). Molecular gas in galaxies. *Annual Review of Astronomy and Astrophysics*, 29:581–625.

Yun, M. S., Reddy, N. A., and Condon, J. J. (2001). Radio Properties of Infrared-selected Galaxies in the IRAS 2 Jy Sample. *The Astrophysical Journal*, 554:803–822.

Zaritsky, D., Harris, J., Grebel, E. K., and Thompson, I. B. (2000). The Morphologies of the Small Magellanic Cloud. *The Astrophysical Journal*, 534:L53–L56.

Zijlstra, A. (2006). Mass loss on the Asymptotic Giant Branch. In Barlow, M. J. and Méndez, R. H., editors, *Planetary Nebulae in our Galaxy and Beyond*, volume 234, pages 55–62, Cambridge: Cambridge. Proceedings of the International Astronomical Union.

Zijlstra, A. A. (1990). A radio study of planetary nebulae. *Astronomy and Astrophysics (ISSN 0004-6361)*, 234:387–395.

Zijlstra, A. A., van Hoof, P. A. M., and Chapman, J. M. andLoup, C. (1994). Radio and infrared emission from a [WC]-type planetary nebula in the LMC. *Astronomy and Astrophysics*, 290:228–234.